Fundamental Studies of the Uptake and Diffusion of Sulfur Mustard Simulants within Zirconium-based Metal-Organic Frameworks

Conor Hays Sharp

Dissertation submitted to the faculty of the
Virginia Polytechnic Institute and State University
in partial fulfillment of the requirements for the degree of

DOCTOR OF PHILOSOPHY
in
Chemistry

John R. Morris, Chair
Diego Troya
Amanda J. Morris
Ayman M. Karim

September 11, 2019
Blacksburg, VA

Keywords: Metal-Organic Framework, Chemical Warfare Agent, Sulfur Mustard, Adsorption, Diffusion, Desorption, Vacuum, Infrared Spectroscopy, Temperature Programmed Desorption

Copyright 2019, Conor Hays Sharp

Fundamental Studies of the Uptake and Diffusion of Sulfur Mustard Simulants within Zirconium-based Metal-Organic Frameworks

Conor Hays Sharp

ABSTRACT

The threat of chemical warfare agent (CWA) attacks has persisted into the 21st century due to the actions of terror groups and rogue states. Traditional filtration strategies for soldier protection rely on high surface area activated carbon, but these materials merely trap CWAs through weak physisorption. Metal-organic frameworks (MOFs) have emerged as promising materials to catalyze the degradation of CWAs into significantly less toxic byproducts. The precise synthetic control over the porosity, defect density, and chemical functionality of MOFs offer exciting potential of for use in CWA degradation as well as a wide variety of other applications. Developing a molecular-level understanding of gas-MOF interactions can allow for the rational design of MOFs optimized for CWA degradation. Our research investigated the fundamental interfacial interactions between CWA simulant vapors, specifically sulfur mustard (HD) simulants, and zirconium-based MOFs (Zr-MOFs). Utilizing a custom-built ultrahigh vacuum chamber with infrared spectroscopic and mass spectrometric capabilities, the adsorption mechanism, diffusion energetics, and diffusion kinetics of HD simulants were determined. For 2-chloroethyl ethyl sulfide (2-CEES), a widely used HD simulant, infrared spectroscopy revealed that adsorption within Zr-MOFs primarily proceeded through hydrogen bond formation between 2-CEES and the bridging hydroxyls on the secondary building unit of the MOFs. Through the study of 1-chloropentane and diethyl sulfide adsorption, we determined that 2-CEES forms hydrogen bonds through its chlorine atom likely due to geometric constraints within the MOF pore environment. Temperature programmed desorption experiments aimed at determining desorption energetics reveal that 2-CEES remain adsorbed within the pores of the MOFs until high temperatures, but traditional methods of TPD analysis fail to accurately measure both the enthalpic and entropic interactions of 2-CEES desorption from a single adsorption site. Infrared spectroscopy was able to measure the diffusion of adsorbates within MOFs by tracking the rate of decrease in overall adsorbate concentrations at several temperatures. The results indicate that 2-CEES diffusion through the pores of the MOFs is a slow, activated process that is affected by the size of the pore windows and presence of hydrogen bonding sites. We speculate that diffusion is the rate limiting step in the desorption of HD simulants through Zr-MOFs at lower temperatures. Stochastic simulations were performed in an attempt to deconvolute TPD data in order to extract desorption parameters. Finally, a combination of vacuum-based and ambient-pressure spectroscopic techniques were employed to study the reaction between 2-CEES and an amine-functionalized MOF, UiO-66-NH_2. Although the presence of water adsorbed within UiO-66-NH_2 under ambient conditions may assist in the reactive adsorption of 2-CEES, the reaction proceeded under anhydrous conditions.

Fundamental Studies of the Uptake and Diffusion of Sulfur Mustard Simulants within Zirconium-based Metal-Organic Frameworks

Conor Hays Sharp

GENERAL AUDIENCE ABSTRACT

Chemical warfare agents (CWAs) are some of the most toxic chemicals on the planet and their continued use by terror groups and rogue nations threaten the lives of both civilians and the warfighter. Our work was motivated by a class of high surface area, highly porous materials that have shown the ability to degrade CWAs, specifically mustard gas, into less harmful byproducts. By determining the adsorption mechanism (how and where mustard gas "sticks" to the material), diffusion rates (how quickly mustard gas can travel through the pores of to reach the binding sites), and desorption energies (how strongly mustard gas "sticks" to the binding sites), we can alter the structure of these materials and to efficiently trap mustard gas and render it harmless. In the research described in this dissertation, we examined these fundamental interactions for a series of molecules that mimic the structure of mustard gas. and linear alkanes within several metal-organic frameworks with varying pore size. We observed the size of the pore environment affects the orientation that a given molecule sticks to binding sites as well as how quickly these compounds diffuse through the MOF. While the majority of these studies were conducted in a low-pressure environment that eliminated the presence of gas molecules in the atmosphere, research that exposed a MOF to a mustard gas mimic in an ambient environment demonstrated that gas molecules present in the atmosphere, especially water, can greatly impact the chemical interactions between mustard gas and zirconium-based MOFs.

for Cheryl

Acknowledgements

While I am the sole author of this dissertation, a countless number of people have contributed to the creation of this document through assistance both within and outside of lab. It takes a village to raise a child and it felt like it took an entire scientific community to raise this graduate student. Below are some notable examples:

Aliya, this all begins and ends with you. You are my compass, and without you, I would have been completely lost. You consoled me during my toughest weeks, celebrated my greatest successes, and helped energize me whenever I got stagnant. Your endless love, support, and patience throughout this journey has only reinforced the knowledge that you are the best friend I have and the best person I know. I am so excited for our life together.

To my family, especially my parents, thank you for everything that you have done to support my graduate school experience. From temporarily funding instrument purchases, to helping house graduate students, to providing some needed perspective as former Ph.D. students, to even a simple phone call wishing me the best, your support has meant everything to me.

Darren and Tyler, you two were my life support here in Blacksburg seemingly from the moment I stepped on campus. I am so grateful not just for how much you taught me and pushed me in graduate school, but also for how much fun we had along the way. I did not foresee having friends as good as you both, but looking back, I don't see how I would have succeeded without you two.

Thank you to John Morris first for finding enough space in your lab to accommodate me and two other incoming graduate students in one year. As your student, you exposed me to a wide variety of research opportunities both at Virginia Tech and abroad, tirelessly promoted my mental health, and fostered my growth and independence as a scientist.

Thank you to Thomas Edwards for providing me with much needed emotional and technical support throughout these past four years. I feel blessed that our paths crossed during graduate school. You were the best roommate that I have had (except for Aliya).

I am very appreciative of all the current and former members of the John Morris group who taught me how to perform experiments, sat in on countless group meeting presentations, assisted me with experiments, and made life working in the basement tolerable. I may have been the person who moved Richard Petty at night, but you are the people who moved me to make lab fun.

I would like to express my gratitude to all of my colleagues in the MultiRAD collaboration, especially Wes Gordon, Diego Troya, Anatoly Frenkel, Craig Hill, Jamaal Musaev, and Mark Mitchell. Your research insights, collaborations, and discussions were critical in my development as a scientist.

Thank you to Frances Houle for your help in learning Kinetiscope, including me in your group's biweekly research meetings, and for all of our incredibly useful discussions.

The Chemistry Department at Virginia Tech is a special place filled with special people. I am grateful for the faculty, research scientists, support staff, and students who graced the halls of Hahn Hall South and Davidson hall while I have been here.

Lastly, I would like to thank all of my former science teachers and chemistry professors, especially Chris Rodger, Stacy Brasfield, Dr. David Statman, Dr. S. Shaun Murphree, and Dr. Ryan Van Horn. You all cultivated my curiosity and taught me that science is so much more than rote memorization. Chemistry is the poetry of life, and you all showed me how to read the sonnets and identify the rhyming pattern.

Table of Contents

Attributions

The work in **Chapter 3** of this dissertation has been previously published in the journal *Journal of Physical Chemistry, C,* with the following reference:

Sharp, C.H.; Abelard, J.; Plonka, A.M.; Guo, W.; Hill, C.L.; Morris, J.R., *The Journal of Physical Chemistry C* **2017**, *121* (16), 8902-8906.

In this work, Conor Sharp collected the experimental spectra, developed the data analysis method, and performed the diffusion data analysis. Wewei Guo synthesized the metal-organic framework used in the manuscript. Thomas Edwards assisted in the development of the MATLAB program.

The work in **Chapter 4** of this dissertation is in manuscript preparation, with the following reference:

Sharp, C.H.; Usov, P.M.; Bonnett, Gordon, W.O.; B.; Jones, N.B.; Troya, D.; Morris, A.J.; Morris, J.R., The Adsorption and Diffusion of Mustard Gas Simulants within Zr-based MOFs, *In Preparation*

In this work, Conor Sharp collected and analyzed the infrared spectra for adsorption and diffusion with assistance from Nathan Jones. Pavel Usov, Brittany Bonnett, and Timur Islamoglu synthesized the UiO-66, UiO-67, and NU-1000 samples, respectively. Diego Troya provided calculated binding geometries of 2-CEES adsorption within UiO-66. Wesley Gordon provided the DRIFTS data for the adsorption of HD on UiO-66. Curt Zanelotti performed the PFG-NMR measurements for 2-CEES self-diffusion.

In **Chapter 5**, Conor Sharp collected the TPD data, performed the TPD data analysis, and attempted to model the TPD spectra. Weiwei Guo, Brittany Bonnett, and Timur Islamoglu synthesized the UiO-66, UiO-67, and NU-1000 samples, respectively. Frances Houle aided in the development of the Kinetiscope model for desorption

In **Chapter 6**, Conor Sharp collected the IR data for the adsorption and diffusion of HD simulants through UiO-66. Pavel Usov synthesized and characterized the UiO-66 sample.

In **Chapter 7**, Conor Sharp collected the TPD data, DR-UV-Vis data, and analyzed the ATR data, XPS data, DR-UV-Vis data, and IR data. The UiO-66-NH_2 sample was provided by Gregory Peterson at the CBC lab. Xu Feng of the VT Surface Analysis Lab collected the XPS spectra. Emerald Greene collected the ATR-IR data. Harrison Siegel collected the PXRD data. Nick Sapienza lent technical expertise to the vacuum-based exposure of UiO-66-NH_2 to 2-CEES.

Publications

Sharp, C.H.; Usov, P.M.; Bonnett, B.; Troya, D.; Morris, A.J.; Morris, J.R., The Adsorption and Diffusion of Mustard Gas Simulants within Zr-based MOFs, *The Journal of Physical Chemistry C,* **2019,** *In Preparation*

Grissom, T.G.; Sharp, C.H.; Usov, P.M.; Troya, D.; Morris, A.J.; Morris, J.R., Benzene, Toluene, and Xylene Transport through UiO-66: Diffusion Rates, Energetics, and the Role of Hydrogen Bonding, *The Journal of Physical Chemistry C,* **2018**, *122* (28), 16060-16069.

Sharp, C.H.; Abelard, J.; Plonka, A.M.; Guo, W.; Hill, C.L.; Morris, J.R., Alkane–OH Hydrogen Bond Formation and Diffusion Energetics of *n*-Butane within UiO-66, *The Journal of Physical Chemistry C,* **2017**, *121* (16), 8902-8906.

Wang, G.; Sharp, C.H.; Plonka, A.M.; Wang, Frenkel, A.I.; Guo, W.; Hill, C.L.; Smith, C.; Kollar, J.; Troya, D.; Morris, J.R., Mechanism and Kinetics for Reaction of the Chemical Warfare Agent Simulant, DMMP (g), with Zirconium (IV) MOFs: An Ultrahigh-Vacuum and DFT Study, *The Journal of Physical Chemistry C,* **2017**, *121* (21), 11261-11272.

Wang, Q.; Chapleski Jr., R.C.; Plonka, A.M.; Gordon, W.O.; Guo, W.; Nguyen-Phan, T.D.; Sharp, C.H.; Marinkovic, N.S.; Senanayake, S.D; Morris, J.R.; Hill, C.L.; Troya, D.; Frenkel, A.I., Atomic-Level Structural Dynamics of Polyoxoniobates during DMMP Decomposition, *Scientific Reports.*, **2017**, *7*, 773.

Plonka, A.M.; Wang, Q.; Gordon, W.O.; Balboa, A.; Troya, D.; Guo, W.; Sharp, C.H.; Senanayake, S.D.; Morris, J.R.; Hill, C.L.; Frenkel, A.I., In Situ Proves of Capture and Decomposition of Chemical Warfare Agent Simulants by Zr-Based Metal Organic Frameworks, *Journal of the American Chemical Society*, **2017**, *139* (2), 599-602.

Chapter 1. Introduction, Motivations, and Background

1.1 Thesis Statement

The objective of this research was to develop a fundamental understanding of the molecular-level interactions between bis(2-chloroethyl) sulfide, commonly known as sulfur mustard, and zirconium-based metal-organic frameworks. Our ultimate goal is to design a zirconium-based metal-organic framework for the capture and degradation of sulfur mustard and other chemical warfare agents to protect military personnel and civilian populations from chemical attacks. By understanding how the chemical structure of each MOF affects the adsorption mechanism, binding strength, and reactivity for sulfur mustard, we can design a highly efficient chemical warfare agent degradation material that can sequester sulfur mustard and render it harmless.

1.2 Introduction to Chemical Warfare Agents

The term "chemical warfare agents (CWAs)" corresponds to a series of molecules with toxic or harmful properties deliberately used to inflict bodily harm on civilian and military populations. While the idea of chemical warfare has existed for several millennia (evidence exists that Hannibal distilled camel feces to use ammonia as a lachrymatory gas in 200 BC), modern chemical warfare began approximately 100 years ago. The four most common modern CWAs are sarin (GB), soman (GD), sulfur mustard (HD), and VX nerve gas (Structures are shown in Figure 1.1).[1] The first letter for each CWA acronym refers either to the nation that first synthesized the chemical or for its chemical properties. Nerve agents (such as GB, GD, and VX) irreversibly bind to acetylcholinesterase, leading to a lethal build-up of the neurotransmitter acetylcholine.[2] While GB and GD are volatile molecules commonly found in the gas phase, VX is a much more stable molecule, which allows it to persist and accumulate under ambient conditions.[1]

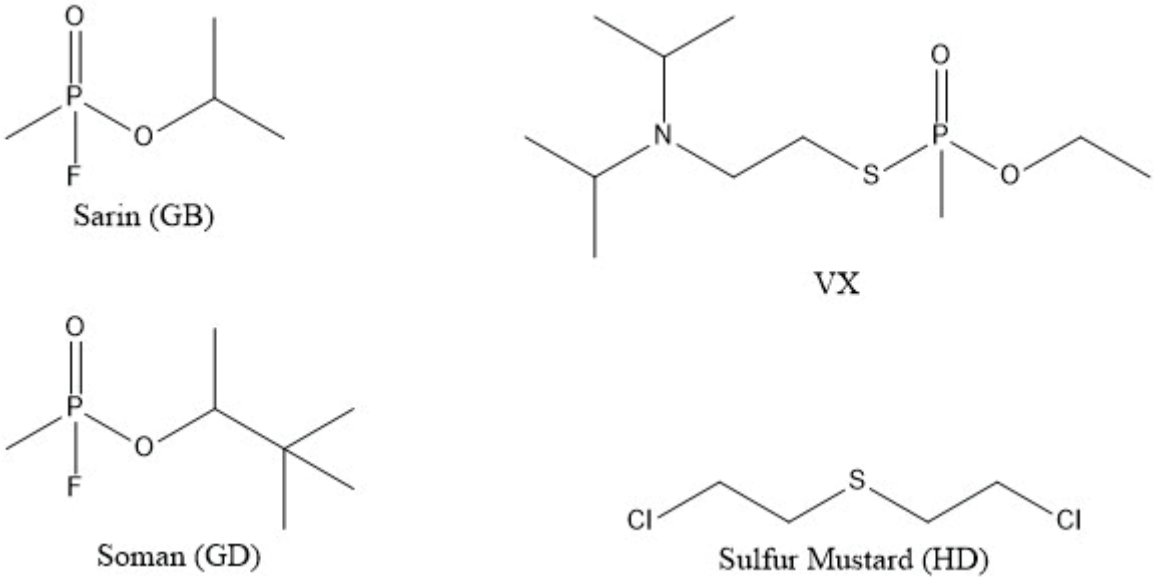

Figure 1.1 Common CWAs

1.2.1 Sulfur Mustard

HD represents a type of CWA known as vesicant agents. Vesicant agents cause the skin to blister.[3] Acute symptoms of HD poisoning include skin blisters, corneal damage, pulmonary edema, (buildup of fluid in the lungs), and diarrhea.[4] Additionally, HD is an alkylating agent that cross-links DNA, RNA, and proteins that can cause long-term tissue damage and cancer. The alkylation of DNA by HD proceeds through the formation of a thiiranium cation intermediate that undergoes a nucleophilic attack by the lone pairs of a guanine nucleotide in DNA (Figure 1.2).[3] The process then repeats for the second 2-chloroethyl side chain. The DNA crosslinking reaction also produces HCl as a reaction byproduct, which can further damage the body through acid burns.

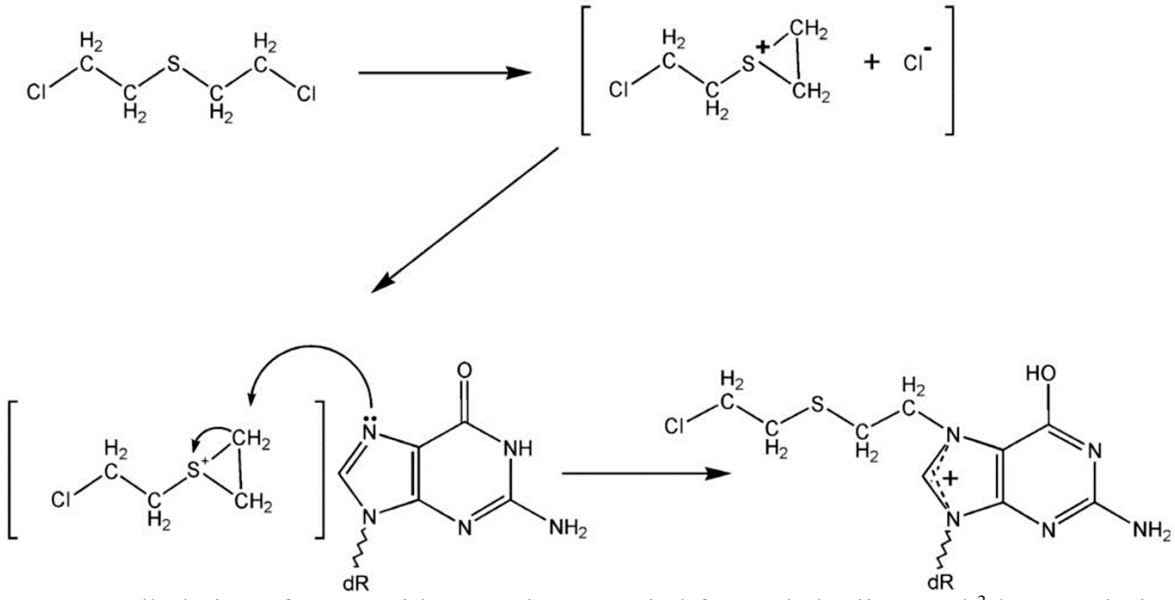

Figure 1.2 Alkylation of DNA with HD. Figure copied from Shakarjian et al.[3] by permission of Oxford University Press.

1.2.2 CWA Simulants

Due to the toxic nature of CWAs, experiments with the actual chemical agents are restricted to government facilities with the proper engineering controls and require specialized safety protocols. For CWA research within academic laboratories, simulants, molecules with similar chemical structures, are often used to mimic CWAs. There are several benefits to studying CWA simulants. First, most simulants are significantly less toxic than the CWA itself, allowing them to be safely handled in a lab setting with the appropriate personal protective equipment. Second, by studying the interactions of simulants with CWA-degradation sorbents and catalysts, researchers can perform experiments to develop structure-function relationships that provide insight into how each functional group on a CWA molecule affects its physical and chemical interactions with surfaces and other molecules. The chemical structures of several common simulants for both nerve agents and sulfur mustard are shown in Figure 1.3.

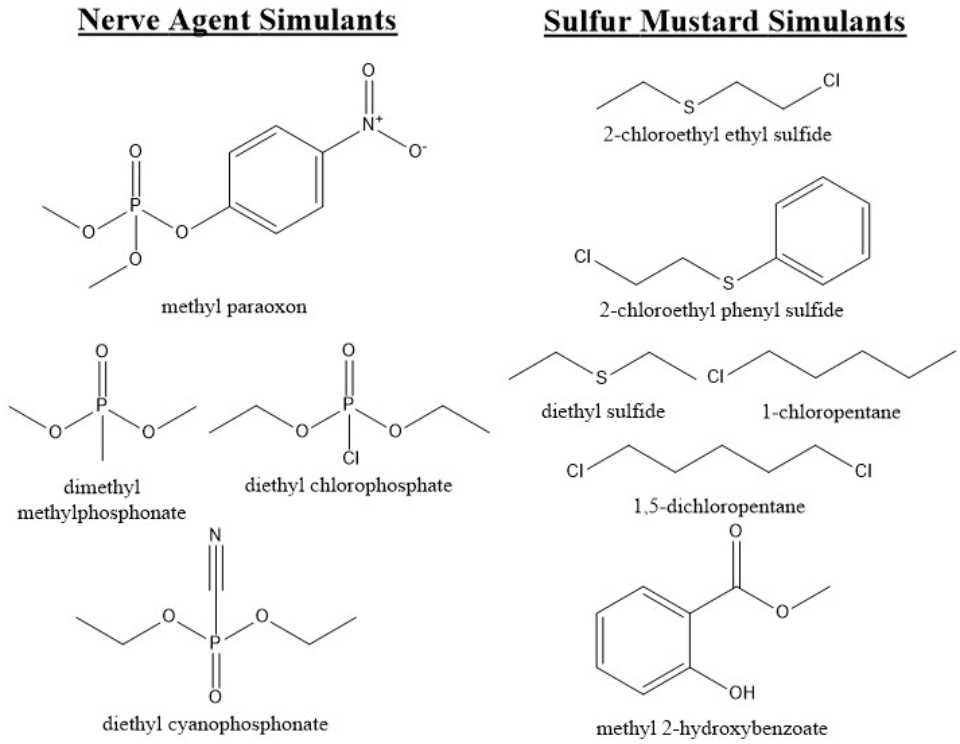

Figure 1.3 Simulants of nerve agents and sulfur mustard.

1.2.3 A Brief History of Chemical Warfare

Approximately 100 years ago, the German military first released HD against Allied soldiers in Ypres, Belgium.[5] This act encouraged both sides to develop and utilize CWAs, ultimately killing 90,000 people and injuring 1,000,000 more during World War I (WWI). CWA development continued after WWI when German scientists at IG Farben synthesized nerve agents GB and GD (named G-series agents after being synthesized by Germany) while developing organophosphate-based fertilizers in 1938. After World War II, English scientists first synthesized VX (which stands for "venomous agent X"). Large-scale employment of HD in the Iran-Iraq War injured over 100,000 Iranians and marked the first time CWAs were deployed in a battlefield setting since WWI.[4, 6] Despite the UN ban on the production and proliferation of CWAs in 1992, CWA use by terrorist organizations and rogue states persists. Specifically, recent chemical attacks on soldiers in Iraq and civilians in Syria have highlighted the continued threat of CWA exposure to both

military and civilian populations, which has led to extensive research to develop effective means to filter and degrade HD and other CWAs.

1.2.4 The Degradation of HD

Several pathways exist for the detoxification of HD, including hydrolysis, dehydrohalogenation, and oxidation (Figure 1.4).[7] For oxidation, the desired product is the partially-oxidized bis(2-chloroethyl) sulfoxide. The fully oxidized bis(2-chloroethyl) sulfone has similar vesicant properties as HD and is quite toxic. The hydrolysis of HD proceeds through nucleophilic attack of the thiiranium intermediate by water, which releases HCl as a byproduct. Full hydrolysis of HD yields bis(2-hydroxyethyl) sulfide, more commonly known as thiodiglycol. Dehydrohalogenation of HD proceeds through the elimination of hydrogen chloride from HD to form a vinyl sulfide species.

Activated carbon materials were traditionally employed to filter HD through non-reactive adsorption, but these materials did not degrade HD. Non-reacted HD could then desorb out of the pores of the activated carbon, creating secondary exposure risks. To date, studies of the degradation of HD and HD simulants have been primarily investigated on metals/metal oxides,[8-16] impregnated activated carbon,[17-18] and zeolites.[19-20] Unfortunately, challenges with efficiency, weight, expense, complete oxidation of HD to the toxic bis(2-chloroethyl) sulfone, and thermal and hydrolytic stability have prompted further materials research.[21] Ideal HD catalysts should possess thermal and chemical stability, high surface areas for large sorption capacities, large pores and strong adsorption sites for the rapid filtration of HD, and active sites that bind HD strongly, and the ability for non-toxic HD degradation byproducts to desorb. Recently, metal-organic frameworks (MOFs) have emerged as a promising class of materials for HD degradation.

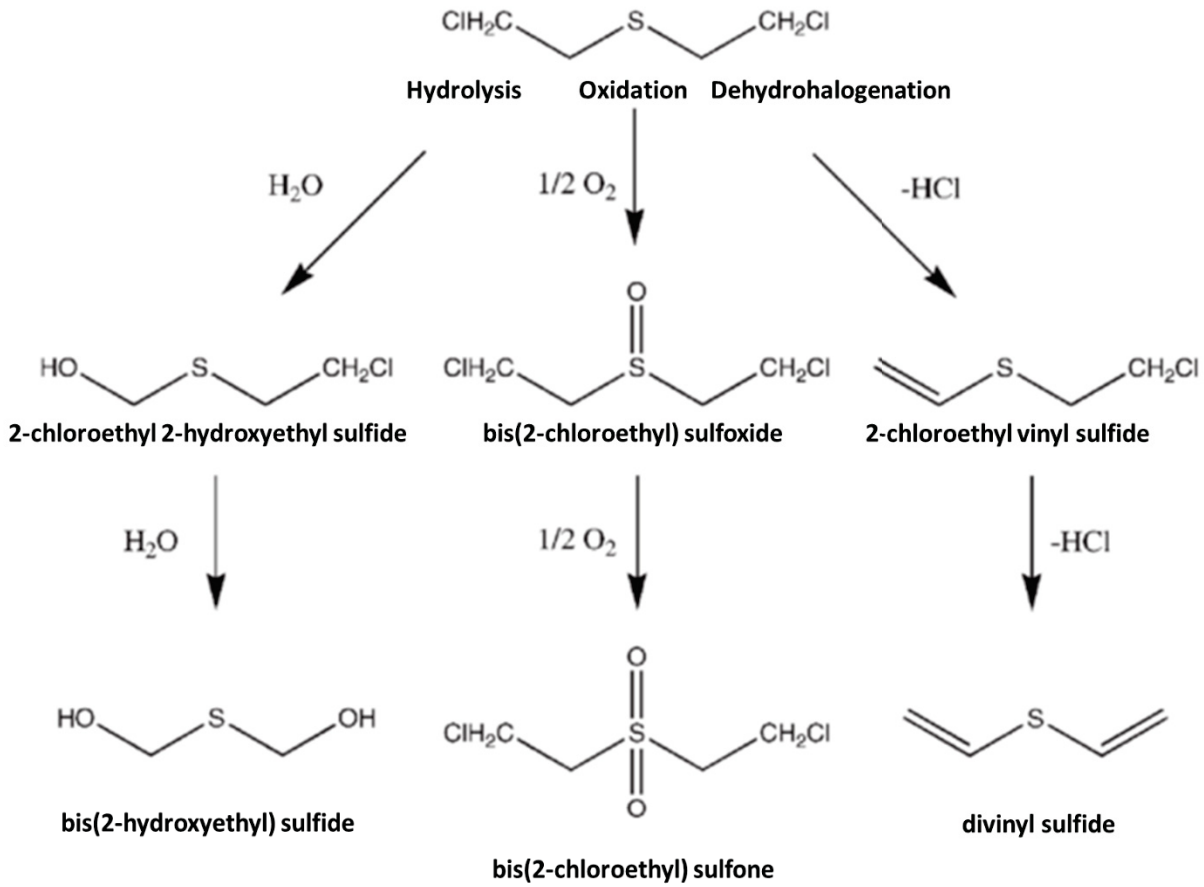

Figure 1.4 Decomposition pathways for HD. Figure adapted from Smith et al.,[7] Adapted from Reference 7 with permission from the Royal Society of Chemistry.

1.3 Metal-Organic Frameworks

Comprised of metal-oxo or metal-based clusters and organic spacers, the MOF classification features a wide variety of compounds.[22] Polydentate organic linkers coordinate with the multiple metal ions or metal oxide clusters to create an extended 3-dimensional network (Figure 1.5). Due to the multitude of metal ions and possible bridging ligands, over 40,000 different MOF structures currently exist in the literature.[23] The ability to control MOF structure, size, and linker functionality as well as porosity and thermal stability make MOFs potentially useful in the field of heterogeneous catalysis and gas storage.[24] Highly porous MOFs provide large interior surface areas, which increase the number of potential active sites compared to a non-porous

catalyst (the highest surface area measured for a MOF to date is 7140 m^2 g^{-1}).[22] Therefore, small quantities of MOFs can store large amounts of reactants. Thermal stability would allow catalytic reactions to occur at varying temperatures without compromising the MOF structure. Synthetic control over the chemical structure of MOF linkers allows for the creation of MOFs designed to selectively bind certain molecules.

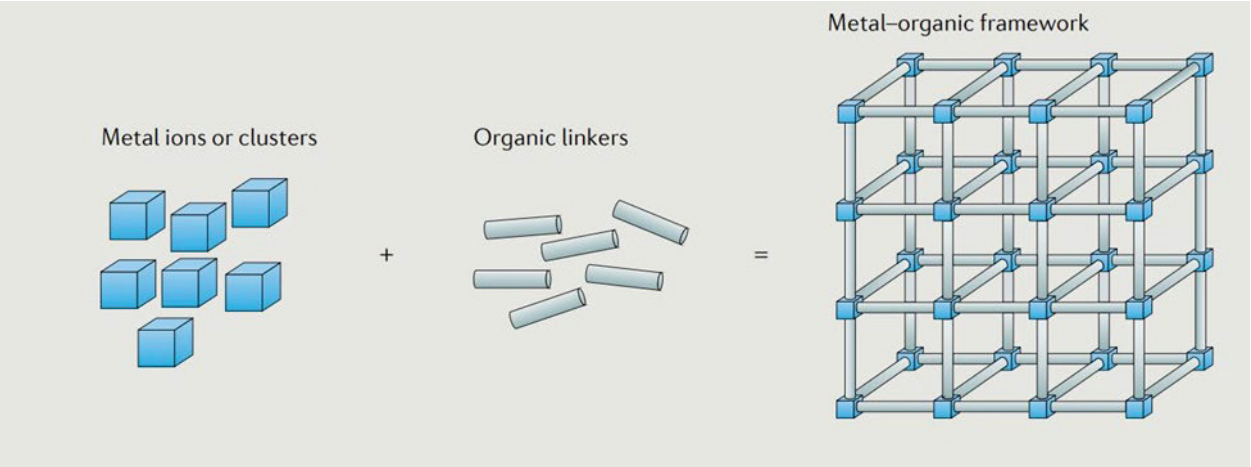

Figure 1.5 Representation of MOFs. Reprinted by permission from Howarth et al.,[25] Copyright 2016.

Recent research has demonstrated that certain MOFs can successfully degrade CWAs in solution. Singh et al. used Cu-BTC (a MOF with copper (II) nodes and benzene tricarboxylate linkers) to hydrolyze nerve agent simulants diethyl chlorophosphate (DECIP) and diethyl cyanophosphonate (DECNP) (Figure 1.2), and sarin in a chloroform solution.[26] In 1 hour at room temperature, 49% of GB degraded into phosphonic acid, ultimately achieving 90% degradation after 4 hours.[26] Furthermore, adding water to the solution increased the degradation rate of DECIP and DECNP.[26] Singh et al. also found that MOF HKUST-1, a substructure of Cu-BTC, showed that both GB and HD simulants degraded into less harmful byproducts when coordinating with the MOF structure.[27] While HKUST-1 decomposed 92% of the HD simulant 2-chloroethyl ethyl sulfide (2-CEES), shown in Figure 1.2, in 40 minutes, catalyst cycling studies suggest that 2-CEES

irreversibly adsorbs onto HKUST-1, effectively reducing the amount of available active sites and poisoning the catalyst.[28] HKUST-1 interactions with CWA simulants also showed that adsorbate size could affect its interactions with MOFs. Larger molecules generate greater steric hindrance and pore aperture sizes limit larger molecules from diffusing into internal pore regions. As we will discuss later, the pore size and the size of adsorbate molecules have a significant impact on the guest-host interactions of CWAs within MOFs.

Barea et al. showed that a zinc-based MOF, [Zn_4(μ4-O)- (μ_4-4-carboxy-3,5-dimethyl-4-carboxy-pyrazolato)$_3$], successfully bound GB simulants as well as HD simulants.[29] This MOF shares structural similarity to MOF-5, which is known for its lack of thermal stability and its easily hydrolyzed zinc-oxygen bonds. Slightly modifying the structure of MOF-5, this new MOF features high thermal stability and resistance to hydrolysis. [Zn4(μ4-O)- (μ_4-4-carboxy-3,5-dimethyl-4-carboxy-pyrazolato)$_3$] was able to bind sarin and mustard gas simulants at ambient humidity.[30] Mechanistic studies of MOF-5 propose that organophosphate CWAs degrade through base-catalyzed hydrolysis of the phosphate group, so ideal MOFs for CWA catalysis must accommodate water to facilitate the decomposition process. As we will discuss in Chapter 7, even under low relative humidity levels, significant amounts of water remain adsorbed within the pores of MOFs and appear to contribute to the degradation of CWAs.

1.3.1 Zirconium-based MOFs.

MOFs containing zirconium (IV) oxo clusters (Zr-based MOFs or Zr-MOFs) and carboxylate-based organic linkers demonstrate tremendous stability in a variety of chemical environments and thermal conditions because of the metal-ligand bond strength.[31-32] The syntheses of Zr-MOFs with bitopic, tritopic, and tetratopic organic linkers yield MOFs with various pore sizes, pore topologies, and number of linkers attached per inorganic node (node connectivities)

(Figure 1.6).[33] Functionalization of the organic linker and Zr cluster with substituent groups allows for further modification of Zr-MOFs. Currently, Zr-MOFs have been studied for a wide array of potential applications, including gas separation, gas storage, filtration, sequestration, heterogeneous catalysis, and chemical sensing.[34-54]

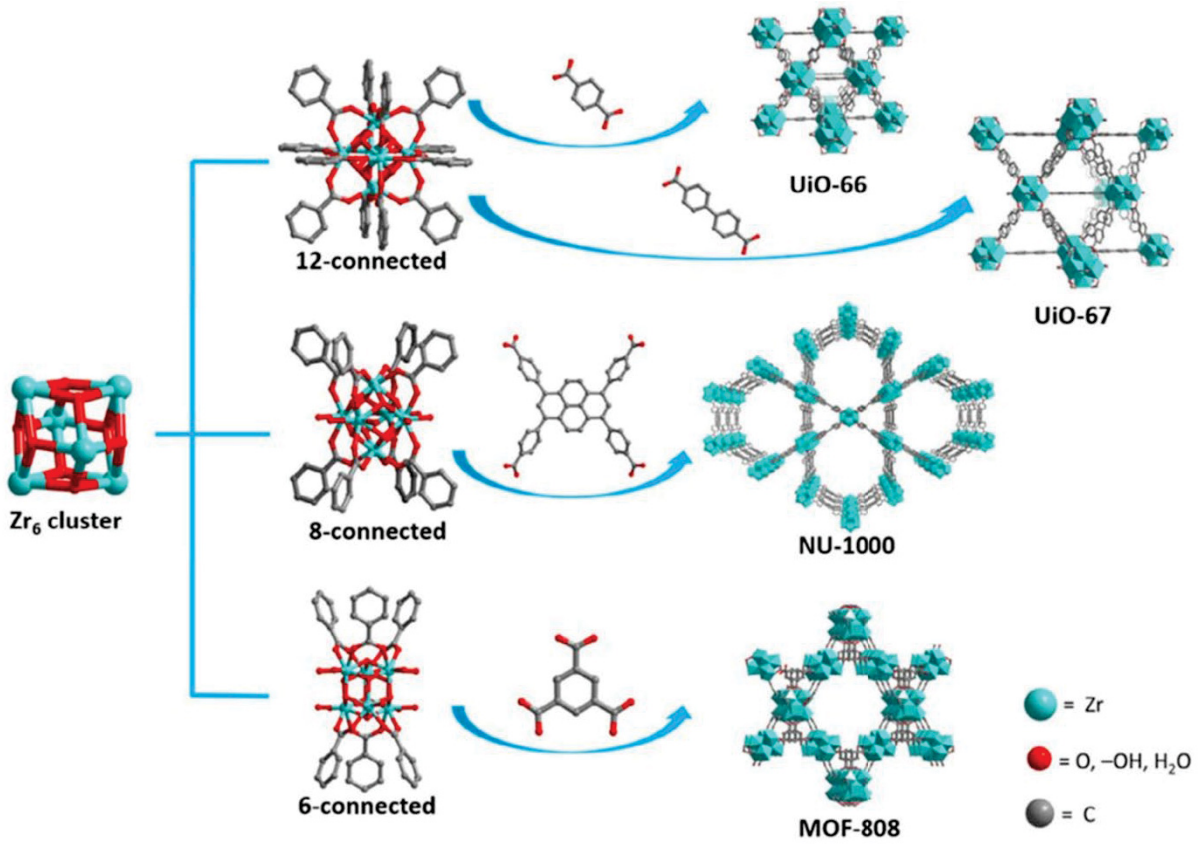

Figure 1.6 Zr-MOFs with various pore topologies and node connectivities. Reprinted from Liu et al.[33] with permission from Elsevier.

UiO-66 (named after the University of Oslo where it was first synthesized in 2008) is comprised of $Zr_6O_4(OH)_4$ nodes connected to 1,4-benzene-dicarboxylate (terephthalate) linkers, creating a face-centered cubic crystal structure (shown in Figure 1.7).[55] The $Zr_6O_4(OH)_4$ node features six 8-coordinated zirconium atoms arranged in an octahedron with μ_3-O and μ_3-OH located at the faces of the octahedron. Each terephthalate linker coordinates with two zirconium nodes through its carboxylate groups. Each zirconium atom is bound to four terephthalate linkers.[55]

Within UiO-66, two distinct pore environments exist. The first pore consists of six-terephthalate linkers and four $Zr_6O_4(OH)_4$ nodes, creating a tetrahedral shape. The second pore exhibits an octahedral shape and consists of six nodes and twelve linker units. The unit cell of a UiO-66 structure is made up of eight tetrahedral pores attached to the faces of a central octahedral pore.[56] The internal pore diameters of UiO-66 are 8 Å for the tetrahedral and 11 Å for the octahedral cavities, which are capped by triangular window apertures with a length of 6 Å. According to DFT calculations, for a MOF with no missing linkers, UiO-66 has a Langmuir surface area of 1187 m^2/g.[56]

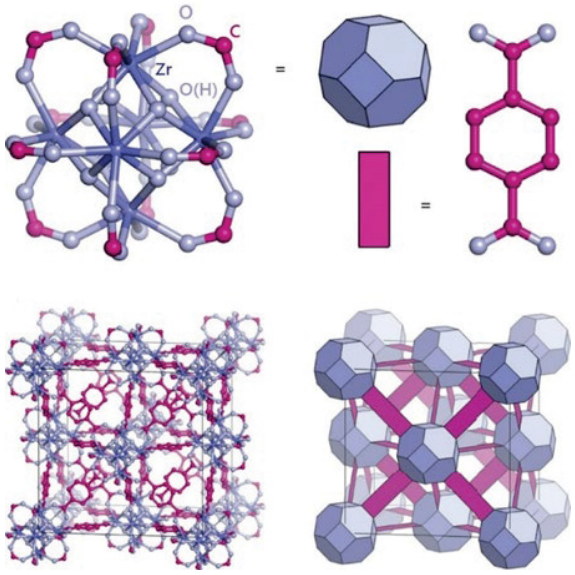

Figure 1.7 Structure of UiO-66. Adapted by permission from Cliffe et al.,[57] Copyright 2014.

Increasing the number of phenyl moieties per linker unit creates other members of the UiO-series of MOFs: UiO-67 (biphenyl dicarboxylate linkers) and UiO-68 (terphenyl dicarboxylate linkers). Longer-chained linkers correspond to higher surface area molecules; UiO-67 has a surface area of 3000 m^2/g and UiO-68 has a surface area 4170 m^2/g.[10] The longer organic linkers increase the triangular pore aperture by 2 Å for each additional phenyl group.[10]

The robustness of these UiO-based MOFs makes them particularly appealing for use in catalysis. DeCoste et al. performed powder X-ray diffraction (PXRD) on UiO-66 exposed to 0.1 M HCl, water, 0.1 M NaOH, and several other common solvents.[58] The results showed little change in the UiO-66 diffraction pattern, indicating that UiO-66 can retain its crystallinity upon exposure to a wide range of chemical environments. Lillerud et al. used PXRD to find that UiO-66 subjected to pressures as high as 10,000 kg/cm^2 did not lose its structural integrity.[55] Using thermogravimetric analysis-mass spectrometry (TG-MS), Lillerud et al. also found that breakdown of the UiO-66 lattice (due to breaking the benzene-carboxylate bond) occurs at 540 ˚C under a 15 mL/min nitrogen flow.[55] UiO-66 does undergo a slight transition around 300 ˚C in a process commonly referred to as dehydroxylation (Figure 1.8).[55]

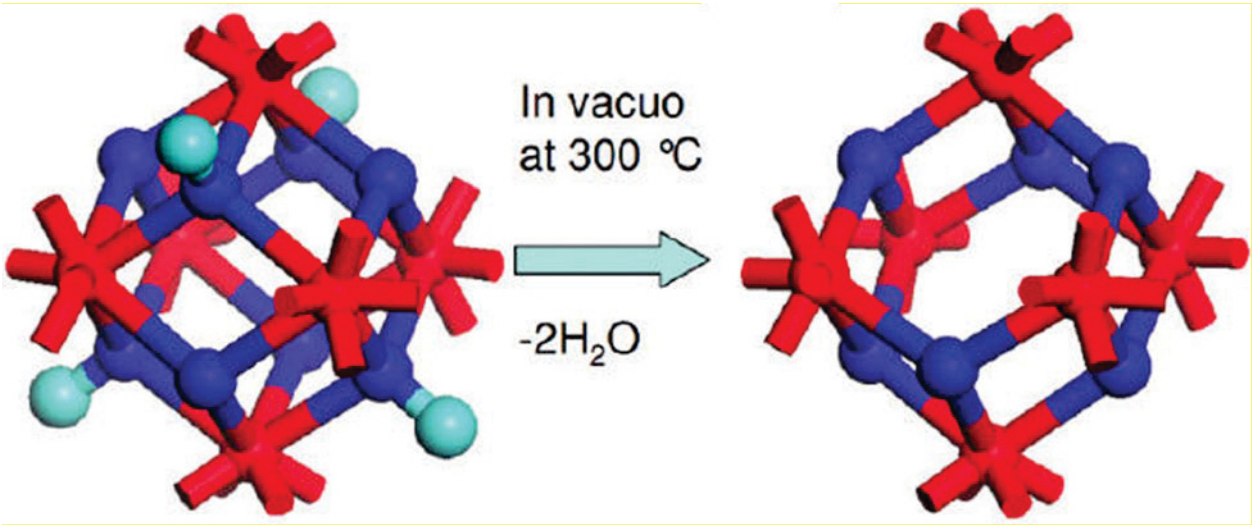

Figure 1.8 Representation of the dehydroxylation of the $Zr_6O_4(OH)_4$ cluster to Zr_6O_6 upon heating at 300 °C in vacuum. Red, blue, and cyan colors refer to Zr, O, and H, respectively. Figure adapted with permission from Valenzano et al.[56] Copyright 2019 American Chemical Society.

At 300 ˚C, UiO-66 dehydroxylates, losing two water molecules from the $Zr_6O_4(OH)_4$ nodes and converting them into Zr_6O_6 nodes where the Zr coordination number changes from 8 to 7 (Figure 1.8).[56] Dehydroxylating the node changes the structure of UiO-66 by compressing the z-direction of the zirconium octahedral cavity (shown later).[56] Under ambient conditions, the

dehydroxylated MOF (also referred to as "dehydrated") rehydroxylates, though rehydroxylation results in a variety of defect μ_3-OH sites, or sites where the bridging hydroxyl group is only bound to one zirconium atom. In the dehydroxylated form, UiO-66 possesses some interesting properties, such as a decreased HOMO-LUMO gap compared to hydroxylated UiO-66.[56]

1.4 A Review of Zr-MOF Studies for the Degradation of Nerve Agents

Zr-MOFs have been extensively studied for the degradation of CWAs, especially nerve agents. While the goal of our research was to investigate the fundamental interactions between sulfur mustard and Zr-MOFs, the literature for nerve agent degradation demonstrates how changes to the MOF's chemical functionality, pore size, pore topology, and node connectivity affect the rate of reaction. If we can understand how mustard gas interacts with Zr-based MOFs, we can design a MOF-based HD catalyst or sorbent that has a high concentration of reaction/adsorption sites, optimized pore sizes so HD molecules can access all available active sites without allowing rapid breakthrough, and an active site to promote the rapid degradation of HD to less toxic byproducts. Furthermore, the ideal Zr-MOF based CWA-degradation catalyst or sorbent should be effective against both nerve agents and mustard agents. As mentioned in 1.2.2, HD can be degraded through hydrolysis, so Zr-MOFs that exhibit catalytic activity for nerve agent hydrolysis may also show potential for HD hydrolysis.

1.4.1 Solution-Phase Studies of Zr-MOF-based CWA Degradation

Recent literature has focused on using UiO-MOFs for the catalytic hydrolysis of G-based nerve agents in aqueous, buffered solutions. Because the Zr-O(H)-Zr in the UiO-66 metal cluster resembles the Zn-O(H)-Zn active site in phosphotriesterase, an enzyme that degrades organophosphates by cleaving the phosphate bond, Joseph Hupp and Omar Farha proposed that UiO-66 would be able to similarly hydrolyze organophosphate CWAs.[59] Due to its high porosity

and structural rigidity, UiO-66 could make a model heterogeneous catalyst for CWA degradation. By monitoring the reaction progression using UV-Vis, Hupp et al. found that UiO-66 hydrolyzed methyl paraoxon into nitrophenoxide and diphenyl phosphate (Figure 1.9) with a reaction half-life of 25 minutes at 300 K. This reaction half-life decreased to 10 minutes when the temperature was increased to 333 K.[59] Without UiO-66 present in the aqueous solution, only 15% of the methyl paraoxon was converted. *N*-ethylmorpholine was used as a buffer to keep the aqueous solution at pH 10 to serve as a proximal base for hydrolysis. The heterogeneity of the catalyst was confirmed by filtering UiO-66 out of the reaction solution after 20 minutes and observing no further conversion of methyl paraoxon.[59]

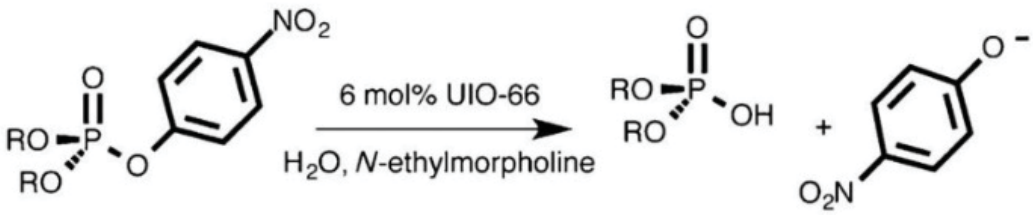

Figure 1.9 Hydrolysis of methyl paraoxon.[60]

During the experiments, while PXRD confirmed the MOF structure's integrity, a decrease in the MOF surface area after the reaction combined with peaks found in a ^{1}H NMR sample not attributed to the terephthalate linker indicates pore clogging within the MOF.[59] Another limit of UiO-66 for the decomposition of G-based nerve agents lies in the fact that the aperture to access the MOF's tetrahedral pores are too small (~6Å long) to allow methyl paraoxon to diffuse into the internal active sites. This limited the number of reactive Zr-node sites to the surface and drastically cut down the catalytic potential of the MOF. By determining the average particle diameter by scanning electron microscopy (SEM) and dynamic light scattering (DLS) experiments to be 400 nm, it was calculated that only 0.75% of all zirconium nodes in the MOF are accessible as active sites.[59] Hupp et al. also hypothesized that defect sites (nodes that do not have full linker attachments and therefore have exposed metal sites) on the surface of the MOF are the active sites.

Because 12 terephthalate linkers are attached to each node in UiO-66 and each zirconium is 8-coordinated, there should be no available coordinatively unsaturated metal sites (CUS) to interact with the methyl paraoxon.

The inability for methyl paraoxon to access the internal reactive sites of UiO-66 due to its small pore apertures limited the reactivity to the surface of the MOF crystallites. Increased linker sizes would result in large pore windows and allow methyl paraoxon to access internal undercoordinated zirconium sites. Peterson et al. studied the reaction of methyl paraoxon on UiO-67 in a buffered solution and observed a decrease in the methyl paraoxon half-life from 25 minutes to 3.5 minutes.[61] Increasing linker size resulted in an increase in the reaction rate due to the ability for methyl paraoxon to access reaction sites within the pores of the MOF. Unfortunately, UiO-67, like UiO-66, has 12 linkers attached to each node, meaning that active sites were still limited to missing linker defects within the MOF.

Research has shown the ability to synthetically control the approximate number of defects in a given MOF sample.[62-64] During the synthesis of UiO-66 from $ZrCl_4$ and terephthalic acid, adding trifluoroacetic acid (TFA) and other modulating acids will increase the number of defect sites. This occurs due to a high affinity for the acid to the metal oxide cluster. Furthermore, post-synthetic heating of the resulting UiO-66 will remove the acid linker, leaving unsaturated metal sites. Besides increasing the number of exposed zirconium sites, defect engineering with different modulator acids will affect the surface area and particle size of UiO-66. Particle sizes of 300 nm and surface areas of 1520 m^2/g were reported for UiO-66 samples modulated with formic acid, while the use of acetic acid creates 10 nm particles with surface areas of 1130 m^2/g. While the generated defects occur randomly within the UiO-66 molecule, control over the surface area and particle size allow for increased control of catalyst preparation.

In addition to increasing the number of defects within the Zr-MOF, defect-sites can be engineered to introduce desired functionality to the UiO-66 node through either acid modulation or post-synthetic modification. With defect-engineering, catalysts or functional groups can be grafted onto the zirconium cluster, either through the unsaturated metal sites or through the bridging hydroxide. Through the use of potassium bisulfate that replaced the acetic acid linker, López-Maya et al. functionalized UiO-66 nodes with a Brønsted-acid site (UiO-66@SO_4H, shown in Figure 1.10).[65] Similarly, introducing lithium tert-butoxide replaced the μ_3-OH with a butoxide group (UiO-66@LiO*t*Bu). While UiO-66@SO_4H showed no increase in catalytic activity compared to UiO-66, UiO-66@LiO*t*Bu displayed an increased rate of hydrolysis for GB simulants DIFP, DMMP and for the hydrolytic degradation of HD simulant 2-CEES (structure shown in Fig. 1.2). The inclusion of a strong basic functional group like an alkoxide on the metal node could allow improved ligand to metal charge transfer than the terephthalate linker.

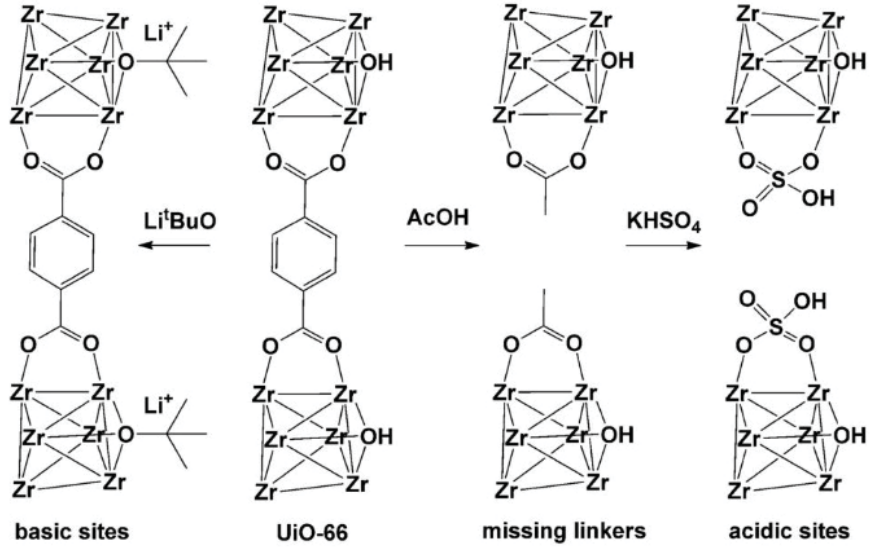

Figure 1.10 Defect/node functionalization of UiO-66. Image copied with permission from López-Maya et al. Copyright 2015 WILEY-VCH Verlag GmbH & Co. KGaA, Weinheim.

The synthesis of Zr-MOFs with different organic linkers that reduce the number of organic linkers coordinated to each Zr-cluster has been shown to increase the number of available Zr_{CUS}

sites and increase the rate of methyl paraoxon hydrolysis. NU-1000 is a Zr-MOF that contains tetratopic 1,3,6,8(*p*-benzoate)pyrene linkers, which has 8 connected linkers per node.[66] The $Zr_6(\mu_3\text{-}O)_4(\mu_3\text{-}OH)_4(H_2O)_4(OH)_4$ cluster of NU-1000 has terminal hydroxyl groups and four coordinated aquo ligands, which can be displaced to generate coordinatively unsaturated zirconium sites (Zr_{CUS}). The hydrolysis of methyl paraoxon within NU-1000 proceeded 30 times faster than within UiO-66.[66] Zr-MOFs synthesized with six linkers per node (MOF-808) and four linkers per node (NU-1400) introduce even more Zr_{CUS} sites and improve the reaction rate for methyl paraoxon hydrolysis.[67-68] In addition to increasing available Zr sites, changes to the node connectivity in Zr-MOFs alters the pore topology, which can allow for faster adsorbate diffusion into internal pores (Figure 1.3).

The addition of substituent groups to the organic linkers of Zr-MOFs, either through postsynthetic modification or through the synthesis of MOFs with functionalized linkers, has been employed to optimize the reaction site for nerve agent degradation. Kalaj et al. studied the effect of the functionalization of UiO-66 linkers with halogens on methyl paraoxon hydrolysis and determined that halogens *ortho* to the Zr_{CUS} active sites form interact with the methoxy group of methyl paraoxon, which leads to a faster rate of hydrolysis.[69] Kalaj et al. expanded on this work by studying the same reaction within UiO-66-based MOFs synthesized with a mixture of several functionalized linkers (Figure 1.11) and found that MOFs with both halogen and amine functionalization yielded the highest rate of hydrolysis.[70]

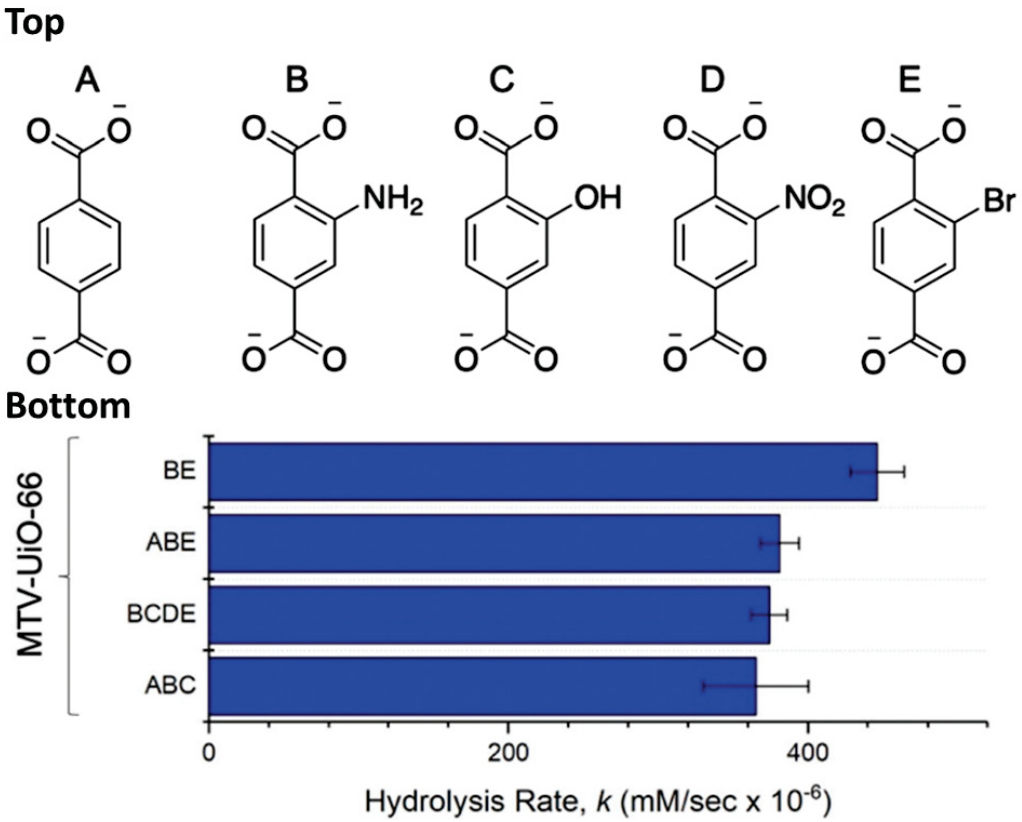

Figure 1.11 1,4-benzene dicarboxylate linkers with the addition of chemical functional groups (Top). Hydrolysis rates for methyl paraoxon in UiO-66 samples containing mixed linker composition (Bottom). Adapted from Reference 70 with permission from the Royal Society of Chemistry.

Of the substituent groups investigated for the degradation of nerve agents with functionalized Zr-MOFs, amine groups have garnered the most interest. The synthesis of a UiO-66 with amine groups on the BDC linkers increased the hydrolysis rate for methyl paraoxon with UiO-66-NH_2 by a factor of 20 compared to UiO-66 with non-functionalized linkers.[71] Islamoglu et al. investigated the effect of the amine group position relative to the Zr node in UiO-67 and NU-1000 and found that amine groups in the ortho position on the linker in UiO-67 and in the meta position on the linker in NU-1000 increased the rate of methyl paraoxon hydrolysis more than amines located elsewhere on the linkers.[72]

1.4.2 Gas-Phase Studies of Zr-MOF-based CWA Degradation

While solution-phase studies have indicated that Zr-based MOFs are active for the catalytic hydrolysis of nerve agents in aqueous, pH-buffered solutions, these experiments do not reflect the actual chemical environment where CWAs are deployed. Studies into the interactions between nerve agents in the vapor phase and MOFs can demonstrate how these materials will perform under realistic conditions. Plonka et al. employed a combination of *in situ* analytical techniques, including X-ray powder diffraction, X-ray absorption spectroscopy, and infrared spectroscopy, to probe the interactions between Zr-MOFs UiO-66, UiO-67, NU-1000, and MOF-808, and the nerve agent simulant dimethyl methylphosphonate (DMMP).[73] Plonka and coworkers found that upon the adsorption of DMMP at Zr_{CUS} sites within the Zr-MOFs, DMMP reacted to form methyl methylphosphonic acid (MMPA). Unlike the solution-phase studies, MMPA strongly bound to the Zr nodes, effectively poisoning the active site from further reactions. These findings were consistent with DFT calculations for the decomposition of sarin on Zr-based MOFs, where sarin reacts at Zr_{CUS} to ultimately form a strongly bound species that does not desorb.[74]

Wang et al. expanded on these findings with a combination of ultrahigh-vacuum-based experiments and computational chemistry that determined the mechanism for the reaction of DMMP to MMPA within Zr-MOFs.[75] DMMP hydrolysis proceeded through the adsorption of DMMP to Zr_{CUS} through the sp^2-hybridized oxygen of DMMP, nucleophilic attack of the phosphorous atom of DMMP by a terminal hydroxyl group on the Zr node, proton transfer from either the terminal hydroxyl group or the μ3-OH, and the subsequent desorption of methanol as a reaction byproduct (Figure 1.12). The bound MMPA product did not desorb despite heating the MOF to 600 K, confirming that MMPA irreversibly adsorbed to the MOF.

Recently, a study by Wang et al. investigated how the presence of adsorbed water in the pores of UiO-66, UiO-67, and UiO-66-NH_2 under ambient conditions may affect the solid-phase hydrolysis of methyl paraoxon.[76] While the solid-phase reaction rates reported were significantly lower than those reported for solution-phase studies with the same MOFs, researchers found that the increase in water loading within UiO-66 corresponded to a significant increase in the hydrolysis rates of methyl paraoxon.[76] Furthermore, the amine groups on UiO-66-NH_2 were found to react with the methoxy group of methyl paraoxon, forming methylated secondary amine species and methyl (4-nitrophenyl) hydrogen phosphate.[76]

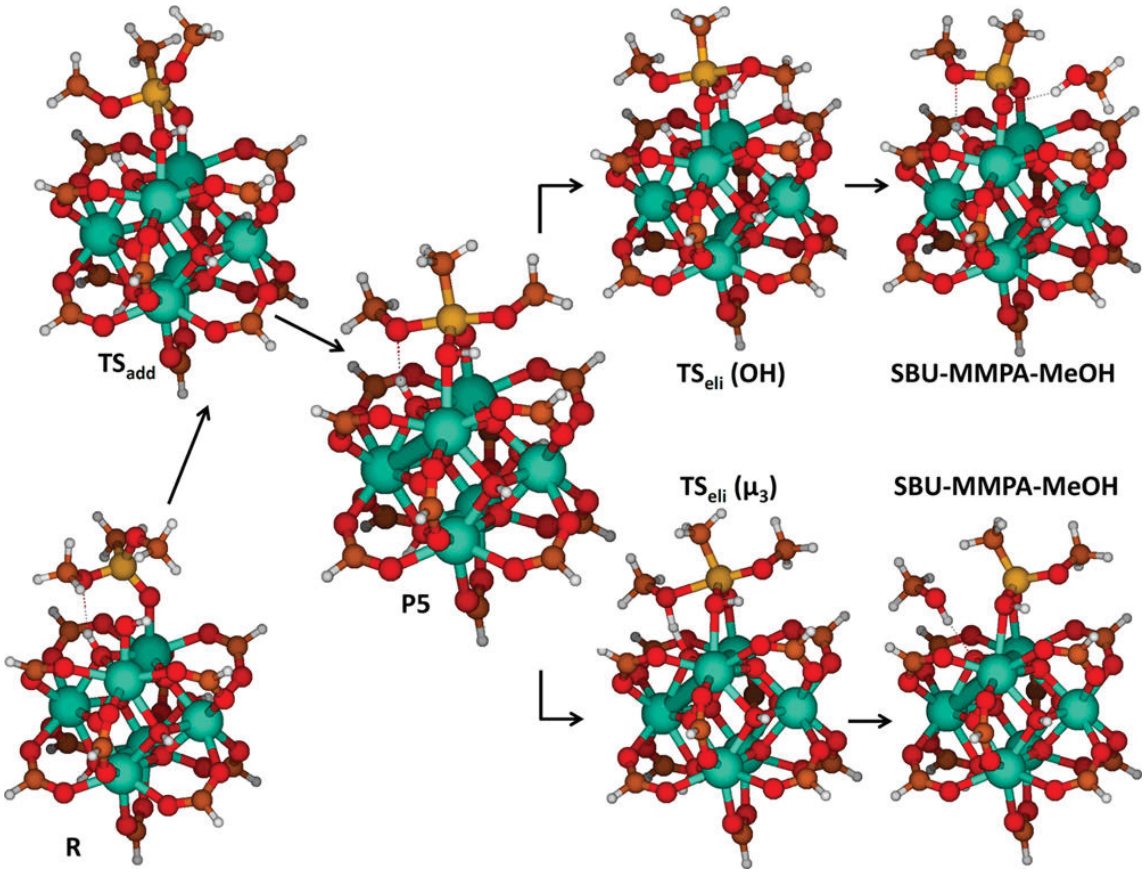

Figure 1.12 Reaction mechanism for the decomposition of DMMP at a Zr_{CUS} in UiO-67 (Teal = Zr, brown = C, gold = P, red = O, and white = H). Reprinted with permission from Wang et al.[75] Copyright 2019 American Chemical Society.

1.4.3 Zr-MOF-based Degradation of HD

While extensive research has focused on adjustments to the structure and chemical functionality Zr-MOFs for the degradation of nerve agents, few studies have investigated Zr-MOF-based materials for the catalytic degradation of HD. In solution-phase studies, the porphyrin-based linkers of PCN-222/MOF-545 partially oxidized the HD simulant 2-chloroethyl ethyl sulfide (2-CEES) to 2-chloroethyl ethyl sulfoxide through the generation of singlet oxygen upon blue light irradiation.[77] Similarly, post-synthetic modification of NU-1000 with photosensitizers has yielded improved 2-CEED oxidation rates compared to PCN-222/MOF-545.[78-79] In addition to oxidation, Zr-MOFs have also been studied for the hydrolysis of HD. Gil-San-Millan et al. studied the hydrolysis of 2-CEES and HD with UiO-66 and UiO-67 under aqueous conditions and found that the introduction of amine functionalization on the organic linker and the incorporation of lithium tert-butoxide on the $Zr_6O_4OH_4$ drastically improved hydrolysis rates.[80]

1.5 Fundamental Gas-Surface Studies

The structure and chemical functionality of Zr-MOFs have been tailored to increase reactivity for nerve agent hydrolysis by altering linker size, node connectivity, and linker functionalization. Molecular-level insight into the interactions of HD within Zr-MOFs will allow us to identify the rate-limiting processes that may lead to slow degradation rates and product inhibition. Furthermore, by determining the mechanism by which HD adsorbs within the Zr-MOFs, we can modify the MOF structure to increase the number of adsorption sites and improve its sorption capacity. If we understand the binding geometry of HD, we can add chemical functional groups near the active sites to increase reaction rates and promote product turnover. To understand the fundamental interactions between HD and Zr-MOFs, we employed ultrahigh vacuum-based studies to determine the adsorption mechanism, measure the diffusion kinetics, and

quantify the desorption energetics of several HD simulants within several MOFs using a variety of spectroscopic techniques.

1.5.1 Infrared Spectroscopy

IR spectroscopy provides insight into the nature of the interactions between adsorbates and the surface by providing *in situ* information on the vibrational modes in the chemical environment of the sample. Using IR spectroscopy, we can characterize the sample surface, identify the adsorption mechanism of gas molec, and reaction of gas-phase molecules.

Infrared spectroscopy has been extensively used to study the interactions of HD and HD simulants on nanoparticulate metal oxide surfaces.[10, 81-86] FTIR studies of HD simulants adsorbed onto silica corresponded to the loss of a free hydroxyl O–H peak and the formation of a broad peak around 3300 cm^{-1}, indicating that chloroalkanes bind to silica via hydrogen bonding.[87] Furthermore, Abelard et al. demonstrated that both the sulfur and chlorine atoms in HD hydrogen bond to silica.[87]

For MOFs, infrared spectroscopy has been employed to study not only the structure of MOFs, but also their interactions with gas molecules. Driscoll et al. used CO as a probe molecule to detect and quantify the amount of Zr_{CUS} within a UiO-66 sample.[88] Transmission IR was utilized to determine the adsorption mechanism and energetics of small molecule adsorption within UiO-66.[89-90] Chakarova et al. examined the Brønsted and Lewis acidity of UiO-66 and UiO-66-NH_2 by monitoring changes in the vibrational spectra upon exposure to a series of small molecules.[91] IR spectroscopy has been used to measure the intracrystalline diffusion kinetics of small molecule transport through MOFs and to identify how co-adsorbed gases affect the energetic barriers to diffusion.[54, 92]

1.5.2 Temperature Programmed Desorption

To quantify the strength of the interaction between HD molecules and the active sites of Zr-MOFs, temperature programmed desorption (TPD) was employed. In TPD, molecules are dosed onto surfaces. A linear temperature ramp is then applied to the sample surface, increasing the thermal energy to allow molecules to either desorb into the gas phase or diffuse to the strongest binding site. Molecules that desorb are monitored by either a pressure gauge or a mass spectrometer. By plotting surface temperature vs. the intensity of the mass spectrometer or pressure signal, it is possible to determine the fractional coverage (coverage at time (t)/total coverage) at a given surface temperature. TPD allows us to determine desorption energy, or the activation energy required for molecules to disassociate from a given surface. This is accomplished through an inversion of the Polanyi-Wigner equation, shown in equation 1:[93-94]

$$\boldsymbol{r(\theta,T) = -\frac{d\theta}{dt}(\theta,T) = \nu_{des}(\theta,T)e^{-E_{des}(\theta)/k_BT}\theta^n} \quad \textbf{(1.1)}$$

Where ν_{des} represents the pre-exponential prefactor for desorption, θ corresponds to a given coverage (amount of molecules on the surface), $E_{des}(\theta)$ stands for desorption energy, T represents the temperature of the surface, k_B is Boltzmann's constant, and n represents the order of desorption. From here, the equation is inverted to solve for the desorption energy at a given coverage (eq. 1.2).[93-94]

$$\boldsymbol{E_d(\theta) = -k_BT\ \ln\left[-\frac{d\theta/dt}{\nu\theta}\right]} \quad \textbf{(1.2)}$$

By determining the pre-exponential factor, it is possible to plot the desorption energy as a function of coverage. The resulting plot has two features: a linear and an exponential decay. The exponential decay results from the fact that defect sites on a given surface will result in stronger binding energies (more noticeable at lower coverages). To determine desorption energy of a defect-free

surface, the linear portion of the plot is extended to extrapolate the binding energy at zero coverage (i.e. a single molecule adsorbing onto a surface).

TPD has been previously used within the Morris group to measure desorption of both CWAs and CWA simulants on silica surfaces.[87, 95-97] Through TPD analysis, it was determined that the desorption energies of sarin and soman from silica are comparable to simulants dimethyl chlorophosphate (DMCP) and trimethyl chlorophosphonate (TMP).[97] Acting as simulants of mustard gas, the desorption of a series of linear chloroalkanes from silica revealed a 5-7 kJ/mol increase in desorption energy per methylene unit, suggesting that the increase in chain length resulted in more dispersion forces with the silica surface.[87] CWA and simulant adsorption onto silica will provide a benchmark to compare with CWA desorption energies measured from UiO-MOFs.

1.6 Organization of Thesis

In Chapter 2, we describe the instrumentation, experimental methods, and data analytic approaches utilized in this work to study the interfacial interactions between small molecules and Zr-MOFs. The majority of experiments documented in this work were performed in a custom-built ultrahigh vacuum chamber that possessed both infrared spectroscopic and mass spectrometric capabilities. Infrared spectroscopy was utilized to determine the adsorption mechanism for linear alkanes and HD simulants with several Zr-MOFs and track the time-dependent concentration profiles of adsorbates to measure their diffusivities. The mass spectrometer was used to measure desorption kinetics for HD simulants from Zr-MOFs through temperature programmed desorption experiments.

Chapter 3 described our investigation into the interactions between linear alkanes and UiO-66. This work studied the adsorption of several linear alkanes to determine the adsorption

mechanism within the pores of UiO-66 and measured the diffusivity of *n*-butane and *n*-pentane through the MOF. The content of Chapter 3 is heavily based on a manuscript, co-authored by Josh Abelard, Anna M. Plonka, Weiwei Guo, Craig L. Hill, and John R. Morris, and has been published in an ACS journal.[98]

The interactions between one HD simulant, 2-chloroethyl ethyl sulfide, and the Zr-MOFs UiO-66, UiO-67, and NU-1000 were studied in Chapter 4. The adsorption mechanism of 2-CEES within UiO-66 was elucidated and compared to the adsorption of 2-CEES within NU-1000 and UiO-67, which both possess larger pore diameters than UiO-66. This chapter also examined the role of hydrogen bonding and pore size on the energetics and kinetics of 2-CEES diffusion through Zr-MOFs.

In Chapter 5, we discussed the surface chemistry of a series of HD simulants within UiO-66. All molecules formed hydrogen bonds with hydroxyl groups on the zirconium oxo cluster of the MOF, with varying extents of charge transfer depending on the functional groups of the HD simulant. The diffusion energetics of each HD simulant through a non-defected UiO-66 sample were calculated to understand how each different substituent groups on HD might affect its transport properties within UiO-66.

In Chapter 6, we focused on an attempt to quantify the enthalpic and entropic energetics of 2-CEES desorption from UiO-66, UiO-67, and NU-1000. The ability to extract the kinetic and energetic parameters from TPD experiments for porous materials is of considerable importance for heterogeneous catalyst design and understanding reaction rates. TPD experiments of 2-CEES desorption from UiO-66, UiO-67, and NU-1000 were performed and analyzed using several analytical methods for the quantitative analysis of the TPD spectra. The stochastic modeling

software Kinetiscope simulated TPD spectra by incorporating the diffusivity information collected in Chapter 4.

In Chapter 7, we studied the reaction between the HD simulant 2-chloroethyl ethyl sulfide and UiO-66-NH_2, specifically trying to understand how adsorbed water within the MOF pores under ambient conditions affect the reaction. A combination of ultrahigh vacuum surface science and ambient pressure spectroscopic techniques were employed to monitor the 2-CEES reaction with UiO-66-NH_2 under a variety of humidity levels. The results demonstrated that UiO-66-NH_2 reacted with 2-CEES without water adsorbed in the pores, but the presence of water likely improves the reaction rate.

Chapter 2. Instrumental Apparatus, Experimental Procedures, and Data Analysis

2.1 Introduction

The goal of our research was to develop an understanding of the interactions between mustard gas simulants and Zr-MOFs at the gas-MOF interface and within the pores of the MOF to ultimately aid in development of highly efficient Zr-MOF-based catalysts and sorbents for protection from mustard gas attacks. Detailed studies probing the adsorption mechanism, diffusion energetics, and desorption kinetics of sulfur mustard simulants within Zr-based MOFs required spectroscopic techniques capable of providing molecular-level insight into adsorbate-surface interactions at binding sites within the MOFs. Experimental methods to extract adsorption enthalpies, such as calorimetry, operate under equilibrium conditions and fail to provide information about the chemical nature of the gas-surface adsorption and kinetics of the adsorption and desorption processes.

Our research combined several spectroscopic techniques to provide atomic level insight into both the strength and the nature of the gas-MOF interactions. Specifically, we used infrared spectroscopy, which probed the vibrational energy of chemical bonds. The presence of vibrational modes associated with gas adsorption and the perturbation of the vibrations attributed to the surface allow for the determination of binding mechanisms, and in the case of reactive systems, product formation. Within the Beer's Law regime, the signal intensity of these vibrational modes was directly correlated with the concentration of molecules throughout the sample. In situ, time-resolved infrared spectroscopy of changes to the relative concentration of adsorbates within the MOF over time provided direct evidence that that can quantify the kinetics and energetics of gas diffusion.

In addition to infrared spectroscopy, the use of a mass spectrometer allows us to perform temperature programmed desorption (TPD) experiments, which have been employed in surface science to measure the kinetics of desorption and determine the strength of the adsorbate-surface interactions. While TPD has traditionally been utilized to study the desorption of gases from single crystals and other two-dimensional surfaces, recent work has focused on trying to apply TPD to study desorption from porous materials.

To selectively probe the chemical and physical interactions between the Zr-MOFs studied in this work and the desired mustard gas simulants, we employed the use of a custom-built ultrahigh vacuum (UHV) chamber. Operating under a UHV environment (~10^{-9} Torr) allowed us to keep our MOF materials clean from contaminant gases, limited the collision of gas molecules that may induce undesired side reactions, and enabled the use of surface sensitive analytical techniques that are only operable under vacuum conditions.

2.1.1 Kinetic Theory of Gases

To study fundamental gas-surface interactions, our surfaces must be free of surface contamination and our gas must be well-characterized. By performing experiments under ultrahigh vacuum (UHV) conditions (~10^{-9} Torr), the concentration of non-analyte gases onto our surface is reduced. This prevents background gas molecules from contaminating our sample surfaces and allows us to selectively monitor the adsorption of gases and vapor of interest. The ideal gas law states:

$$\boldsymbol{PV = Nk_bT} \tag{2.1}$$

Where $\boldsymbol{P}$ is the pressure of system, $\boldsymbol{V}$ is the volume of the system, $\boldsymbol{N}$ is the number of gas molecules, $\boldsymbol{k_b}$ is the Botlzmann constant, and $\boldsymbol{T}$ is the temperature of the system. At ambient temperature and pressure (300 K and 760 Torr, respectively), the number density, or the number of gas molecules

per unit volume, is 2.45 × 10^{25} molecules m^{-3}, or 2.35 × 10^{22} molecules L^{-1}. Gas molecules are in constant motion, with the average velocity given by the equation:

$$\boldsymbol{v_{ave}} = \sqrt{\frac{\boldsymbol{8k_bT}}{\boldsymbol{\pi m}}} \tag{2.2}$$

Where $\boldsymbol{v_{ave}}$ is the average molecular velocity and $\boldsymbol{m}$ is the mass of the gas. For nitrogen gas, the most abundant gas in our atmosphere, the average molecular velocity at 300 K is 476 m s^{-1}. The mean free path, or average distance a gas molecule travels before colliding with another gas molecule, is determined by the equation:

$$\boldsymbol{\lambda} = \frac{\boldsymbol{k_bT}}{\sqrt{\boldsymbol{2}}\boldsymbol{\pi d^2 nP}} \tag{2.3}$$

Where $\boldsymbol{\lambda}$ is the mean free path, $\boldsymbol{d}$ is the diameter of the molecules, and $\boldsymbol{n}$ represents the gas number density. At 300 K and 760 Torr, the mean free path for nitrogen is approximately 96 nm. This short mean free path, combined with the velocity of nitrogen gas, means that nitrogen molecules will collide approximately every 0.2 ns. When gas molecules collide with a 2D surface, they can scatter (both elastically and inelastically), adsorb, or diffuse along the surface. The rate of gas adsorption on a surface is described by eq. 2.4:

$$\boldsymbol{rate_{ads}} = \boldsymbol{\gamma Flux} \tag{2.4}$$

Where $\boldsymbol{\gamma}$ represents the sticking coefficient, which represents the probability that a given gas molecule adsorbs onto a surface (γ values are 0 to 1), and the flux is the rate of that molecules collide per unit area with a surface (eq. 2.5).

$$\boldsymbol{Flux} = \frac{\boldsymbol{1}}{\boldsymbol{4}}\boldsymbol{nv_{ave}} \tag{2.5}$$

At 300 K and 760 Torr, the flux for nitrogen is 2.92 × 10^{23} molecules cm^{-2} s^{-1}. Approximately half of a mole of nitrogen hits a 1 cm^2 surface every second at atmospheric pressure. If we assume that every nitrogen molecule that hits a 1 cm^2 surface adsorbs (γ=1) and

that the 1 cm^2 surface has 10^{15} adsorption sites, a typical value for self-assembled monolayers, then nitrogen would form a monolayer in 3.9 ns. While nitrogen is unlikely to strongly adsorb and contaminate a surface, at ambient pressure, the presence of water vapor at a relative humidity of even 10% at 300 K would form a monolayer in 735 ns.

At reduced pressure, the mean free path of gases increases, which minimizes reactions due to gas-gas collisions and allows us to focus exclusively on reactions occurring at the gas-surface interface. Table 2.1 provides the vacuum properties for nitrogen at 300 K. In addition to keeping surface clean and minimizing gas-gas collisions, operating experiments at low-pressures allow us to utilize surface sensitive analytical techniques, such as mass spectrometry and X-ray photoelectron spectroscopy. While the infrared spectroscopy employed in our research can be used at any pressure, low-pressure environments remove signal from ambient gases like carbon dioxide and water and improve our sensitivity to subtle changes to the vibrational spectra of MOF samples.

Table 2.1 Vacuum properties of nitrogen at 300 K.

Pressure (Torr)	**Number Density (cm^{-3})**	**Mean Free Path (cm)**	**Surface Flux (molecules cm^{-2} s^{-1})**	**Time to form Monolayer (s)***
760	2.45×10^{19}	9.6×10^{-6}	2.92×10^{23}	3.9×10^{-9}
1	3.18×10^{16}	7.4×10^{-3}	3.80×10^{20}	3.0×10^{-6}
1×10^{-3}	3.18×10^{13}	7.4×10^{-0}	3.80×10^{17}	3.0×10^{-3}
1×10^{-6}	3.18×10^{10}	7.4×10^{3}	3.80×10^{14}	3.0×10^{0}
1×10^{-9}	3.18×10^{7}	7.4×10^{6}	3.80×10^{11}	3.0×10^{3}

*Assumes a surface site density of 10^{15} cm^{-2} and sticking coefficient of 1

2.2 Chamber Design

The UHV chamber described below (Figure 2.1) was initially designed and built by Joshua Uzarski, then further modified by both Amanda Wilmsmeyer and Joshua Abelard to investigate gas-surface interactions between chemical warfare agent simulants and metals, metal oxides, and metal-organic frameworks.[99-101] This dissertation will re-present the key components of the UHV chamber and provide a detailed description of the instrumentation and experimental methods most relevant to the research discussed later.

The chamber consists of two main compartments: the main chamber and a mass spectrometer chamber. The main chamber was pumped by a 2000 L/s turbomolecular pump (Pfeiffer, HiMag® 2400) and backed by an oil-free scroll pump (Edwards nXDS-10). A pneumatic right-angle valve (Kurt J. Lesker, SA0100PVQF) allowed for the turbo pump to be isolated from the scroll pump while a manual gate valve (Kurt J. Lesker) and enabled us to isolate the main vacuum chamber from the turbo pump. The pressure in the main chamber was monitored by a full-range gauge (Pfeiffer, PKR 251). In addition to the attached mass spectrometer chamber, a residual gas analyzer (Stanford Research Systems, RGA 200) was mounted on the main chamber to monitor possible gas-phase reaction products and aid in leak detection. The X-ray photoelectron spectrometer (XPS) installed in the chamber was not utilized due to an inability to properly align the sample to the X-ray beam. Instead, ex situ XPS analysis was performed by the Virginia Tech Surface Analysis lab as needed.

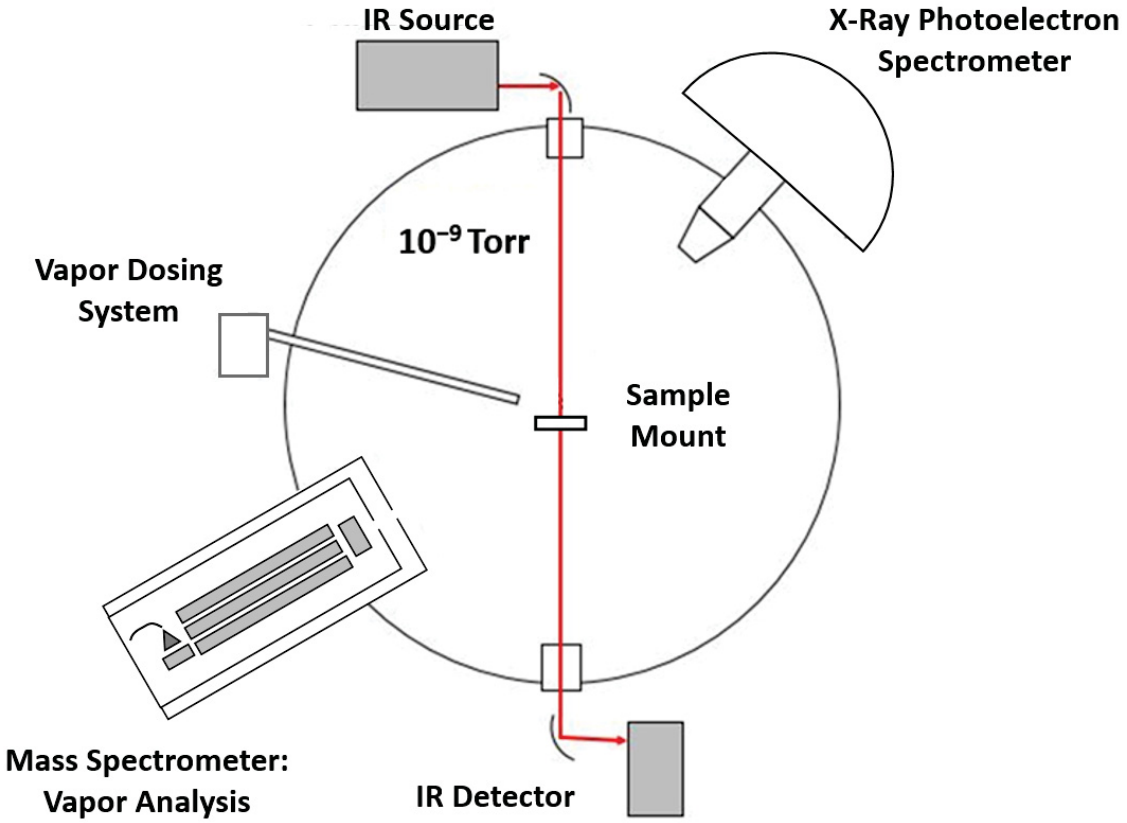

Figure 2.2 Diagram of UHV chamber used from a top-down perspective.

2.2.1 Sample Manipulator

MOF samples were suspended in the UHV chamber by pressing MOF crystallites into the 200 μm × 200 μm void spaces of a 50 μm thick tungsten mesh (Figure 2.2). The sample design was based on designs for an infrared cell previously described by Basu et al.[102] Pelletization of MOF samples in the tungsten mesh allowed us to suspend MOF particles within the vacuum environment without the loss of the powder sample. Furthermore, the tungsten mesh is partially IR transmissive, allowing us to utilize transmission IR spectroscopy. K-type thermocouple wires were spot-welded at the top of the tungsten mesh to monitor the sample temperature. Temperature control of the sample was accomplished through resistive heating and liquid nitrogen cooling of copper power leads attached to stainless steel support clamps that were bolted to the tungsten mesh.

A power feedthrough (Lesker part no. TFT1KY2C302, Figure 2.3) was used to connect the thermocouple wires and copper leads within the vacuum chamber to connections on the ambient pressure side of the chamber. These connections passed through the liquid nitrogen reservoir and were ultimately attached to a proportional-integral-derivative controller (Honeywell) and custom-built power supply. The PID controller and custom power supply allowed for resistively heating the sample meshes at constant heating rates.

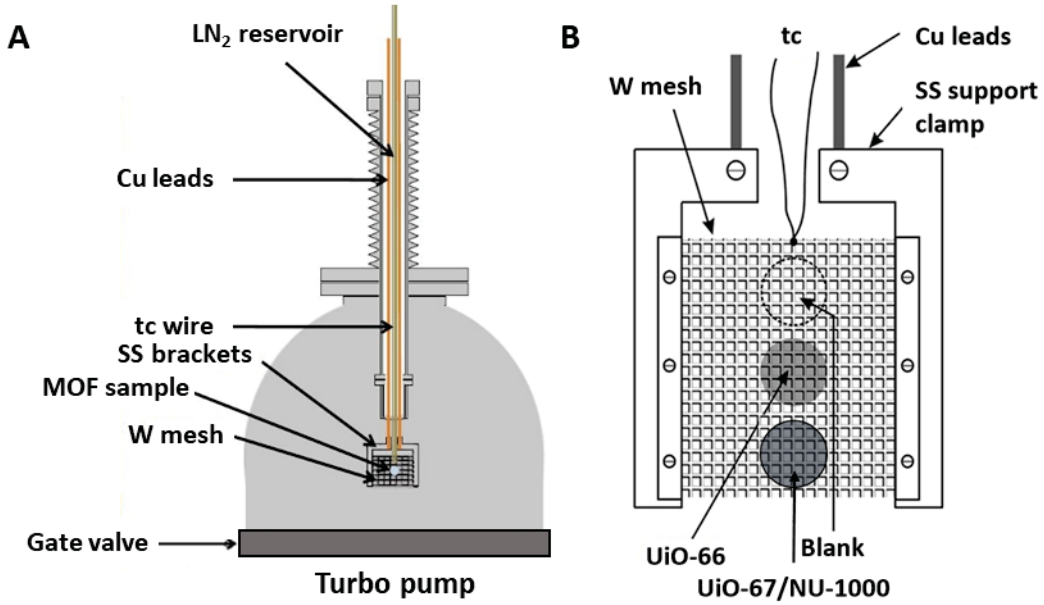

Figure 2.2 Schematic of sample manipulator (A) and sample mount (B).

The pumps, valves, gauges, and mass spectrometer were electronically connected to a home-built LabVIEW-based computer interface (interlock) system to protect the vacuum chamber from power outages, pump failures, and unexpected pressure rises. The interlock program featured programmable pressure set points for the main chamber, mass spectrometer chamber, and every roughing pump foreline valve. If the pressure within the chamber exceeded the set point, typically 1×10^{-6} Torr when no experiments were being performed, the LabVIEW program would shut down the pumps, gauges, and would turn off the mass spectrometer filament. During experiments, set points could be adjusted to accommodate the dosing of vapor simulants at higher pressures and

were employed to accommodate a pure nitrogen purge during chamber venting. If the pressure in the chamber exceeded atmospheric levels, causing the chamber to pressurize, a burst disk, designed to open at 1.7 bar, was installed onto the chamber.

2.2 Sample Preparation

Before sample preparation, the sample mesh, thermocouple wires, and any tools exposed to the vacuum-side of the UHV chamber were cleaned using a combination of acetone and methanol to remove grease and other contamination that would persistently outgas within the vacuum chamber. For this same reason, stainless steel tools were used for sample installation. The typical procedure for cleaning for UHV introduction (UHV-cleaning) involved sonicating materials in acetone for 10 minutes followed by sonicating samples in methanol for an additional 10 minutes. After sonication in methanol and clean-air drying, tools and sample materials were either stored in clean aluminum foil or handled using nitrile gloves that had not previously come into contact with any material that had not been "UHV clean". Throughout the sample installation process, once gloves came into contact with anything that was not UHV clean, they were discarded and a new set of gloves were used.

The K-type thermocouple wires were spot-welded to the sample mesh, ensuring that the contact point between the mesh and thermocouple wires occurred at the junction of the two wires (alumel and chromel). Excess thermocouple wire was left above the sample mesh to spot-weld the wires onto the power feedthrough attached to the UHV sample manipulator. MOF samples were prepared by pressing approximately 10-15 mg of MOF powder into the void spaces of the tungsten mesh at a pressure range of 3.4×10^7 to 6.9×10^7 N m^{-2} for 1 min via a pneumatic laboratory press (Carver, 3851). After pelletization of the sample, excess sample was removed from the surface of the mesh to ensure that the sample thickness remained at approximately 50 μm.

When were new samples were installed, the vacuum chamber had to be opened to ambient pressure to attach the new sample mesh to the sample manipulator. The process of The vacuum chamber was vented by turning off all turbo and roughing pumps and introducing an ultrapure nitrogen purge gas into the chamber after all the pumps stopped rotating. Once the system reached approximately 760 Torr, the gate valve on the main chamber was closed and the sample manipulator was then removed from the main chamber. Sample meshes were bolted onto the stainless steel support clamp and thermocouple wires were spot-welded to the proper connections on the power feedthrough (Lesker part no. TFT1KY2C302, Figure 2.3). Prior to bolting the sample manipulator back onto the vacuum chamber, the thermocouple connections were tested to ensure that the proper connections were made and the samples were aligned to the mass spectrometer or the infrared source through adjustments to the horizontal (x- and y-) and vertical (z-) positions on the manipulator.

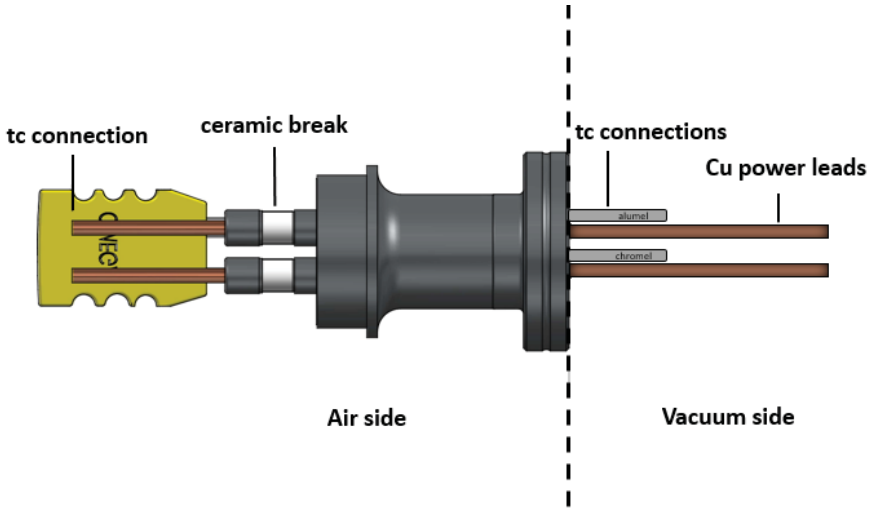

Figure 2.3 Schematic of power feedthrough. Figure adapted from Lesker.com.[103]

NOTE: In one instance when sample installation occurred without closing the main chamber gate valve, a small bolt that was part of the mesh sample clamp fell off the manipulator and into the

main turbo pump. No damage was done to the pump as a direct result of this incident and the bolt was successfully removed from the pump. Operation of the turbo pump with a bolt or other solid debris trapped inside could have caused catastrophic damage to the pump itself and would have posed a significant safety risk to all occupants present in the laboratory.

Upon evacuation, the MOF samples were thermally activated, typically for 12-72 hours at temperatures above 373 K to remove weakly bound guest molecules adsorbed within the MOF. The thermal activation of MOF samples prior to vacuum studies ensured a clean sample free from contamination that may have otherwise altered the interactions of gases with the MOF. The activation temperature depended on the MOF sample. UiO-66 is more thermally stable than NU-1000 and was therefore activated at a higher temperature. UiO-66 samples were thermally activated at 438 K (Figure 2.4) to remove residual solvents from synthesis as well as physisorbed water. For UiO-66 samples that were dehydroxylated, samples were heated to 573 K overnight to remove the bridging hydroxyls from the zirconium cluster.

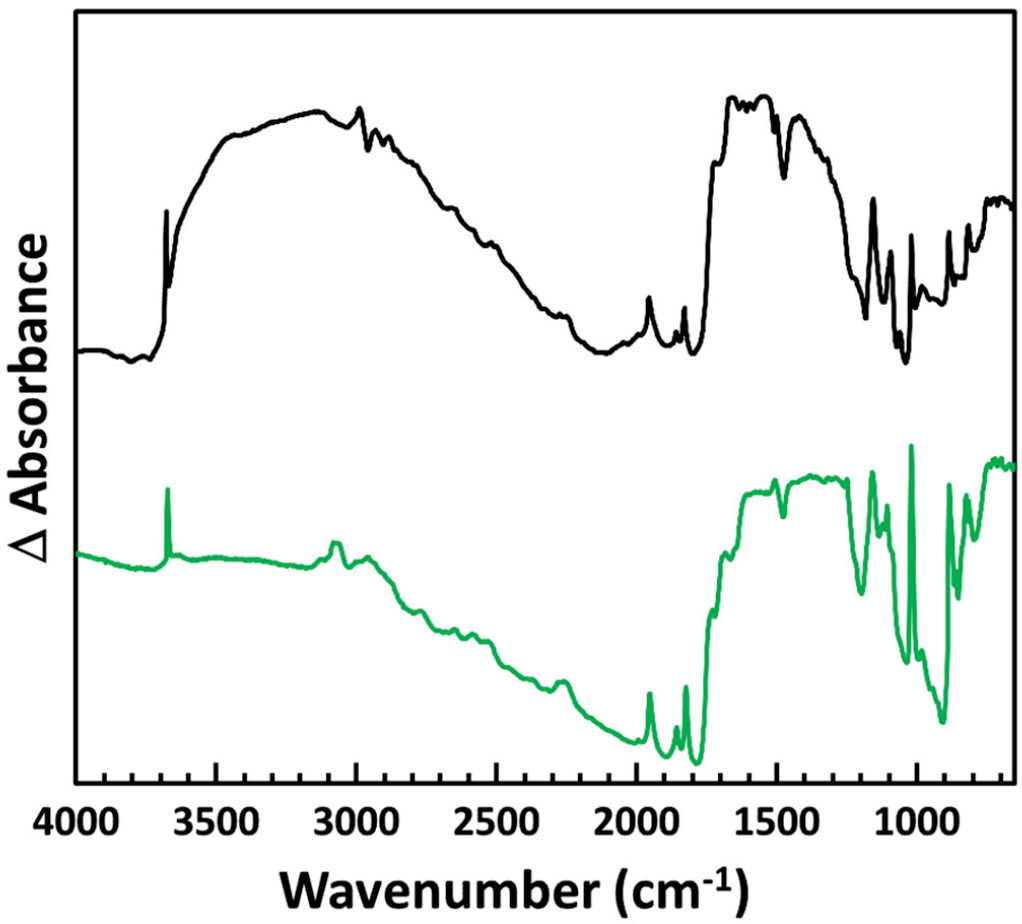

Figure 2.4 IR spectra of a UiO-66 sample before (black) and after (green) thermal activation at 438 K.

2.4 Gas Dosing

The controlled exposure of MOF samples under vacuum to our vapor- and gas-phase molecules was accomplished through the use of a custom dosing system and vapor manifold, which allowed for the controlled flux of purified gas onto our MOF surfaces. The doser is a glass capillary array doser, which provides directionality to the dosing gas. The schematic of the doser is provided in Figure 2.5. The doser was constructed from a 2-3/4" conflat flange containing a gas feedthrough (Lesker) with ¼" VCR male connections. On the vacuum side of the doser, a 1 1/3" mini CF connection attached a machined stainless steel cylinder and cover plate to the feedthrough. The cylinder contained a glass capillary array (Photonis) with 10 μm pores spaced 12 μm apart. A ¼" stainless steel tube was press-fit into the cover plate to increase the directionality of the doser.

The feedthrough was attached to a 1-dimensional translation stage (McAllister, BLT27C-4), which allowed us to align the doser as close as possible to the MOF sample. Because the translation stage only adjustable in one direction, a stainless steel bolt was often placed next to the bellows of the translation stage to torque the doser into the ideal position. A variable leak valve attached to the atmospheric side of the doser allowed the fine control over the dosing pressure within the chamber. During the dosing of simulant gases into the MOFs, the chamber pressure was kept between 1×10^{-6} Torr and 2×10^{-5} Torr. Prolonged vacuum pressures above 1×10^{-4} Torr caused strain on the main chamber turbo pump and was avoided. On rare occasions, when it was necessary to exceed dosing pressures of 1×10^{-4} Torr, the gate valve that connected the main chamber to the turbo pump was closed, which allowed the pressure in the main chamber to increase. This process was known as backfilling. The chamber was backfilled with simulant vapors to pressures as high as 4 Torr. Such a significant increase in the main chamber pressured would cause the mass spectrometer chamber pressure to increase as well, so the mass spectrometer filament was turned off prior to backfilling.

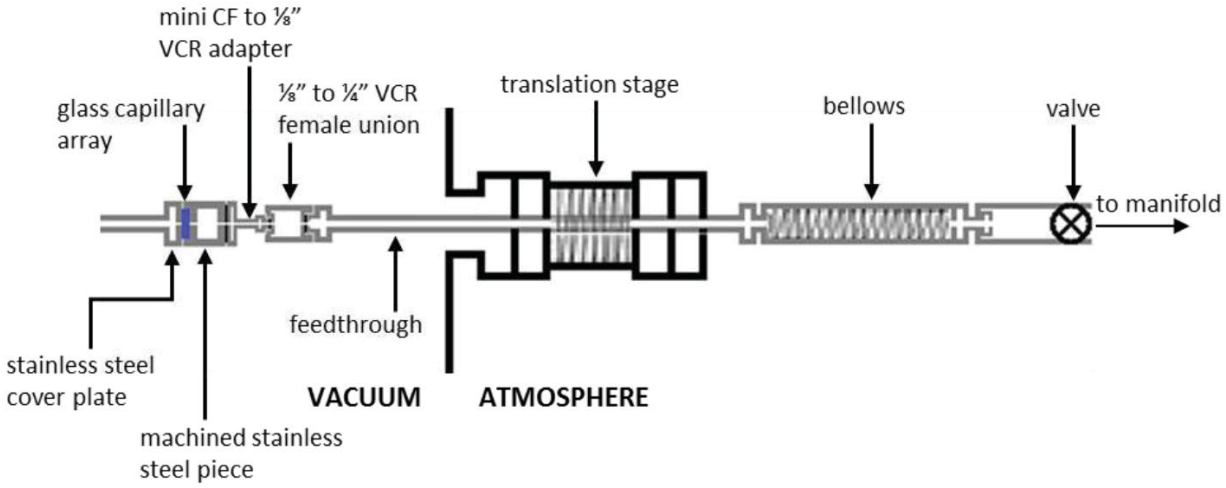

Figure 2.4 Schematic of glass capillary array doser.

The leak valve was connected to a custom gas manifold (Figure 2.6) constructed of stainless steel tubing and bellows-sealed valves (Dibert Valve, SS-4BG-V51). The manifold was

pumped by a 60 L/s ion pump (Duniway Stockroom, rebuilt Varian 911-5034) when not in use and a sorption pump (MDC Vacuum, SP-150) was used when initially pumping away simulants in the manifold. The base pressure for the manifold was in the high vacuum range (below 1×10^{-6} Torr).

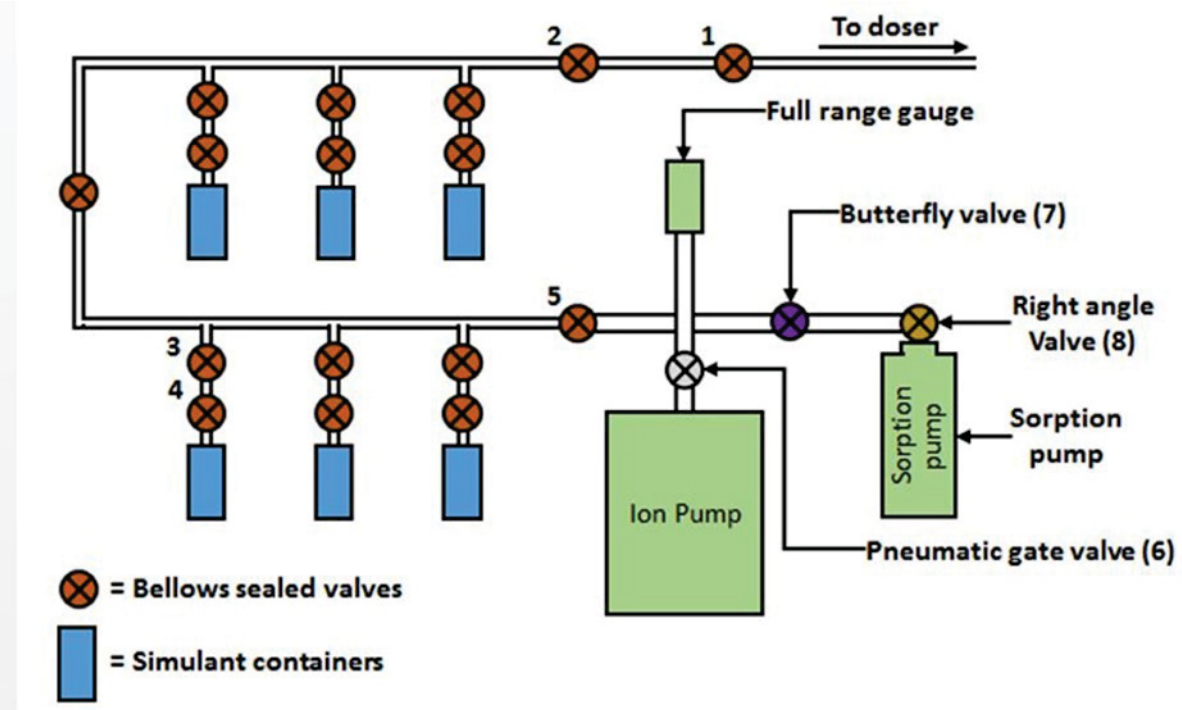

Figure 2.5 Schematic of the gas manifold

Neat liquid samples were pipetted into stainless steel dosing cylinders and attached to the sealed valves through a ¼" VCR connection, while stainless steel bellows with VCR connections were used to attach gas regulators to the manifold. After attaching the stainless steel dosing bulbs, the liquid simulants were purified through multiple freeze-pump-thaw cycles. Liquid nitrogen was used to freeze the simulants while the sorption pump would pump out any contamination. Before installing a new sample simulant onto the manifold, the manifold was baked out the night prior with heating tape.

2.4.1 Dosing Procedure

For any given experiment, vapor dosing into the vacuum chamber followed this general procedure: Initially, valves 1, 2, 3, 7, and 8 were closed and all other valves were open. valve 5 was closed to isolate the manifold from the ion pump. valve 3 was open to allow the volume between valves 2 and 5 to fill with simulant vapor. Valve 2 was opened and then valve 1 (the leak valve) was carefully opened to control the flux of simulant into the chamber, keeping the chamber dosing pressure between 1×10^{-6} to 2×10^{-5} Torr. At the end of dosing, valves 3, 2, and 1 were closed in that order.

2.5 Infrared Spectroscopy

Transmission IR spectra reported in this dissertation were recorded on a Nicolet Nexus 670 spectrometer purged with dry air. The spectrometer contained a SiC mid-IR source with a 650-4000 cm^{-1} range, an aperture wheel, and a Michelson interferometer with a KBr beamsplitter. The schematic of the IR instrument and the vacuum chamber is shown in Figure 2.7. The IR beam was directed into an adjacent dry-air-purged optics box. Within the optics box, a flat mirror (Bruker Optics IM190-GH) and a parabolic mirror (Bruker Optics IM137-GH; f=250 mm) were used to focus the IR beam onto the sample through a wedged KBr viewport on the chamber. After exiting the chamber through another KBr viewport, IR beam would enter a second dry-air-purged optics box that contained two parabolic mirrors and a flat mirror to collimate the beam then focus the light into a liquid-nitrogen-cooled mercury-cadmium-telluride (MCT-A) detector. Most IR scans reported in this thesis used the following spectrometer settings. 1.89 cm/s scanner velocity, 32 mm aperture, 8V gain, and either 4 cm^{-1} or 2 cm^{-1} resolution. To optimize the signal-to-noise as well as temporal resolution for various experiments, the number of scans per spectrum varied between 16, 64, 128, and 256 scans.

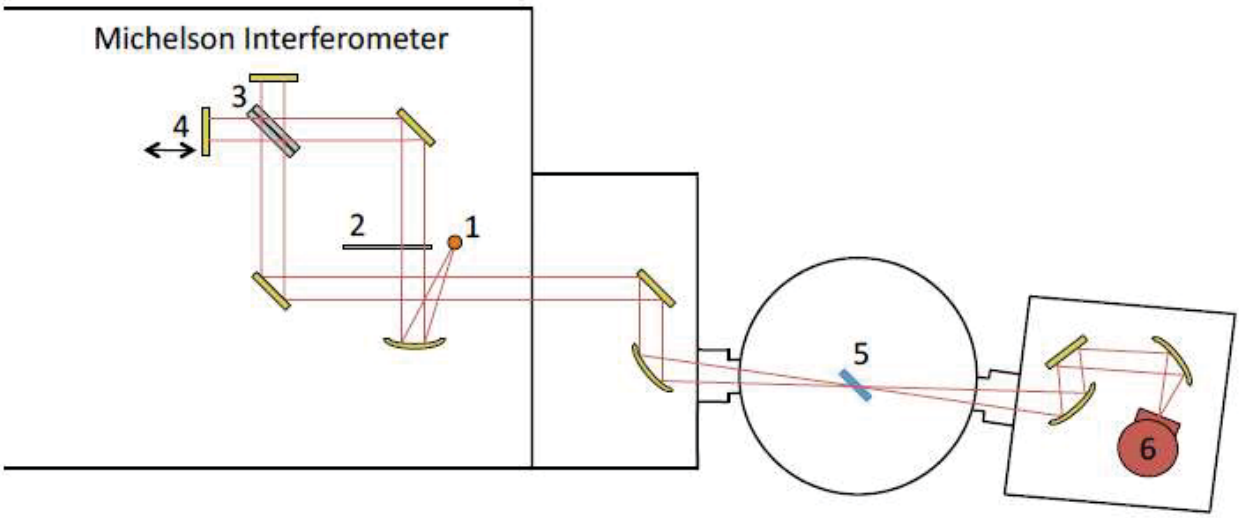

Figure 2.7 Schematic of IR instrument set-up. The components numbered are: 1) SiC IR source, 2) aperture wheel, 3) KBr beamsplitter, 4) moving mirror, 5) sample surface, and 6) MCT-A detector.

2.6 Mass Spectrometry

A quadrupole mass spectrometer (Extrel, MAX1000880APP3/4P8) with a 2-1000 m/z range and < 1 amu resolution was used to detect gas-phase molecules after they desorbed from the MOF surface. Incoming gas molecules were ionized by the filament of the axial ionizer. Ion fragments of different mass-to-charge (m/z) ratios were separated by four 19 mm diameter quadrupole rods and detected with a channel electron multiplier. Pressed mesh samples were aligned so that the mass spectrometer was in the direct line-of-sight of the sample surface. Two pinhole apertures (Figure 2.11) separated the main vacuum chamber from the mass spectrometer, and the mass spectrometer chamber had two stages of differential pumping. The mass spectrometer signal was proportional to the amount of gas molecules in the ionizer area, and any gas molecule not ionized through its first pass through the ionizer was most likely pumped out of the chamber (the base pressure of the MS chamber was below 9×10^{-9} Torr). Signal was therefore inversely proportional to the rate that molecules entered the ionizer. As will be discussed later, we correct for this in our TPD experiments.

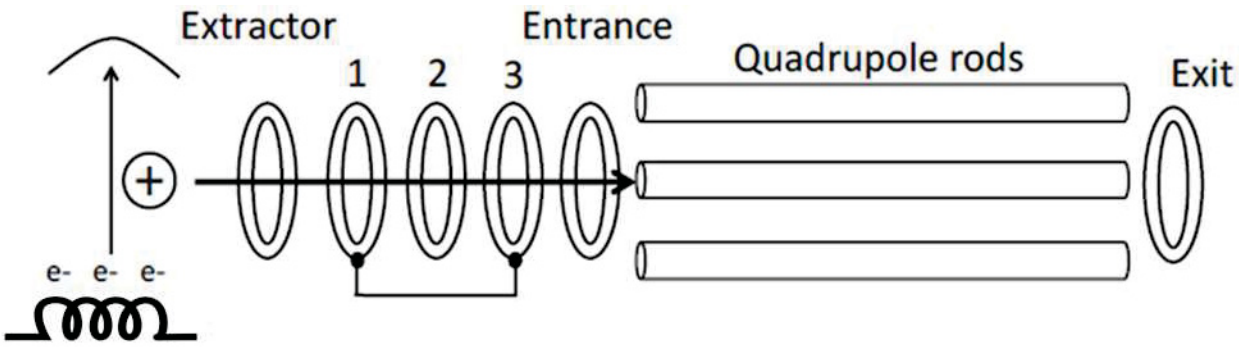

Figure 2.8 Schematic of quadrupole mass spectrometer ion optics.

To ensure that the mass fragments ionized by the ionizer filament have the appropriate flight path to be detected, the ion optics within the mass spectrometer must be properly tuned. Figure 2.8 shows a simple schematic of the ion optics. The filament voltage was kept sufficiently high to generate high-energy electrons that can efficiently ionize gas molecules. Next, the ions are drawn away from the ion region by the extractor lens held at a small negative voltage. Ions then travel through three Einzel lenses to focus ions before the quadrupole. Einzel lenses 1 and 3 are kept at the same slight negative voltage to slow down the ions while lens 2 is held at a strongly negative voltage to accelerate the ions. The additional lenses in the ion optics are used to direct ions through the mass filter. After each sample installation, the settings for mass spectrometer ion optics were tuned to optimize mass spectrometer signal. One iteration of the tune parameters for the mass spectrometer data is provided in Table 2.2. Despite the UHV base pressures, several background gases such as water, nitrogen, and carbon dioxide are present in the mass spectrum. A typical mass spectrum between 10-50 m/z is shown in Figure 2.9.

Table 2.2 Sample tune file settings used for a portion of work presented in this thesis.

Mass Spec Parameters	Settings
Filament voltage (V)	-70
Filament current (mA)	2.00
Ion Region (V)	10
Extractor Lens (V)	-18
Lens 1 & 3 (V)	-15
Lens 2 (V)	-175
Quadrupole Entrance Lens Min/Max (V)	-16/-13
Quadrupole Exit Lens	-300
Dynode (V)	5000
Multiplier (V)	2100

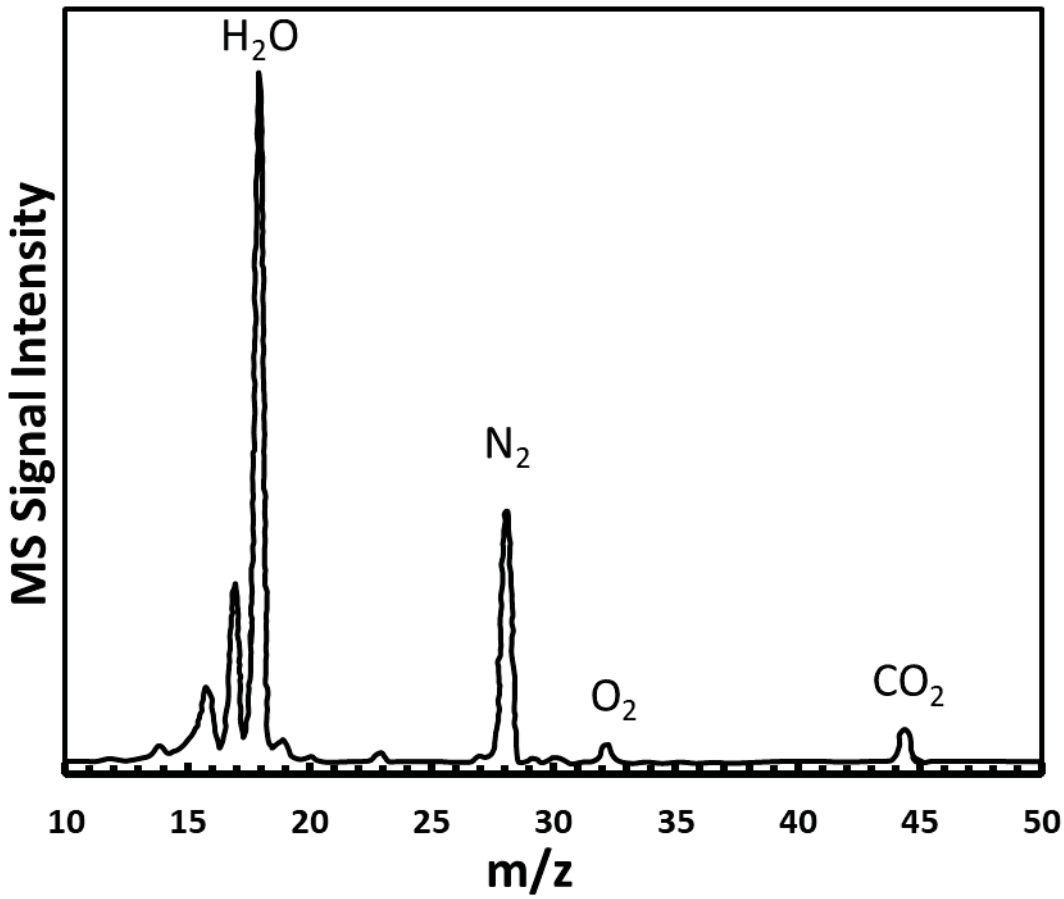

Figure 2.6 Mass spectrum of background gasses present in the chamber under UHV conditions.

As gases desorbed from within the MOFs during TPD experiments, the main chamber pressure often exceeded 10^{-5} Torr, well above the mass spectrometer operational pressure range. To keep the mass spectrum baseline unaffected by main chamber pressure fluctuations and to only

detect gas molecules desorbing from the sample surface, the mass spectrometer chamber was designed to be differentially pumped (Figure 2.10) with two pinhole apertures restricting molecular transport into the mass spectrometer chamber. With this set-up, the mass spectrometer background pressure remained unaffected by main chamber pressures up to 1×10^{-3} Torr. The first stage is a custom ConFlat cross attached to a 200 L/s turbo pump (Edwards) backed by a dry scroll pump (Edwards XDS 10). The second stage was pumped by a 400 L/s turbo pump (Edwards) and is also roughed by the same scroll pump.

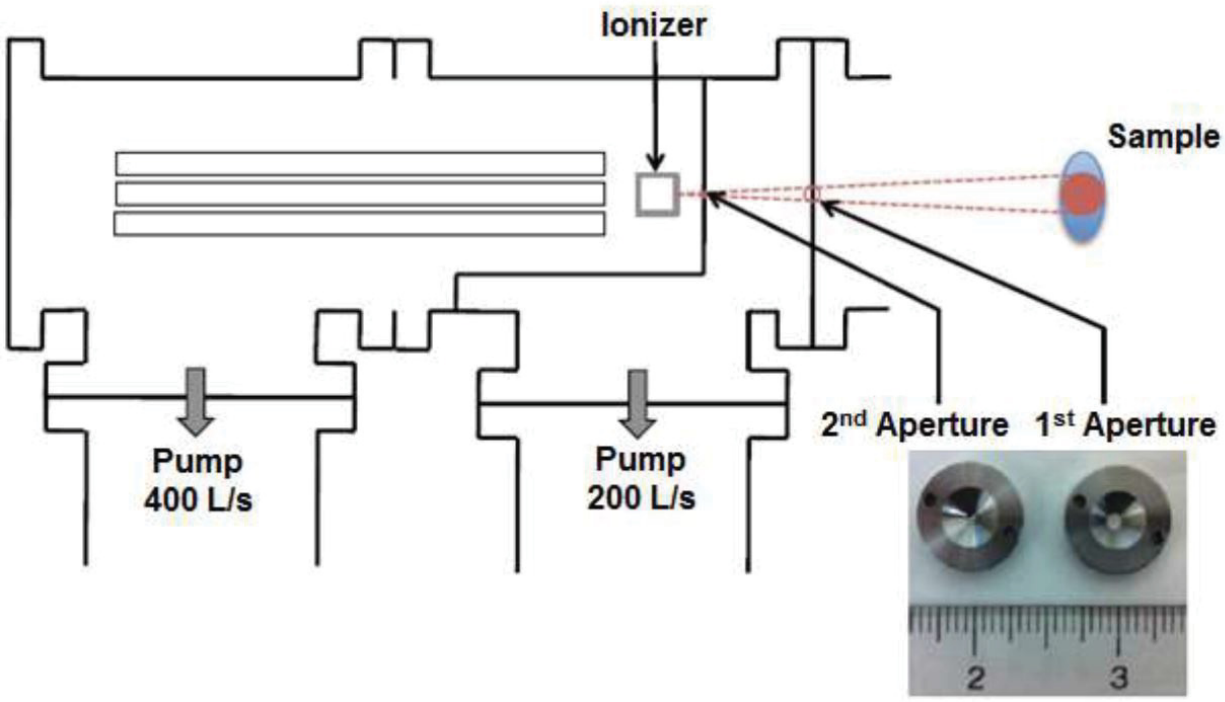

Figure 2.7 Schematic of the mass spectrometer chamber

The apertures prevent molecules that have desorbed from sample spots not directly aligned to the mass spectrometer, although multilayer desorption features that cause significant pressure increases are still detected by the mass spectrometer. Figure 2.11 shows the geometry of the aperture system.

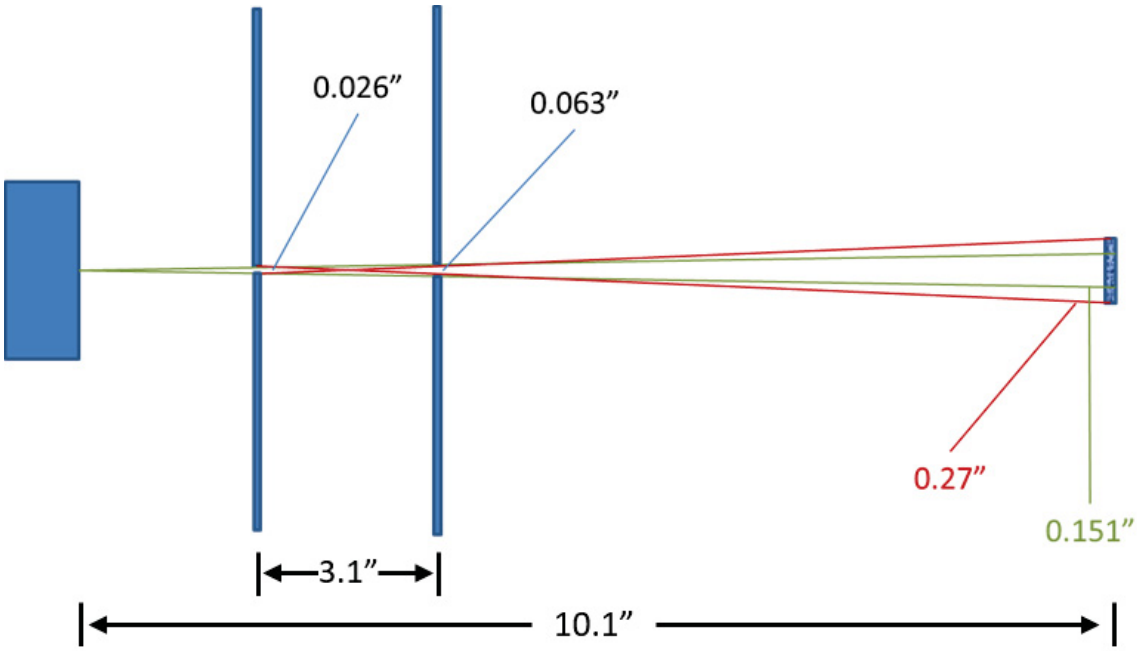

Figure 2.11 Diagram of the line-of-sight path defined by the mass spectrometer chamber apertures.

2.7 Temperature Programmed Desorption

Temperature programmed desorption (TPD) experiments, briefly mentioned in Chapter 4 and more extensively discussed in Chapter 6, were utilized to quantify the strength of the surface-adsorbate interactions for HD simulant molecules adsorbed within Zr-MOFs and understand the entropic changes to 2-CEES upon adsorption. This work was based heavily on previous studies by Abelard et al., who analyzed their TPD data using inversion analysis.[104]

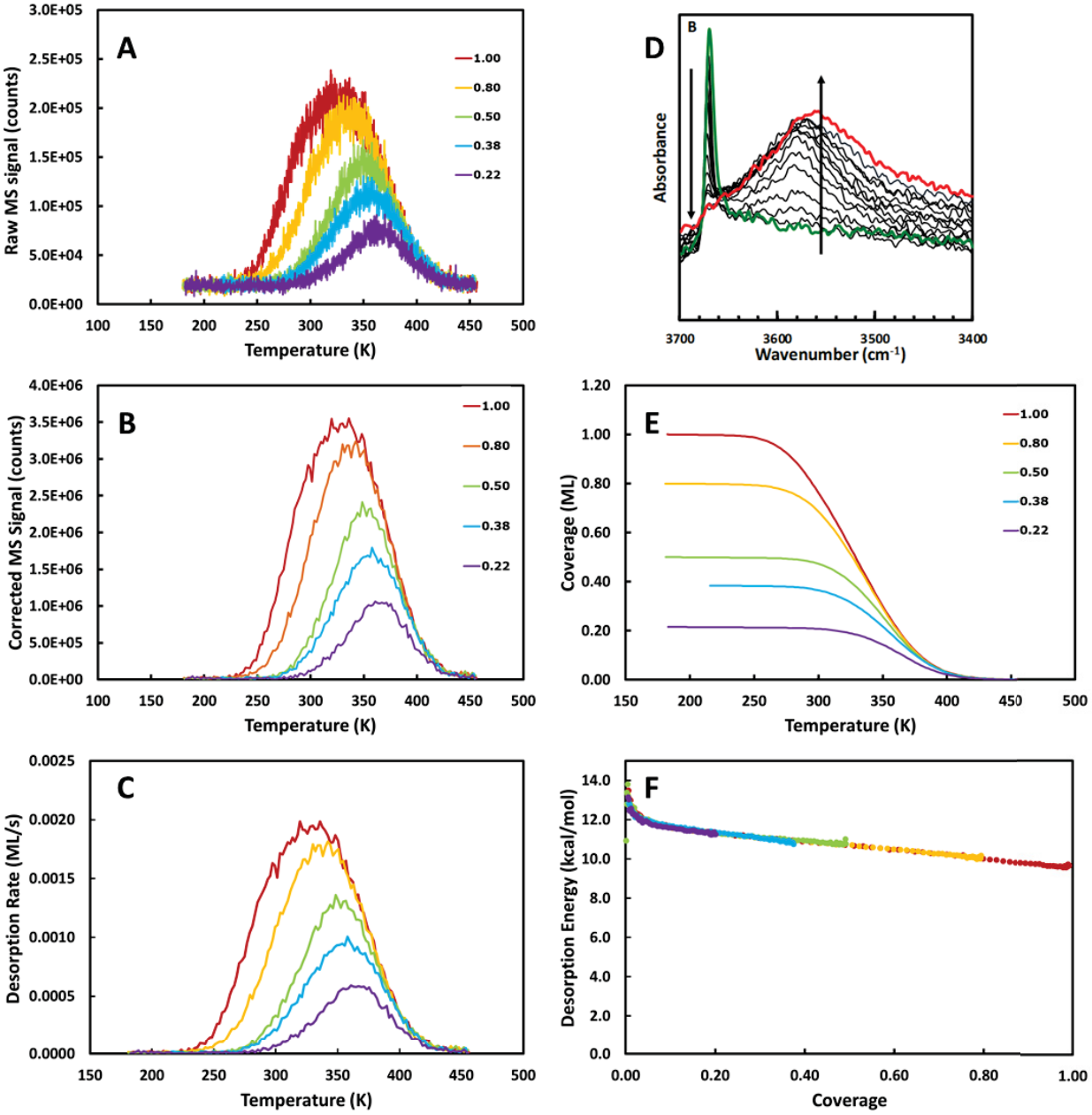

Figure 2.12 Data analysis for the TPD of 2-CEES on UiO-66. A) Raw mass spectrometer signal vs. temperature. B) Mass spectrometer signal vs. temperature after signal averaging and corrections for baseline, 1/v factor, and sensitivity factors (see text). C) Desorption rate vs. temperature. D) IR spectra that show the complete depletion of the IR band at 3674 cm^{-1} used to determine initial surface coverage. E) Coverage vs. temperature. F) Desorption energy vs coverage.

2.7.1 Inversion Analysis

In the TPD experiments discussed in Chapter 6, the sample surface was heated at a constant, linear heating rate (0.2 K/s for all experiments) and the rate that adsorbed molecules desorb from the surface is measured using the mass spectrometer. Surface coverage, or the fraction of occupied adsorption sites, were determined spectroscopically at the beginning of the TPD experiment by comparing the intensity of the bridging hydroxyl band prior to dosing to the same feature after dosing. Desorption is an activated process and follows the Arrhenius equation. Therefore, the desorption rate constant increases exponentially as temperature increases. At the same time, as molecules desorb, the number of molecules on the surface decrease, causing the overall desorption rate to reach zero once all molecules have desorbed from the surface. The Polanyi-Wigner equation expresses the overall rate of desorption as a combination of both the increase of the rate constant with temperature and the decrease in surface concentration with temperature (eq. 2.6). Inversion of the Polanyi-Wigner equation (2.7) solves for the activation energy of desorption.

$$\boldsymbol{R_d = -\frac{d\theta}{dt}(\theta, T) = \nu(\theta, T)\theta^n e^{-\frac{E_{des}(\theta)}{K_b T}}} \tag{2.6}$$

$$\boldsymbol{E_{des}(\theta) = -K_b T \cdot \ln\left(-\frac{d\theta/dt(\theta, T)}{\nu(\theta, T)\theta^n}\right)} \tag{2.7}$$

Where $\boldsymbol{\theta}$ = coverage, or the fraction of occupied adsorption sites, $\boldsymbol{t}$ is time, $\boldsymbol{T}$ is temperature, $\boldsymbol{\nu}$ is desorption pre-exponential factor (prefactor), $\boldsymbol{K_b}$= the Boltzmann constant, $\boldsymbol{E_{des}}$= the activation energy of desorption, and $\boldsymbol{n}$ is the desorption order. Our TPD experiments provided us with the overall desorption rate and then the following methods were used to solve for the desorption energy and the desorption prefactor. For our TPD experiments, we assumed a constant prefactor that was not dependent on coverage or temperature.

The data analysis for our TPD experiments is heavily based on previously published research from the Kay group,[105-110] who developed a methodology for solving for Polanyi-Wigner equation to extract the desorption prefactor and activation energies of desorption. The method requires multiple TPD experiments with different initial coverages to solve for the desorption prefactor.

The raw TPD data was the mass spectrometer signal intensity (counts per second) for selected ion fragments over time (Figure 2.12A). To maximize signal-to-noise, multiple ion fragments were summed together. The temperature controller is an analog instrument and does not log temperatures, so the sample temperature was manually recorded every 15 seconds during TPD experiments. The data output from the K-type thermocouple was in units of mV and was converted into Kelvin through the use of a rational polynomial function provided by Mosaic Industries.[111] Abelard compared the Mosaic polynomial to the NIST ITS-90 Thermocouple database and found that the Mosaic function demonstrated less error between calculated and tabulated values.[99] While the temperature was recorded every 15 seconds, the mass spectrometer recorded data approximately every 1 second, so a linear interpolation was generated in Excel to estimate the temperature for each data point.

Next, the raw mass spec signal intensity was baseline corrected. TPD experiments were designed so that the rate of desorption was zero for the first 60 seconds. The average signal intensity during that time was averaged and subtracted from the raw data. The data was then multiplied by $\sqrt{T}$ to account for the relationship between the number of desorbed molecules and the number of molecules ionized in the mass spectrometer. Daschbach et al. observed that the ionization probability decreases for a gas molecule as its average velocity increases, so by correcting for the decline in mass spectrometer signal, we can correct our data to reflect the actual

number of molecules desorbing.[105] After the temperature conversion, baseline correction, and normalization, the TPD data resembled the graph in Figure 2.12B.

The initial coverage the each TPD experiment was based on IR spectroscopy and the fractional signal intensity of the IR band at approximately 3674 cm^{-1} before and after dosing, attributed to μ_3-OH groups on the Zr cluster. The decrease in the signal intensity at 3674 cm^{-1} occurred due to of hydrogen-bond formation between the MOF and adsorbates, so complete saturation of that IR feature (Figure 2.12D) corresponded to the maximum initial coverage of 1. For traditional 2D surfaces, a fractional coverage of 1 is known as a monolayer (ML). For our experiments, we refer to a monolayer as the adsorbate concentration when all μ_3-OH groups are hydrogen bonded. Once the maximum initial coverage was determined, the initial coverage of the rest of the TPD experiments was determined by the relative integrated area under the TPD curve compared to the 1.00 ML experiment. Once initial coverages for each TPD run were calculated, the data was plotted as the change in desorption rate as a function of temperature (Figure 2.12C) and coverage vs. temperature (Figure 2.12E) to confirm that the trailing edge of each desorption curve aligned. At least three TPD experiments, each with different initial coverages, were performed for the desorption of 2-CEES from each Zr-MOF studied.

Next, a "guess" desorption prefactor was used to solve the Polanyi-Wigner equation for the TPD curve with the highest initial coverage, which will be referred to as the master curve. From the master curve, the activation energy of desorption at each coverage was determined. A set of simulated desorption spectra based on the "guess" desorption prefactor and the activation energies of desorption were created for each TPD curve (2.21F). An Excel macro was used to test a range of desorption prefactor values and the sum of the squared residuals (SSR) was calculated to compare the goodness of fit between the simulated TPD spectra and the actual experimental

spectra (Figure 2.13). Figure 2.14 compares good and poor agreement between simulated and experimental desorption rates with several prefactor values. A plot of SSR versus the log of the prefactor was fit to a 6th-order polynomial function and Solver was used in Excel to determine the prefactor term with the minimum SSR value (Figure 2.13).

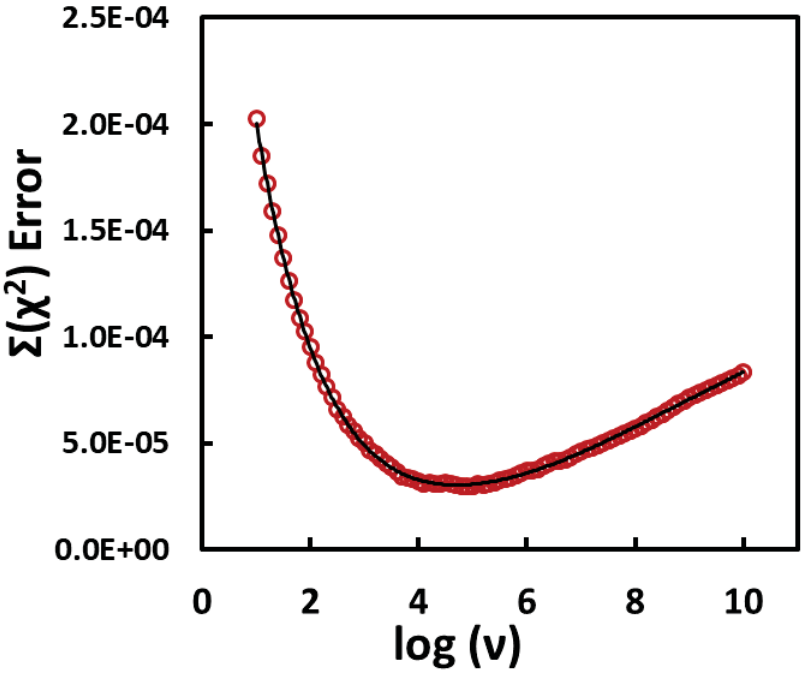

Figure 2.13 Sum of the squared residuals for experimental rates for a range of prefactor values (open circles) and the polynomial function used to find the prefactor value (black line).

The method validation for instrumental accuracy and of the inversion analysis are described in considerable detail by Abelard.[99] Experimentally determined values for the multilayer (desorption of molecules at $\theta > 1$ dominated by adsorbate-adsorbate interactions and not adsorbate-surface interactions) desorption of several functionalized benzene molecules from silica agree well with reported literature values for their enthalpies of sublimation. Digitized TPD data previously published by Zubkov et al.[108] was analyzed using our inversion analysis method, which yielded an activation energy of desorption of 10.4 kJ/mol, within 6% of the literature value (11 kJ/mol).

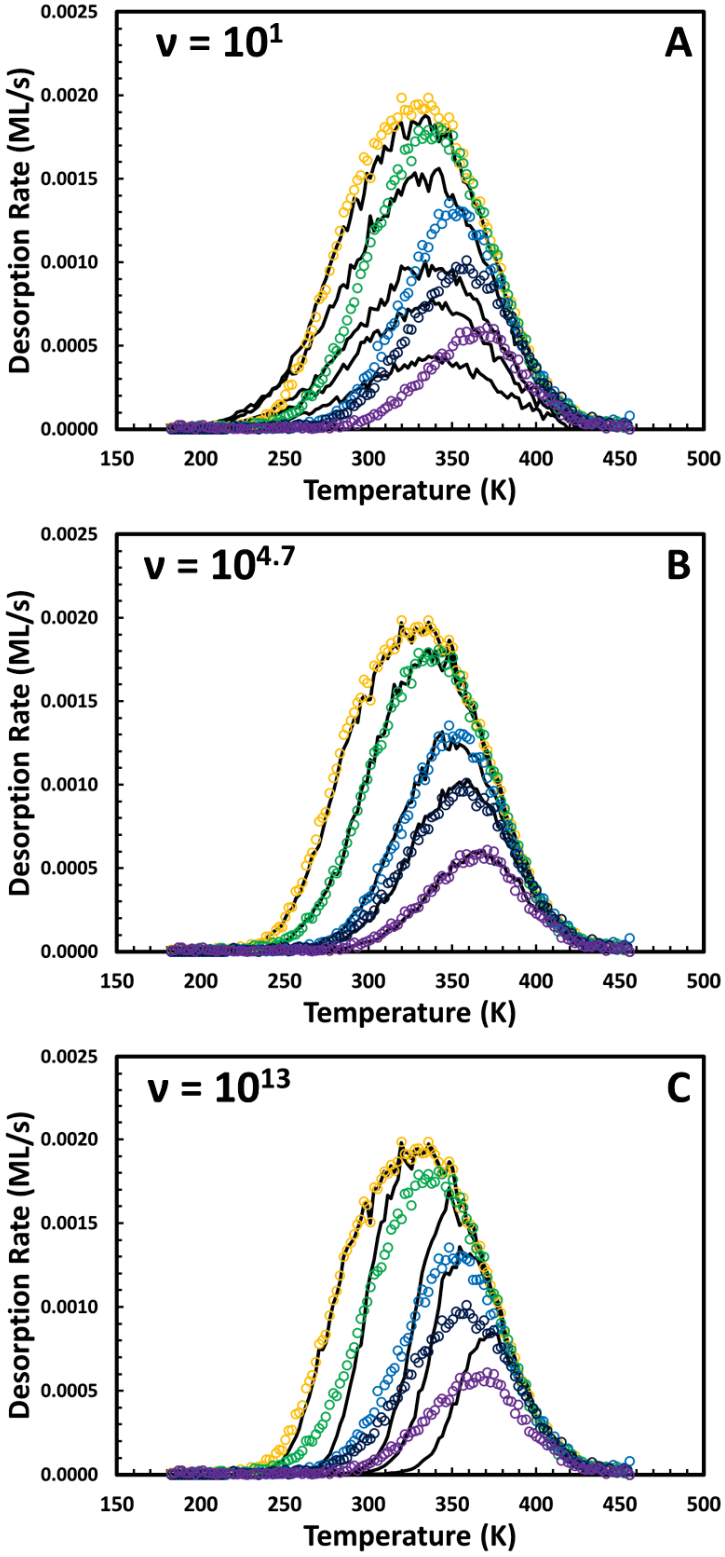

Figure 2.14 Simulated (black lines) and experimental (colored circles) desorption rate plots for prefactor values that are too high (A), optimized (B), and too low (C).

2.8 Isothermal Diffusion Experiments

The majority of the research discussed in this thesis focused on determining the diffusivity of adsorbed molecules through MOFs. The isothermal diffusion experimental method was based on published work by the Yates group,[112-114] who studied the diffusion of adsorbed molecules on metal oxide surfaces. Simulants were dosed until the IR spectra indicated that all possible hydrogen-bonding adsorption sites were occupied with adsorbed simulants. Samples were then heated at 0.2 K/s to remove multilayers, weakly-bound simulants that condensed on the external crystal surfaces of the MOF samples during dosing. The desorption of the multilayers on MOF samples was measured through a combination of monitoring the pressure change in the main chamber as well as infrared spectroscopy. Once the adsorbed multilayers were removed, samples were rapidly cooled to a temperature where the rate of diffusion out of the MOF sample was likely zero. The vacuum chamber pressure was allowed to equilibrate to prevent the readsorption of simulants during the diffusion experiments. For the isothermal diffusion experiment, samples were heated at the maximum heating rate of 2.0 K/s until the desired sample temperature was reached. The sample was held at the desired temperature for two hours and IR spectra were collected approximately every minute using an OMNIC macro. After the two-hour diffusion, samples were heated to desorb remaining adsorbates.

2.8.1 Data Analysis

To extract diffusivities from IR bands associated with adsorbates within MOFs, data analysis was performed through a combination of Excel, Python, and MATLAB programs. A custom Python program designed by N. Jones was used to prepare experimental data for model fitting. First, .spa files of IR spectra pulled from the IR spectrometer software were converted to .csv files that are readable in Excel. Next, a spectrum of unexposed MOF from each experiment

was used to background subtract the MOF vibrational modes from all other spectra to convert the raw IR spectra to difference spectra. Timestamps were extracted to provide precise time information for each data point during the diffusion process. The IR band(s) of interest for each experiment were integrated over pre-determined integration bounds. Finally, data were exported which provided a decrease in total integrated signal over time as well as the relative intensity of the integrated signal over time (relative to the intensity at time = 0 s).

A MATLAB program was developed to fit the raw diffusion data to the Fickian diffusion model to extract the diffusion coefficient and coverage term fitting parameters. The data were fitted using a function derived from Fick's 2nd law of Diffusion:

$$\frac{\boldsymbol{I_t}}{\boldsymbol{I_0}} = \sum_{\boldsymbol{n=0}}^{\boldsymbol{100{,}000}} \frac{\boldsymbol{8}}{\boldsymbol{(2n+1)^2\pi^2}} \boldsymbol{e}^{\left[-\frac{\boldsymbol{D(2n+1)^2\pi^2 t}}{\boldsymbol{l^2}}\right]} \tag{2.8}$$

Where $\boldsymbol{D}$ represents the diffusivity at a given temperature, $\boldsymbol{l}$ is the length of sample, and $\boldsymbol{t}$ is the time. $\boldsymbol{n}$ was set to 100,000 as any changes at higher levels of $\boldsymbol{n}$ did not alter the diffusion coefficient within the significant figures of our measurement techniques and minimized computational time compared to higher-level n-values. The experimental diffusion data were fit by utilizing a rigorous Levenberg-Marquardt algorithm with a bisquares weighting. The bisquares weighting seeks to minimize a weighted sum of squares. Each data point is weighted by how well it fits the model in an attempt to minimize the effects that experimental outliers have on the overall model fit. Before each fit, several guess diffusivities were used to ensure that the output parameters were not a result of local error minima.

2.8.3 Method Validation

The validation of the MATLAB-based diffusion analysis program was accomplished by digitizing isothermal diffusion data reported by Green et al.[114] for the diffusion of pyridine through

TiO_2 and comparing our calculated diffusivities to their work. Green et al. described two parallel diffusion processes for the diffusion of pyridine through TiO_2 and modeled their data with a linear combination of two different Fickian diffusion functions (Eq. 2.9). To reproduce their results, our MATLAB program was altered to allow us to calculate the two different diffusion coefficients at each temperature.

$$\frac{I_t}{I_0} = \theta_{Fast} \sum_{n=0}^{\infty} \frac{8}{(2n+1)^2\pi^2} e^{\left[-\frac{D_{Fast}(2n+1)^2\pi^2 t}{4l^2}\right]} + \theta_{Slow} \sum_{n=0}^{\infty} \frac{8}{(2n+1)^2\pi^2} e^{\left[-\frac{D_{Slow}(2n+1)^2\pi^2 t}{4l^2}\right]} \quad \textbf{(2.9)}$$

The diffusivity data was digitized using DataThief digitization software.[115] Our calculated activation energy of diffusion from the faster diffusion term was 35.5 ± 3.8 kJ/mol, which is well within one standard deviation of the reported value of 35.8 ± 3.8 kJ/mol.[114] The calculated activation energy of the slow diffusion value (87.6 ± 18.7 kJ/mol) also agreed well with the literature value of 90.0 ± 17.8 kJ/mol. The comparison of the diffusion fits for at each temperature is shown in Figure 2.15. On average, the MATLAB calculated diffusivities varied from the reported diffusivities by less than 13%.

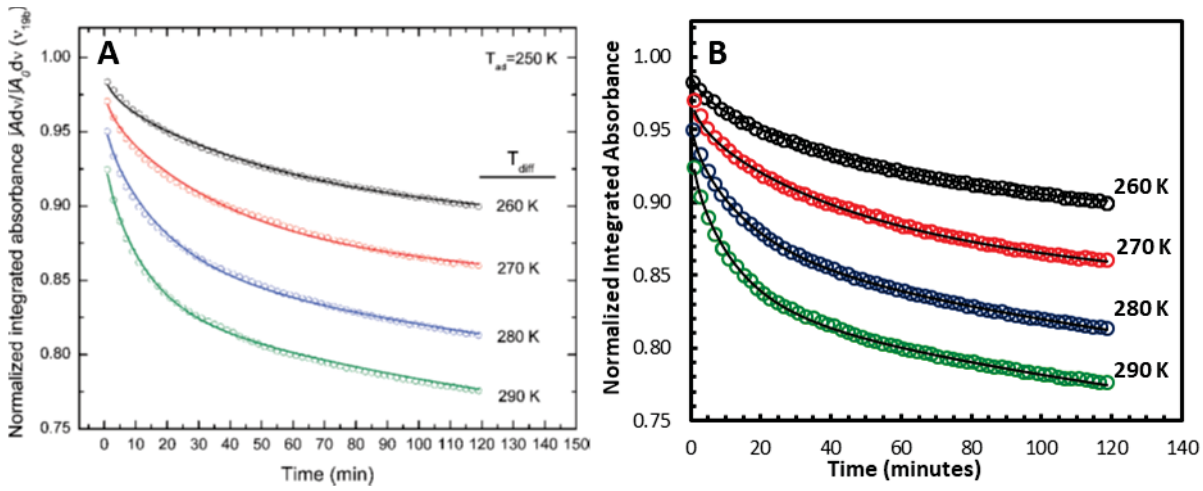

Figure 2.15 Comparison of diffusion fits for pyridine diffusion through TiO_2 published by Green et al. (A) and analyzed using our MATLAB data analysis method (B). The colored circles represent the experimental data while the black lines represent the Fickian diffusion fit. Figure adapted with permission from Green et al.[114]

Data analysis for the isothermal diffusion experiments assumed a uniform sample thickness of 50 µm. To address the effect that variations in sample thickness had on the calculated diffusivities, the diffusivities of 2-CEES through UiO-66 were fit assuming a 20% variation in sample thickness (45 µm to 55 µm). As shown in Table 2.3, changing the sample thickness by 10 % resulted in less than a 20% change in the diffusivity on average.

Table 2.3 Diffusion coefficients of 2-CEES through UiO-66 assuming different sample thicknesses.

Diffusion Temp (K)	D at l = 45 µm (10^{-10} cm^2 s^{-1})	D at l = 50 µm (10^{-10} cm^2 s^{-1})	D at l = 55 µm (10^{-10} cm^2 s^{-1})
253	0.363 ± 0.015	0.448 ± 0.019	0.542 ± 0.023
263	1.07 ± 0.03	1.32 ± 0.04	1.60 ± 0.06
273	2.76 ± 0.14	3.41 ± 0.16	4.13 ± 0.20
283	5.93 ± 0.19	7.32 ± 0.24	8.85 ± 0.29
293	11.2 ± 0.4	13.8 ± 0.5	16.7 ± 0.6

When plotting diffusivity versus temperature to determine the Arrhenius parameter for diffusion activation energy (Figure 2.16), the increase in the uncertainty of diffusivities calculated at each temperature due to sample thickness results in an increase in the uncertainty of the slope of the

best-fit line. The activation energy of the diffusion fitting parameter for 2-CEES through UiO-66 changes from 53.0 ± 1.9 kJ/mol to 53.0 ± 6.2 kJ/mol. Therefore, a 20% deviation in the sample thickness results in a 12% deviation in the determined activation energy of diffusion for UiO-66.

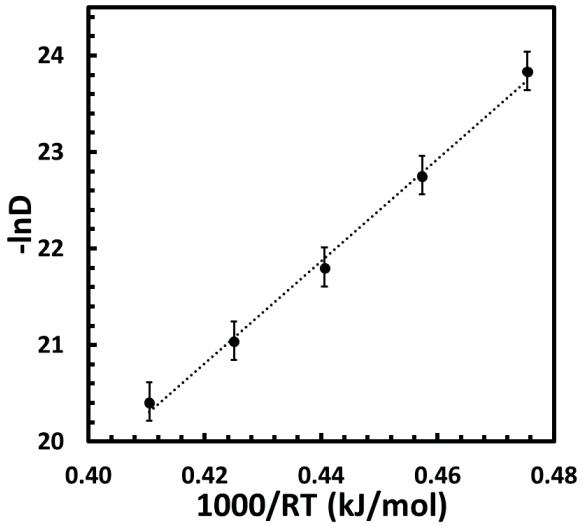

Figure 2.16 Arrhenius plot for the diffusion of 2-CEES through UiO-66 at various temperatures. The error bars represent the uncertainty in the diffusivity value at each temperature due to variations in sample thickness.

2.9 Summary

To provide comprehensive insight into the fundamental gas-MOF interactions between sulfur mustard simulants and Zr-based MOFs, considerable effort was required to develop experimental methods and data analysis procedures that provided accurate and reproducible data. To simplify the sample environment, a custom-designed ultrahigh vacuum chamber with infrared spectroscopy and mass spectrometric capabilities were used to keep MOF surfaces clean and limit gas-gas collisions. Samples were pressed into the void spaces of an IR transmissive tungsten sample grid, which allowed for precise thermal control and the ability to align the sample to maximize signal-to-noise.

IR spectroscopy probed the creation of bonds upon simulant uptake within Zr-MOFs and measured the time-dependent concentration of adsorbed simulants as they diffused out of the MOF samples. The mass spectrometer chamber was designed to selectively detect gas molecules that desorbed from the MOF sample surface. The rate of gas desorption was measured to determine desorption energies and entropic information about adsorbed species. TPD spectra were interpreted with the inversion analysis using established data analysis procedures. The diffusivities of adsorbed molecules within the MOF were determined through a Fickian diffusion model that is consistent with previously published methods.

Chapter 3. The Adsorption and Diffusion of *n*-Alkanes within the Metal-Organic Framework UiO-66

Reproduced in part with permission from Sharp, C.H.; Abelard, J.; Plonka, A.M.; Guo, W.; Hill, C.L.; Morris, J.R. Alkane-OH Hydrogen Bond Formation and Diffusion Energetics of *n*-Butane within UiO-66. *J. Phys. Chem. C* **2017,** *121* (16), 8902-8906. Copyright 2017 American Chemical Society.

3.0 Abstract

Hydrocarbon diffusion and binding within porous molecular networks are critical to catalysis, separations, and purification technologies. Fundamental insight into *n*-alkane uptake and mobility within a new class of materials for separations, metal-organic frameworks (MOFs), has been gained through *in situ* infrared spectroscopy. These ultrahigh vacuum (UHV)-based measurements revealed that adsorption of several *n*-alkanes within UiO-66 proceeds through the formation of hydrogen bonds between the alkane molecules and hydroxyl groups located at the inorganic node of UiO-66. Modeling gas transport of *n*-butane and *n*-pentane through UiO-66 using Fick's 2nd Law of Diffusion yielded diffusion coefficients at several temperatures. The Arrhenius parameter for the activation energy for diffusion was found to be 21.0 ± 1.2 kJ/mol for *n*-butane and 36.5 ± 1.2 kJ/mol for *n*-pentane. These studies have further shown that the rate-determining step for diffusion is the dissociation of *n*-alkanes from a binding site located within the tetrahedral pores of UiO-66.

3.1 Introduction

The widespread interest in metal-organic framework (MOF) materials for hydrocarbon separation, catalytic conversion, and purification is motivated largely by their high sorption capacities and tunable functionality.[116] Such applications rely on the efficient transport and diffusion of gas streams through the porous networks of the MOF. Although recent experimental efforts have employed quasi-elastic neutron scattering, concentration-swing frequency response, and microbalance-based methods to derive diffusion coefficients and activation energies of diffusion, there remains little known about the molecular-level binding mechanism and transport of hydrocarbons within MOFs.[117-120] We have therefore employed ultrahigh-vacuum-based surface science methods to explore the dynamics of molecule-MOF uptake and transport.

The efficient separation of hydrocarbons is extremely important to the petrochemical industry. Butane and other small alkanes are common contaminants in shale gas, while branched alkanes are favored over linear alkanes in industrial gasoline manufacturing due to their higher research octane number.[121] MOFs have emerged as a strong candidate for the efficient and facile separations of hydrocarbons from both natural gas streams and fossil fuel mixtures.

UiO-66 is one of the most widely studied MOFs – the result of high stability under harsh conditions, small pores for selective capture of specific compounds, and extremely high surface area. Comprised of $Zr_6O_4(OH)_4$ nodes connected to 12 (for the ideal crystal) 1,4-benzene dicarboxylate (BDC) linkers, UiO-66 is a physically, thermally, and chemically stable MOF that has been well-characterized by a variety of methods.[55-56, 122] The MOF exhibits two distinct pore environments: 8 Å diameter, octahedral pores consisting of six inorganic nodes (Figure 3.1A) and 11 Å, tetrahedral pores comprised of four nodes (Figure 3.1B).[56, 123] The faces of each octahedral pore are capped with tetrahedral pores, which feature triangular pore apertures with a length of 6.5 Å (Figure 3.1C).[55]. The pore structure of UiO-66 dictates that in order for a molecule to

transport through the material, they must alternate between the tetrahedral and octahedral pores, each time passing through a small triangular pore aperture.

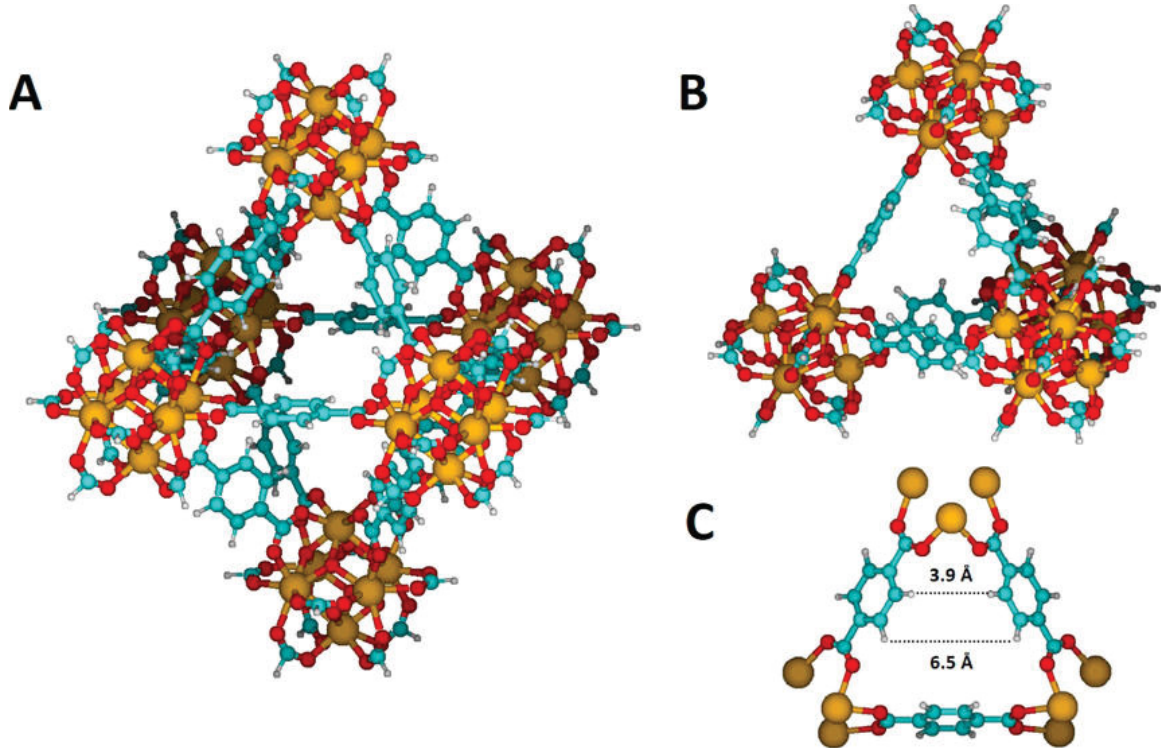

Figure 3.1 Illustration of UiO-66 pore environments: (A) octahedral pore, (B) tetrahedral pore, and(C) triangular pore aperture. The zirconium, oxygen, carbon, and hydrogen atoms are shown in yellow, red, blue, and white, respectively.

We have employed *in situ* infrared (IR) spectroscopy with precision dosing under ultrahigh vacuum (UHV) conditions to study the uptake and diffusion of *n*-butane and *n*-pentane, through UiO-66 (See Experimental section). Spectroscopic signatures of hydrogen bond formation during uptake and desorption of *n*-alkanes revealed that the binding mechanism within UiO-66 involves hydrogen bonds between the bridging hydroxyl groups of the zirconium node and butane molecules, which is to our knowledge the first reported instance of alkane hydrogen bonding within a MOF. Rupture of this alkane-OH hydrogen bond activates diffusion, the rates and energetics of which have been determined through application of Fick's 2nd law of diffusion.[124]

3.2 Experimental

The UiO-66 sample was synthesized following well-established methods.[125] Approximately 15 mg of UiO-66 was pressed into a 50-μm tungsten mesh grid (Tech-Etch) at 6500 psi for 60 seconds, forming a uniform sample that fully occupied the voids in the grid. K-type thermocouple wires were spot-welded onto the tungsten mesh adjacent to the sample to monitor sample temperature, and the mesh was affixed to a sample manipulator using stainless steel clamps attached to copper power leads. Power leads connected to an external power supply allowed for fine control over the sample temperature through resistive heating. Once the sample manipulator was mounted into the UHV chamber, it was evacuated to approximately 5×10^{-9} Torr. The UiO-66 sample was activated *in vacuo* by heating the sample to 473 K for 30 minutes to remove residual DMF from the synthesis, physisorbed water, and hydrocarbon contaminants. Scientists have shown that UiO-66 is stable up to 648 K in air while activation at 473 K under vacuum is commonly reported.[56, 126] Thermally activated UiO-66 showed no difference in the IR spectrum of the MOF compared to UiO-66 activated through solvent exchange. In addition, solvent-exchanged samples and thermally activated samples produced identical results within the diffusion study reported below.

Infrared spectra were recorded using a Thermo-Fischer Nicolet Nexus 670 IR spectrometer through an external beam port that passed through KBr windows attached to the UHV chamber. The IR beam passed through the sample mesh containing the pressed UiO-66 sample and was detected using a liquid-nitrogen-cooled MCT-A detector. Each spectrum was recorded as an average of 64 scans with a resolution of 4 cm^{-1}. A bare section of mesh was used to record background spectra in order to differentiate absorbance due to the mesh and the MOF sample.

The isothermal diffusion measurements build from previous work, which demonstrated that infrared spectroscopy could be used to track small molecule gas diffusion through

nanocrystalline materials.[112-113, 127] Upon the saturation of UiO-66 with *n*-butane at 124 K, the chamber was evacuated for approximately 30 minutes to remove excess gas-phase butane and prevent re-adsorption. The sample was then heated to the desired temperature at a rate of 2.0 K/s and maintained at that temperature while infrared spectra of sample were recorded. Following each measurement, the sample was heated to 473 K to remove residual butane. The IR spectra of UiO-66 following the isothermal experiments and post-exposure annealing were identical to the IR spectra of the as-synthesized sample after activation in the UHV chamber, to within the level of precision for the spectrometer.

3.3 Results and Discussion

3.3.1 Infrared Spectroscopic Characterization of UiO-66

The infrared spectrum of UiO-66, shown in Figure 3.2, reveals narrow bands characteristic of a highly crystalline sample. Conversely, previous studies of amorphous films of 1,4-benzene dicarboxylate (the MOF linker responsible for the low-energy IR features) show relatively broad IR bands throughout the spectra.[128] For example, the band at 1020 cm^{-1}, assigned to the aromatic breathing motion of the BDC linker, exhibits a FWHM of only 14 cm^{-1} in the MOF, yet this same motion produces bands that are greater than 30 cm^{-1} in width for the amorphous film.[129] In addition, the high reproducibility of the infrared spectra over time suggests that UiO-66 is stable over many months of thermal cycling and exposure to saturated hydrocarbons, such as *n*-butane.

The absorbance bands observed for the UiO-66 sample agree well with prior computational and experimental IR spectra for this MOF.[56, 130] The band at 3675 cm^{-1} can be assigned to the ν(O-H) vibration for the μ_3-OH group on the UiO-66 inorganic node.[56] Each node has four μ_3-OH and four μ_3-O groups situated on the faces of the Zr_6 octahedron such that the hydroxyl groups are located at the corners of the smaller, tetrahedral pores.[55] The two bands at 3084 cm^{-1} and 3066

cm^{-1} are assigned to the ν(C-H) modes associated with the 1,4-benzene dicarboxylate linkers. The presence of bands at 3001 cm^{-1}, 2957 cm^{-1}, and 2935 cm^{-1} are not associated with pristine UiO-66; rather, they are likely due to hydrocarbon contamination on the MOF. Others have shown that the organic solvent (methanol) reacts with coordinatively unsaturated Zr sites (that exist due to missing linkers within the MOF structure) during synthesis to form node-bound alkoxy groups.[130] We note that these bands do not change in energy or intensity upon thermal treatment up to 473 K, and they are not affected during the *n*-alkane adsorption or desorption experiments described below.

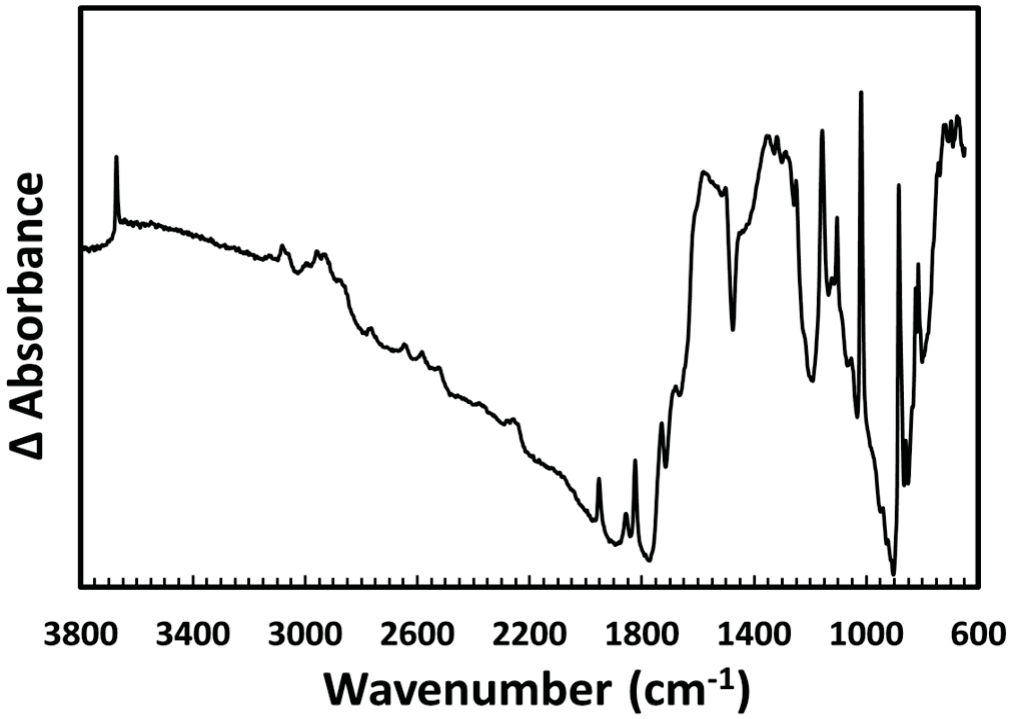

Figure 3.2 Infrared absorption spectrum of activated UiO-66 collected under UHV conditions.

3.3.2 Adsorption and Diffusion of *n*-Butane

Upon exposure of the clean UiO-66 to butane, the molecules appear to readily diffuse into the MOF and bind, through weak hydrogen bonding interactions, to the free hydroxyl groups located within the tetrahedral pores of the MOF. We have tracked the free hydroxyl group intensity during

exposure of UiO-66 to *n*-butane at 124 K to find that the band at 3675 cm^{-1} decreases while a broader IR feature at 3641 cm^{-1} emerges (Figure 3.3). Previous research has shown similar spectroscopic evidence for hydrogen bonding of saturated alkanes to the surface of zeolites.[131] Within those systems, surface hydroxyl groups have been suggested to act as Brønsted acid hydrogen bond donors to slightly more electronegative alkanes.[131-132] Furthermore, theoretical studies of alkane hydrogen bond formation indicate that the σ-bonding orbital of the C-H bond transfers electron density into the σ*-antibonding orbital of the O-H bond, which weakens the bond, thereby redshifting the O-H stretching frequency.[133-134] For *n*-butane hydrogen bonded to UiO-66, we observed an O-H redshift of 34 cm^{-1}. The complete disappearance of the free hydroxyl band at 3674 cm^{-1} suggests that butane can access every hydroxyl group within the MOF.

Following exposure, the MOF was heated to a desired temperature and the concentration of MOF-bound butane was tracked in real time using infrared spectroscopy as the molecules diffused through the sample and desorbed into the gas phase where they were efficiently removed from the UHV chamber. An example of the change in the IR spectra for an isothermal desorption experiment is shown in Figure 3.3A. The relative intensity of the IR absorbance for the C-H stretches of adsorbed *n*-butane were tracked over time and plotted in Figure 3.3B. Overall, we observe a monotonic decrease in IR signal for bands associated with the adsorbate. The rate of decrease depends on MOF sample temperature, as expected for activated diffusion (see below). Importantly, we also found that the rate of decrease of signal in the C-H stretching region correlated directly with the rise (return) in signal of the free hydroxyl groups at higher wavenumber. This is consistent with the hypothesis that *n*-butane binds within the tetrahedral pores of UiO-66 where the bridging μ_3-OH groups reside.

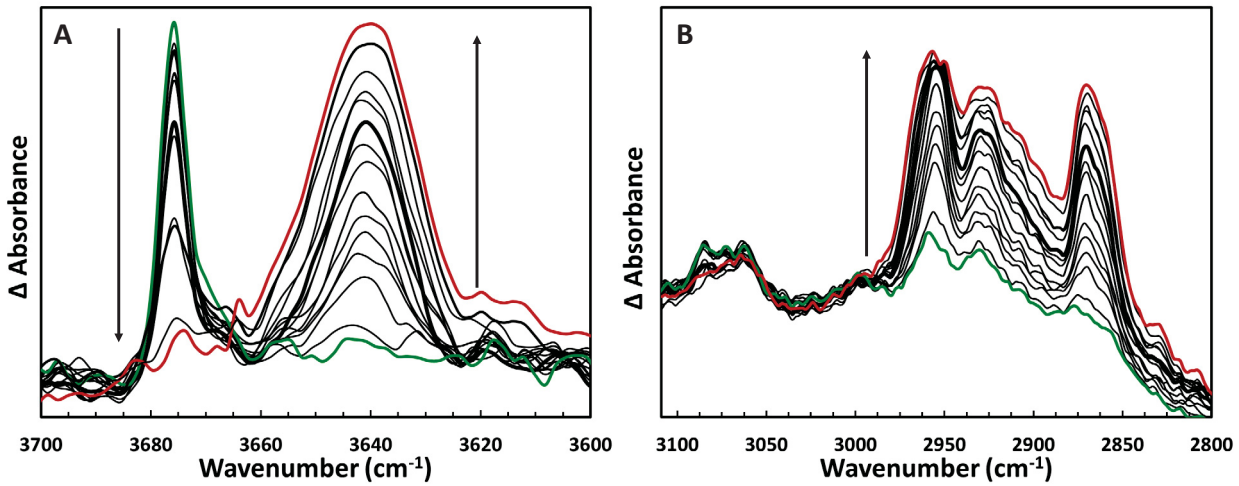

Figure 3.3 IR spectra recorded during *n*-butane exposure to UiO-66 for the O-H stretching region (**A**) and C-H stretching region (**B**). Exposure was conducted with the sample at 124 K and an approximate rate of exposure of 10^3 Langmuir per scan. The spectrum shown in green is that of the UiO-66 sample prior to exposure, while the spectrum shown in red is from the sample following prolonged exposure. The arrows highlight the reduction or development of bands over time during exposure.

The rate of desorption of *n*-butane from UiO-66 was found to be consistent with a Fickian diffusion model, which has been applied to determine energetics and diffusivities. Equation 3.1 provides the functional form for the time dependence of the relative IR intensity as molecules diffuse through the sample, reach the vacuum-MOF interface, and desorb at a specific temperature:[113]

$$\frac{I_t}{I_0} = \theta \sum_{n=0}^{\infty} \frac{8}{(2n+1)^2\pi^2} e^{\left[-\frac{D(2n+1)^2\pi^2 t}{l^2}\right]} \qquad (3.1)$$

In Eq. 3.1, I_t represents the total integrated IR absorbance at time t, I_0 represents the total integrated IR absorbance at saturation coverage, θ represents the initial coverage at a given temperature, l represents the thickness of our UiO-66 sample (50.0 μm), and D represents the diffusion coefficient.

The two unknown parameters of the model, D and θ, were determined by least-squares fitting of the data in Figure 3.3B.[135] The best-fit curves for each isothermal diffusion measurement

are shown in Figure 3.3B (colored lines), and the fitting parameters for each temperature examined are listed in Table 1. The diffusion coefficients range from 5.38×10^{-11} cm^2 s^{-1} to 8.75×10^{-10} cm^2 s^{-1}.

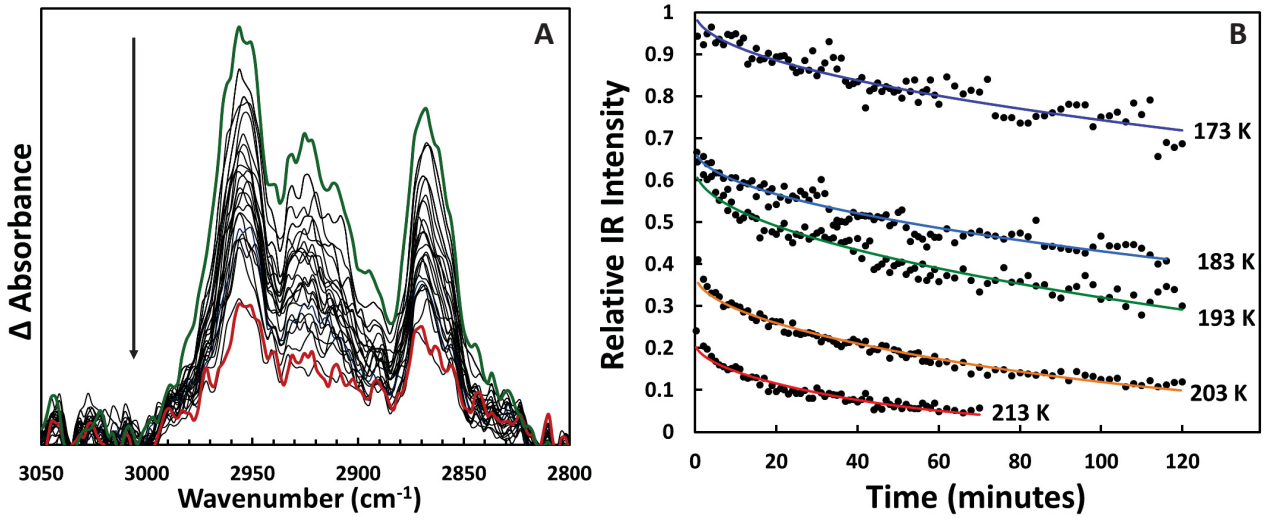

Figure 3.3 Loss of IR intensity over time for *n*-butane through UiO-66 under UHV conditions. Panel **A** shows the decrease in IR intensity for the C-H stretching region over time at 213 K. Panel **B** shows the change in coverage as a function of time at each temperature. The black dots indicate the experimental data while the solid lines represent the Fickian diffusion model (see text) best-fit curves.

The diffusion coefficients of a wide range of linear alkanes have been previously determined in a variety of porous materials.[136-138] Using molecular dynamic (MD) simulations, researchers have recently calculated that the self-diffusivity of *n*-butane in UiO-66 at 270 K falls between 1.67×10^{-8} and 7.7×10^{-8} cm^2 s^{-1}, depending on loading.[117] Although we were unable to perform an isothermal diffusion experiment at 270 K (due to the rapid diffusion of *n*-butane at that temperature) to experimentally mimic the computational study, the measured diffusion coefficients were found to depend exponentially on temperature; therefore, our results can easily be extrapolated to the higher temperature. Extrapolation of the data in Table 1 to 270 K yields an estimated diffusion rate of 1×10^{-8} cm^2 s^{-1}, in excellent agreement with the previously calculated coefficient.[117]

Table 3.1 Fitting parameters for the Fickian diffusion model shown in Figure 3.3. The uncertainty values correspond to the 95% confidence intervals for each fitting

Temp (K)	θ	D (10^{-10} cm^2 s^{-1})
173	0.98	0.538 ± 0.077
183	0.67	1.08 ± 0.11
193	0.64	1.96 ± 0.16
203	0.41	3.99 ± 0.16
213	0.24	8.75 ± 0.72

The exponential relationship between temperature and diffusion coefficient is indicative of an activated process. We have therefore used the Arrhenius equation to gain insight into the magnitude of the activation energy for diffusion. Specifically, the temperature-dependent diffusion coefficient follows Equation 3.2:

$$\boldsymbol{D(T) = D_0 e^{\left(\frac{-E_{a_{diff}}}{RT}\right)}} \tag{3.2}$$

where $\boldsymbol{D(T)}$ is the diffusion coefficient at temperature $\boldsymbol{T}$, $\boldsymbol{D_0}$ represents the diffusion coefficient at infinite temperature, $\boldsymbol{R}$ is the ideal gas constant, and $\boldsymbol{E_{a_{diff}}}$ is a fitting parameter that has been interpreted as the activation energy of diffusion.

The Arrhenius analysis, together with the infrared spectra, suggest that the rate-limiting step in the diffusion of *n*-butane through UiO-66 is the rupture of the hydrogen bond and dissociation from the strongest adsorption site within the tetrahedral pores of UiO-66. Within the constructs of an Arrhenius analysis of the data, the activation energy for the diffusion of for *n*-butane through UiO-66 was found to be 21.0 ± 1.2 kJ/mol. The prior computational studies of *n*-butane diffusion through a dehydroxylated UiO-66 MOF reported an activation energy of 11.3 kJ/mol,[117] which was attributed to the dispersive forces between the *n*-butane molecules and the walls of the UiO-66 tetrahedral pores. We speculate that the lower activation energy determined from the prior calculations, relative to our experimental results, is due to the lack of μ_3-OH groups

on the zirconium nodes for the model. Our results indicate that *n*-butane–MOF binding is enhanced by the dispersion forces and hydrogen bonding.

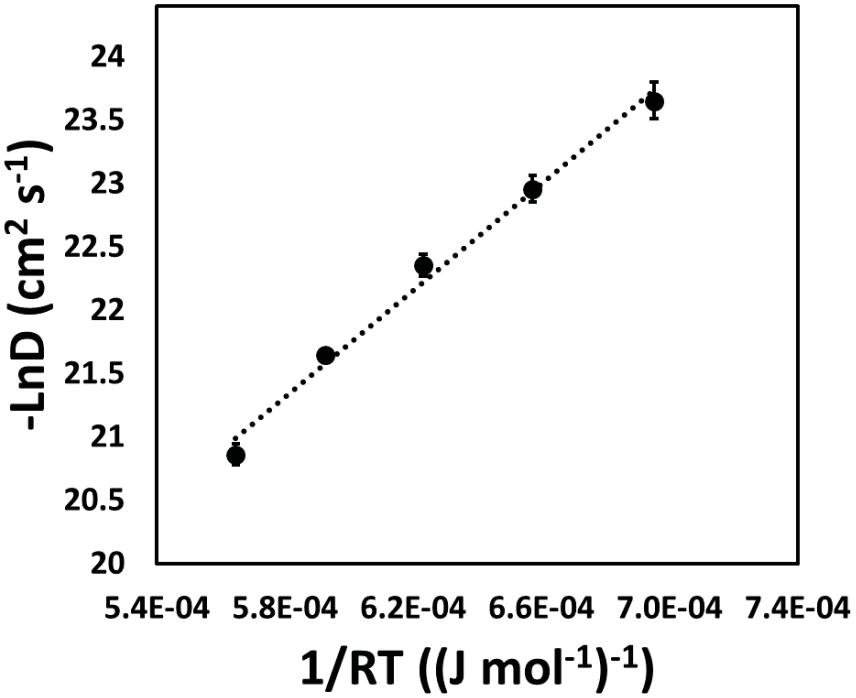

Figure 3.4 Arrhenius plot for n-butane diffusion through UiO-66. Error bars represent the 95% confidence interval for each data point based on the Fickian diffusion model best-fit line. The activation energy of diffusion for butane in UiO-66 was found to be 21.0 ± 1.2 kJ/mol with $\mathbf{D_0} = 1.08 \times 10^{-4}$ cm^2 s^{-1}.

The hydroxyl groups in the MOF provide sites for hydrogen bond formation, as revealed by the IR spectra recorded during uptake (Figure 3.3). Alkane─OH hydrogen bond enthalpies have been previously calculated to range from 2-17 kJ/mol.[139] Studies of *n*-butane diffusion in the zeolite ZSM-5, where hydrogen bonds between *n*-butane and Brønsted acid sites were observed, reported an activation energy for diffusion of 18 ± 1 kJ/mol,[132, 140] which is quite similar to the activation energy reported here for diffusion through hydroxylated UiO-66. Other prior work suggested that the diffusion of small alkanes through UiO-66 occurs via a "jump sequence mechanism", in which alkanes rapidly move within octahedral pores, but become momentarily trapped once they enter the tetrahedral pores.[117] Our results are consistent with this diffusion

mechanism, where hydrogen bonds involving hydroxyl groups within the tetrahedral pores combine with dispersion forces to provide energetically favorable binding sites relative to in the octahedral pores. The adsorption and diffusion of *n*-butane through UiO-66 was investigated with infrared spectroscopy under ultrahigh vacuum conditions. *N*-butane was able to fully diffuse through small, triangular pore apertures of UiO-66 to form hydrogen bonds with all μ_3-OH groups within the tetrahedral pores of the MOF. The diffusivity of *n*-butane through UiO-66 at several temperatures was determined by applying the Fickian diffusion model to time-resolved infrared spectra. The activation energy of diffusion was found to be 21.0 ± 1.2 kJ/mol from an Arrhenius analysis of the measurements.

Based on these results, we decided to examine the adsorption and diffusion of longer-chained linear alkanes within UiO-66. The consistent kinetic diameter (4.3 Å) for linear alkanes suggest that longer-chained alkanes should be able to diffuse through the 6.5 Å triangular pore apertures of UiO-66.[141] However, due to the confined pore environment of UiO-66, alkyl chain length may affect the ability for linear alkanes to hydrogen bond with all available μ_3–OH groups in the tetrahedral pores. Furthermore, developing an understanding of how chain length affects the activation energy of diffusion will provide insight into the dispersion interactions between adsorbed alkanes and the pore walls of the MOF.

3.3.3 Uptake and Diffusivity of Higher Order Alkanes

The study of alkyl chain-length effects on alkane─OH hydrogen bonding within UiO-66 was examined by measuring the adsorption of *n*-pentane, *n*-hexane, and *n*-octane with infrared spectroscopy. By tracking the fractional occupation of the μ_3–OH vibrational mode at ~3675 cm^{-1}, we were able to observe whether, and to what extent each alkane was able to form hydrogen bonds within the pores of UiO-66.

We measured the diffusion of *n*-pentane through UiO-66 to begin to provide insight into the effect that increased dispersive interactions between additional methylene groups and the internal pore walls have on the energetics and kinetics of diffusion. Previous studies of the desorption and diffusion of *n*-alkanes on two-dimensional crystal surfaces have revealed a linear correlation between activation energies and chain length. Brand et al. studied the desorption and diffusion of *n*-alkanes (N=3-6) on Ru(001) and reported that the addition of a methylene group increased the activation energy of diffusion by ~2-4 kJ/mol and increased the activation energy of desorption by ~4-8 kJ/mol.[142] In porous materials, Eder investigated the adsorption of linear alkanes within zeolites H-MOR and H-FAU and determined that each additional methylene group increased the adsorption enthalpy by 7-9 kJ/mol. We hypothesized that an increase in alkyl chain length would result in increased dispersion forces between adsorbed alkanes and the pore walls of UiO-66, resulting in a slower diffusivity.

The adsorption of *n*-pentane, *n*-heptane, and *n*-octane within UiO-66 were studied with a different UiO-66 sample than described in the Experimental section. This new lot was synthesized following a procedure described in Shearer et al. that yielded minimal missing linker and missing node defects.[143] The synthetic details of the new UiO-66 sample were described Chapter 4 and also reported by Grissom et al.[54]

3.3.3.1 Adsorption of *n*-Pentane

Upon exposure of UiO-66 to *n*-pentane at 124 K, *n*-pentane was able to diffuse into the pores of UiO-66 and form hydrogen bonds with the μ_3–OH groups of the zirconium oxo-clusters (Figure 3.5). The decrease in the ν(O–H) band at 3675 cm^{-1} coincided with the formation of a broader IR feature at 3641 cm^{-1}. The extent of the ν(O–H) band redshift upon *n*-pentane adsorption was identical to the redshift for *n*-butane adsorption within UiO-66 under similar conditions

(34 cm^{-1}). In addition to the growth of the IR band at 3641 cm^{-1}, the IR features from 2800 cm^{-1} to 3000 cm^{-1} agreed well with the ν(C–H) vibrations of *n*-pentane. At full saturation of the 3675 cm^{-1} band (which indicates that *n*-pentane had accessed all the internal hydroxyls of the UiO-66 sample), additional IR vibrational modes (3660 cm^{-1} and 3630 cm^{-1}) consistent with bonded ν(O–H) features were observed which indicates multiple hydrogen bonds may be present. Upon thermal treatment, the bands at 3660 cm^{-1} and 3630 cm^{-1} decrease more rapidly than the band at 3641 cm^{-1}.

The presence of three features attributed to hydrogen-bonded n-pentane upon the saturation of the free hydroxyl band at 3675 cm^{-1} suggested that at high loadings, *n*-pentane was adsorbed in multiple different hydrogen-bond orientations within UiO-66. The shift in the vibrational frequency of the ν(O–H) mode upon hydrogen-bond formation depends on the extent of electronic charge transfer between the σ-bonding orbital of the C-H bond and the σ*-antibonding orbital of the O–H bond, which is highly sensitive to the distance between hydrogen bond acceptor and donor. Rozenberg et al. demonstrated that the length of the hydrogen bond correlates with the magnitude of the νO–H redshift.[144] Based on this interpretation, the feature assigned to hydrogen-bonded *n*-pentane at 3630 cm^{-1} forms shorter hydrogen bonds than adsorbed *n*-pentane species reflected in the 3641 cm^{-1} band.

While the "Badger Bauer relationship" indicates a linear relationship between the ν(O–H) redshift and the strength of the hydrogen bond,[145] the hydrogen-bonded *n*-pentane feature at 3630 cm^{-1} desorbed before the feature at 3641 cm^{-1}. We hypothesize that despite the smaller ν(O–H) redshift, the feature at 3641 cm^{-1} represents the most stable adsorption geometry, possibly due to increased electrostatic interactions with the pore walls of UiO-66.

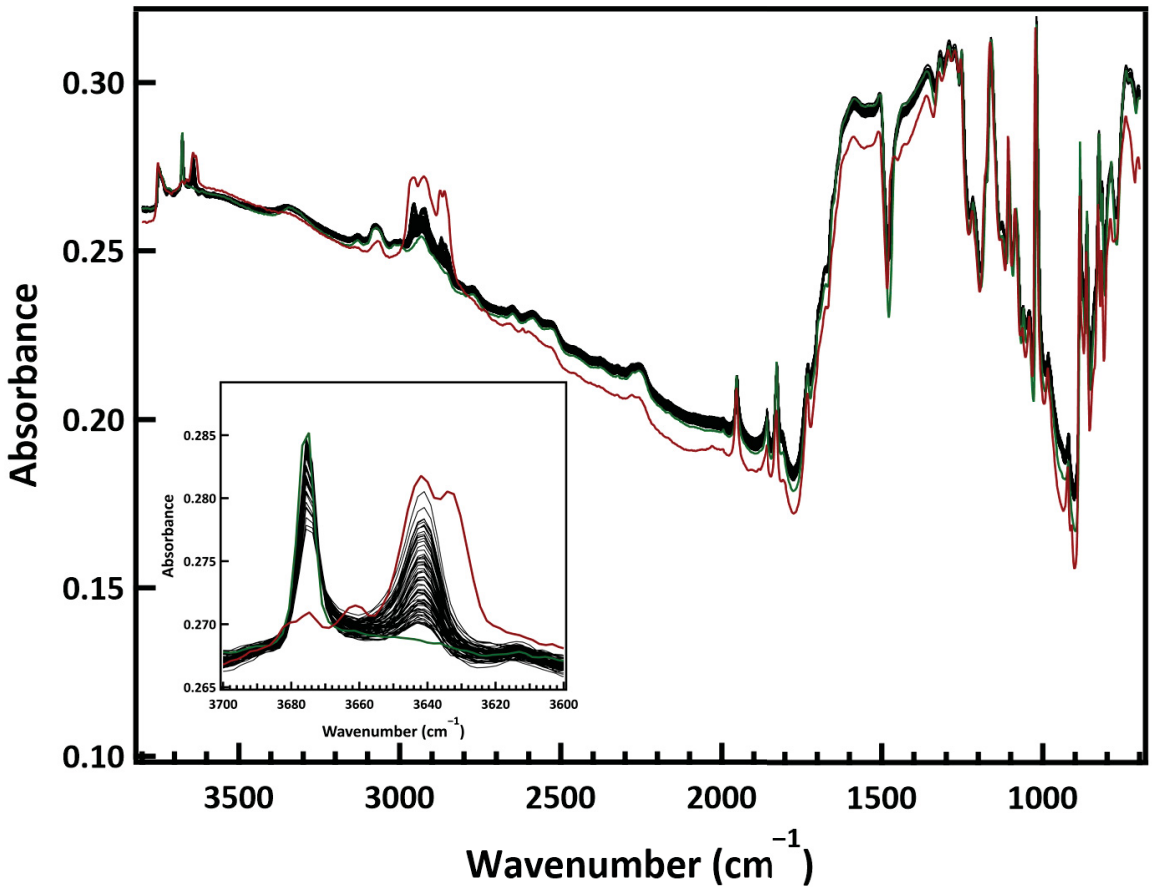

Figure 3.5 IR spectra of n-pentane adsorption within UiO-66 at 124 K. The green spectrum represents the clean, unexposed MOF, while the red spectrum represents the MOF at the end of dosing. The inset shows an expanded version of the ν(O-H) stretching region.

3.3.3.2 Diffusion of *n*-Pentane

Similar to n-butane, diffusivities of *n*-pentane through UiO-66 were determined by tracking the decrease of IR bands associated with adsorbed pentane over time. The change in the normalized integrated intensity of the ν(C–H) vibrations at 2957 cm^{-1}, 2927 cm^{-1}, 2870 cm^{-1}, and 2861 cm^{-1} over time (Figure 3.6A) were then modeled using eq. 3.2 (Figure 3.6B). The diffusion coefficients for *n*-pentane between 193 K and 233 K ranged from 2.58×10^{-11} cm^2 s^{-1} to 1.38×10^{-11} cm^2 s^{-1} (Table 3.2).

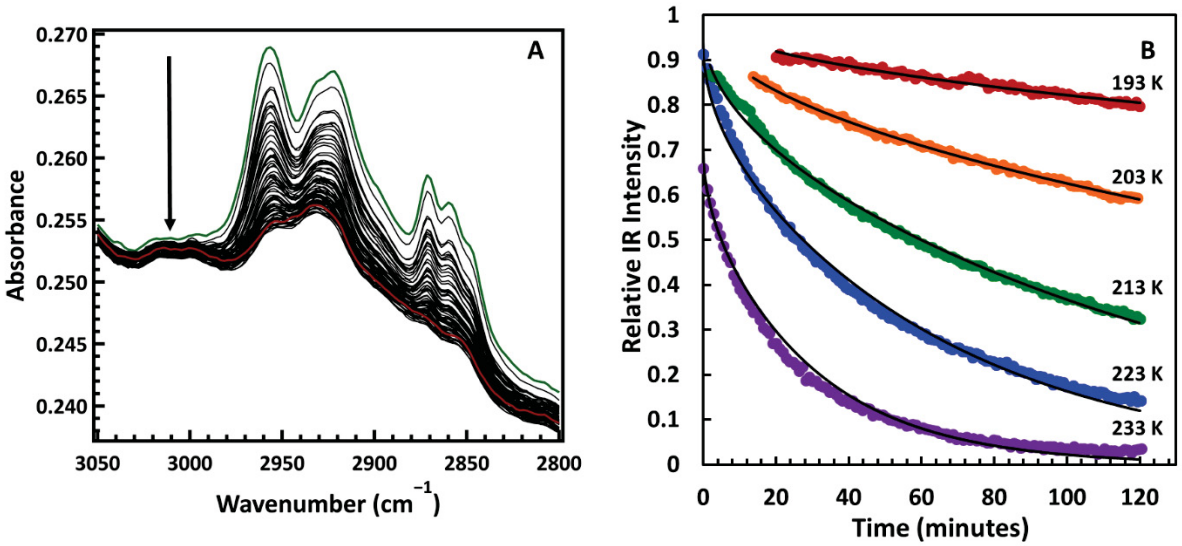

Figure 3.6 Loss of IR intensity over time for n-pentane through UiO-66 under UHV conditions. Panel **A** shows the decrease in IR intensity for the C-H stretching region over time at 233 K. Panel **B** shows the change in coverage as a function of time at each temperature. The black dots indicate the experimental data while the solid lines represent the Fickian diffusion model (see text) best-fit curves.

Table 3.2 Fitting parameters for the Fickian diffusion model shown in Figure 3.6B. The uncertainty values correspond to the 95% confidence intervals for each fit.

Temp (K)	θ	D (10^{-10} cm^2 s^{-1})
193	1.00	0.258 ± 0.013
203	1.00	1.15 ± 0.03
213	0.97	3.23 ± 0.05
223	0.91	6.48 ± 0.12
233	0.66	13.8 ± 0.4

An Arrhenius fit of the diffusivities of *n*-pentane versus temperature was used to determine an $\boldsymbol{E_{a_{diff}}}$ term of 36.5 ± 2.4 kJ/mol, a 15 kJ/mol increase from *n*-butane diffusion through UiO-66 (Figure 3.7). Duerinck et al. measured an adsorption enthalpy of −48.2 kJ/mol for *n*-pentane within UiO-66 from inverse pulse gas chromatography and calculated adsorption enthalpies for a series of alkanes in UiO-66.[146] Eder et al. measured the heats of adsorption for linear alkanes that adsorbed within the zeolite H-MFI through alkane─OH hydrogen bond formation and reported that the adsorption enthalpy increased by approximately 12 kJ/mol for every additional methylene

group.[131] Due to the small pores of UiO-66, dispersion interactions between adsorbed alkanes and the pore walls are likely greater than the interactions of alkanes bound to a two-dimensional surface. Based on van der Waals volumes, adsorbed *n*-pentane within UiO-66 occupies 80% of the tetrahedral pore volume (~175 Å).[147]

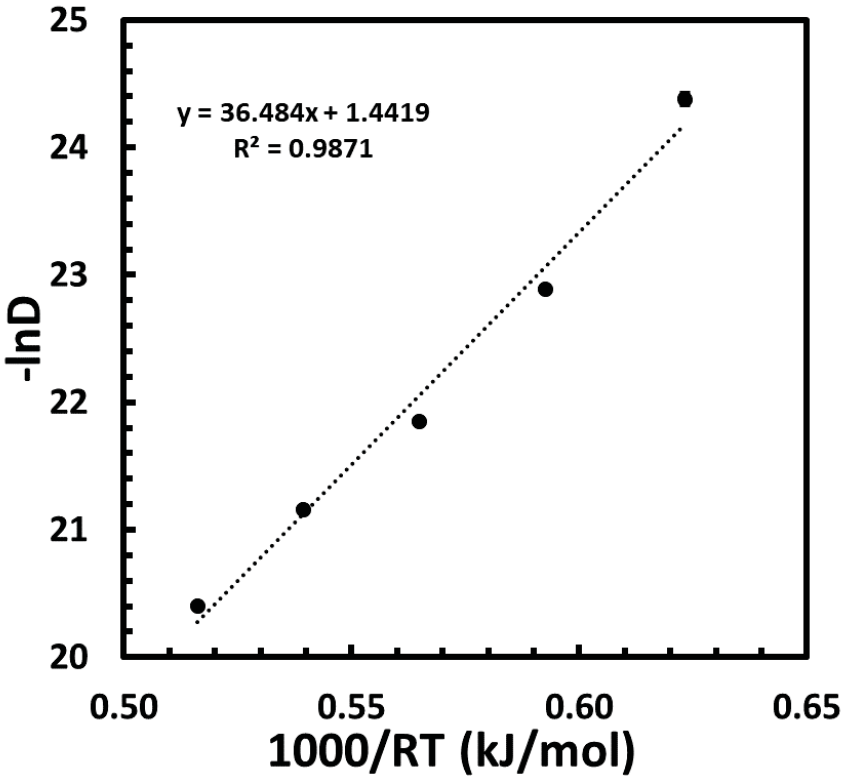

Figure 3.7 Arrhenius plot for *n*-pentane diffusion through UiO-66. Error bars represent the 95% confidence interval for each data point based on the Fickian diffusion model best-fit line. The activation energy of diffusion for butane in UiO-66 was found to be 36.5 ± 2.4 kJ/mol with $\mathbf{D_0} = 2.36 \times 10^{-1}$ cm^2 s^{-1}.

3.3.3.3 Adsorption of *n*-Heptane and *n*-Octane

While the diffusivities of linear alkanes within UiO-66 were only measured for *n*-pentane and *n*-butane, the adsorption of *n*-heptane and *n*-octane were preliminarily studied as part of another project that examined the effect that adsorbed vapors within UiO-66 had on the adsorption rate of the mustard gas simulant 2-CEES. In these experiments, we observed that longer-chained

alkanes also form weak hydrogen bond-like interactions with the hydroxyls on the MOF, suggesting that higher order alkanes can diffuse through the internal pore windows of UiO-66.

UiO-66 was exposed to approximately 5×10^{-5} Torr of *n*-heptane for 20 minutes at 142 K (Figure 3.8). The increase in the bands between 2800-3000 cm^{-1} were attributed to the ν(C–H) modes of *n*-heptane. While high background absorbance levels partially obscured the ν(O–H) feature at 3676 cm^{-1}, the decrease in the ν(O–H) feature at 3676 cm^{-1} and the growth of a new vibrational band at 3640 cm^{-1} is indicative of hydrogen bond formation between *n*-hexane and UiO-66. The adsorption *n*-heptane resulted in a ν(O-H) redshift of 36 cm^{-1}, a 2 cm^{-1} increase compared to *n*-butane and *n*-pentane adsorbed within UiO-66 ($\Delta\nu$ =34 cm^{-1}).

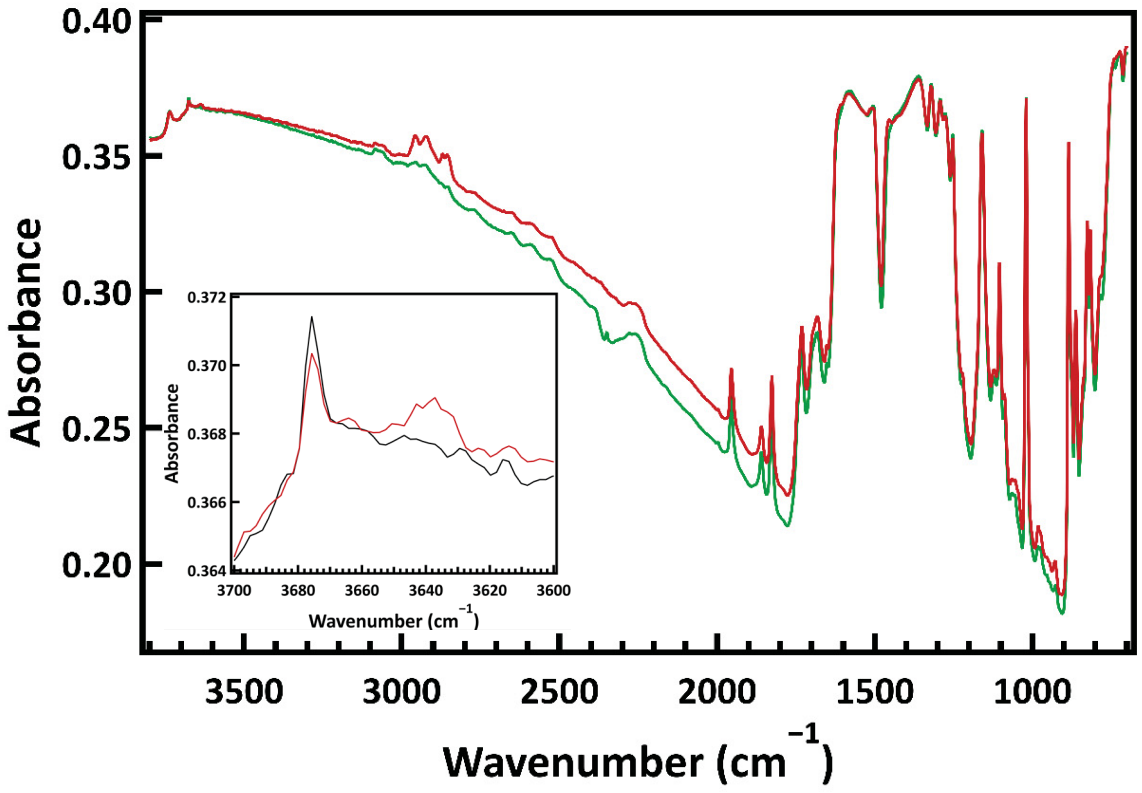

Figure 3.8 IR spectra of n-octane adsorption within UiO-66 at 142 K. The green spectrum represents the clean, unexposed MOF, while the red spectrum represents the MOF at the end of dosing. The inset shows an expanded version of the ν(O–H) stretching region.

For the *n*-octane study, UiO-66 was exposed to approximately 3×10^{-1} Torr of *n*-octane for 20 minutes at 298 K (Figure 3.9). During the adsorption of octane, a feature attributed to a hydrogen-bonded O–H species at 3637 cm^{-1} appeared as the ν(O–H) band at 3674 cm^{-1} decreased to approximately half of its initial intensity. The observed IR redshift was 37 cm^{-1}, a 3 cm^{-1} increase compared to *n*-butane adsorption within UiO-66. The IR data indicated that under these experimental conditions, *n*-octane was able to hydrogen bond with only half of the hydroxyl groups within UiO-66.

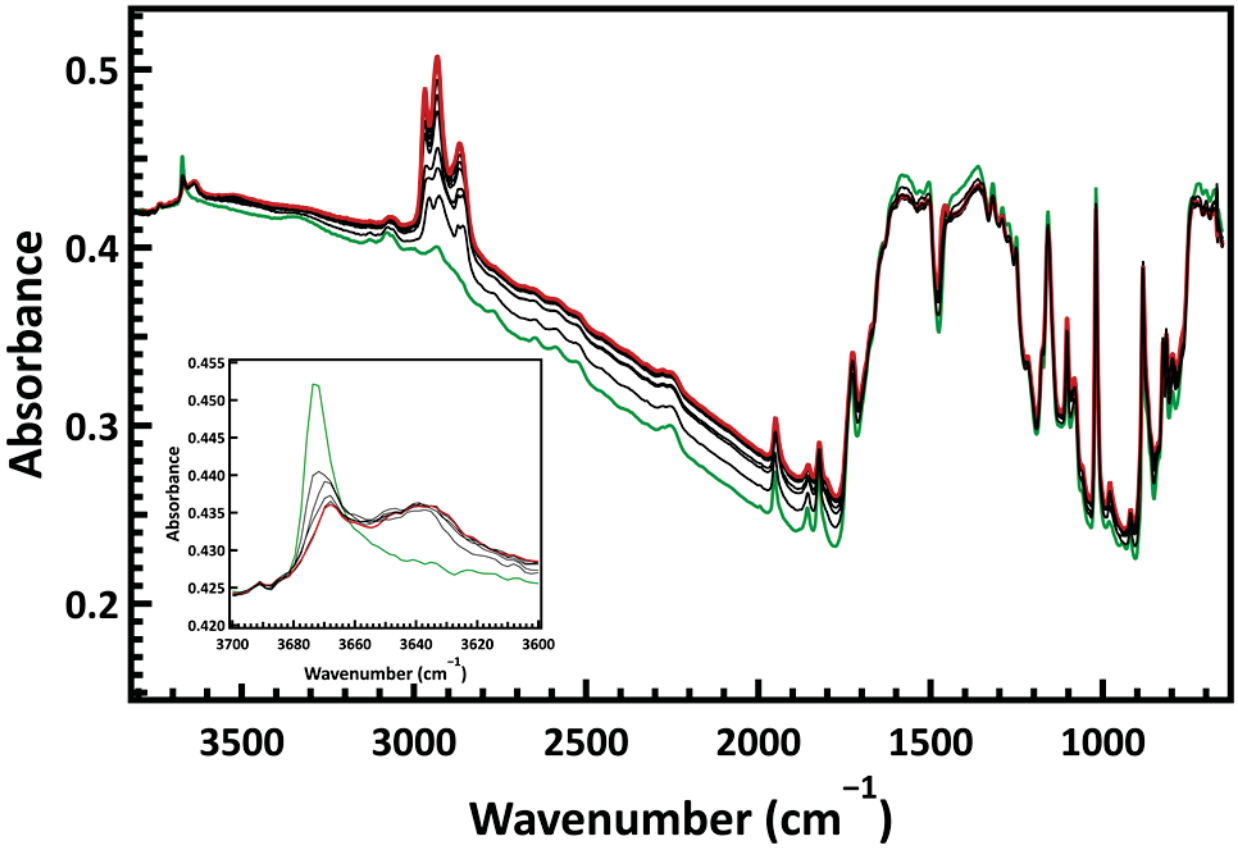

Figure 3.9 IR spectra of n-octane adsorption within UiO-66 at 298 K. The green spectrum represents the clean, unexposed MOF, while the red spectrum represents the MOF at the end of dosing. The inset shows an expanded version of the νO–H stretching region.

3.3.3.5 Chain-length Dependence on Alkane Hydrogen Bonding

The increase in alkyl chain length from *n*-butane to *n*-octane resulted in a subtle increase in the ν(O–H) redshift from 34 cm^{-1} to 37 cm^{-1}. Eder et al. observed a similar trend for the adsorption linear alkanes within zeolites and attributed ν(O–H) redshift to the increased polarizability of longer-chained alkanes.[131] While the "Badger Bauer relationship" correlates the increase in ν(O–H) redshift to the strength of the hydrogen bond,[145] the 15 kJ/mol increase in the diffusion activation energy from n-butane to n-pentane is likely due to the increased in electrostatic interactions between n-pentane and the pore walls of UiO-66.

3.4 Summary

The adsorption mechanism and diffusion kinetics were studied for a series of linear alkanes within UiO-66. The adsorption mechanism was determined to be the formation of alkane-OH hydrogen bonds with the bridging hydroxyls on the Zr node. The increase in alkyl chain length resulted in a modest increase in the observed redshift of the ν(O–H) species, and was attributed to the increase in polarizability of the adsorbed molecule. While *n*-butane and *n*-pentane were able to interact with every hydroxyl species, the presence of multiple features attributed to hydrogen-bonded *n*-pentane suggests that *n*-pentane is unable to adopt a single binding geometry due to steric constraints within the UiO-66 pore environment. Future research is required to determine whether *n*-heptane or *n*-octane are able to access every hydrogen bond donor, but preliminary results show that at least a fraction of them are.

A more systematic investigation of the effect of alkyl chain length and extent of branching on the uptake and transport of alkane isomers through UiO-66 and other MOFs with small pore apertures would provide significant insight into the fundamental forces that govern alkane adsorption and separations. Furthermore, a study of alkane adsorption within other MOFs with

varying levels of Brønsted acidity may provide more information on the effect of hydrogen bonding on the diffusion activation energy. Insight into the diffusion rates and binding mechanisms of hydrocarbons within MOFs will be important as these relatively new materials continue to be developed for fuel separation, purification, and catalysis.

Chapter 4. Pore Size Effects on the Adsorption and Diffusivity of 2-CEES through Zr-based MOFs

4.1 Introduction

Despite the multilateral ratification of the Chemical Weapons Convention (CWC) in 1993, which aimed to halt the development and proliferation of chemical weapon stockpiles, chemical warfare agent (CWA)-based attacks have continued due to rogue nations and terror groups.[148] Due to the continued risk posed by CWAs to military and civilian personnel, the development of novel sorbents and catalysts for CWA mitigation is paramount. Recently, several metal-organic frameworks (MOFs) have emerged as potential materials for CWA capture and decontamination. MOFs are a class materials comprised of polytopic organic linkers coordinated to multiple metal/metal oxide inorganic clusters to form extended 2D and 3D porous networks.[149] Currently, over 40,000 MOF structures exist in the Cambridge Structural Database,[23] with surface areas up to 7800 m^2/g.[150] Due to their periodic porosity, high surface, and the ability to alter the chemical properties of the MOF through altering metal centers and ligand functionalization, MOFs, particularly those containing zirconium(IV) oxo clusters, offer high promise as heterogeneous catalysts,[151-152] catalyst supports,[153-154] and sorbent materials.[39-40] Zr-based MOFs (Zr-MOFs) demonstrate exceptional thermal and chemical stability, likely due to the strength of the interaction between Zr(IV) sites and carboxylate-based organic linkers.[31]

Significant research has focused on the development of MOF-based CWA decontamination materials, specifically Zr-based MOFs.[33, 155] Katz et al. first reported that Zr-MOF UiO-66 was catalytically active for the hydrolysis of nerve agent simulant methyl paraoxon in aqueous, buffered solutions.[60] Due to the narrow pore apertures of UiO-66 (6.5 Å), the adsorption of methyl paraoxon at undercoordinated Zr sites was limited to defect sites on external crystal surfaces.[156] Further solution-based studies have demonstrated that the synthesis of MOFs

with increased pore size and higher concentrations of undercoordinated Zr sites, such as UiO-67, NU-1000, and MOF-808, result in significantly faster reaction rates for the hydrolysis of methyl paraoxon.[66-68, 71, 157] Additional research has examined how functionalizing the organic linker with halogens, amine groups, and have affected the rate and mechanism of nerve agent hydrolysis.[61, 69, 158]

Recent chemical attacks on soldiers in Iraq and civilians in Syria with sulfur mustard (HD) have highlighted the need to develop MOFs that active for the decontamination of HD in addition to nerve agents. Several pathways exist for the detoxification of HD, including hydrolysis, dehydrohalogenation, and oxidation.[7] In solution-phase studies, the porphyrin-based linkers of PCN-222/MOF-545 partially oxidized the HD simulant 2-chloroethyl ethyl sulfide (2-CEES) to 2-chloroethyl ethyl sulfoxide through the generation of singlet oxygen upon blue light irradiation.[77] Post-synthetic modification of NU-1000 with photosensitizers has also yielded improved reaction kinetics.[78-79] In addition to oxidation, Zr-MOFs have also be studied for the hydrolysis of HD. The hydrolysis rates of 2-CEES and HD with UiO-66 and UiO-67 in aqueous solutions were increased through the introduction of amine-functionalized linkers and the attachment of basic sites to the $Zr_6O_4(OH)_4$ node.[80]

While solution-phase studies provided the groundwork for surveying the potential of MOF-based CWA decontamination, it is necessary to study the fundamental interactions of MOF-CWA at the gas-surface interface to understand how the MOFs will perform against vapor-based CWA exposure. Our work aims to provide high-level spectroscopic insight into the adsorption mechanism and transport of HD through Zr-based MOFs. An understanding of the effects that MOF linker size and pore topography have on the uptake and diffusion of mustard

simulants can allow for the rational design of MOF-based materials that allow high catalytic activity without sacrificing fast breakthrough times.

The Zr-MOFs studied in this paper were UiO-66, UiO-67, and NU-1000. First reported by Cavka et al.,[55] UiO-66 and UiO-67 are isoreticular to one another and comprised of $Zr_6O_4(OH)_4$ nodes connected to twelve dicarboxylate linkers (1,4 benzene dicarboxylate for UiO-66 and biphenyl-4,4'-dicarboxylate linkers for UiO-67) which create a face-centered cubic structure. The $Zr_6O_4(OH)_4$ node features six 8-coordinated zirconium atoms arranged in an octahedron with μ_3–O and μ_3–OH located at the faces of each octahedron.[56] Within the UiO-MOFs, two pore environments exist: a tetrahedral pore consisting of six linkers and four nodes, and an octahedral pore consisting of six nodes and twelve linkers. Access into the pores of the UiO-series MOFs is restricted by triangular pore apertures of 6.5 Å and between 8.5 and 11.5 Å for UiO-66 and UiO-67, respectively.[55] NU-1000 contains $Zr_6(O)_4(OH)_8(H_2O)_4$ nodes connected to eight tetratropic 1,3,6,8(*p*-benzoate) pyrene (TBAPy) linkers. In addition to the μ_3–OH hydroxyls present on the node of UiO-66 and UiO-67, the Zr-node of NU-1000 also contains four terminal hydroxyl groups and aqua ligands coordinated to four coordinatively unsaturated Zr-sites.[130] The MOF possesses hexagonal channels with a diameter of 31 Å surrounded by four triangular channels of 11 Å. Due to the decrease in linker connectivity to the Zr node, the nodes on NU-1000 contain coordinated aqua ligands and terminal hydroxyl groups.[130, 159]

Due to safety concerns, our research primarily mimicked HD with simulant molecules; molecules with a similar chemical structure to sulfur mustard, but much lower toxicities. An added benefit of using simulants is that we can systematically probe the effects that each molecular substituent group may have on the gas-MOF interactions, allowing us to develop a structure-

function relationship. The primary simulant molecule used was 2-CEES, which closely mimics the structure of HD.

4.2 Experimental

4.2.1 HD Simulants

2-CEES (Sigma-Aldrich), 1-chloropentane (Sigma-Aldrich), and diethyl sulfide (Sigma-Aldrich) were pipetted into stainless steel dosing bulbs (Swagelok) and attached to a custom-built vapor-dosing manifold. Three freeze-pump-thaw cycles were performed for each simulant to remove potential contamination before sample exposure.

4.2.2 MOF Synthesis

UiO-66 was prepared following a procedure reported by Shearer et al.[143] and described explicitly by Grissom et al.[54] 378 mg (1.62 mmol) of $ZrCl_4$ and 539 mg (3.24 mmol) of 1,4-benzenedicarboxylic acid were suspended in 10 mL of DMF. HCl (37%, 0.286 mL, 3.24 mmol) was added to the 6-dram vial and the solution heated to 343 K for 30 minutes to fully dissolve the MOF precursors.[54] The solution was transferred to a Teflon-lined Parr reactor and heated at 493 K for 24 hours. After cooling room temperature, the white product powder was separated via centrifugation, washing with 4-10 ml aliquots of DMF, “then soaked in DMF (10 mL) for 3 days, the solvent was replaced every 24 hours. The resultant framework was dried in air at 333 K for 24 hr followed by 473 K for 1 hr.” Detailed characterization of the UiO-66 sample was provided by Grissom et al.[54]

UiO-67 was synthesized following a method described by Øien-Ødegaard et al.[160] 4,4’-biphenyldicarboxylic acid (0.14g, 0.58 mmol), $ZrCl_4$ (0.13g, 0.56 mmol), difluoroacetic acid (1.76 mL, 28 mmol), and DMF (20 mL) were combined in a 6-dram vial and heated to 120 °C for 2

days. The resulting white powder was isolated via centrifugation, washed three times with DMF then three times with acetone, dried, and then heated at 473 K for 1 hr.

NU-1000 was synthesized and activated by Dr. Timur Islamoglu from the Omar K. Farha group at Northwestern University.

4.2.3 MOF Sample Preparation

The preparation of MOF samples for UHV-based analysis followed a previously described process.[98] Approximately 10-15 mg of each MOF sample was pressed into the void spaces of a 50.0 μm thick tungsten mesh (Tech-Etch) at 5000-6500 psi. A K-type thermocouple was spot-welded onto the mesh to allow for the accurate measurement of sample temperature. The tungsten meshes were bolted to stainless steel support clamps that were attached to copper power leads to allow for resistive heating of the sample mesh. Sample cooling was achieved through the use of a liquid-nitrogen-filled dewar that the power leads ran through. Upon evacuation of the UHV chamber to below 5×10^{-8} Torr, UiO-66 and UiO-67 were thermally treated at 438 K for 72 h to remove residual DMF from synthesis and other weakly bound adsorbates. The received NU-1000 was previously activated and was heated at 373 K for 12 h to remove water physisorbed within the MOF pores.

4.2.4 Vapor Dosing and Isothermal Diffusion Experiments

MOF samples were exposed to 2-CEES at 5×10^{-6} Torr for approximately 30 minutes. After dosing, samples were heated at 0.2 K/s to 223 K to remove multilayers of 2-CEES adsorbed on the external crystal surfaces of the MOFs. Samples were then immediately cooled to 164 K and the UHV chamber was allowed to pump out any desorbed 2-CEES and reach baseline pressure for at least one hour before running isothermal diffusion experiments. For each isothermal diffusion experiment, samples were heated to the desired experiment temperature with a 2.0 K/s temperature

ramp. IR spectra were recorded approximately every minute for 120 minutes. After each experiment, each MOF was heated to 375 K for 1 hour to ensure all adsorbates had desorbed.

4.2.5 IR Spectroscopy

The adsorption and diffusion of HD simulants within Zr-MOFs were monitored using in situ Fourier-transform infrared (FTIR) spectroscopy. The IR spectra were recorded on a Thermo-Fischer Nicolet Nexus 670 IR spectrometer with a liquid-nitrogen-cooled MCT-A detector integrated into the custom-built UHV system. UiO-66 spectra were recorded with 64 scans to average and 4 cm^{-1} resolution, while NU-1000 and UiO-67 spectra were recorded with 56 scans to average and 2 cm^{-1} resolution. The reference background for each MOF spectra was an empty section of the tungsten mesh.

4.2.6 HD Exposure to UiO-66

The adsorption of actual HD chemical agent within UiO-66 was monitored via *in situ* Diffuse Reflectance Infrared Spectroscopy (DRIFTS) following a procedure previously described by Guo et al.[161] 6.152 mg of UiO-66 was sample dried over four days under a nitrogen purge and then placed into a 6 mm porous ceramic cup. The sample cup was transferred to a Pike Technologies Diffuse IR cell with a KBr window and purged under a 5 mL/min He flow for approximately two hours. IR spectra were recorded with 128 scans per spectrum and 2 cm^{-1} resolution. Prior to HD exposure, a reference background was collected of the MOF. He saturated with HD vapor was introduced via a saturator cell held at 25 °C. DRIFTs spectra were collected with a Thermo Nicolet 6700 spectrometer using a liquid-nitrogen-cooled MCT-A detector. Spectra were recorded as difference spectra relative to the background spectrum.

4.3 Results and Discussion

The uptake mechanism and diffusion of the HD simulant, 2-CEES, through the Zr-based MOFs UiO-66, UiO-67, and NU-1000 were studied under UHV conditions using *in situ* infrared spectroscopy. This work seeks to build an understanding of the intermolecular interactions that govern 2-CEES adsorption within UiO-66 and how chemical and structural changes to the MOF affect gas transport. Our results indicate that 2-CEES reversibly adsorbs through the formation of hydrogen bonds between the chlorine atom on 2-CEES and hydroxyl groups located on the secondary building units of each MOF. The rate of 2-CEES diffusion through the Zr-MOF-based MOFs is controlled by both the presence of hydrogen bond donors and the size of the MOF pore apertures.

4.3.1 Adsorption of 2-CEES within UiO-66

Upon exposure of UiO-66 to vaporous 2-CEES, infrared spectra reveal that molecules readily diffuse throughout and adsorb within the MOF. Spectra recorded during exposure of UiO-66 to 2-CEES are provided in Figure 4.1. Band assignments for the 2-CEES adsorbate are provided in Table 4.1. The increase in the intensity of IR features assigned to 2-CEES (Table 4.1) adsorbed within UiO-66 are similar to those previously assigned to physisorbed 2-CEES on the surface of metal oxides,[86, 162] which suggest that no reactions between 2-CEES and UiO-66 occur at low temperatures. We found no evidence for 2-CEES decomposition or MOF degradation throughout the entire thermal regime employed in these studies.

The uptake of 2-CEES appears to be driven by hydrogen bonding interactions within the MOFs. As 2-CEES adsorbed, a decrease in the sharp infrared absorbance band at 3674 cm^{-1}, which corresponds to the stretching frequency for the free μ_3–OH groups on the zirconium hydroxide node,[56] coincided with the emergence of a broader feature at 3558 cm^{-1} (Figure 4.1B). Spectral

redshifts and line broadening associated with hydroxyl groups are indicative of hydrogen-bond formation,[104] where electronic charge from either the sulfur or chlorine atoms in 2-CEES partially populates the σ* anti-bonding molecular orbitals of the bridging hydroxyls on the UiO-66 inorganic node.[163] These findings are consistent with prior research, which suggest that hydrogen bonding occurs in solution-phase interactions between 2-CEES and Zr_6-MOFs.[98, 164] Because the μ_3–OH groups are situated in the smaller tetrahedral pores and likely on the surface of UiO-66 crystallites,[55, 60, 165] the complete depletion of the band at 3674 cm^{-1} indicates 2-CEES can readily diffuse throughout and access the internal pores of UiO-66.

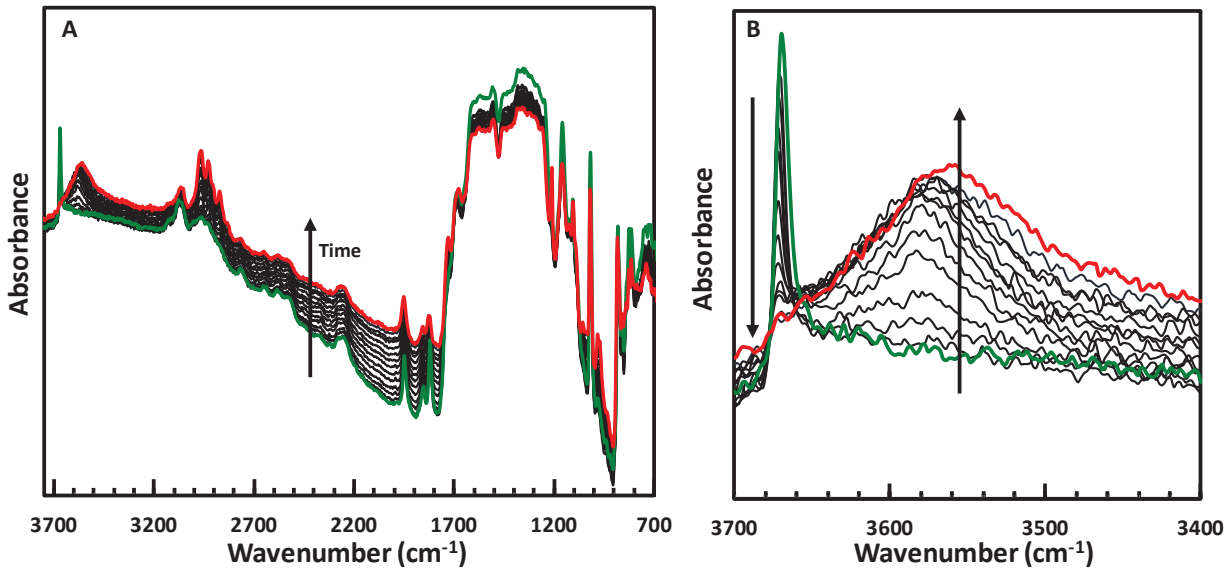

Figure 4.1 Transmission IR spectra recorded of 2-CEES exposure to UiO-66 at 205 K in the full IR region (A) and O-H stretching region (B). The green spectrum represents the clean, unexposed UiO-66 sample, while the red spectrum corresponds to the MOF after dosing had ended. The reference background for each spectrum is a blank W-mesh spot.

Table 4.1 IR band assignments for gas-phase 2-CEES and 2-CEES adsorbed within UiO-66.

Assignment[166-167]	**Gas phase 2-CEES (cm^{-1})**[166]	**2-CEES adsorbed on UiO-66 (cm^{-1})**
$\nu(CH_2)_{as}$	2967	2967
$\nu(CH_3)_{as}$	2928	2928
$\nu(CH_2)_{s,bent}$	2871	2872
$\omega C(CH_2)$	1213	1212
$\nu(C\text{-}C)_{as}$	1055	1056
$\rho C(CH_2)$, $\tau C(CH_2)$	971	973

ν: stretch, ω:wag, ρ:rock, τ:twist

4.3.1.1 2-CEES Adsorption Mechanism

Figure 4.1 demonstrates that 2-CEES adsorbs within UiO-66 via hydrogen bond formation with the μ_3–OH hydroxyls on the zirconium node, but does not directly reveal the bonding motif. Previously published IR spectra of 2-CEES adsorption on metal oxide surfaces showed two discernable redshifted ν(O–H) features and have indicated that 2-CEES can adsorb via hydrogen-bond formation through either the sulfur or the chlorine, though likely not both simultaneously.[85, 104] Specifically, in the case of amorphous silica, the redshift of the terminal hydroxyl bands associated with hydrogen bonding through the sulfur and chlorine was 393 cm^{-1} and 152 cm^{-1}, respectively.[104] Even in the microporous zeolite NaZSM-5, IR spectra revealed that 2-CEES adsorption can proceed through hydrogen bond formation between either the sulfur or chlorine hydrogen bond acceptors.[162] In contrast, the presence of only one feature assigned to a hydrogen-bonded OH group in the IR spectra of Figure 4.1 suggests that 2-CEES adsorbs to the MOF through only one type of hydrogen bond interaction.

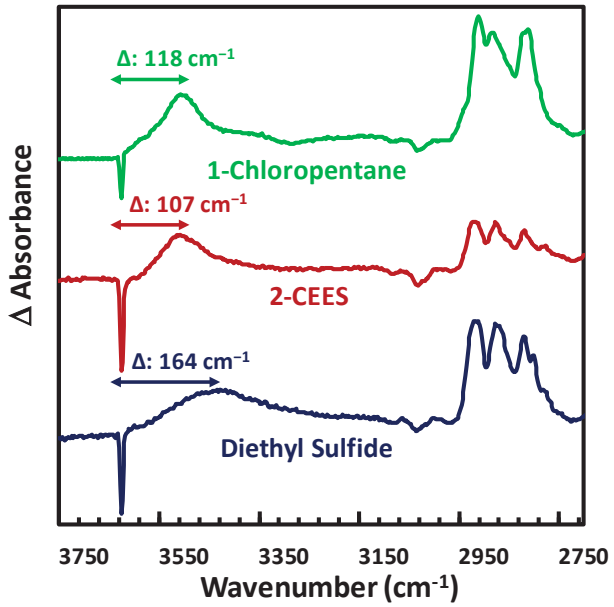

Figure 4.2 Hydrogen bonding of 2-CEES and HD simulants 1-chloropentane and diethyl sulfide within UiO-66. The high wavenumber region (2750-3800 cm^{-1}) of the difference IR spectra (relative to an unexposed UiO-66) of adsorbed HD simulants to UiO-66.

We employed the probe molecules, 1-chloropentane and diethyl sulfide, to uncover the specific binding motif. A comparison of the spectral signatures associated with hydrogen bonding for the uptake of 2-CEES, 1-chloropentane, and diethyl sulfide provide evidence that hydrogen-bond donation through the chlorine group is responsible for the uptake of 2-CEES. Because 1-chloropentane interacts with the μ_3O–H groups predominately through the lone pair electrons on the chlorine atom, while diethyl sulfide binds exclusively through the central sulfur atom, the infrared spectra in Figure 3.2 provide spectral benchmarks for characterizing the primary binding interaction for 2-CEES. The band shapes and wavenumbers associated with the interactions of the μ_3O–H groups and 2-CEES within UiO-66 are very similar to those of 1-chloropentane. Specifically, the redshift of the ν(O–H) band when 2-CEES adsorbs onto UiO-66 is 107 cm^{-1} (FWHM=104 cm^{-1}) and the IR redshift for adsorbed 1-chloropentane is 118 cm^{-1} (FWHM=74 cm^{-1}). In contrast, the IR redshift for adsorbed diethyl sulfide is 164 cm^{-1} (FWHM=193 cm^{-1}).

Therefore, our results support the hypothesis that the predominant interaction for 2-CEES adsorption within UiO-66 is through hydrogen bonding between the chlorine of 2-CEES and the bridging hydroxyls of UiO-66. Binding between the 2-CEES chlorine group and the μ_3O–H hydroxyls is likely favored over binding through sulfur due to steric effects within the pore environments. The orientation of the μ_3O–H hydroxyls in the corners of the tetrahedral cavities of UiO-66 keep sulfur atoms of 2-CEES from orienting as closely to the hydroxyls as it would on a planar surface (Figure 4.3).

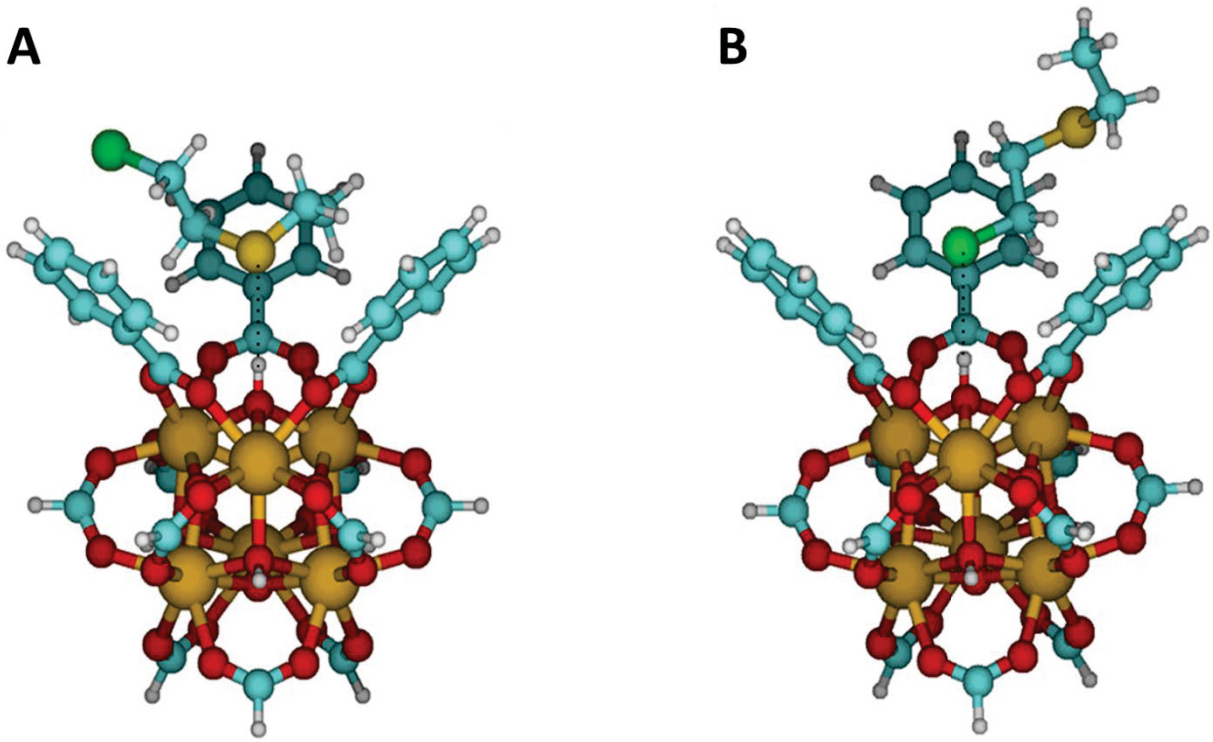

Figure 4.3 Calculated binding orientations of 2-CEES hydrogen bonding with UiO-66 through the sulfur atom (A) and chlorine atom (B). Atom colors are C: cyan, O: red, H: white, Zr: gold, Cl: green, S: yellow.

4.3.1.2 HD Uptake within UiO-66: Simulant-Agent Correlation

To ensure that the adsorption of 2-CEES within UiO-66 under vacuum conditions agree well with the uptake of actual sulfur mustard at ambient pressures and temperatures, diffuse-

reflectance infrared Fourier-transform spectroscopy (DRIFTS) was utilized to track the adsorption of HD within UiO-66 (Figure 4.4). Similar to 2-CEES adsorption within UiO-66, upon exposure of HD to UiO-66, the vibrational IR feature at 3674 cm^{-1} decreased in intensity while a broad band simultaneously formed at 3588 cm^{-1} (FWHM = 74 cm^{-1}). We assigned this band as a hydrogen-bonded ν(O–H) feature that was redshifted 86 cm^{-1} from the bridging hydroxyls of UiO-66. The shift of the ν(O–H) attributed to hydrogen-bonded HD was smaller than the shift for 2-CEES (107 cm^{-1}), potentially due to steric restrictions that prevent HD from forming a closer hydrogen bond or decreased dipole-dipole interactions relative to 2-CEES (the dipole moments for 2-CEES and HD are 1.645 D and 0.78 D, respectively).[168-169] The presence of a single band attributed to a hydrogen-bonded νO–H is consistent with the uptake of 2-CEES on UiO-66 and suggests that HD also adsorbs through hydrogen bond formation between hydroxyl groups on UiO-66 and the chlorine groups of HD. The growth of additional vibrational features (Table 4.2) at lower frequencies is consistent with previously reported spectra of HD and suggests that, much like 2-CEES, HD does not react upon adsorption within UiO-66.

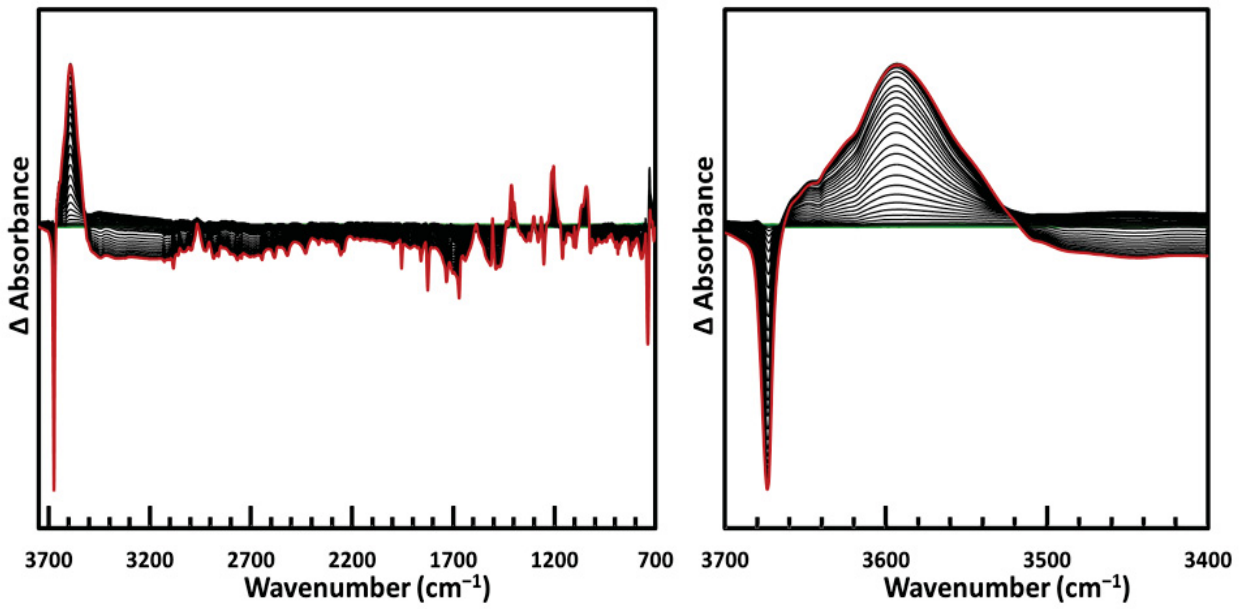

Figure 4.4 DRIFTS spectra of HD adsorption on UiO-66 in the full IR region (A) and O-H stretching region (B). The green spectrum represents the UiO-66 sample prior to HD exposure while the red spectrum corresponds to the MOF at the end of dosing. The reference background for each spectrum is the clean, unexposed UiO-66 sample.

Table 4.2 IR band assignments for HD adsorbed within UiO-66.

Assignment[166-167]	**HD adsorbed on UiO-66 (cm^{-1})**
ωS(CH_2)	1265
ωC(CH_2)	1212
ν(C-C)	1067
ν(C-C)	1038

4.3.2 Pore Size Effects on the Adsorption of 2-CEES within Zr-MOFs

We hypothesized that the steric constraints within the tetrahedral pores of UiO-66 results in 2-CEES hydrogen bonding to the μ_3–OH hydroxyls through the chlorine and not through the lone pairs on the sulfur. Because MOFs offer the ability to change both size pore size and pore topology through the use of different organic linkers, Zr-MOFs with larger pore sizes may accommodate 2-CEES, and more importantly HD), hydrogen bonding through the sulfur. We examined how changes to the pore size affect the ability for 2-CEES to hydrogen bond to the μ_3O–H hydroxyls on the secondary building unit of Zr_6 MOFs. The adsorption of 2-CEES within UiO-

67 and NU-1000, two Zr-MOFs with larger pore sizes than UiO-66, was investigated using IR spectroscopy. UiO-67, which is isoreticular to UiO-66, has 4,4' biphenyl-dicarboxylate (BDPC) linkers instead of BDC linkers, which increases the triangular pore aperture to between 8 and 11.5 Å and the internal cavity diameters to 11.5 Å and 23 Å for the tetrahedral and octahedral pores, respectively (Figure 4.5).[55, 170] NU-1000 has hexagonal channels with a diameter of 31 Å and smaller triangular channels with a diameter of approximately 12 Å (Figure 4.5).[66] Unlike UiO-66 and UiO-66, NU-1000 has only 8 linkers per node, which means that the Zr-nodes of NU-1000 also contain four terminal hydroxyl groups and four aquo ligands.[130]

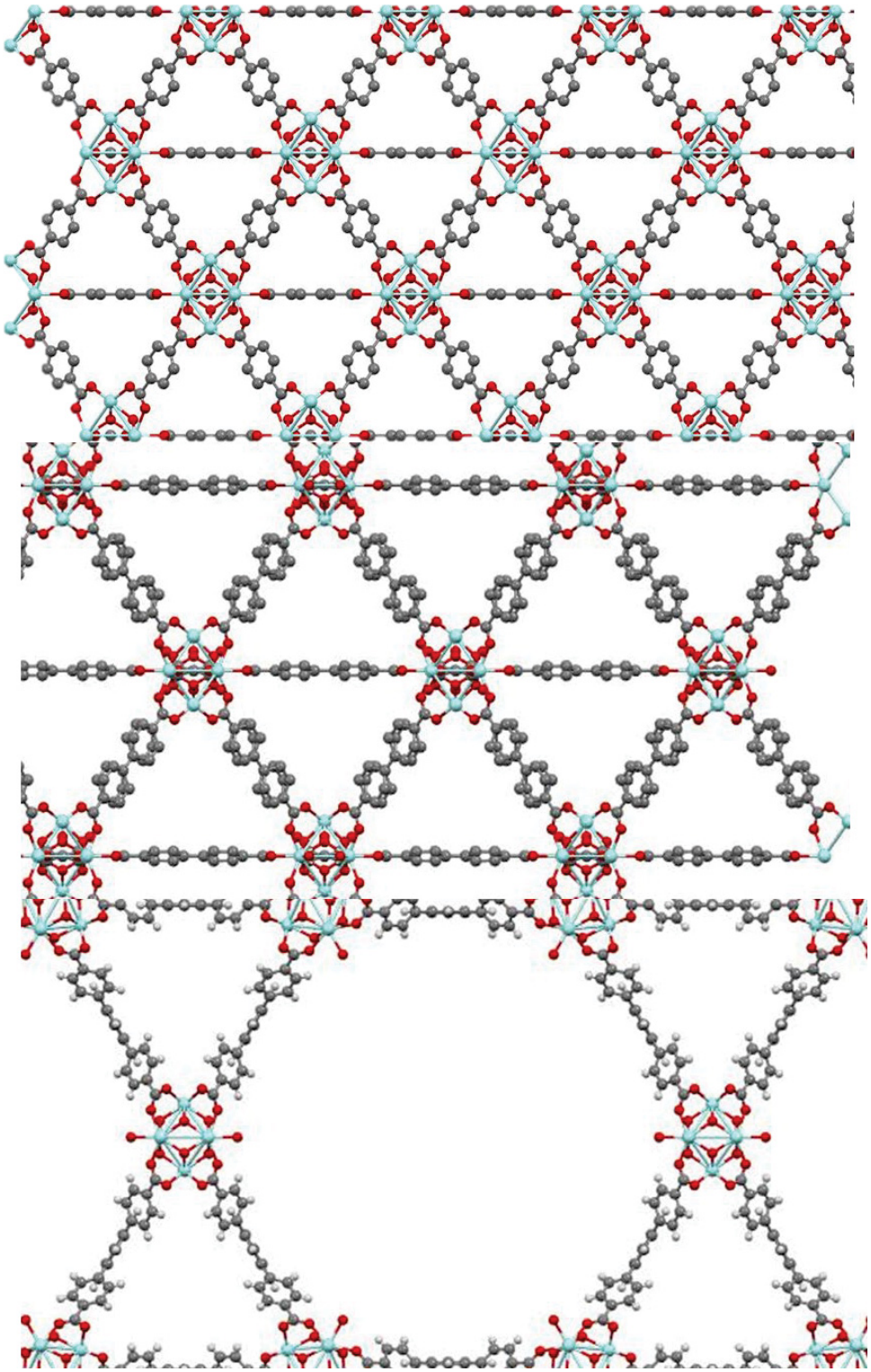

Figure 4.5 Representations of UiO-66 (top), UiO-67 (center), and NU-1000 (bottom). Hydrogen atoms in the UiO-66 and UiO-67 structures were omitted for clarity. Atom colors are C:grey, O: red, H: white, Zr: cyan.

The vibrational spectra of NU-1000 and UiO-67 prior to 2-CEES exposure were consistent with previously published IR data.[130] The free hydroxyl in UiO-67 is largely obscured due to a high absorbance baseline above 2000 cm^{-1}. The vibrational modes attributed to adsorbed 2-CEES within UiO-67 and NU-1000 agree with adsorbate features observed in the uptake of 2-CEES within UiO-66. While sample alignment prevented the collection of time-resolved IR data during the exposure of UiO-67 to 2-CEES, the spectra of the MOF before and after dosing revealed two overlapping hydrogen bond features at 3562 cm^{-1} and 3501 cm^{-1}, suggesting that 2-CEES can undergo hydrogen bond formation in UiO-67 through both the sulfur and chlorine moieties.

Time-resolved IR spectra of 2-CEES adsorption within NU-1000 at 176 K reveal that 2-CEES adsorption proceeds initially through the formation of a hydrogen bond feature redshifted 105 cm^{-1} from the hydroxyl peak at 3677 cm^{-1}, consistent with hydrogen bond formation through the chlorine group of 2-CEES within UiO-66. At higher coverages, a second hydrogen bond feature emerges at 3461 cm^{-1}, a 216 cm^{-1} redshift. This hydrogen bond feature could be possibly due to 2-CEES hydrogen bonding through its sulfur atom at the bridging hydroxyl sites, or 2-CEES hydrogen bond formation with the terminal hydroxyl groups present on the Zr nodes of NU-1000. The ν(O–H) band for terminal and bridging hydroxyl groups appear at the same frequency,[130] making it difficult to distinguish. Upon heating the MOF, this secondary band disappears first, potentially indicating that while 2-CEES may hydrogen bond to the Zr-node of NU-1000 through the sulfur group, this binding motif is not as energetically favorable as hydrogen bonding through the chlorine.

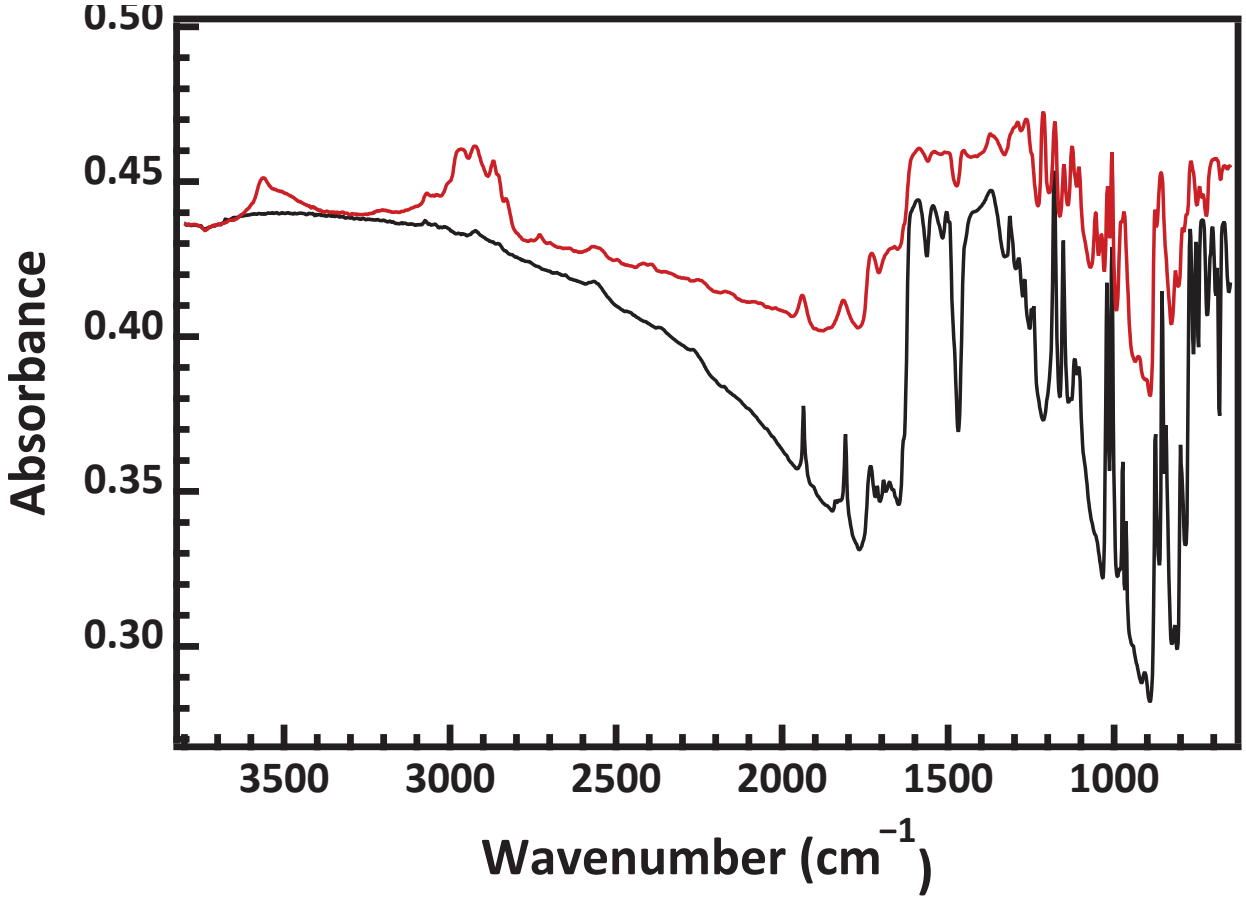

Figure 4.6 Transmission IR spectra recorded of 2-CEES exposure to UiO-67 at 176 K. The black spectrum represents the clean, unexposed UiO-67 sample, while the red spectrum corresponds to the MOF after dosing.

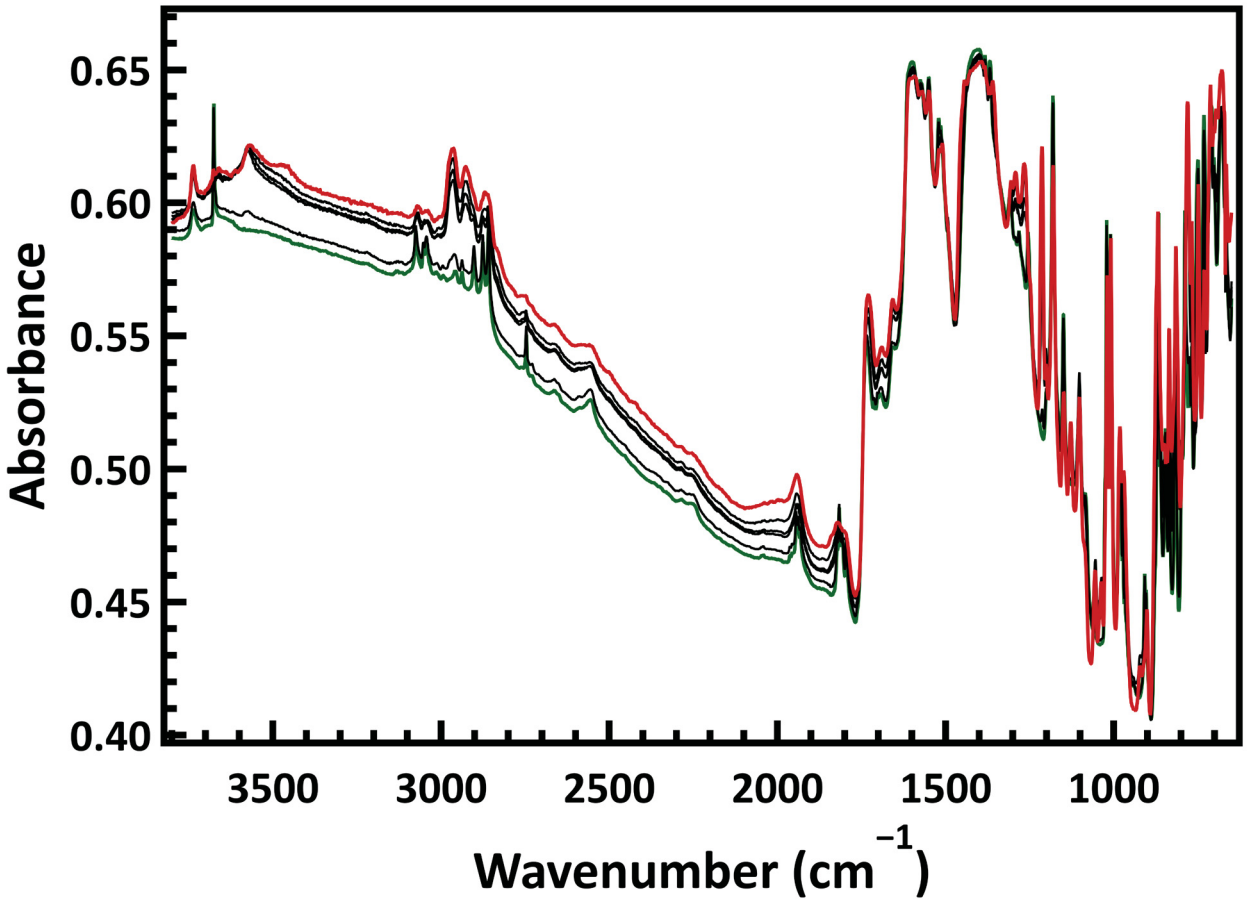

Figure 4.7 Transmission IR spectra recorded of 2-CEES exposure to NU-1000 at 176 K. The black spectrum represents the clean, unexposed UiO-67 sample, while the red spectrum corresponds to the MOF after dosing.

4.3.3 2-CEES Transport through UiO-66

For 2-CEES trapped within the tetrahedral pores of UiO-66 following exposure, adsorbates that gain sufficient thermal energy to break the μ_3-OH---2-CEES hydrogen bond may traverse the MOF pores and desorb from the sample. Using *in situ* infrared spectroscopy, we monitored the changes in the intensity of vibrational bands associated with adsorbed 2-CEES over time, which provides a direct measure of the relative concentration of 2-CEES that remained bound to the MOF. Figure 4.6A shows the decrease of the $\omega C(CH_2)$ absorbance band assigned over time to adsorbed 2-CEES at 273 K.

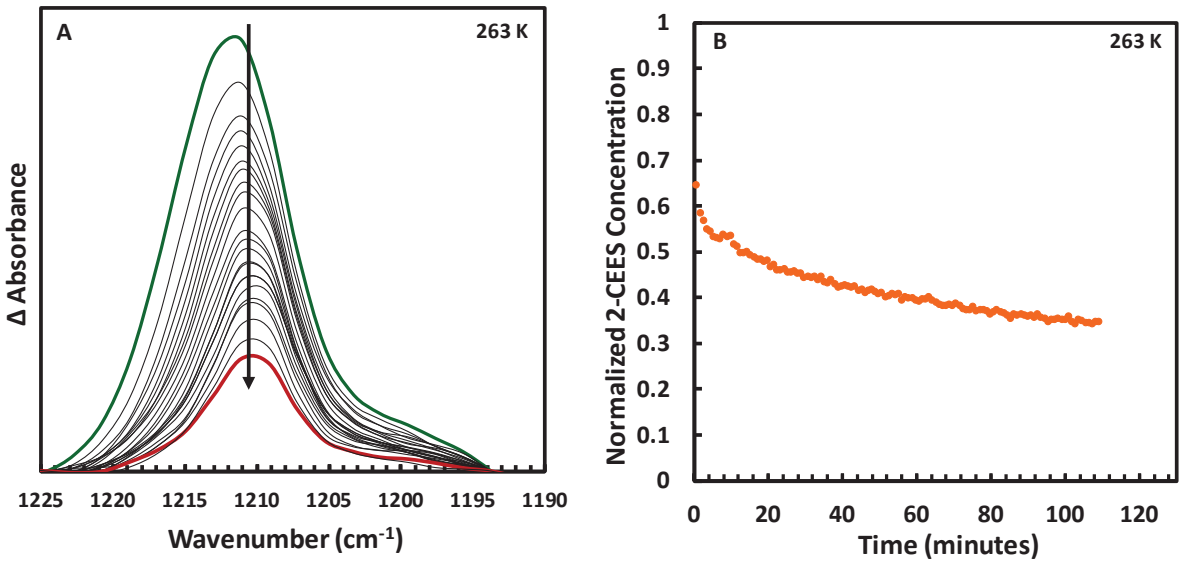

Figure 4.8 Results from the isothermal diffusion of 2-CEES through UiO-66 at 263 K. **A** shows the difference spectra showing the decrease in the ω(C(CH$_2$)) band at 1212 cm^{-1} over time while **B** shows the decrease in the normalized peak area of the ω(C(CH$_2$)) band over time.

The monotonic decrease of the integrated ω(C(CH$_2$)) band for 2-CEES adsorbed within UiO-66 was modeled using a single diffusion-term equation based on Fick's 2nd law of diffusion, which has been previously used to calculate gas diffusivity through UiO-66, as well as other complex materials including metal oxide nanoparticles.[54, 83, 98, 112-114] The model has the form:

$$\frac{I_t}{I_0} = \theta \sum_{n=0}^{\infty} \frac{8}{(2n+1)^2 \pi^2} e^{\left[-\frac{D(2n+1)^2 \pi^2 t}{4l^2}\right]} \qquad \textbf{(5.1)}$$

In eq. 1, I_t represents the integrated IR absorbance at time t, I_0 represents the integrated IR absorbance at t=0, l represents the diffusion path length (50 μm), D represents the diffusion coefficient, and θ represents a normalization factor for the diffusion coefficient. The diffusion coefficients for isothermal 2-CEES diffusion through UiO-66 are listed in Table 4.3. These coefficients range from 4.48 × 10^{-11} cm^2 s^{-1} to 1.38 × 10^{-9} cm^2 s^{-1} (model fits shown in Figure 4.8). The measured diffusivity of 2-CEES at 295 K UiO-66 were a seven order-of-magnitude decrease compared to 2-CEES vapor diffusion in air (5.46 × 10^{-2} cm^2 s^{-1}) and a four order-of-

magnitude decrease compared to the self-diffusion of 2-CEES liquid (2.43×10^{-5} cm^2 s^{-1}) as measured by pulse-field gradient NMR (Supplemental).[171]

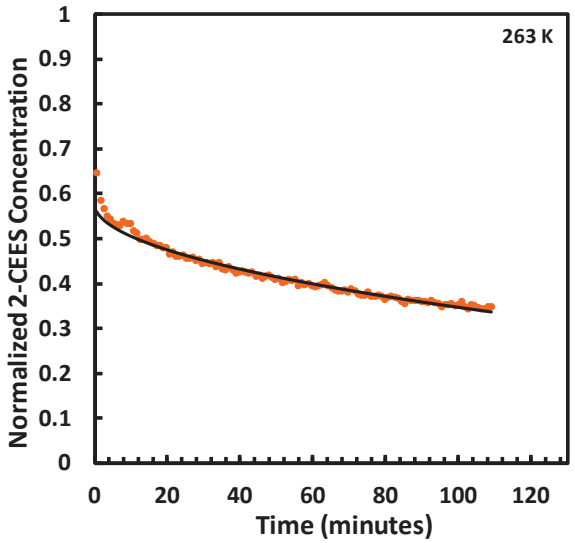

Figure 3.7 Isothermal diffusion of 2-CEES through UiO-66 at 263 K modeled using Eq. 1.The colored dots represent the experimental data and the solid lines indicate the model fit.

Deviations of experimental data from the Fickian model have been attributed to a possible combination of 2-CEES concentration gradients within the MOF prior to the start of the experiment as well as contributions from grain boundary diffusion. Previously published literature on the diffusion of gases through MOFs employed a two-term diffusion model to describe the contributions of both intracrystalline and grain boundary diffusion.[119, 172] We hypothesize that the intracrystalline diffusion of strongly bound adsorbates through the pores of the MOFs acts as the rate-limiting step for the diffusive process. Further analysis of the intracrystalline diffusion can provide fundamental insight into the rates and energetics of 2-CEES transport within UiO-66.

Table 4.3 Fitting parameters for the Fickian diffusion model described in Equation 1 (employed in Figure 3.8)

T (K)	θ	D (10^{-10} cm^2 s^{-1})
253	0.799	0.448 ± 0.019
263	0.579	1.32 ± 0.04
273	0.409	3.41 ± 0.17
283	0.328	7.32 ± 0.23
293	0.435	13.8 ± 0.5

The diffusion coefficient of 2-CEES through UiO-66 shows an exponential increase with increasing temperature that suggests an activated process for diffusion.[173] Therefore, we describe the temperature-dependent diffusion coefficient via the equation:

$$\boldsymbol{D(T) = D_0 e^{(-\frac{E_{a_{diff}}}{RT})}} \quad \textbf{(4.3)}$$

Where ***D(T)*** is the diffusion coefficient at temperature ***T***, $\boldsymbol{D_0}$ is the diffusion coefficient at infinite temperature, ***R*** is the gas constant, and $\boldsymbol{E_{adiff}}$ is a fitting parameter associated with the activation energy of diffusion. By creating an Arrhenius plot (Figure 4.8) of the diffusivity of 2-CEES at five temperatures, the fitting parameter for the activation energy of diffusion of 2-CEES through UiO-66 was determined to be 53.0 ± 0.8 kJ/mol.

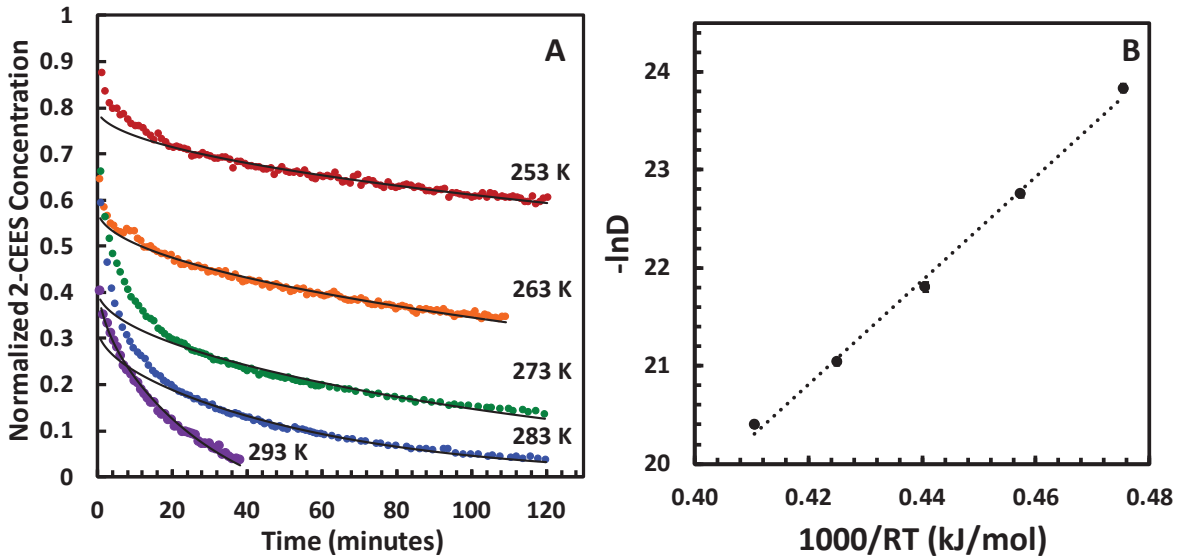

Figure 4.8 Diffusivities of 2-CEES through UiO-66 at varying temperatures. A shows the decrease in adsorbed 2-CEES over time at each temperature (colored dots indicate experimental data while black lines indicate the Fickian diffusion fit. B shows the Arrhenius plot for 2-CEES diffusion through UiO-66. The activation energy of diffusion was determined to be 53.0 ± 1.7 kJ/mol with $D_0 = 14.8 \pm 0.4$ cm^2 s^{-1}. Error bars represent the 95 % confidence interval for the measured diffusion coefficient.

4.3.3.1 Role of Hydrogen Bonding on 2-CEES Diffusivity

The infrared spectra of 2-CEES adsorption within UiO-66 revealed that uptake proceeded through the formation of hydrogen bonds with the μ_3O–H groups on the zirconium node. The energy requirement for the rupture of the hydrogen bonds between 2-CEES and UiO-66 may explain the activation energy required for intraparticle diffusion. We explored this hypothesis by interrogating the extent to which hydrogen bonding affected the rate and energetics of 2-CEES diffusion through the UiO-66 sample, the MOF was heated at 573 K overnight in UHV to dehydroxylate the sample. The dehydroxylation process removed the bridging hydroxyls of UiO-66 through the loss of two water molecules, converting the node from $Zr_6O_4(OH)_4$ to Zr_6O_6 and changing the coordination number of the Zr atoms from 8 to 7.[56, 174-175] In addition to the loss of the bridging hydroxyls on the Zr node, dehydroxylation induces a compression in the Zr_6 octahedron,[56] though the structure of the rest of the MOF remains unaltered. Infrared spectra of

UiO-66 before and after heating revealed that the loss of the ν(O–H) band at 3674 cm^{-1} represented the only change to UiO-66 observed in the IR. (Appendix A).

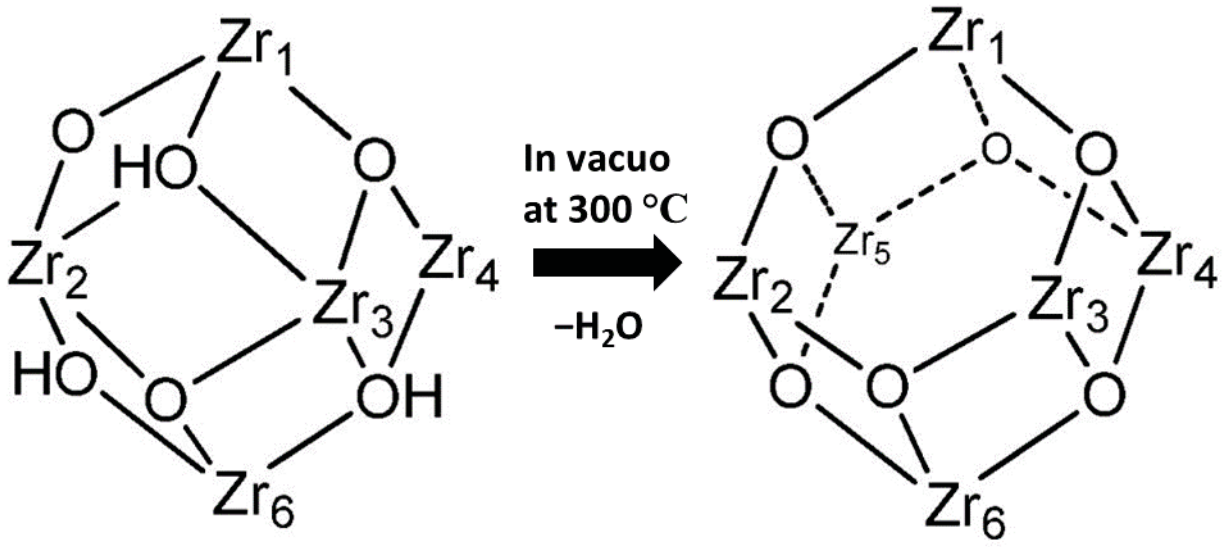

Figure 4.9 Representation of the dehydroxylation of the $Zr_6O_4(OH)_4$ cluster to Zr_6O_6 upon heating at 300 °C in vacuum. Adapted from Corma et al.[175] with permission from The Royal Society of Chemistry.

After dehydroxylation, another set of isothermal diffusion experiments were performed with 2-CEES. A comparison of the diffusion coefficients revealed that 2-CEES diffused approximately a factor of five times faster through the dehydroxylated UiO-66 than in the hydroxylated MOF (Figure 4.10). However, when comparing the Arrhenius plot fits for each, the activation energy for the diffusion for 2-CEES diffusion through dehydroxylated UiO-66 was 54.7 ± 1.9 kJ/mol (as compared to 53.0 ± 1.7 kJ/mol for the hydroxylated UiO-66). The similarity in energies suggested that hydrogen bonding does not contribute to the energetic barrier for the diffusion process. Instead, dispersion forces between the adsorbed 2-CEES and the walls of the tetrahedral pores of UiO-66 primarily contributed to the activation energy of diffusion. The distortion of the Zr_6 may have subtle effects on the pore geometry of UiO-66, which could also affect the interactions of 2-CEES with the pore walls.[56] Additionally, the dehydroxylation process

generated coordinatively unsaturated Zr(IV) sites on the node,[56] which may serve as Lewis Acid sites which may interact more strongly with 2-CEES than the hydroxyl groups.[82, 112]

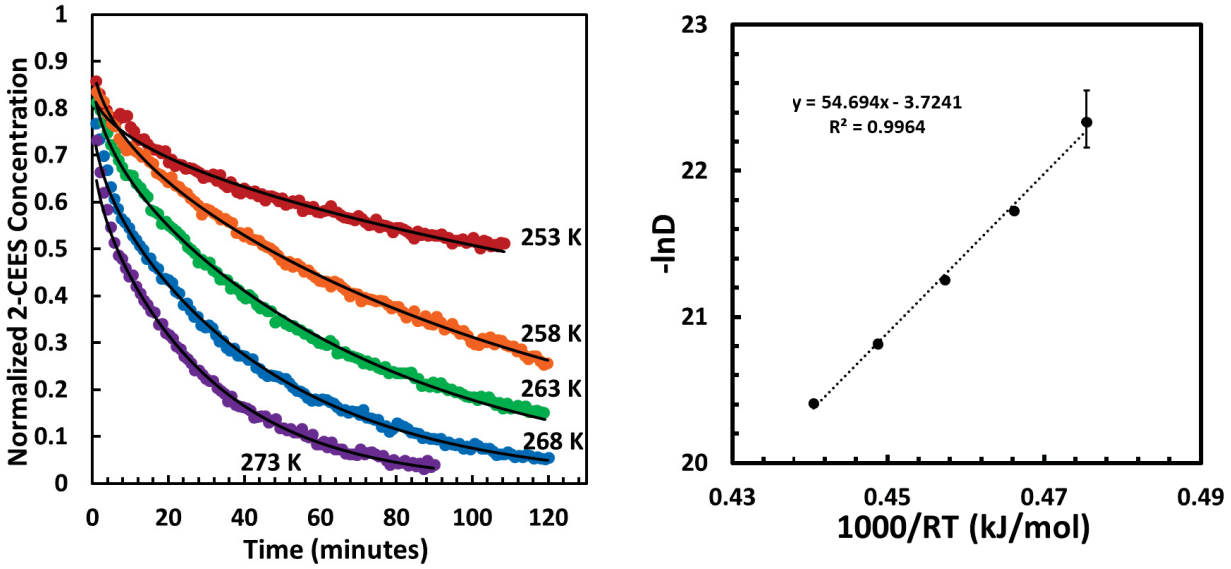

Figure 4.10 Diffusivities of 2-CEES through dehydroxylated UiO-66 at varying temperatures. **A** shows the decrease in adsorbed 2-CEES over time at each temperature (colored dots indicate experimental data while black lines indicate the Fickian diffusion fit. B shows the Arrhenius plot for 2-CEES diffusion through the dehydroxylated UiO-66. The activation energy of diffusion was determined to be 54.7 ± 1.9 kJ/mol with D_0 = 41.4 ± 0.4 cm^2 s^{-1}. Error bars represent the 95 % confidence interval for the measured diffusion coefficient.

4.3.4 Pore Size Effects on the Diffusion of 2-CEES within Zr-MOFs

UiO-66 possesses the smallest pore diameters and window apertures of the UiO series of MOFs.[55] To understand how porosity affects the rate of 2-CEES diffusion, the diffusivities of 2-CEES through UiO-67 and NU-1000 at 273 K were also studied. At 273 K, the diffusion coefficient for UiO-67 was 5.09 × 10^{-10} cm^2 s^{-1}, a factor of two increase compared to UiO-66. For NU-1000, the measured diffusion coefficient for 2-CEES at 273 K was 3.14 × 10^{-8} cm^2 s^{-1}; 2-CEES fully desorbed from the NU-1000 in approximately 6 minutes. Arrhenius plots of the diffusivity of 2-CEES through UiO-67 and NU-1000 (Figure 4.11) revealed activation energies of diffusion of 42.4 ± 5.0 kJ/mol and 43.7 ± 2.2 kJ/mol, respectively.

For UiO-67, the increase in pore aperture and cavity size compared to UiO-66 likely decreases the number of gas-pore wall collisions compared to UiO-66 as well as potential steric strain that may occur when 2-CEES passes through the triangular pore aperture.[118, 176] 2-CEES must travel through multiple triangular pore apertures in the UiO-MOFs to fully diffuse out of the crystallites. For NU-1000, the structural anisotropy and large channel sizes suggests that 2-CEES diffusion is limited by transport from the 12 Å triangular to the 31 Å hexagonal channels.[177] Once a 2-CEES molecule enters the 31 Å wide hexagonal channel, gas-wall collisions and dispersion interactions between the diffusing 2-CEES molecules and NU-1000 are likely lower compared to UiO-67, which may explain the faster diffusivity of 2-CEES through NU-1000 than UiO-67.

We hypothesize that the similarity in diffusion activation energies for UiO-67 and NU-1000 is to size of their respective pore environments. The triangular channels in NU-1000 are 11 Å in diameter,[178] comparable to the tetrahedral pores of UiO-67 (literature values for the triangular pore aperture of UiO-67 vary from 8.5 to 11.5 Å).[55, 61] The dispersion interactions between 2-CEES within the tetrahedral pores of UiO-67 are therefore likely similar to the dispersion interactions of 2-CEES within the triangular channels in NU-1000. This hypothesis suggests that the diffusion rate of small molecules through Zr-MOFs is significantly affected by the size of pore environment where adsorption occurs, due to the non-bonding interactions between the pore walls and the adsorbate. Based on this, we expected HD to diffuse at a similar rate as 2-CEES, though the presence of an additional chlorine atom may affect the diffusion rate. The effect of HD simulant size on diffusivity through UiO-66 is examined further in Chapter 5.

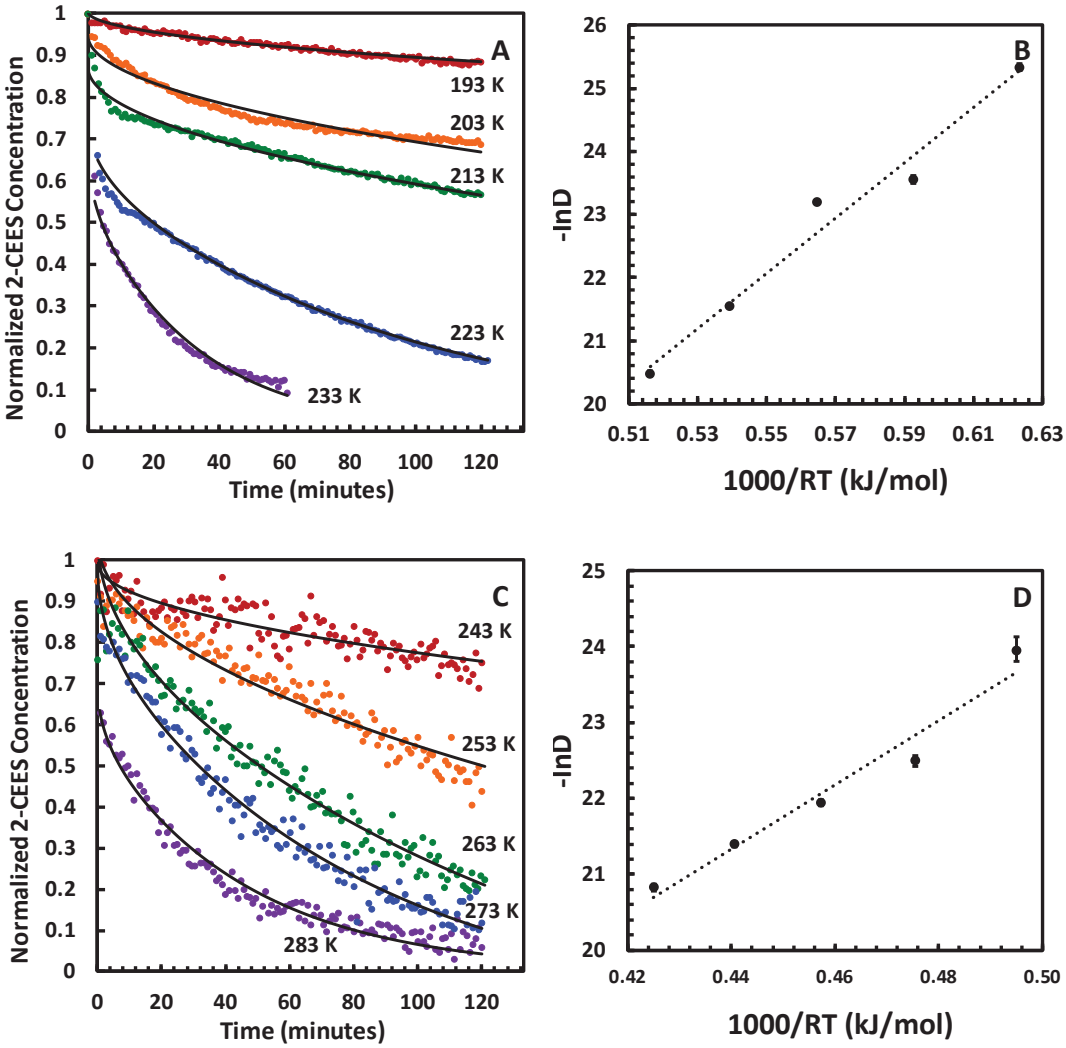

Figure 4.11 Diffusivities and Arrhenius plots of 2-CEES diffusion through NU-1000 (A+B) UiO-67 (C+D) at various temperatures. The colored dots indicate experimental data while the black lines are the Fickian diffusion model fit. The activation energy of diffusion was determined to be 43.7 ± 2.2 kJ/mol with D_0 = 7.2 ± 0.1 cm^2 s^{-1} for NU-1000 and 42.4 ± 5.0 kJ/mol with D_0 = 0.068 ± 0.099 cm^2 s^{-1}. Error bars represent the 95 % confidence interval for the measured diffusion coefficient.

4.4 Summary

This work aimed to provide fundamental insight into the adsorption and transport of mustard gas through the Zr-MOFs UiO-66, UiO-67, and NU-1000. We have provided spectroscopic evidence that the adsorption of 2-CEES within Zr-MOFs occurs through the formation of hydrogen bonds between hydroxyl groups on the zirconium oxo clusters and the

chlorine group of 2-CEES. DRIFTS spectra of HD adsorption on UiO-66 demonstrated good simulant-agent agreement. Interestingly, the 2-CEES hydrogen bonds do not appear to regulate the transport. The diffusivity of 2-CEES through the MOFs was measured at various temperatures with infrared spectroscopy by monitoring changes in the intensity of adsorbates over time. We found that while the presence of hydroxyl groups affect the overall rate of diffusion, the energetics of diffusion does not change significantly. Increasing the linker size resulted in both an increase in the diffusivity and a decrease in the activation energy of diffusion, suggesting that transport through the pore aperture may serve as the rate-limiting step for diffusion. Insight into how MOF structure affects the diffusion rates and adsorption mechanisms for HD simulants can allow for the continued development of zirconium-based MOFs as CWA sorbents and degradation catalysts.

Chapter 5. The Adsorption and Diffusion of HD Simulants within UiO-66

5.1 Introduction

First used in World War I during the Third Battle of Ypres in 1917,[148] sulfur mustard (HD) is a vesicant agent that is capable of alkylating and cross-linking DNA to cause blisters, eye irritation, tissue damage, cancer and in the most extreme cases, death. The use of HD during the Iran-Iraq war resulted in thousands of casualties, many of whom still struggle with the after-effects today.[6] Despite the near-unanimous ratification of the Convention on the Prohibition of the Development, Production, Stockpiling, and Use of Chemical Weapons and on their Destruction (CWC) in 1992, the threat of chemical warfare agent (CWA) attacks have persisted into the 21st century.[148] Recent CWA attacks have included the use of sulfur mustard on both military personnel and civilian populations.[179-180] The continued deployment of CWAs by terror groups and rogue nations have prompted research into the design and development of novel materials for the catalytic degradation of HD and other CWAs.

Recently, metal-organic frameworks (MOFs), especially MOFs containing Zr-based inorganic clusters, have emerged as promising materials for the degradation of CWAs, including HD.[33, 61, 67-69, 72, 76, 181-187] MOFs are a series of compounds consisting of polydentate organic linkers that coordinate to metal ions or metal oxide clusters to form extended porous two-dimensional or three-dimensional networks. The pore topology and chemical functionality of MOFs can be altered through the modulation of both the organic linker and the metal cluster. Due to their high surface area and uniform porosity, MOFs have been studied for use as gas sorption,[39-40, 188] chemical sensors,[189-193] and heterogeneous catalysts.[24, 51, 194-197] MOFs containing Zr_6-based oxo clusters

have demonstrated excellent stability in a variety of thermal conditions and chemical environments.[31, 125]

UiO-66, first synthesized at the University of Oslo in 2008,[55] is one of the most studied Zr-MOFs. UiO-66 is composed of $Zr_6O_4(OH)_4$ inorganic clusters (nodes) coordinated to twelve 1,4-benzenedicarboxylic acid linkers. Two pore environments exist within UiO-66; an octahedral pore made up of 6 clusters and 12 BDC linkers and tetrahedral pores consisting of 4 clusters and 6 BDC linkers.[56] The diameters of the octahedral and tetrahedral pores are 11 Å and 8 Å, respectively.[56] The tetrahedral pores are located on each of the octahedral pores, so access into the pores of UiO-66 is restricted by the 6.5 Å triangular pore windows on the tetrahedral pores.[198] Remarkably stable, UiO-66 retains crystallinity in a wide variety of chemical,[125] physical,[122] and thermal environments.

UiO-66 and UiO-66-based MOFs have previously shown activity for the degradation of HD in both aqueous and solid-phase studies. Gil-San-Millan reported on the hydrolysis of the HD simulant 2-chloroethyl ethyl sulfide (2-CEES) and HD within UiO-66 in aqueous conditions.[80] The introduction of amine groups to the organic linkers and basic lithium *tert*-butoxide sites to the Zr nodes of UiO-66 both resulted in faster hydrolysis rates. Ploskonka et al. reported that 2-CEES vapor readily reacts to alkylate the amine groups of UiO-66-NH_2 under ambient conditions, suggesting another pathway for HD degradation within UiO-based MOFs.[199] While these studies have demonstrated the reactivity of 2-CEES within UiO-66, questions remain about the adsorption mechanism of HD within UiO-66 and its ability to access the internal pores of the MOF.

Due to the extremely toxic nature of HD, the majority of CWA degradation research employs CWA simulants, which mimic the structure and chemical properties of the live agent while possessing much lower toxicities (Table 5.1). The structures of several common HD

simulants are shown in Figure 5.1. While HD simulants such as diethyl malonate and methyl salicylate have similar physical properties to HD, they lack the same chemical functionality of the live agent. 2-chloroethyl ethyl sulfide (2-CEES), also known as half-mustard, is the simulant most chemically similar to HD (Figure 5.1) and is often used to study the reaction chemistry of HD as scientists can investigate how both the sulfur and chlorine moieties interact with other chemicals. Furthermore, 2-CEES accurately mimics the Cl–C–C–S and C–C–S–C torsion angles of HD, which is important for predicting how HD may interact with a surface.[200]

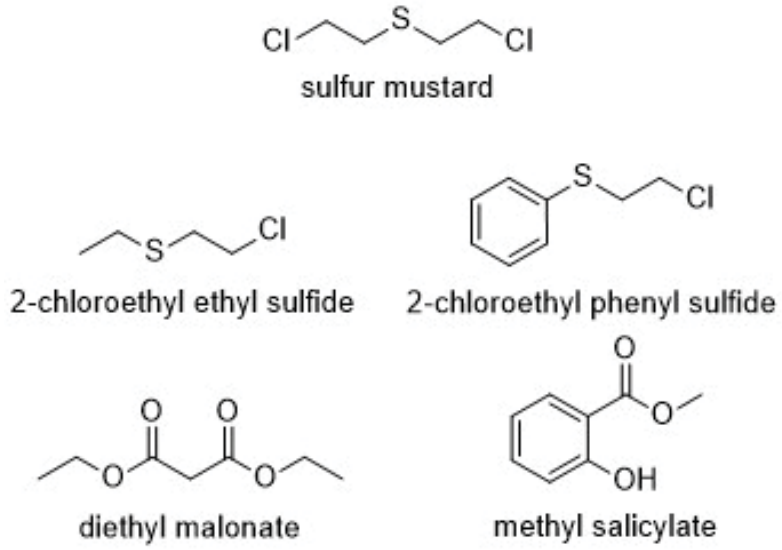

Figure 5.1 Common sulfur mustard simulants.

Table 5.1 Physical, chemical, and toxicological properties for sulfur mustard and four common HD simulants.[201]

Molecule	Mass (g/mol)	Vapor pressure at 298 K (Torr)	Melting point (K)	Solubility in H_2O (mg/L)	Boiling point (K)	Oral LD_{50} (mg/kg)
Sulfur mustard	159	0.11	218	684	492	20
2-chloroethyl ethyl sulfide	124	3.4	157	1062	431	566
2-chloroethyl phenyl sulfide	172	0.019	257	84	531	
Diethyl malonate	160	0.27	200	23200	474	15000
Methyl salicylate	152	0.0039	223	700	497	887

Previous studies of 2-CEES adsorption on hydroxylated metal oxide surfaces have indicated that 2-CEES can form hydrogen bonds through both sulfur and chlorine atoms.[85, 104] Published literature has demonstrated the ability for the μ_3–OH groups on the Zr clusters of UiO-66 to act as a hydrogen bond donor for the adsorption of small molecules, as also demonstrated in Chapter 3 with linear alkanes.[89-91] However, the location of the hydroxyl groups in the corners of the tetrahedral pores of UiO-66 may create a constrained environment that affects the binding geometry of 2-CEES. To identify the mechanism of 2-CEES adsorption, we simulated 2-CEES with 1-chloropentane and diethyl sulfide (Figure 5.2) to isolate the contributions that the sulfur and chlorine atoms have on the interfacial interactions between HD and UiO-66.

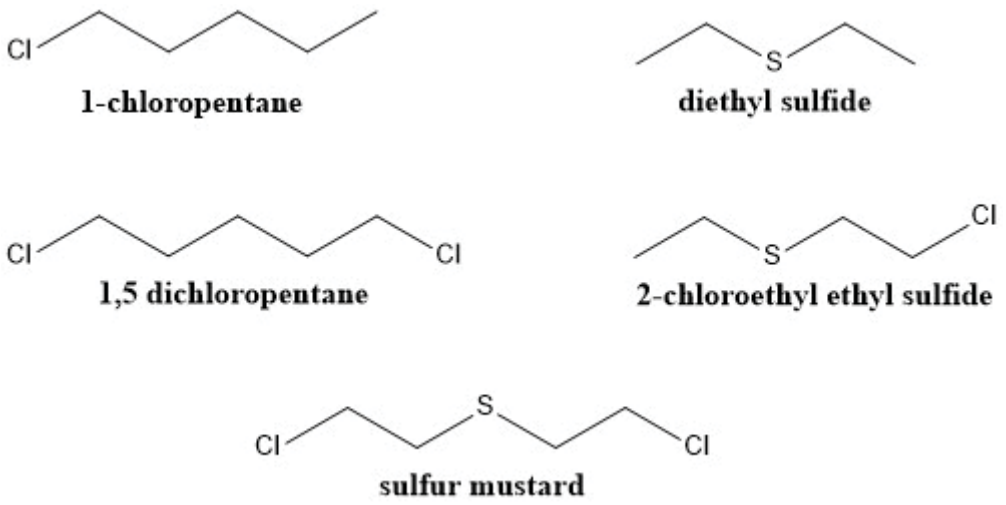

Figure 5.2 HD simulants used in this study.

Table 5.2 Physical and chemical properties of HD and the HD simulants used in this study.[202]

Molecule	Molar mass (g/mol)	Vapor pressure at 298 K (Torr)	Density (g/mL)	Melting point (K)	Boiling point (K)
sulfur mustard (HD)	159	0.11	1.27	218	492
2-chloroethyl ethyl sulfide	124	3.4	1.07	157	431
diethyl sulfide	90	60.2	0.837	193	365
1-chloropentane	107	31.1	0.882	107	285
1,5-dichloropentane	141	1.1	1.11	200	452

In addition to identifying the mechanism by which HD adsorbs within UiO-66, determining the accessibility of HD to the internal pore sites within the MOF is important for evaluating the potential for UiO-66 as an HD degradation catalyst. 2-CEES is not sufficiently large enough to mimic the size of HD, so we monitored the adsorption of 1,5-dichloropentane to predict whether HD would be able to adsorb within the pores of UiO-66. Due to the location of the hydroxyl groups within the tetrahedral pores of UiO-66, monitoring the fractional occupation of ν(O–H) band at 3674 cm^{-1} in the IR spectrum will provide a quantitative probe of pore accessibility.

In Chapter 4 we investigated how changes to the Zr-MOF structure affected the rate and energetics of 2-CEES diffusion. We observed that the increase in pore size resulted in both an increase in diffusivity and a decrease in the activation energy of diffusion. Furthermore, we determined that the presence of hydroxyl groups, which act as hydrogen-bonding sites for 2-CEES adsorption, slowed the diffusion of 2-CEES through UiO-66. In Chapter 3, our studies of the uptake and transport of linear alkanes within UiO-66 revealed that the size of the alkyl chain length affected the intermolecular interactions with UiO-66. In the work presented in this chapter, we studied the adsorption mechanism and diffusion kinetics of several key HD simulants within the Zr-MOF UiO-66 to provide information about the fundamental intermolecular interactions that govern the adsorption, and transport of HD within Zr-MOFs. The insights gathered from this work can provide benchmarks for the study of HD reactivity within UiO-66 and other MOFs.

The UiO-66 sample was synthesized following published methods for a “defect-free” UiO-66 to minimize the effects of missing linker and missing node defects on the uptake and transport of HD simulants. As will be discussed briefly, we measured the uptake and diffusivity of 2-CEES through several UiO-66 MOF samples synthesized with different methods and found that changes in the MOF structure resulted in different diffusivities, though the overall activation

energy of diffusion remained similar. The synthetic methods used for the other UiO-66 samples, sample characterization, and 2-CEES uptake and diffusion data can be found in Appendix B of this dissertation. We studied UiO-66 in its hydroxylated form because dehydroxylated UiO-66 readily reacts with water vapor in ambient environments to rehydroxylate the Zr node.

Transmission infrared spectroscopy was employed to probe changes to the vibrational features of UiO-66 upon simulant uptake, identify the formation of hydrogen bonds between the HD simulants and hydroxyl groups on the Zr nodes, and measure the diffusion of adsorbed simulants through UiO-66. These experiments were performed under ultrahigh vacuum (UHV) conditions to ensure that the UiO-66 sample remained free from contamination during the time of the experiments.

5.2 Experimental

5.2.1 MOF Synthesis

UiO-66 was prepared by Dr. Pavel Usov following a procedure reported by Shearer et al.[143] and described explicitly by Grissom et al.[54] 0.378 g (1.62 mmol) of $ZrCl_4$ and 0.539 g (3.24 mmol) of 1,4-benzenedicarboxylic acid were suspended in 10 mL of DMF and heated to 343 K for 30 minutes to fully dissolve the MOF precursors.[54] The solution was transferred to a Teflon-lined Parr reactor then heated at 493 K for 24 hours. After cooling room temperature, the white product powder was separated via centrifugation, washing with 4 aliquots of 10 ml of DMF, then immersed in 10 mL for 3 days, replacing the solvent each day. The final MOF product was dried in air at 333 K for 24 hours then 473 K for 1 hr.

5.2.2 Sample Preparation

Approximately 10-15 mg of UiO-66 were pressed into the void spaces of a 50.0 μm thick tungsten mesh (Tech-Etch). Excess MOF powder was scraped off the surface of the tungsten mesh

to ensure that the sample thickness remained at 50.0 μm. The sample mesh was installed onto the stainless steel sample clamps that were attached to two copper power leads. Type-k thermocouple wires were spot-welded onto the mesh to monitor the surface temperature. A schematic of the sample mesh can be found in Chapter 2. Upon the installation of the UiO-66 sample and the evacuation of the UHV chamber, UiO-66 was activated at 438 K for 72 hours to remove physisorbed water and residual DMF trapped in the pores.

5.2.3 Infrared Spectroscopy

Transmission infrared spectra of the UiO-66 samples were recorded on a Nicolet Nexus 670 IR spectrometer with a liquid-nitrogen-cooled MCT-A detector attached to the UHV chamber (Chapter 2). All spectra were recorded as 64 scans-to-average with a 4 cm^{-1} resolution. All IR spectra referenced an empty spot of the tungsten mesh as the reference background.

5.2.4 Vapor Dosing of HD Simulants onto UiO-66.

2-CEES, diethyl sulfide, 1-chloropentane, and 1,5-dichloropentane (all purchased from Sigma-Aldrich) were transferred into stainless steel dosing bulbs with sterile syringes and installed onto the custom-built gas-handling manifold described in Chapter 2. Several freeze-pump-thaw cycles were performed to purify each simulant before introduction into the UHV chamber. The controlled dosing of the HD simulants onto the UiO-66 samples was accomplished using a glass capillary array doser attached to a variable leak valve. The temperatures and pressures of dosing for each HD simulant on UiO-66 are discussed later.

5.2.5 Isothermal Diffusion Experiments

The isothermal diffusion experiments for HD simulant diffusion through UiO-66 were based on previously published work that demonstrated the use of infrared spectroscopy to measure the diffusion of small gas molecules through MOFs and other nanocrystalline materials.[54, 98, 112-

[114, 118] After the exposure of UiO-66 to the simulant of interest, the chamber was evacuated for approximately 30 minutes to allow the chamber to equilibrate and prevent the re-adsorption of gas-phase simulant. The sample was then heated to the desired isothermal diffusion temperature at a rate of 2.0 K/s. Once the desired temperature was reached, the sample was held at a constant temperature while infrared spectra of the sample were recorded every minute for 120 minutes. Following each experiment, the sample was heated to remove residually adsorbed simulant, as measured by IR spectroscopy.

5.2.6 Characterization of UiO-66

Before measuring the adsorption and uptake of HD simulants within UiO-66, we characterized the UiO-66 sample to determine the crystallinity, phase purity, surface area, and defect density of our sample through the use of scanning electron microscopy (SEM), powder X-ray diffraction (PXRD), nitrogen adsorption isotherms, and thermogravimetric analysis (TGA). The details for each method are listed in Appendix B and are also described in Grissom et al.[54]

5.3 Results and Discussion

The adsorption and diffusion of several HD simulants within UiO-66 were studied to provide fundamental insight into the hydrogen-bonding interactions and dispersive forces of HD within Zr-based MOFs. The use of a UiO-66 sample with a low defect density ensured that the adsorption of 2-CEES within UiO-66 occurred predominantly at μ_3–OH hydrogen bonding sites and not at coordinatively unsaturated Zr (Zr_{CUS}) sites. The interactions of 2-CEES with UiO-66, previously described in Chapter 4, are summarized first.

5.3.1 The Adsorption of 2-CEES within UiO-66

Upon exposure of UiO-66 to 2-CEES at 205 K, 2-CEES was able to diffuse through the triangular pore apertures of UiO-66 and access the μ_3–OH groups. The infrared spectra of the

adsorption of 2-CEES within UiO-66 (Figure 5.3) show the monotonic decrease in the intensity of the ν(O–H) band at 3674 cm^{-1} concurrent with the appearance of a broad vibrational feature at 3567 cm^{-1}. The presence of additional IR features consistent with the gas-phase spectra of 2-CEES (Table 5.3) suggested that 2-CEES molecularly adsorbed within UiO-66 and did not react.

As previously discussed in Chapter 4, these findings were consistent with hydrogen bond formation between the μ_3–OH groups on the $Zr_6O_4(OH)_4$ clusters and 2-CEES. The redshift in the IR frequency of the ν(O–H) occurred because of electronic charge donation from the hydrogen bond acceptor of 2-CEES to the σ* anti-bonding molecular orbitals of the O–H bond, thereby reducing the bond order.[145, 203] The increase in the intensity of the ν(O–H*)* band upon hydrogen-bond formation was attributed to the increase in the oscillator strength of the O–H.[203] The increase in peak width of the feature attributed to hydrogen-bonded ν(O–H) was due to the inhomogeneity of the hydrogen bonding interactions with 2-CEES.[13] The complete saturation of the band at 3674 cm^{-1} indicated that 2-CEES accessed all the hydroxyl groups within the internal pores of UiO-66.

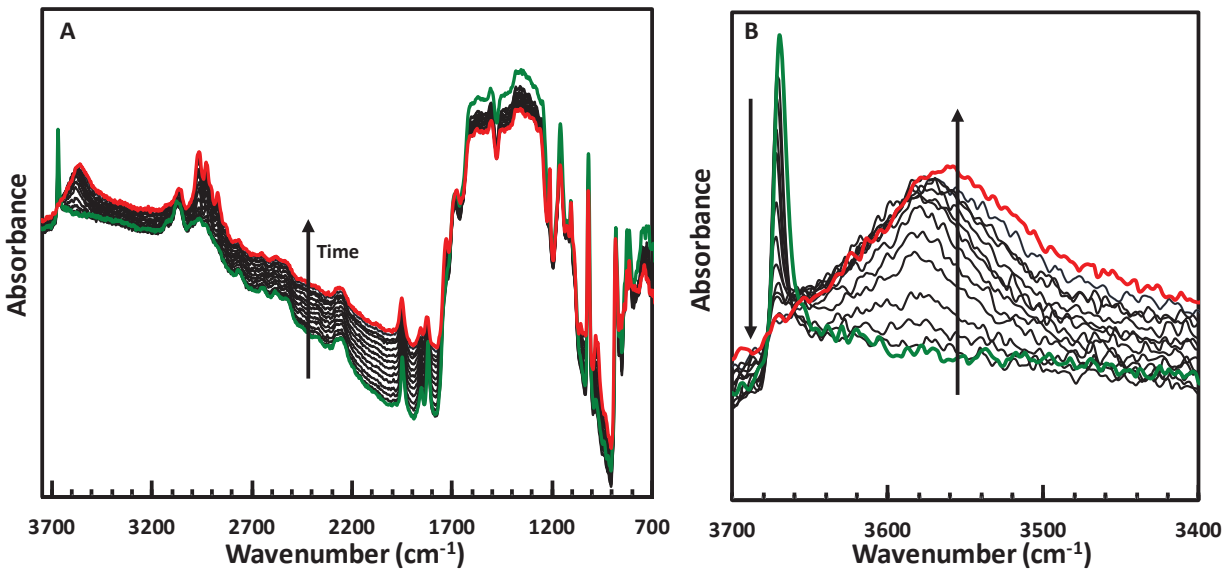

Figure 5.3 Transmission IR spectra of 2-CEES exposure to UiO-66 at 205 K in the full IR region (A) and O-H stretching region (B). The green spectrum represents the clean, unexposed UiO-66 sample, while the red spectrum corresponds to the MOF after dosing had ended. The reference background for each spectrum is a blank W-mesh spot.

Table 5.3 IR band assignments for gas-phase 2-CEES and 2-CEES adsorbed within UiO-66.

Assignment[166-167]	Gas phase 2-CEES (cm^{-1})[166]	2-CEES adsorbed in UiO-66 (cm^{-1})
$\nu(CH_2)_{as}$	2967	2967
$\nu(CH_3)_{as}$	2928	2928
$\nu(CH_2)_{s,bent}$	2871	2872
$\omega C(CH_2)$	1213	1212
$\rho C(CH_2)$, $\tau C(CH_2)$	1055	1056
$\nu(C\text{-}C)_{as}$	971	973

ν: stretch, ω:wag, ρ:rock, τ:twist

5.3.2 2-CEES Diffusivity through UiO-66.

The diffusivity of 2-CEES through UiO-66 was measured isothermally from 253 K to 293 K by tracking the decrease in the ω(C(CH_2)) vibrational mode at 1212 cm^{-1} over time and fitting the data to the Fickian diffusion model previously described in Chapter 3:

$$\frac{\boldsymbol{I_t}}{\boldsymbol{I_0}} = \boldsymbol{\theta} \sum_{\boldsymbol{n=0}}^{\boldsymbol{\infty}} \frac{\boldsymbol{8}}{\boldsymbol{(2n+1)^2\pi^2}} \boldsymbol{e}^{\left[-\frac{\boldsymbol{D(2n+1)^2\pi^2 t}}{\boldsymbol{l^2}}\right]} \quad \textbf{(5.1)}$$

Where $\boldsymbol{I_t}$ is the integrated intensity of the ω(C(CH_2)) mode at time $\boldsymbol{t}$, $\boldsymbol{I_0}$ is the integrated intensity of the ω(C(CH_2)) mode at time 0, $\boldsymbol{\theta}$ is the normalized concentration of adsorbed 2-CEES, $\boldsymbol{D}$ is the diffusion coefficient ($cm^2\ s^{-1}$), and $\boldsymbol{l}$ is the sample thickness (50.0 μm).

The measured diffusivities of 2-CEES through UiO-66 ranged from 4.48×10^{-11} $cm^2\ s^{-1}$ to 1.38×10^{-9} $cm^2\ s^{-1}$ (Table 5.4). These values were attributed to the intracrystalline diffusion of 2-CEES molecules through the UiO-66 sample and out to the MOF-vacuum interface, where 2-CEES then desorbed into the gas-phase. The measured diffusivity of 2-CEES through UiO-66 at 273 K was several orders of magnitude lower than previously measured self-diffusivities for neat liquid 2-CEES and the diffusivity of 2-CEES through air.[171]

Table 5.4 Fitting parameters for the Fickian diffusion of 2-CEES through UiO-66

T (K)	θ	D (10^{-10} cm^2 s^{-1})
253	0.799	0.448 ± 0.019
263	0.579	1.32 ± 0.04
273	0.409	3.41 ± 0.17
283	0.328	7.32 ± 0.24
293	0.435	13.8 ± 0.5

The exponential increase in diffusivity as the diffusion temperature increased indicated that the diffusion process followed an Arrhenius-like relationship with temperature. The diffusion coefficient was therefore expressed as a function of temperature via the equation:

$$D(T) = D_0 e^{(-\frac{E_{a_{diff}}}{RT})} \quad (5.2)$$

Where $D(T)$ is the diffusion coefficient at temperature T, D_0 is the diffusion coefficient at infinite temperature, R is the gas constant, and E_{adiff} is a fitting parameter associated with the activation energy of diffusion.

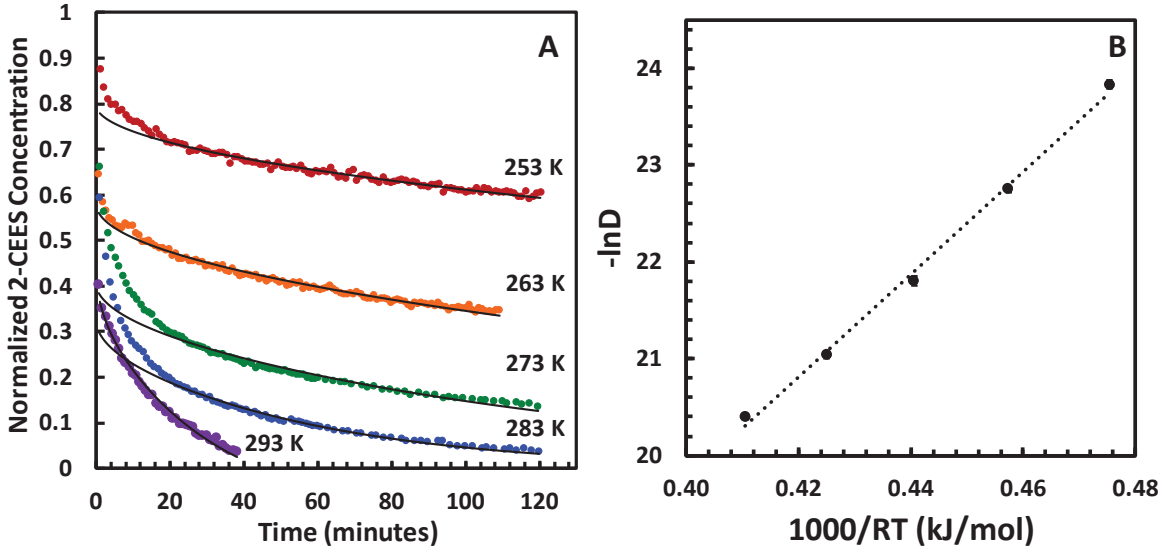

Figure 5.4 Diffusivities of 2-CEES at varying temperatures. **A** shows the decrease in adsorbed 2-CEES over time at each temperature (colored dots indicate experimental data while black lines indicate the Fickian diffusion fit. **B** shows the Arrhenius plot for 2-CEES diffusion through UiO-66. The activation energy of diffusion was determined to be 53.0 ± 1.7 kJ/mol with D_0 = 14.8 ± 0.4 cm^2 s^{-1}. Error bars represent the 95 % confidence interval for the measured diffusion coefficient.

5.3.2.1 Comparison of 2-CEES Diffusion between UiO-66 samples.

While the synthesis of the UiO-66 studied in this work had a low defect density, defect levels within MOFs can significantly vary, even when following the same synthetic procedure. While this work intentionally focused on studying the diffusivity of 2-CEES through a non-defected UiO-66, we wanted to assess how variations in the defect density and crystallinity of UiO-66 affected the transport of 2-CEES. The diffusion of 2-CEES at 273 K was measured for several UiO-66 samples synthesized with different methods (Appendix B). The diffusion coefficients (Table 5.5) ranged from 1.65×10^{-10} cm^2 s^{-1} to 3.64×10^{-10} cm^2 s^{-1} with a mean diffusivity of $2.71 \pm 0.89 \times 10^{-10}$ cm^2 s^{-1}.

The variation in diffusivity between samples likely resulted from a combination of variations defect density in between MOF samples, the MOF crystallite sizes, and the pelletization pressure into the tungsten mesh. Despite the difference in measured diffusion coefficients at 273 K, the average activation energy for 2-CEES diffusion through UiO-66 (for 3 samples) was 57.3 ± 6.0 kJ/mol. The 10% variation in the average activation energy of diffusion suggested that while the kinetics of adsorbate transport through UiO-66 may depend on sample composition, the overall energetics of the diffusion process remain similar.

Table 5.5 Comparison of the diffusivities of 2-CEES diffusion through the various UiO-66 samples at 273 K.

Sample	Pelletization Pressure (psi)	Diffusivity at 273 K (10^{-10} cm^2 s^{-1})
UiO-66-I	6500	1.65 ± 0.12
UiO-66-II	6500	2.84 ± 0.28
UiO-66-Defected	5000	1.99 ± 0.13
UiO-66-Ideal	7500	3.41 ± 0.17
UiO-66-NonModulated	5000	3.64 ± 0.33
Average	N/A	2.71 ± 0.89

5.3.3 Adsorption of HD Simulants within UiO-66

IR spectroscopy of the adsorption of the HD simulant 2-CEES within UiO-66 revealed that 2-CEES adsorbs through the formation of hydrogen bonds with the μ_3–OH groups on the Zr node of the MOF. Due to the presence of the electron-rich sulfur and chlorine atoms on 2-CEES, 2-CEES can form hydrogen bonds through either atom. Abelard et al. investigated the adsorption of 2-CEES on amorphous silica and observed the formation of multiple hydrogen bond features, which indicated that 2-CEES adsorbed to terminal hydroxyl groups of silica in multiple binding motifs. Understanding how 2-CEES adsorbs can allow us to predict how HD will adsorb within UiO-66. To isolate the electrostatic contributions of the sulfur and chlorine atoms for the adsorption of 2-CEES within UiO-66, we employed the simulants 1-chloropentane and diethyl sulfide (Figure 5.2).[104]

While IR spectroscopy suggested that 2-CEES was able to access the internal pores of UiO-66 and hydrogen bond with every bridging hydroxyl on the Zr node, 2-CEES is a smaller molecule than HD. As was demonstrated in Chapter 3, the increase in adsorbate size can affect the accessibility of the internal μ_3–OH groups. To more accurately mimic the size of HD, we also studied the adsorption and transport of 1,5-dichloropentane (Figure 5.2).

5.3.3.1 Adsorption of Diethyl Sulfide

The adsorption of diethyl sulfide within UiO-66 was studied to examine how the sulfur atom in HD affects its adsorption mechanism. Diethyl sulfide was dosed at 1×10^{-5} Torr for 30 minutes at 171 K. Upon the adsorption of diethyl sulfide, the IR spectra (Figure 5.5) exhibited the increase of a broad (FWHM = 193 cm^{-1}) feature at 3512 cm^{-1}, which indicated the formation of a hydrogen bond between the sulfur and the μ_3–OH groups of UiO-66. The IR feature at 3512 cm^{-1} attributed to the diethyl sulfide-hydrogen-bonded ν(O–H) band was redshifted by 164 cm^{-1}, 57

cm^{-1} greater than the feature attributed to 2-CEES hydrogen bonded to UiO-66. The full assignment of IR features attributed to adsorbed diethyl sulfide is listed in Table 5.6.

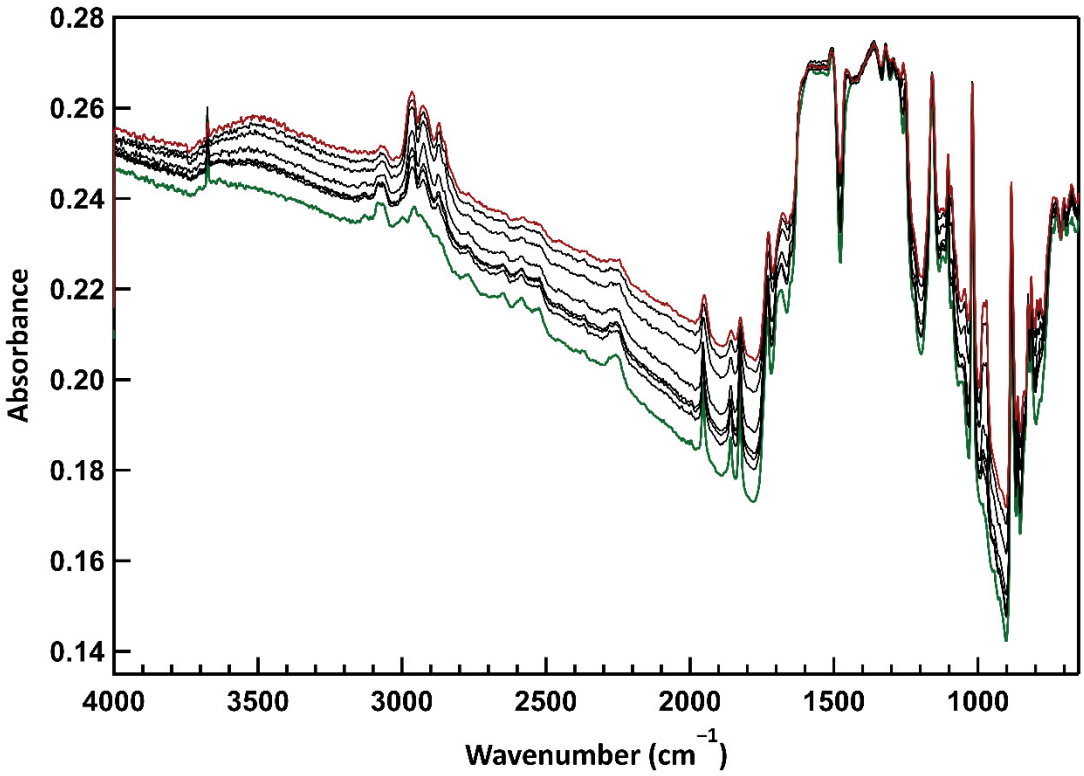

Figure 5.5 IR spectra of diethyl sulfide adsorption within UiO-66 at 171 K. The green spectrum represents the clean MOF before dosing and the red spectrum represents the MOF after diethyl sulfide exposure. The background spectrum was a blank mesh spot.

Table 5.6 Vibrational assignments for diethyl sulfide adsorbed within UiO-66.

Assignment[166]	**Gas-phase (cm^{-1})**[167]	**Adsorbed on UiO-66 (cm^{-1})**
$\nu(CH_2)_{asym}$	2970	2966
$\nu(CH_2)_{asym}$	2928	2926
$\nu(CH_3)_{sym}$	2871	2871
$\nu(CH_2)_{sym}$	2853	2851
$\rho(CH_3)/\nu(C\text{-}C)$	1074	1093
$\nu(C\text{-}C)$		980
$\nu(C\text{-}C)$	972	972
		795
$\rho(CH_2)$	780	786

ν: stretch, ω:wag, ρ:rock, τ:twist

5.3.3.2 Adsorption of 1-Chloropentane

1-Chloropentane was dosed into UiO-66 at 5×10^{-6} Torr for 80 minutes (24000 L) at 176 K. Upon the exposure of UiO-66 to 1-chloropentane, the intensity of the free hydroxyl at 3676 cm^{-1} decreased and two hydrogen-bonded ν(O-H) features, a small band at 3639 cm^{-1} of ($\Delta\nu$ = 37 cm^{-1}) and a larger, broader (FWHM =74 cm^{-1}) band at 3557 cm^{-1} ($\Delta\nu$ = 119 cm^{-1}), emerged (Figure 5.6). 1-Chloropentane was able to hydrogen bond with every μ_3–OH group, as evidenced by the complete saturation of the ν(O–H) band at 3676 cm^{-1}. Additional IR vibrational modes assigned to adsorbed 1-chloropentane are consistent with a reference IR spectrum of 1-chloropentane and suggest no degradation or reaction upon adsorption (Table 5.7).

The band at 3639 cm^{-1} was attributed to the hydrogen-bonded ν(O–H) species of 1-chloropentane adsorbed through the methyl groups of 1-chloropentane. The 37 cm^{-1} redshift of the ν(O–H) band was consistent with the bands assigned as hydrogen-bonded ν(O–H) for the adsorption of linear alkanes within UiO-66 described in Chapter 3. Upon thermal treatment, the feature at 3639 cm^{-1} disappeared first, suggesting that the band at 3557 cm^{-1} represented the more stable binding conformation of 1-chloropentane within UiO-66. We attributed the feature at 3577 cm^{-1} to 1-chloropentane hydrogen-bonded to UiO-66 through its chlorine atom.

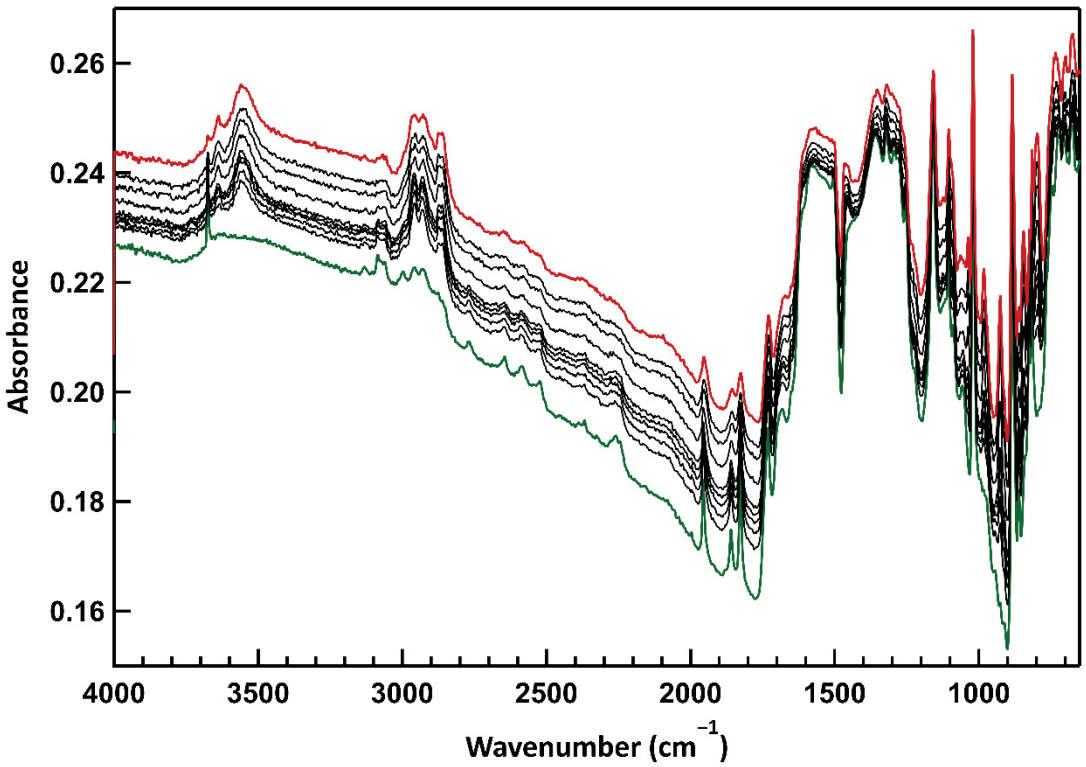

Figure 5.6 IR spectra of 1-chloropentane adsorption within UiO-66. The green spectrum represents the clean MOF before dosing and the red spectrum represents the MOF after 1-chloropentane exposure. The background spectrum was a blank mesh spot.

Table 5.7 Vibrational assignments for 1-chloropentane adsorbed on UiO-66 and comparison to reference IR spectrum of 1-chloropentane.

Assignment[204]	**Liquid film (cm^{-1})**[205]	**Adsorbed on UiO-66 (cm^{-1})**
$\nu(CH_3)_{asym}$	2960	2957
$\nu(CH_2)_{asym}$	2934	2927
$\nu(CH_3)_{sym}$	2875	2876
$\nu(CH_2)_{sym}$	2863	2859
δ(C-C) / $\gamma(CH_2)_{asym}$	1468/1457	1463
ν(C-C)	1037	1038
	989	984
$\rho(CH_2)$	926	927
	845	846
$\rho(CH_2)$	790	798

ν: stretch, ω:wag, ρ:rock, δ:in-plane bend, γ:out-of-plane bend

5.3.3.3 Adsorption of 1,5-Dichloropentane.

1,5-Dichloropentane was dosed onto UiO-66-I at 1×10^{-5} Torr for 80 minutes at 233 K. The IR spectra of 1,5-dichloropentane adsorption within UiO-66 (Figure 5.7) revealed a similar adsorption mechanism as 1-chloropentane, 2-CEES, and diethyl sulfide, with the monotonic growth of a broad feature (FWHM = 81 cm^{-1}) that we attributed to a hydrogen-bonded ν(O–H) species at 3568 cm^{-1} ($\Delta\nu = 108$ cm^{-1}). IR vibrational modes assigned to adsorbed 1,5-dichloropentane in UiO-66 are consistent with a reference spectrum for 1,5-dichloropentane (Table 5.8), but most vibrational modes are shifted by 3-5 cm^{-1}. These shifts likely result from dispersion interactions with the pore walls of UiO-66 and the restricted molecular degrees of freedom for adsorbates.[104] The full depletion of the free hydroxyl feature at 3676 cm^{-1} indicated that 1,5-dichloropentane was able to access all the internal hydroxyl groups of the UiO-66 sample and suggests that HD is capable of accessing all the pores within UiO-66.

Table 5.8 Comparison of 1,5-dichloropentane adsorbed on UiO-66 to a reference IR spectrum for 1,5-dichloropentane.

Liquid film (cm^{-1})[206]	**Adsorbed on UiO-66 (cm^{-1})**
	2991
2958	2961
2944	2949
	2900
2869	2868
2845	2847
	1037
1000	996
981	985
	906
	779

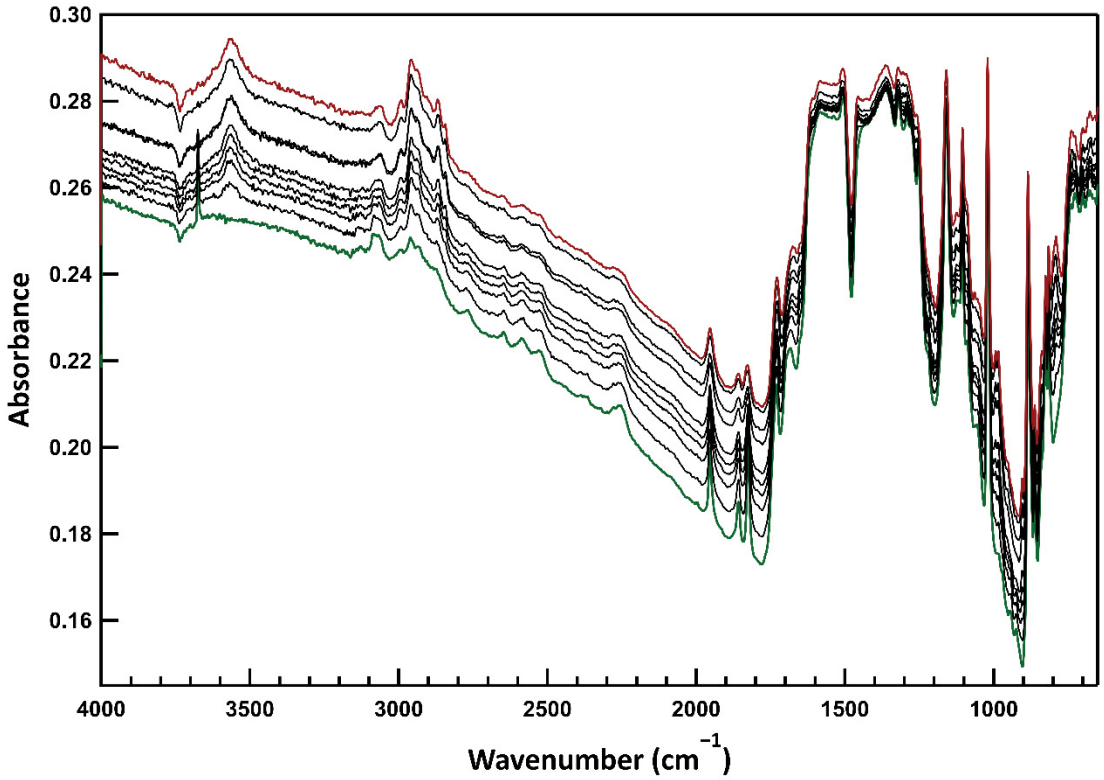

Figure 5.7 IR spectra of 1,5-dichloropentane adsorption on UiO-66. The green spectrum represents the clean, unexposed MOF and the red spectrum represents the sample after 1,5-dichloropentane dosing. The background spectrum was a blank mesh spot.

5.3.3.4 Charge Transfer and Electrostatic Interactions

A comparison of the redshifts of the ν(O–H) band upon hydrogen-bond formation between 2-CEES and the other HD simulants with the μ_3–OH groups of UiO-66 (Table 5.9) can provide insight into the adsorption mechanism for 2-CEES as well as the strength of the hydrogen bond interaction. The redshift of the ν(O–H) band upon 2-CEES adsorption ($\Delta\nu$ = 107 cm^{-1}) closely resembled the observed redshifts for 1-chloropentane ($\Delta\nu$ = 118 cm^{-1}) and 1,5-dichloropentane ($\Delta\nu$ = 108 cm^{-1}) and suggests that 2-CEES formed hydrogen bonds with the hydroxyl groups of UiO-66 through the chlorine moiety. In previously published work on 2-CEES adsorption onto silica and silica-titania, hydrogen-bond formation was observed through both the sulfur and chlorine moieties; however, neither material has the same restrictive pore environment as UiO-66.[85, 104] The observed redshift attributed to diethyl sulfide hydrogen-bonded to the hydroxyls of

UiO-66 suggests that diethyl sulfide can form hydrogen bonds with its sulfur. 2-CEES, with its chlorine atom, likely is too large to form hydrogen bonds through the sulfur within the tetrahedral pores of UiO-66.

The hypothesis that the steric environment within the pores of UiO-66 is partially supported when comparing our results to the adsorption of the same HD simulants on silica. The redshift of the ν(O–H) features upon the hydrogen-bond formation of diethyl sulfide ($\Delta\nu$ = 164 cm^{-1}) and 1-chloropentane ($\Delta\nu$ = 118 cm^{-1}) within UiO-66 are much smaller than the redshifts that ν(O–H) that Abelard et al. reported for the adsorption of diethyl sulfide ($\Delta\nu$ = 485 cm^{-1}) and 1-chloropentane ($\Delta\nu$ = 190 cm^{-1}), respectively.[104] Rozenberg et al. found a correlation between the magnitude of the vibrational redshift of the ν(O–H) upon hydrogen bond formation and the length of the hydrogen bond.[144] We hypothesize that the pore environment where the μ_3–OH hydroxyls are located in UiO-66 prevents the formation of short, strong hydrogen bond interactions due to steric repulsion from the pore walls.

For intermolecular hydrogen bonding in the gas phase, in solution, and at the gas-surface interface, the magnitude of the ν(O–H) redshift upon hydrogen-bond formation correlates with the strength of the hydrogen bond, where greater redshifts correspond to stronger hydrogen bonds.[145] However, Abelard et al. determined that the activation energy of desorption for diethyl sulfide (37.5 kJ/mol) was lower than the activation energy of desorption for 1-chloropentane (43.7 kJ/mol) despite the larger redshift of the ν(O–H) feature for diethyl sulfide ($\Delta\nu$ = 485 cm^{-1} vs. $\Delta\nu$ = 190 cm^{-1}).[104] Abelard et al. speculated that increased non-bonding interactions between the 1-chloropentane and silica surface resulted in a higher activation energy of desorption.[104] Due to the small pores of UiO-66, we hypothesized that adsorbed HD simulants would have increased dispersion interactions with the interior MOF surface than silica.

5.3.4 Diffusivity of HD Simulants through UiO-66

In Chapter 4, we hypothesized that the rate of 2-CEES diffusion through MOFs was affected by both the pore aperture size and the presence of hydrogen bonding sites. From Chapter 3, we speculated that increased dispersion interactions result in a higher activation energy of diffusion. An examination of the diffusion rates and energetics of the HD simulants diethyl sulfide, 1-chloropentane, and 1,5-dichloropentane through UiO-66 provide insite into how the hydrogen bond strength and dispersion interactions of the HD simulants affected their diffusivities.

5.3.4.1 Energetics of HD Simulant Diffusion through UiO-66

Isothermal diffusion studies of 1-chloropentane, diethyl sulfide, and 1,5-dichloropentane through UiO-66 were performed at several temperatures to evaluate the energetic contributions of each molecule (Figures 5.8-5.10). The Arrhenius fitting parameters for the activation energy of diffusion and the diffusion prefactor for each HD simulant studied are listed in Table 5.9.

Similar to the findings of Abelard et al., which studied the adsorption mechanism and desorption energetics of mustard simulants on amorphous silica,[104] the extent of charge transfer upon hydrogen bond formation did not correlate with the activation energies of diffusion. While the adsorption of diethyl sulfide within UiO-66 resulted in the largest redshift of the ν(O–H) mode at 3676 cm^{-1} (164 cm^{-1}), which suggested the formation of the strongest hydrogen bond with the Zr cluster, the activation energy of diffusion for diethyl sulfide through UiO-66 was the lowest of the simulants studied. The redshifts observed for 2-CEES, 1,5-dichloropentane, and 1-chloropentane were quite similar, but their resulting activation energies of diffusion varied by 6 kJ/mol. This finding suggested that in addition to hydrogen bond strength, dispersion forces between the pore walls of UiO-66 and the adsorbed HD simulants affect the energetics of diffusion.

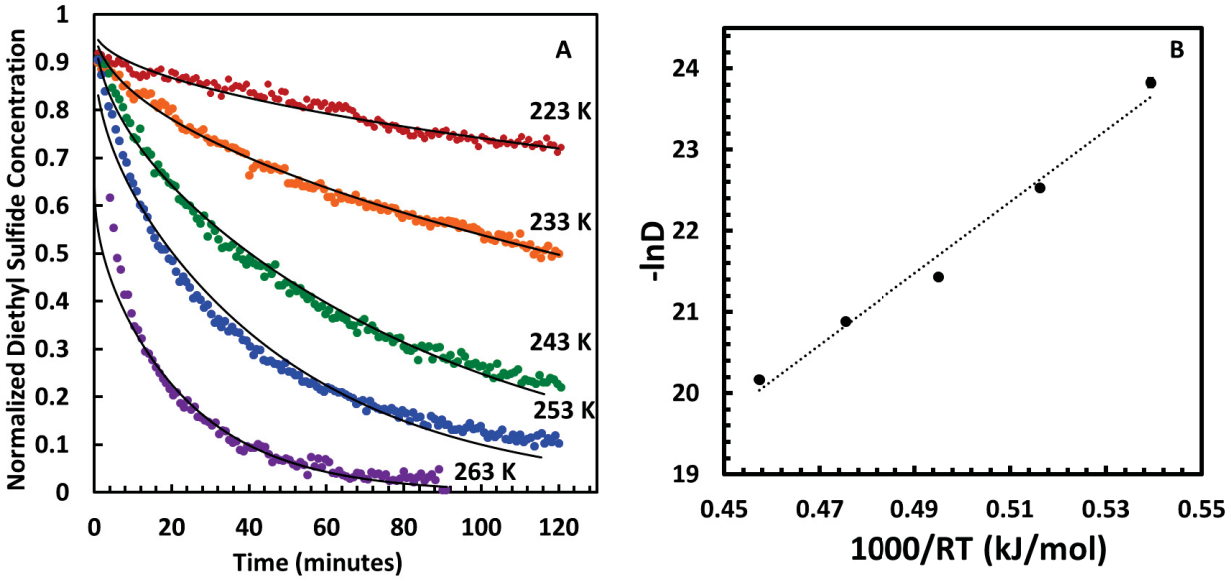

Figure 5.8 Diffusivities of diethyl sulfide at varying temperatures. **A** shows the decrease in adsorbed diethyl sulfide over time at each temperature (colored dots indicate experimental data while black lines indicate the Fickian diffusion fit). **B** shows the Arrhenius plot for diethyl sulfide diffusion through UiO-66.

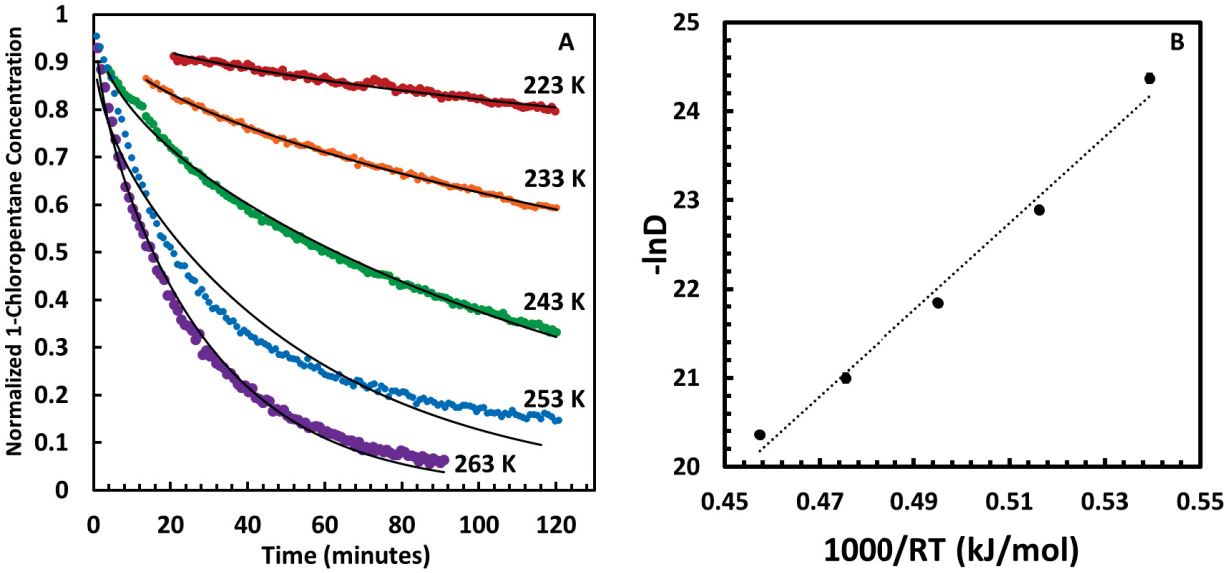

Figure 5.9 Diffusivities of 1-chloropentane at varying temperatures. **A** shows the decrease in adsorbed 1-chloropentane over time at each temperature (colored dots indicate experimental data while black lines indicate the Fickian diffusion fit). **B** shows the Arrhenius plot for 1-chloropentane diffusion through UiO-66.

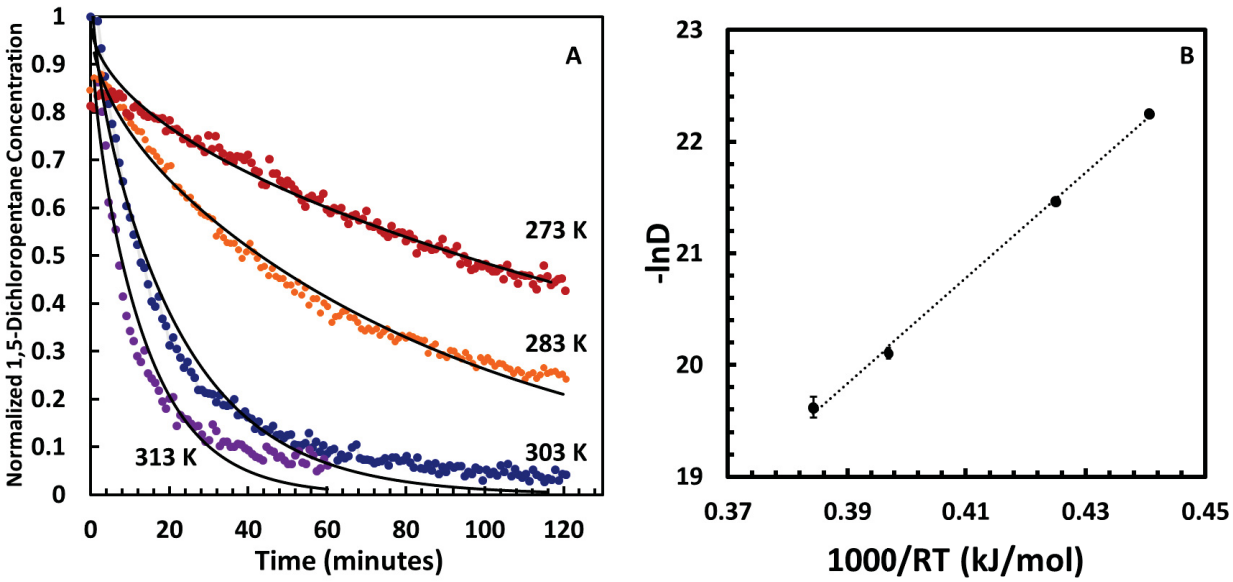

Figure 5.10 Diffusivities of 1,5-dichloropentane at varying temperatures. A shows the decrease in adsorbed 1,5-dichloropentane over time at each temperature (colored dots indicate experimental data while black lines indicate the Fickian diffusion fit). **B** shows the Arrhenius plot for 1,5-dichloropentane diffusion through UiO-66

Table 5.9 Arrhenius fitting parameters for the diffusion of HD simulants through UiO-66 and the extent of IR redshift.

Simulant	Temp Range (K)	Δν (cm^{-1})	Ea (kJ/mol)	D_0 (cm^2 s^{-1})
1-Chloropentane	223-263	118	48.7 ± 3.2	7.97
Diethyl sulfide	223-263	165	44.0 ± 3.2	1.09
2-CEES	253-293	107	53.0 ± 1.9	11.5
1,5-Dichloropentane	283-313	108	47.2 ± 1.3	0.236

Using *n*-pentane as the base structure, we can begin to create a structure-function relationship that examines how the presence of different functional groups on the HD simulants affects their diffusion energetics through UiO-66 based on hydrogen bond strength and dispersion forces. From Chapter 3, the activation energy of *n*-pentane diffusion through UiO-66 was 36.5 ± 2.4 kJ/mol. The introduction of an electronegative atom to the *n*-pentane base increased the activation energy of diffusion by 7.5-12.2 kJ/mol. In addition to forming stronger hydrogen bonds, as evidenced by the larger redshift of the ν(O-H) group on the zirconium cluster, the heavier

1-chloropentane and diethyl sulfide molecules exhibited increased dispersion interactions with the pore walls of UiO-66.

In the case of 2-CEES, the presence of two electron-rich atoms further increased the activation energy of diffusion by increasing the dispersion forces between the walls of the MOF pore and the adsorbate. The activation energy for 2-CEES is 4.3 kJ/mol and 9 kJ/mol higher than 1-chloropentane and diethyl sulfide, respectively.

Finally, to more accurately simulate the size of sulfur mustard, the diffusion of 1,5-dichloropentane through UiO-66 was studied. Surprisingly, while 1,5-dichloropentane diffused the slowest of all molecules, the activation energy of diffusion for 1,5-dichloropentane was determined to be 47.2 ± 1.3 kJ/mol, lower than 2-CEES and within one standard deviation of the activation energy of 1-chloropentane. We hypothesized that 1,5-dichloropentane interacts with the pore apertures of UiO-66 in a similar manner as 1-chloropentane, which may explain the similarity in diffusion energetics. Based on this theory, we would expect the activation energy of diffusion for HD through UiO-66 to be similar to 2-CEES, though HD will likely diffuse more slowly.

5.4 Summary

The adsorption and diffusion of a series of HD simulants through several UiO-66 samples were studied with infrared spectroscopy. All HD simulants adsorbed through the formation of hydrogen bonds with the free hydroxyl on the Zr nodes of the MOF. While changes in the UiO-66 structure resulted in differences in the kinetics of diffusion, the measured activation energies showed good agreement. Furthermore, from the systematic study of HD simulant diffusion through a UiO-66 sample with virtually no defects, we were able to begin to understand the effect of dispersion interactions and hydrogen bond strengths that will govern the adsorption and transport

of HD through UiO-66. Future work that investigates how changes to crystal size affect the diffusivity of adsorbates through MOFs may provide further insight into the effects that intercrystalline and intracrystalline diffusion play in the overall diffusion mechanism.

Chapter 6. TPD of 2-CEES from Zr-MOFs and the Creation of a Stochastic Model to Simulate TPD Data

6.1 Introduction

Temperature programmed desorption (TPD) is an important surface science technique that provides information about the interaction strength of gas molecules adsorbed at various binding sites on a catalyst surface. TPD can be employed as to determine the Brønsted and Lewis acidity of surfaces by studying the adsorption of probe molecules like carbon monoxide, ammonia, and pyridine.[207-209] More importantly, the quantitative analysis of the TPD spectra provides information about both the desorption energy and the kinetic prefactor for desorption, which is critical for understanding gas-phase heterogeneous catalysts. The kinetic rate equation for desorption follows an Arrhenius-type behavior (eq. 6.1), where $\boldsymbol{\theta}$ is the relative concentration of adsorbed species on the surface, $\boldsymbol{n}$ is the desorption rate order, $\boldsymbol{k_b}$ represents the Boltzmann constant, $\boldsymbol{T}$ represents the surface temperature, $\boldsymbol{E_{des}}$ is the activation energy of desorption, $\boldsymbol{\nu_{des}}$ is the preexponential factor.

$$\mathbf{r_{des} = \theta^{n} \nu_{des} e^{\left(\frac{-E_{des}}{k_b T}\right)}} \qquad \textbf{(6.1)}$$

6.1.1 Transition state theory

From transition state theory (TST), the rate constant for a first-order desorption process (k_{des}) can be described by eq. 6.2:[210]

$$\mathbf{k_{des} = \frac{k_b T}{h} \frac{q^0_{TS}}{q^0_i} e^{\left(\frac{-\Delta E^0_{TS}}{k_b T}\right)}} \qquad \textbf{(6.2)}$$

Where $\boldsymbol{h}$ represents Planck's constant, $\boldsymbol{q_{TS}^0}$ represents the partition function for the transition state, $\boldsymbol{q_i^0}$ is the partition function for the adsorbate, and $\boldsymbol{\Delta E_{TS}^0}$ is the energy change for the transition state. The kinetic prefactor for desorption is therefore described as:

$$\boldsymbol{\nu_{des} = \frac{k_b T}{h} \frac{q_{TS}^0}{q_i^0} e^{\frac{\Delta S_{TS}^\circ}{k_b T}}} \quad \textbf{(6.3)}$$

Where $\boldsymbol{\Delta S_{TS}^\circ}$ is the change in entropy change for the transition state. The $\boldsymbol{\frac{k_b T}{h}}$ term of eq. 6.3 is often used to approximate the desorption prefactor to of 1×10^{13} s^{-1} for desorption between 250 K and 2000 K. While the desorption prefactor in a lot of TPD experiments is often assumed as 1×10^{13} s^{-1}, Tait et al. analyzed the TPD of linear alkane desorption from several metal and metal oxide surfaces using inversion analysis and found that the desorption prefactor increased with alkyl chain length.[106, 110] For alkane desorption from MgO(100), the desorption prefactors for methane and *n*-decane varied by six orders of magnitude.[110] Campbell et al. developed an equation (eq. 6.4) that provides an accurate estimate of desorption prefactors for the desorption of gas molecules from single crystal surfaces.[210]

$$\boldsymbol{\nu_{des} = \frac{k_b T}{h} \exp\{\frac{0.30 S_{gas}^0}{R} + 3.3 - (\frac{1}{3})\{18.6 + \ln\left[\left(\frac{m}{m_{ar}}\right)^{\frac{3}{2}} + \left(\frac{T}{298K}\right)^{\frac{5}{2}}\right]\}\}} \quad \textbf{(6.4)}$$

Where $\boldsymbol{S_{gas}^0}$ represents the standard molar entropy of the adsorbed species, $\boldsymbol{R}$ is the gas constant, $\boldsymbol{m}$ is the molar mass of the gas, and $\boldsymbol{m_{ar}}$ is the molar mass of argon.

The desorption energy and desorption prefactor provide insight into the surface residence time, or the time that an adsorbed molecule remains bound to a binding site at a given temperature. Surface residence time is important for understanding the overall rate kinetics for a catalytic process. The Sabatier principle states that in catalysis, gas molecules that adsorb either too strongly or too weakly at a catalyst surface negatively affect the reaction rate. Weakly bound adsorbates

may not reside at the active site long enough to undergo a reaction, while strongly adsorbed molecules can either slow the turnover frequency of reaction or poison an active site.

Developing an understanding of the mechanisms and strengths of CWA interactions within MOFs can allow for the design of MOF-based catalysts in which reactant gases adsorb long enough to react, but the subsequent reaction products do not poison the catalyst and inhibit product turnover. Unfortunately, the ability to extract kinetic and energetic information from the TPD of gas desorption from porous materials is complicated by the contributions of diffusion to the overall rate of desorption. Adsorbed molecules within the bulk of a MOF crystal must first diffuse through a series of pore apertures and channels before reaching the external crystal surface of the MOF, where they can desorb into the gas phase. Attractive interactions between pore walls and diffusing adsorbates can slow the diffusion process. If the diffusion of molecules through the pores of the MOF is the rate-limiting process for desorption, the measured desorption kinetics and energetics from TPD experiments will reflect the overall kinetics of the diffusion-desorption rate and not just the desorption process.

6.1.2 Analysis of TPD Spectra

Several methods exist for the quantitative interpretation of TPD spectra. The desorption rate for molecules desorbing from a surface is described by the Polanyi-Wigner equation (eq. 6.5).

$$\mathbf{R_d = -\frac{d\theta}{dt}(\theta, T) = \nu(\theta, T)\theta^n e^{-\frac{E_{des}(\theta)}{K_b T}}} \qquad \mathbf{(6.5)}$$

6.1.2.1 Redhead Analysis

One of the oldest methods of TPD analysis to determine desorption energies is Redhead analysis.[211] Redhead analysis evaluates the Polanyi-Wigner equation at the temperature of the

highest desorption rate (T_{max}), where the first derivative of the desorption rate is zero ($-\frac{d\theta^2}{dT^2} = 0$). For first-order desorption processes, the activation energy of desorption can be determined from eq. 6.6, where $\boldsymbol{\beta}$ is the heating rate (in K/s).

$$\mathbf{E_{des} = RT_{max}\left[\ln\left(\frac{\nu_{des} T_{max}}{\beta}\right) - 3.64\right]} \quad \textbf{(6.6)}$$

Redhead analysis typically assumes a constant desorption prefactor of 1×10^{13} s^{-1} and an activation energy of desorption that is independent of surface coverage and temperature. Redhead analysis can be used to determine the desorption prefactor by varying the heating rate and plotting the natural log of the desorption rate as a function of heating rate, but this requires the ability to change the heating rate by at least two orders of magnitude.

6.1.2.2 Leading Edge Analysis

The Habenschaden-Küppers analysis method, more commonly known as leading edge analysis, evaluates a linearized form of the Polanyi-Wigner equation (eq. 6.7).[212] For small coverage changes (< 10%) at the leading edge of the TPD spectrum, coverage is assumed to be constant. The slope and y-intercept of the best-fit line of the Arrhenius plot of eq. 6.7 can be used to determine the activation energy of desorption and the desorption prefactor, respectively. Leading edge analysis provides information about both the energy of desorption and desorption prefactor at discrete initial coverages.

$$\mathbf{\ln(r_{des}) = \ln(\nu_{des}\,\theta^n) - \frac{E_{des}}{RT}} \quad \textbf{(6.7)}$$

6.1.2.3 Inversion Analysis

Inversion analysis, described in detail in Chapter 2, requires a series of TPD spectra with varying initial surface coverages. The desorption rate data from the experimental TPD curve with

the highest initial coverage and a guess desorption prefactor are used to solve a rearranged version of the Polanyi-Wigner equation (eq. 6.8) for the activation energy of desorption at every coverage. The calculated activation energy of desorption at each coverage is then used to generate a series of simulated TPD spectra to replicate the experimental data at lower initial coverages. The guess pre-exponential factor is then changed to find the minimum error between the simulated TPD spectra and simulated spectra at each initial coverage.

$$\mathbf{E_{des}(\theta) = -K_b T \cdot \ln\left(-\frac{d\theta/dt(\theta, T)}{\nu(\theta, T)\theta^n}\right)} \quad \textbf{(6.8)}$$

Inversion analysis assumes that desorption prefactor is independent of coverage and temperature and requires at least three TPD spectra of varied initial coverage. The reported activation energy of desorption for inversion analysis is often the activation energy of desorption at zero coverage, which represents the energy required for a single gas molecule to desorb from the surface. Inversion analysis has been previously utilized to experimentally determine the desorption prefactor for the desorption of gas molecules from porous surfaces.[107-108]

In this chapter, we performed a series of TPD experiments for the desorption of 2-CEES from UiO-66, UiO-67, and NU-1000 and analyzed the data using Redhead analysis, leading edge analysis, and inversion analysis to determine the activation energies of desorption and desorption prefactors. A stochastic model of the desorption of adsorbates from MOFs was developed to try and model the TPD spectra after the experimental results suggested that diffusion likely acts as the rate limiting step for the majority of the TPD experiments.

6.2 Experimental

6.2.1 MOFs Studied

The MOFs used in the TPD experiments have been described in detail in previous chapters. The UiO-66 used was the UiO-66 sample used to study the adsorption of *n*-butane within UiO-66 in Chapter 3, while the UiO-67 and NU-1000 samples were the samples analyzed in Chapter 4.

6.2.2 Vapor Dosing

2-CEES was dosed onto each MOF sample at 176 K through the capillary array doser described in Chapter 2. The flux of 2-CEES was kept consistent throughout the dosing process between TPD experiments for each MOF. The adsorption of 2-CEES was monitored via IR spectroscopy to ensure that all hydrogen-bonding sites were occupied at the end of dosing. After dosing, the MOF samples were heated at 0.2 K/ to drive off adsorbed 2-CEES to vary the initial surface coverage. Once the sample reached the desired temperature, they were immediately cooled back to 176 K and held there for at least one hour to let the chamber pressure equilibrate.

6.2.3 TPD Experiments

TPD experiments were performed following the methods described in Chapter 2. TPD experiments were conducted from 176 K to 450 K at a heating rate of 0.2 K/s, controlled by a Honeywell PID and custom power supply. The line-of-sight quadrupole mass spectrometer was tuned to detect the most abundant ion fragments of 2-CEES, which were m/z's 27, 47, and 75. The sample was kept at 450 K for one hour after the TPD experiment while the liquid nitrogen reservoir was purged with dry air.

6.3 Results and Discussion

6.3.1 TPD of 2-CEES through Zr-MOFs

For the TPD of 2-CEES from UiO-66 (Figure 6.1), two major curves were present: a large, exponentially shaped curve with a T_{max} of 229 K, and a much smaller, higher temperature curve with T_{max} = 335 K. The first feature can be described as a zeroth order desorption feature, where the desorption rate increases until there are no more adsorbed molecules to desorb. Zeroth-order desorption is often attributed to the sublimation of adsorbed molecules where the adsorbate-adsorbate interactions are stronger than the adsorbate-surface interactions. Zeroth-order desorption is commonly referred to as multilayer desorption. The second curve in the TPD spectra was attributed to the first-order desorption of 2-CEES from UiO-66 and corresponded to the decrease in 2-CEES molecules adsorbed through hydrogen-bonding at bridging hydroxyls within UiO-66, as determined by IR spectroscopy. T_{max} = 335 K for the highest initial coverage, but the T_{max} increased to 365 K as the initial coverage decreased, which suggested either a distribution of adsorption sites with various binding strengths or a coverage dependence on the desorption energy. 2-CEES fully desorbed from the UiO-66 sample by 445 K, which was confirmed by IR spectra recorded after the TPD experiment.

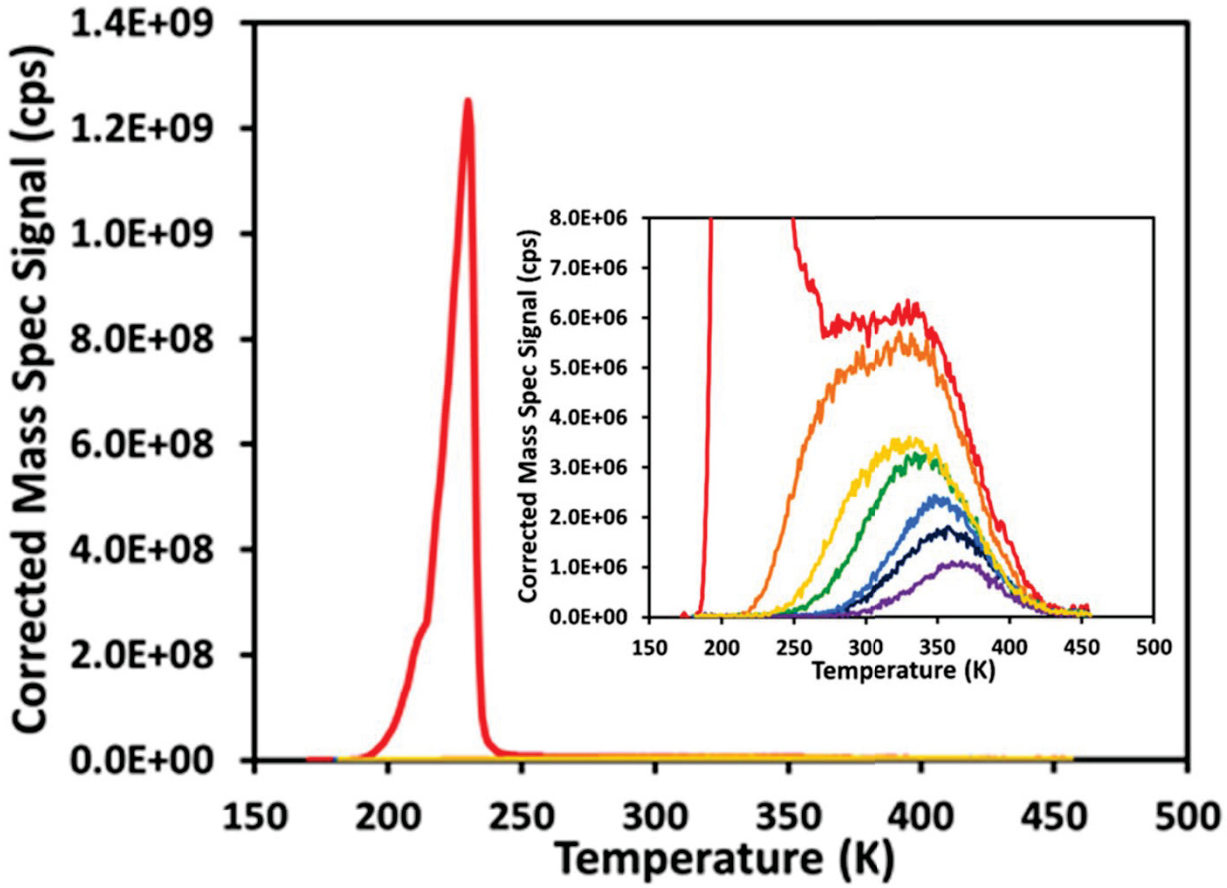

Figure 6.1 TPD spectra of 2-CEES desorption from UiO-66. Inset: Zoomed in TPD spectra from 150-450 K. Each colored curve represents a different initial coverage. Initial coverages were θ = 51.33 ML (red), θ = 1.9 ML (orange), θ = 1.0 ML (yellow), θ = 0.86 ML (green), θ = 0.54 ML (light blue), θ = 0.38 ML (dark blue), and θ = 0.22 ML (purple).

The TPD spectra for 2-CEES desorption from UiO-67 (Figure 6.2) strongly resembled the TPD spectra from UiO-66. The presence of two features with peaks at 285 K and 305 K were attributed to multilayer desorption from the mesh sample in a spot not directly aligned with the pinhole apertures between the main chamber and the mass spectrometer (Chapter 2). The first multilayer curve has a peak at 224 K. For the first-order desorption feature, the T_{max} increased from 328 K to 344 K with decreasing initial surface coverage, a smaller shift than observed in the UiO-66 TPD spectra. The elongated trailing edge of the first-order desorption curve suggests the

presence of defect sites with stronger surface-adsorbate interactions. 2-CEES fully desorbs from UiO-67 by 428 K, approximately 15 K lower than in UiO-66.

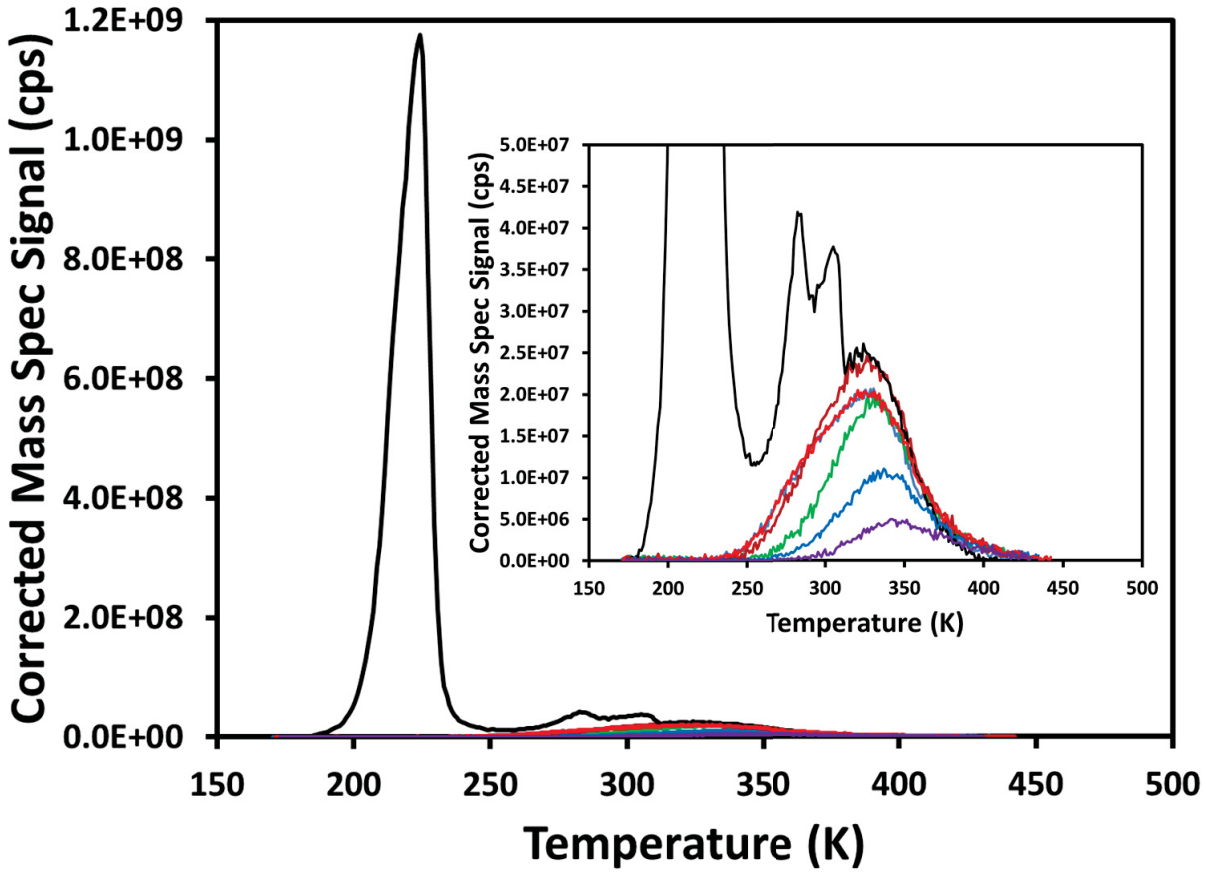

Figure 6.2 TPD spectra of 2-CEES desorption from UiO-67. Inset: Zoomed in TPD spectra from 150-450 K. Each colored curve represents a different initial coverage. Initial coverages were θ = 12.1 ML (black), θ = 1.00 ML (orange), θ = 0.94 ML (red), θ = 0.71 ML (green), θ = 0.41 ML (blue), and θ = 0.19 ML (purple).

The TPD spectra for 2-CEES desorption from NU-1000 had two features (Figure 6.3), a multilayer desorption feature at 226 K, and a first-order desorption curve with T_{max} = 311 K for the highest initial coverage of 2-CEES within NU-1000. Unlike the previous TPD spectra for UiO-66 and UiO-67, TPD curves with lower initial 2-CEES coverages resulted in a decrease in T_{max} from 311 K to 260 K. The decrease in T_{max} with surface coverage suggests that attractive forces between nearby adsorbed 2-CEES molecules result in an increased desorption energy.

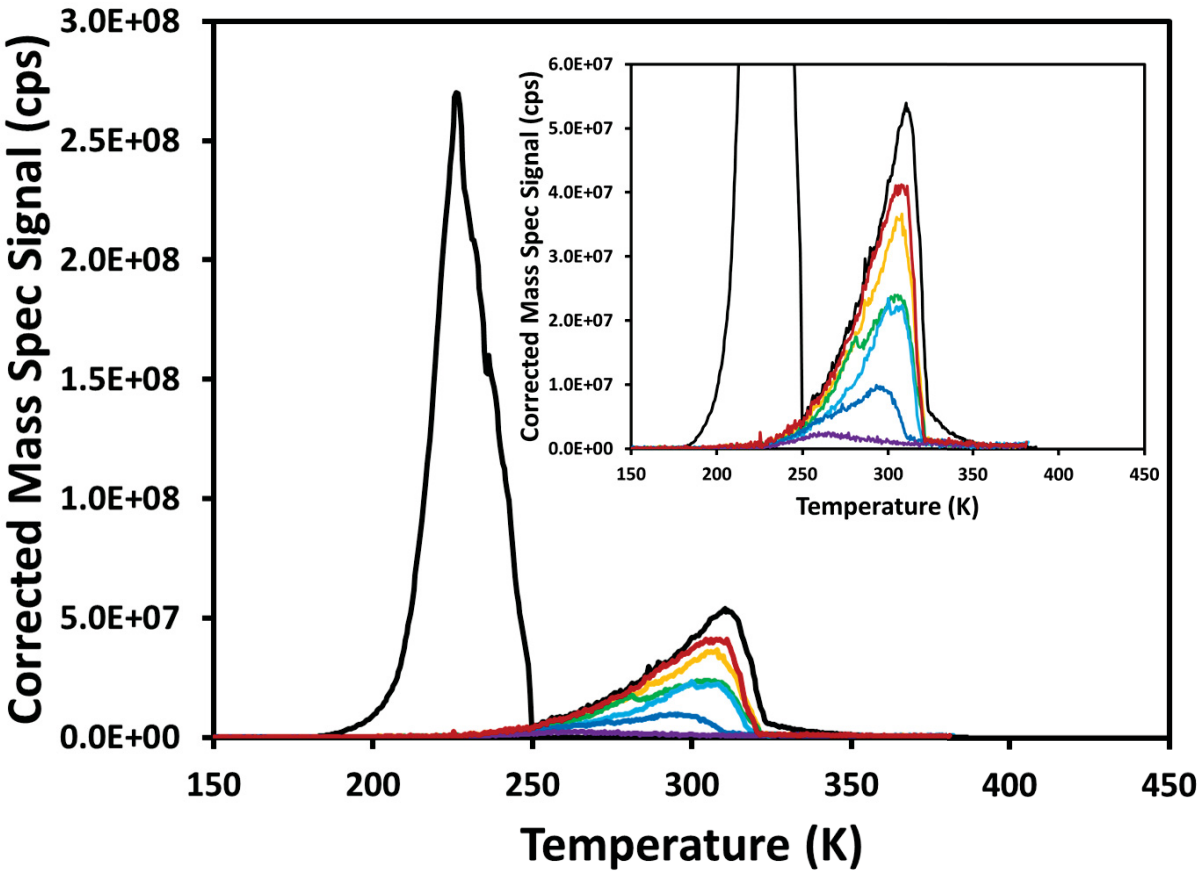

Figure 6.3 TPD spectra of 2-CEES desorption from NU-1000. Inset: Zoomed in TPD spectra from 150-350 K. Each colored curve represents a different initial coverage. Initial coverages were θ = 4.0 ML (black), θ = 0.82 ML (red), θ = 0.70 ML (yellow), θ = 0.54 ML (green), θ = 0.44 ML (light blue), θ = 0.23 ML (dark blue), and θ = 0.07 ML (purple).

We used eq. 6.3 to predict the desorption prefactor for the desorption of 2-CEES from the exterior crystal surface of each MOF using the T_{max} values for temperature and the molar entropy of 1-chloropentane (cannot find molar entropy for 2-chloroethyl ethyl sulfide). From Table 6.1, the predicted desorption prefactors were all above 10^{14} s^{-1}.

Table 6.4 Estimated desorption prefactors from experimental T_{max} values.

MOF	T_{max} (K)	ν_{des} (s^{-1})
UiO-66	335	$10^{14.7}$
UiO-67	328	$10^{14.7}$
NU-1000	309	$10^{14.6}$

6.3.1.1 Analysis of Multilayer Desorption Feature

The first feature in each TPD curve was attributed to 2-CEES multilayers desorbing from the external crystal surfaces of the MOFs. The exponential growth of the desorption rate with temperature is consistent with zeroth-order desorption (n = 0), and the desorption rate equation becomes:

$$\mathbf{r_{des}} = -\frac{\mathbf{d\theta}}{\mathbf{dt}} = \boldsymbol{\nu} \mathbf{e}^{-\frac{\mathbf{E_{des}}}{\mathbf{RT}}} \tag{6.9}$$

Multilayer desorption can also be described as the sublimation of 2-CEES. The sublimation energy for 2-CEES was determined by leading edge analysis.[212] This method of TPD analysis evaluates a linearized form of the Polanyi-Wigner equation (eq. 6.10):

$$\mathbf{ln}(\mathbf{r_{des}}) = \mathbf{ln}(\boldsymbol{\nu}) - \frac{\mathbf{E_{des}}}{\mathbf{RT}} \tag{6.10}$$

Plotting $\mathbf{ln}(\boldsymbol{r_{des}})$ as a function of $\frac{\mathbf{1}}{\boldsymbol{RT}}$ allowed us to determine both the multilayer desorption energy and desorption prefactor from the slope and the y-intercept of the best-fit line, respectively. Figure 6.4 shows an example of the leading edge analysis for the 2-CEES multilayer desorption from UiO-66. The calculated average multilayer desorption energy between all Zr-MOFs was found to be 63.4 ± 2.5 kJ/mol with a desorption prefactor of $10^{14.3}$ s^{-1}. Stephenson and Malanowski reported an enthalpy of vaporization of 44.4 kJ/mol at 308 K.[213]

Currently no experimental data exists for the sublimation energy for 2-CEES, but since the enthalpy of sublimation is a combination of the enthalpy of fusion and the enthalpy of vaporization, it was possible to estimate those values using the Joback method. The Joback method relies on group contributions in order to predict thermophysical properties of chemicals.[214] Using the Joback

method, the calculated the enthalpy of sublimation for 2-CEES at 225 K was 59.8 kJ/mol, in close agreement with our measured multilayer desorption energy.

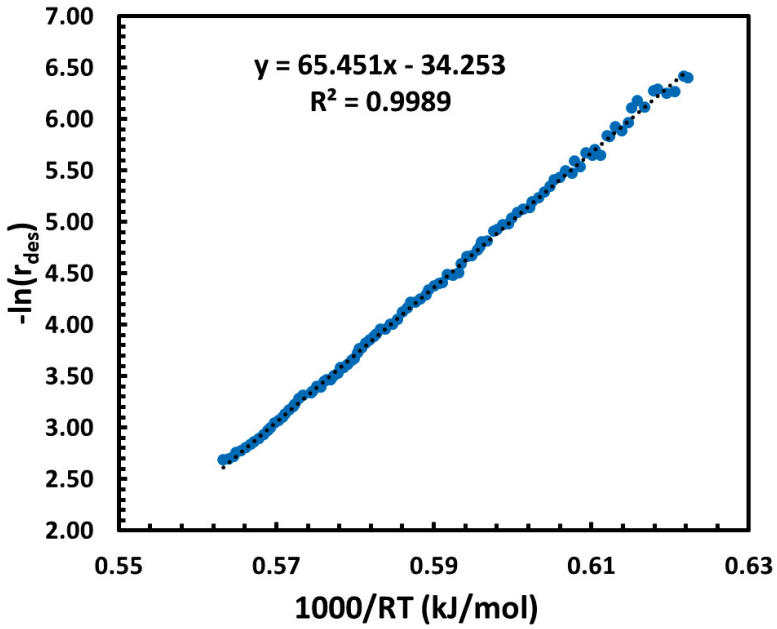

Figure 6.4 Arrhenius plot of leading-edge analysis for the multilayer desorption of 2-CEES from UiO-67.The blue dots represent the experimental data and the black dots represent the best-fit line.

6.3.1.2 Redhead Analysis Results

The activation energies of desorption for 2-CEES from UiO-66, UiO-67, and NU-1000 were first determined by analyzing the TPD data with Redhead analysis. We assumed a desorption prefactor of 1.0×10^{13} s^{-1} due to our inability to perform TPD experiments at a wide range of heating rates. The activation energies of desorption for 2-CEES from each MOF were determined by plugging the experimentally determined T_{max} values and the heating rate (0.2 K/s) into eq. 6.6. The activation energies of desorption for 2-CEES from UiO-66, UiO-67, and NU-1000, determined by Redhead analysis, are listed in Table 6.2. 2-CEES desorption from UiO-66 yielded the highest desorption energy of 94.4 kJ/mol and NU-1000 was the lowest with 87.5 kJ/mol.

Table 6.2 Desorption energetics and desorption prefactors determined through Redhead analysis

MOF	E_{des} (kJ/mol)	ν (s^{-1})
UiO-66	94.4	1.0×10^{13}
UiO-67	92.4	1.0×10^{13}
NU-1000	87.5	1.0×10^{13}

6.3.1.3 Leading Edge Analysis Results

Leading edge analysis of the TPD data for 2-CEES desorption was performed by linearizing the experimental data for the first-order desorption feature and plotting the natural log of the desorption rate as a function of temperature. Data that corresponded to the decrease in 2-CEES coverage from 1 to 0.9 were analyzed to assume a constant coverage term in eq. 6.7. Activation energies of desorption and desorption prefactors were determined by the slope and intercept of the best-fit line (Figure 6.5). The activation energies for desorption determined by leading edge analysis (Table 6.3) were approximately 50 kJ/mol lower than the values determined by Redhead analysis, while the pre-exponential factors were 7-10 orders of magnitude lower.

Table 6.3 Desorption energies and desorption prefactors determined through leading edge analysis

MOF	E_{des} (kJ/mol)	ν (s^{-1})
UiO-66	43.2	1.9×10^{5}
UiO-67	46.6	1.0×10^{6}
NU-1000	32.1	2.8×10^{3}

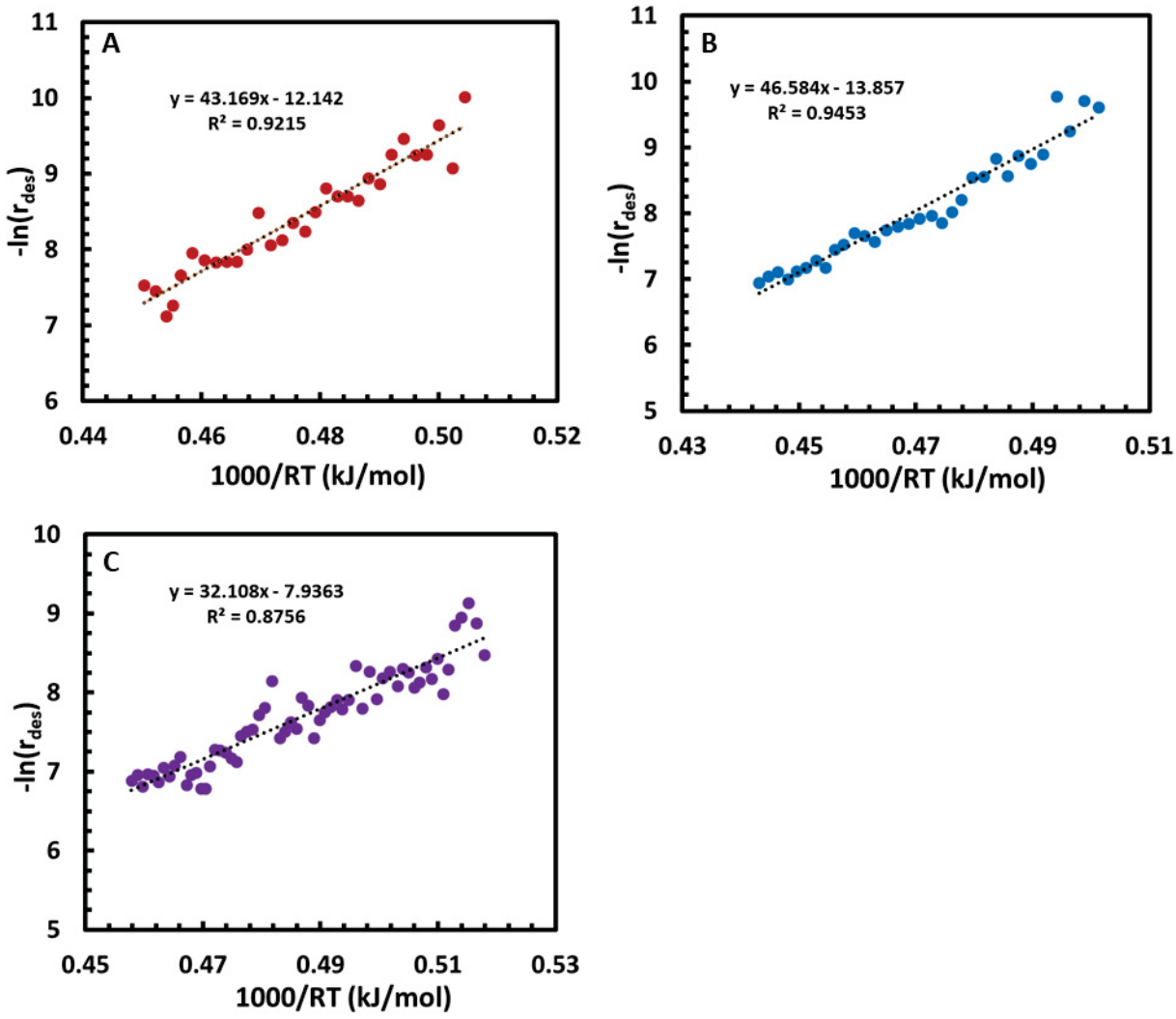

Figure 6.5 Leading edge TPD analysis data for 2-CEES desorption from UiO-66 (A), UiO-67 (B), and NU-1000 (C). The dotted black lines indicate the line of best-fit while the colored dots represent the experimental data.

6.3.1.4 Inversion Analysis Results

The first-order desorption kinetics for 2-CEES desorption from UiO-66, UiO-67, and NU-1000 were analyzed via inversion analysis. The determined desorption prefactors and desorption energies at zero coverage for 2-CEES desorption from UiO-66, UiO-67, and NU-1000 are listed in Table 6.4 and the inversion analysis data for each MOF are shown in Figures 6.6-6.8. For UiO-66, the determined E_{des} was 49.2 kJ/mol and $\nu = 5.0 \times 10^4$ s^{-1}. Compared to the values in Table 6.1, the desorption prefactors were as much as 11 orders of magnitude lower than predicted.

For 2-CEES desorption from NU-1000, the simulated TPD spectra (Figure 6.8) showed poor agreement with the experimental data, and unlike UiO-66 and UiO-67, the determined activation energy of desorption increased as coverage increased (6.8D).

Table 6.4 Desorption energetics and desorption prefactors determined through inversion analysis

MOF	$E_{des}(\theta = 0)$ (kJ/mol)	ν (s^{-1})
UiO-66	49.2	5.0×10^4
UiO-67	38.6	4.9×10^3
NU-1000	43.8	1.0×10^6

6.3.1.5 Comparison to Literature Values

For context of the desorption energies, Abelard et al. used inversion analysis to calculate E_{des} was 42.9 kJ/mol and $\nu = 5.0 \times 10^7$ s^{-1} for 2-CEES desorption from amorphous silica,[104] similar energetics to those determined for each Zr-MOF. The low desorption prefactor was attributed to the readsorption of gas-phase 2-CEES molecules as they traveled through the sample. While the energetics were similar, when comparing the TPD spectra, 2-CEES fully desorbed from silica at 275 K (T_{max} = 225 K), 85 K lower than NU-1000. Thompson et al. also performed TPD experiments for 2-CEES desorption from TiO_2(110) and calculated an E_{des} = 105 kJ/mol with a $\nu = 1.0 \times 10^{14}$ s^{-1}.[86] In the case of TiO_2, 2-CEES desorbed from 300-400 K, which was same temperature range that the majority of 2-CEES desorbed from UiO-66 and UiO-67.

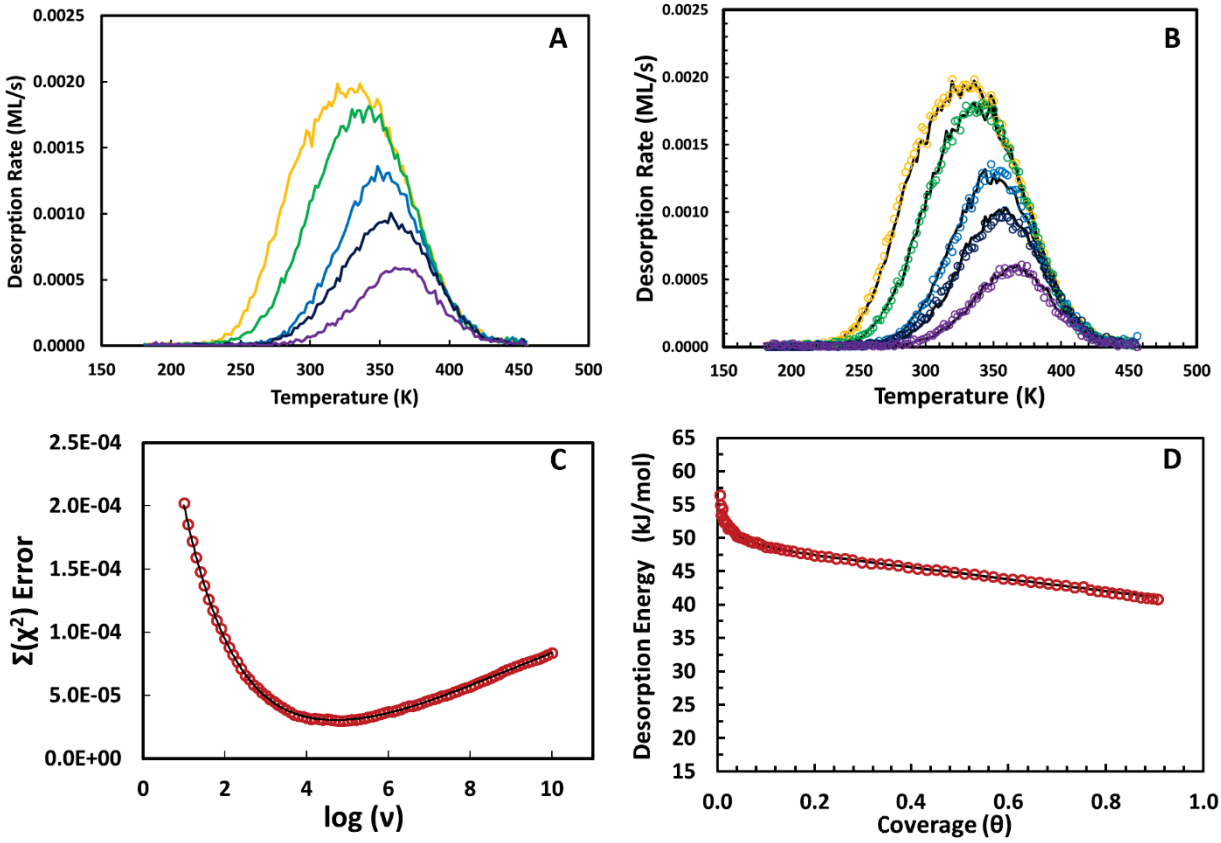

Figure 6.6 Inversion analysis data for 2-CEES desorption from UiO-66. A) Plot of experimental desorption rate vs. temperature B) Comparison of experimental desorption rate data (colored circles) to simulated TPD spectra (black lines). Plot of sum of squared residuals (SSR) vs log(v) to determine prefactor. D) Plot of E_{des} vs. coverage.

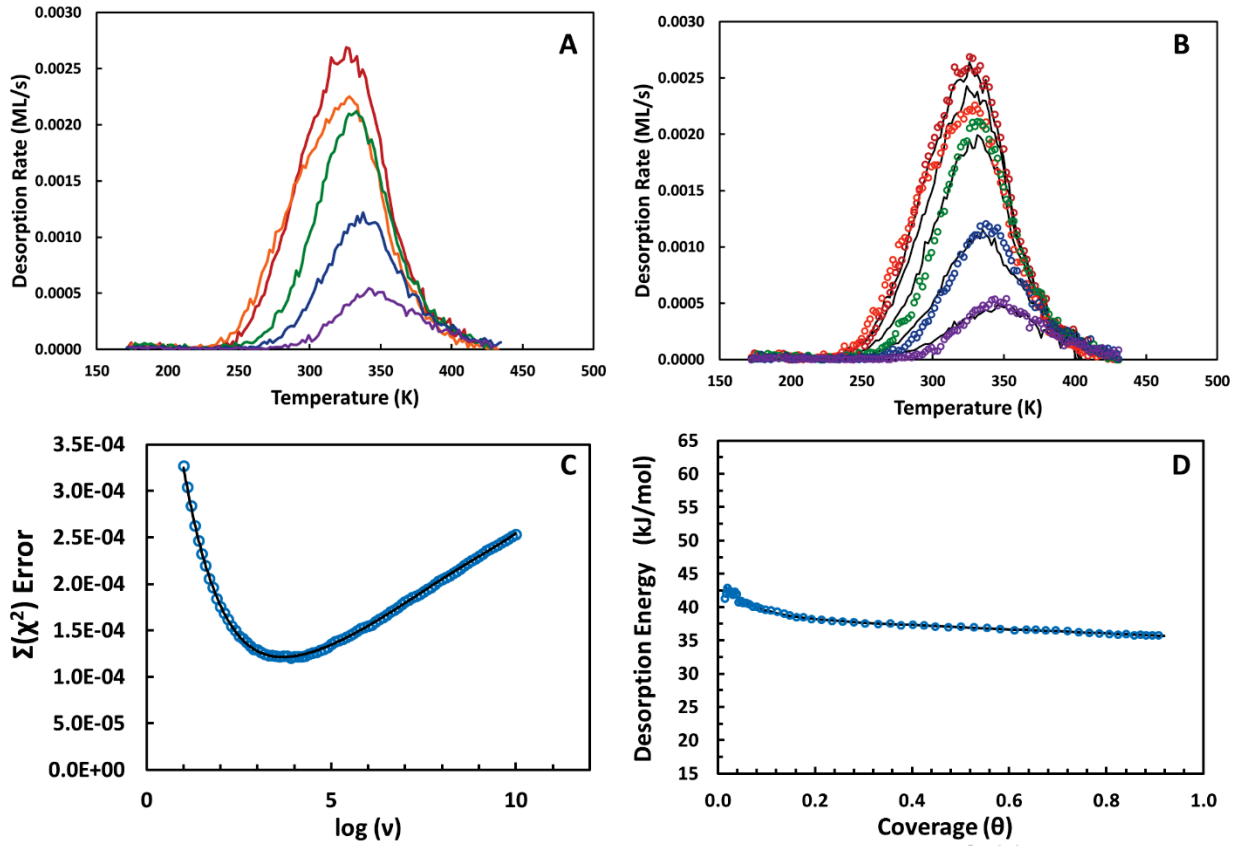

Figure 6.7 Inversion analysis data for 2-CEES desorption from UiO-67. A) Plot of experimental desorption rate vs. temperature B) Comparison of experimental desorption rate data (colored circles) to simulated TPD spectra (black lines). Plot of sum of squared residuals (SSR) vs log(v) to determine prefactor. D) Plot of E_{des} vs. coverage.

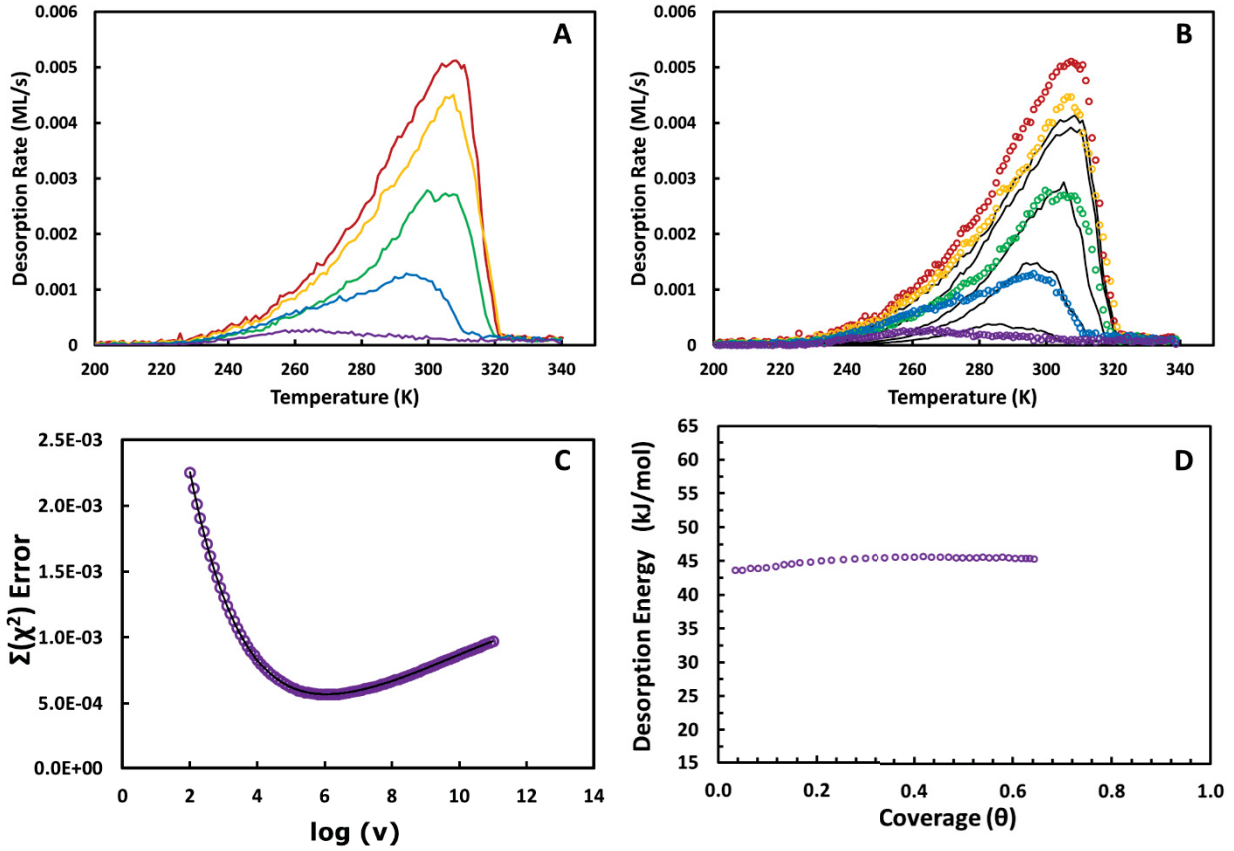

Figure 6.8 Figure 3 Inversion analysis data for 2-CEES desorption from NU-1000. A) Plot of experimental desorption rate vs. temperature B) Comparison of experimental desorption rate data (colored circles) to simulated TPD spectra (black lines). C) Plot of sum of squared residuals (SSR) vs log(v) to determine prefactor. D) Plot of E_{des} vs. coverage.

6.3.1.6 Effect of Diffusion on Desorption Kinetics

At approximately 225 K when 2-CEES adsorbed within UiO-66 begins to desorb, the calculated diffusion coefficient, based on the Arrhenius equation for 2-CEES diffusion through UiO-66, would be 2.12×10^{-12} cm^2 s^{-1}. At that diffusivity, using the mean squared displacement equation (eq. 6.11) where D is the diffusion coefficient and $|x(t) - x_0|$ is the displacement distance, it would take the average adsorbed 2-CEES molecule at the center of the 50 μm thick sample 1.47×10^6 seconds (over 400 hours) to desorb diffuse out of the MOF sample and desorb into the gas phase. In order for the average molecule to diffuse fully out from the center of the sample and get detected in the mass spectrometer in one second, the diffusivity of the 2-CEES

molecule must exceed 3.13×10^{-6} cm^2, which occurs at 452 K. The slow diffusivity of 2-CEES throughout the TPD experiment suggests that the rate-limiting step for the desorption of 2-CEES from UiO-66 is the diffusion through the pores of the MOF throughout the entire desorption process. In the case of NU-1000, the MOF that 2-CEES diffused the fastest through, diffusion likely acts as the rate-limiting step for the desorption process until 359 K, after 2-CEES has already fully desorbed from the sample. Therefore, in the case of 2-CEES desorption from the Zr-MOFs studied, our TPD experiments were unable to directly measure the energetics and rate kinetics of the desorption of 2-CEES from the exterior surface of the UiO-66 crystals.

$$\mathbf{2Dt} = \left[(\mathbf{x(t)} - \mathbf{x_0})^2\right] \tag{6.11}$$

6.3.2 Development of a TPD Model

From the results of our TPD data, the slow kinetics of diffusion throughout the TPD experiment prevent us from isolating and determining the energetics and kinetics of surface desorption process. We attempted to develop a model of the desorption process that incorporated the diffusion energetics determined in Chapter 4 to attempt to simulate the experimental TPD data. Various approaches have been previously employed in order to extract desorption kinetic and energetic information from TPD experiments of porous catalysts, including analytical solutions[215-217] and kinetic models.[218] In particular, F.A. Houle and W.D. Hinsberg extensively reported on the use of stochastic simulations in order to determine desorption kinetics from complex TPD spectra.[219] Stochastic methods provide a discrete method to model kinetic data and are based a series of reaction rate equations to create an overall reaction mechanism. Houle and Hinsberg developed Kinetiscope, a stochastic simulation software program that can be used to model a wide variety of processes, including multi-phase, heterogeneous chemical reactions, the transport of gases through polymer membranes, oxidation chemistry, and TPD experiments.[220-223]

The goal of our model was to replicate the experimental set-up in our TPD experiments in order to resolve the contributions of both desorption and diffusion processes to the overall desorption rate. The dimensions of the model are based on a single void-space within our tungsten mesh grid with dimensions 200 µm wide × 200 µm tall × 50 µm thick. Assuming that no void spaces exist within our pressed mesh sample, we assumed in our model that the MOF sample was effectively a single crystal. In Kinetiscope, we created a 3D model made up of 52 total compartments (Figure 6.9). Within compartment *n*, unoccupied adsorption sites are designated as "A_n", while occupied sites are designated "A-CEES".

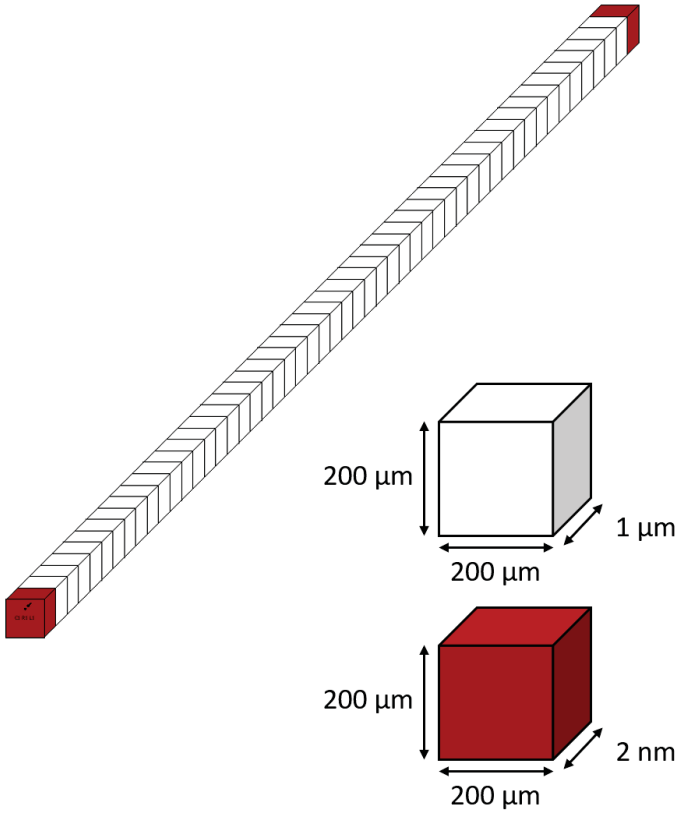

Figure 6.9 Diagram of Kinetiscope model. Red compartments represent the external crystal surface of the MOFs while the white compartments represent the bulk of the MOF sample.

This model is based on the assumption that intracrystalline diffusion is the only diffusion process that occurs; the pressed mesh sample effectively represents a single MOF crystal. The desorption of adsorbed 2-CEES molecules into the gas phase therefore can only proceed at the outermost compartments of the model. 2-CEES can either desorb as a multilayer or as a monolayer, and the rates of each desorption process are independent of one other. We assume that once a molecule desorbs into the gas-phase, it is immediately pumped away so that no re-adsorption occurs. Gas-phase 2-CEES molecules are "pumped" out of the system in order to replicate the UHV environment of the sample and to better mimic the TPD data. The rate processes in the outermost compartments are:

$$\text{Multilayer-CEES} \rightarrow \text{CEES}_{(g)} \quad \textbf{(6.12)}$$
$$\text{Adsorbed-CEES} \rightarrow \text{CEES}_{(g)} + \text{A} \quad \textbf{(6.13)}$$
$$\text{CEES}_{(g)} \rightarrow \text{pumped} \quad \textbf{(6.14)}$$

6.3.2.1 Desorption Kinetics in Kinetiscope

The kinetics of multilayer desorption are modeled by the zeroth-order desorption rate equation:

$$\mathbf{r_{des,multi} = \nu_{multi} e^{-\frac{E_{des,multi}}{RT}}} \quad \textbf{(6.15)}$$

where ν_0 represents the zeroth order desorption prefactor (with units of molecules $(cm^3)^{-1}$ s^{-1}) and $E_{des,multi}$ represents the multilayer desorption energy (units of kJ mol^{-1}). The monolayer desorption of 2-CEES follows first-order desorption kinetics:

$$\mathbf{r_{des,mono} = \nu_{mono}[aCEES]e^{-\frac{E_{des,mono}}{RT}}} \quad \textbf{(6.16)}$$

Where ν_{mono} represents the monolayer desorption prefactor (units of s^{-1}), $[aCEES]$ represents the concentration of adsorbed 2-CEES, and $E_{des,mono}$ is the monolayer desorption energy (units of kJ

mol^{-1}). While the TPD experiments indicated that the desorption energy for 2-CEES within each MOF was coverage-dependent, we decided to start with a coverage-independent desorption energy for simplicity. Finally, the rate of 2-CEES pump-out was governed by a temperature-independent first order rate law:

$$\mathbf{r_{pump} = k_{pump}[gCEES]} \quad \textbf{(6.17)}$$

Where k represents the pumping rate constant and $[gCEES]$ represents the concentration of gas-phase 2-CEES. The rate constant was set to 200 s^{-1} to mimic the pumping speed of the turbomolecular pump on the mass spectrometer chamber.

6.3.2.2 Diffusion Kinetics in Kinetiscope

The diffusion of 2-CEES through the bulk of the MOF sample and into the outer compartments is governed by the transfer of adsorbed 2-CEES between compartments. Adsorbed 2-CEES molecules in a given compartment may transport into adjacent compartments assuming that available adsorption sites are present. As such, diffusion is considered bidirectional, but because desorption only occurs at the outermost compartments of the model, the diffusion of adsorbed 2-CEES molecules proceeds from areas of high concentration (the center of the sample) to areas of low concentration (the outer edges of the sample). Within a given compartment, available adsorption sites and adsorbed species are instantly mixed. For the transfer between compartment A and B (Figure 6.9), diffusion was governed by site-exchange between sample compartments, described by equation (6.18):

$$\mathbf{A_a\text{-}CEES + A_b \leftrightarrow A_b\text{-}CEES + A_a} \quad \textbf{(6.18)}$$

Where A_n represents available adsorption sites in compartment N and A_n-CEES reflects 2-CEES adsorbed in compartment N. Within each sample compartment

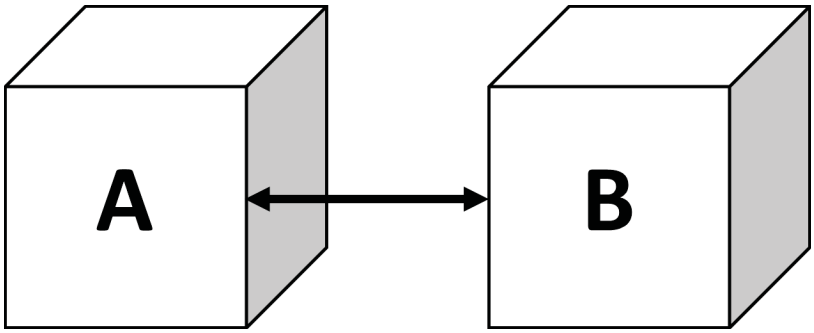

Figure 6.10 Sample compartments to illustrate the diffusion process modeled by Kinetiscope.

The kinetics of diffusion between each compartment were modeled by the rate equation:

$$\mathbf{rate} = \mathbf{D_0 e^{-\frac{E_{diff}}{RT}} \nabla a \cdot area} \tag{6.19}$$

Where D_0 represents the diffusion prefactor, E_{diff} is the activation energy of diffusion, ∇ is the gradient operator, a represents the amount of available adsorption sites within the adjacent compartment, and $area$ represents the area of the diffusion cross section at the interface of each compartment.

6.3.3 Modeling 2-CEES Diffusion through NU-1000

To validate the set-up of the Kinetiscope model prior to attempting to replicate TPD data of 2-CEES desorption from MOFs, we first modeled the isothermal diffusion of 2-CEES from NU-1000. The relative concentration of adsorbed 2-CEES within the sample at any given time was determined by adding up the amount of A-CEES species in each compartment and dividing that value by the total concentration of A-CEES at time = 0 s. The diffusion coefficient at each temperature was based on the best-fit parameters from the Arrhenius plot of 2-CEES diffusivity through NU-1000 mentioned in Chapter 4. We initially assumed no activation energy for the desorption process, meaning that any 2-CEES molecule that desorbed into the outermost sample compartments instantly desorbed into the gas-phase. The model parameters used for the isothermal

diffusion of 2-CEES through NU-1000 are listed in Table 6.5. The comparison of the model-determined isothermal diffusion of 2-CEES through NU-1000 (Figure 6.11) to the experimental data reported in Chapter 2 demonstrated reasonable agreement. The underestimation of diffusivity at 203 K and overestimation at 213 K were consistent with the deviation of the experimental data points from the Arrhenius best-fit line.

Table 6.5 Model parameters for Kinetiscope model of 2-CEES diffusion through NU-1000.

Parameter	Value
D_0	7.19 cm^2 s^{-1}
E_{diff}	43.7 kJ/mol
ν_{mono}	10^{13} s^{-1}
$E_{des,multi}$	0 kJ/mol

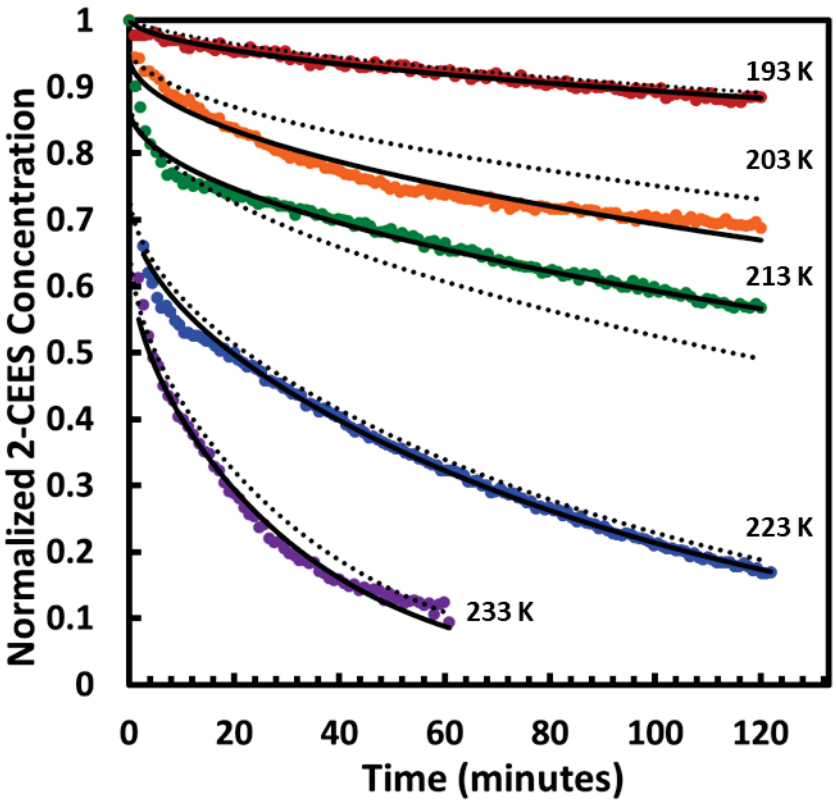

Figure 6.11 Isothermal diffusion experiment of 2-CEES through NU-1000. The experimental data is represented by colored dots while the modeled diffusivities are plotted as several dotted black lines.

6.3.4 Modeling 2-CEES TPD

6.3.4.1 Multilayer Desorption of 2-CEES

Our first TPD test of the Kinetiscope model evaluated the multilayer desorption feature at ~229 K, which was present in every sample studied. The kinetic parameters used for the model were based on the results of the leading-edge analysis for the multilayer feature (Table 6.6). In the first model attempt, no gas-phase CEES signal appeared in the model. This was due to the fact the multilayer desorption is a zeroth-order rate process in regards to the concentration of adsorbates. Because the rate equation in Kinetiscope has of molecules cm^{-3} s^{-1} and not monolayers s^{-1}, the multilayer rate constant needed to account for the concentration of adsorption sites within the model (10^{20} sites cm^{-3}) to convert the units of the prefactor to match the experimental data. The second model attempt (Figure 6.12) shows good agreement in the desorption peak temperature with the experimental data.

Table 6.6 Kinetiscope parameters for modeling the multilayer desorption of 2-CEES.

Attempt #	θ (ML)	ν_{multi}(molecules cm^{-3} s^{-1})	$E_{des,multi}$ (kJ/mol)
1	50	$10^{14.3}$	64.8
2	50	$10^{34.9}$	64.8

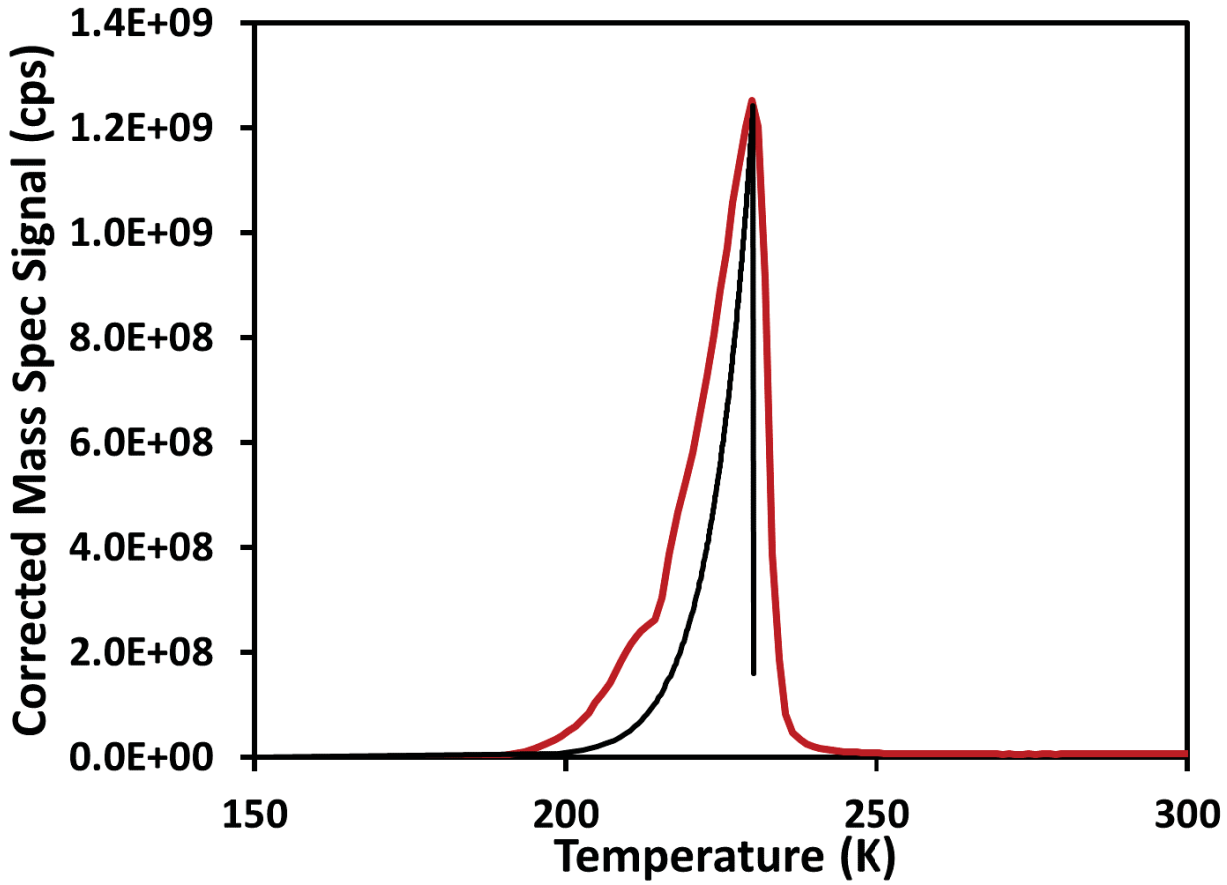

Figure 6.12 Comparison of experimental data (red line) to the Kinetiscope model (black line) for the multilayer desorption of 2-CEES from UiO-66.

6.3.4.2 TPD of 2-CEES from NU-1000

The first-order TPD data for 2-CEES from NU-1000 was simulated using the parameters listed in Table 6.6. For the first simulation, we assumed no activation energy of desorption. Initial coverages within each compartment were set by the ratio of the fraction of A-CEES to total A and uniform concentration through the sample was assumed. Simulated TPD spectra were run from 175 K to 400 K at a 0.2 K/s heating rate. The simulated TPD spectra for 2-CEES from NU-1000 with no desorption energy had a similar shape to the experimental spectra (Figure 6.13), but the T_{max} for the simulated spectra was approximately 30 K lower. While the T_{max} for the experimental

TPD data decreased with decreasing coverage, the T_{max} of the simulated spectra did with initial coverage. Finally, the experimental TPD signal decays more rapidly after the T_{max}.

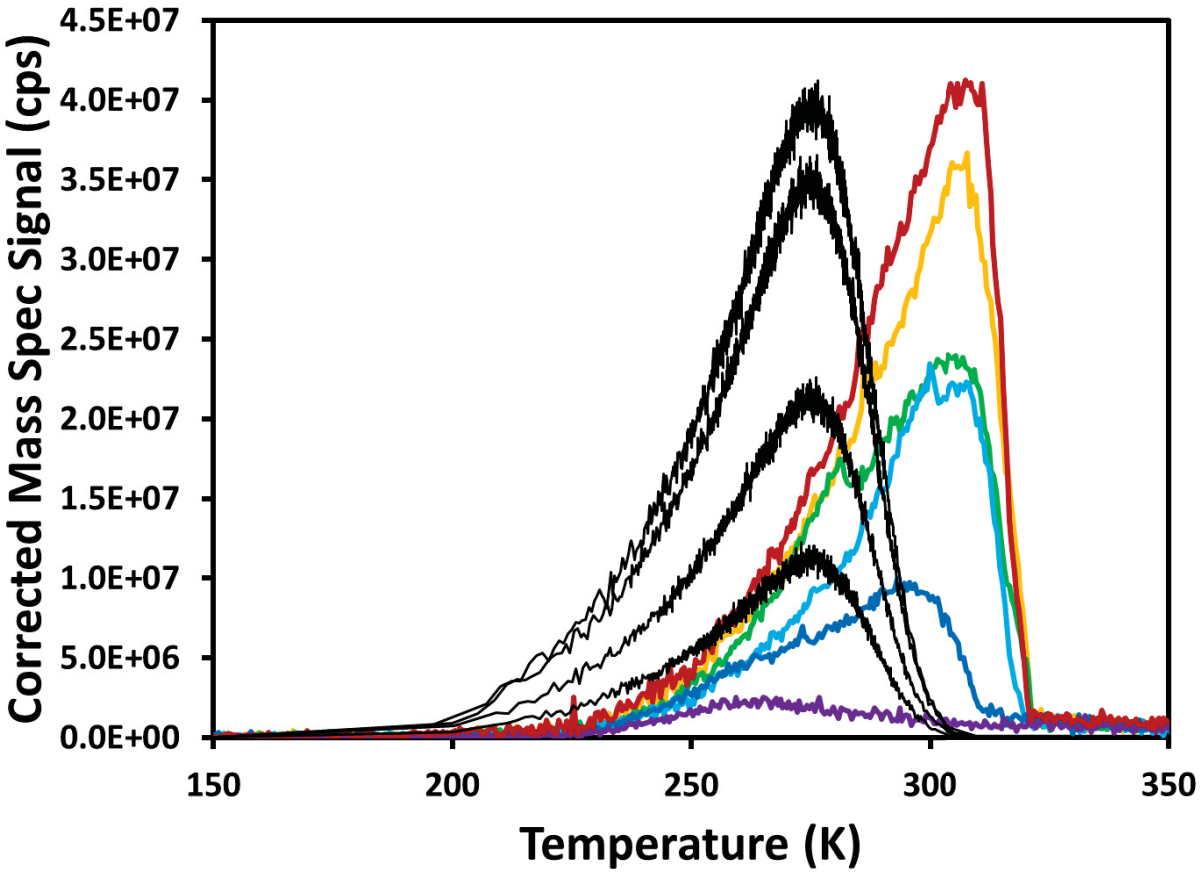

Figure 6.13 Comparison of Experimental TPD spectra (colored lines) to Kinetiscope model data (black lines) for 2-CEES desorption from NU-1000. Experimental coverages were θ = 0.82 ML (red), θ = 0.70 ML (yellow), θ = 0.54 ML (green), θ = 0.44 ML (light blue), θ = 0.23 ML (dark blue), and θ = 0.07 ML (purple).

As we introduced activation energies of desorption into the model (Table 6.7, Figure 6.14), we observed no change to the TPD spectrum when the activation energy was 64 kJ/mol. This suggests that the intracrystalline diffusion for 2-CEES through NU-1000 likely acts as the rate-limiting for process for desorption for any activation energy below 64 kJ/mol (assuming the same). When the desorption energy was set to 70 kJ/mol, there was no change to the T_{max}, but the temperature in which 2-CEES begins to desorb from NU-1000 increases from 200 K to 225 K.

The change in the simulated TPD spectral shape for desorption energies above 70 kJ/mol suggest that the overall desorption rate for 2-CEES under those conditions is desorption-limited and not diffusion-limited. While the simulated spectra with $E_{des,mono}$ = 82.5 kJ/mol had a similar T_{max} to the experimental TPD spectra, the simulated spectra had a different curve shape and did not begin to desorb until approximately 265 K.

Table 6.7 Model parameters for the TPD of 2-CEES from NU-1000 shown in Figure 6.12.

Attempt # (color)	θ (ML)	$\nu_{mono}(s^{-1})$	$E_{des,mono}$ (kJ/mol)	k_{pump} (s^{-1})
1 (red)	0.82	2.0×10^{14}	0	200
2 (yellow)	0.82	2.0×10^{14}	64	200
3 (light green)	0.82	2.0×10^{14}	70	200
4 (dark green)	0.82	2.0×10^{14}	75	200
5 (light blue)	0.82	2.0×10^{14}	80	200
6 (dark blue)	0.82	2.0×10^{14}	82.5	200
7 (purple)	0.82	2.0×10^{14}	85	200

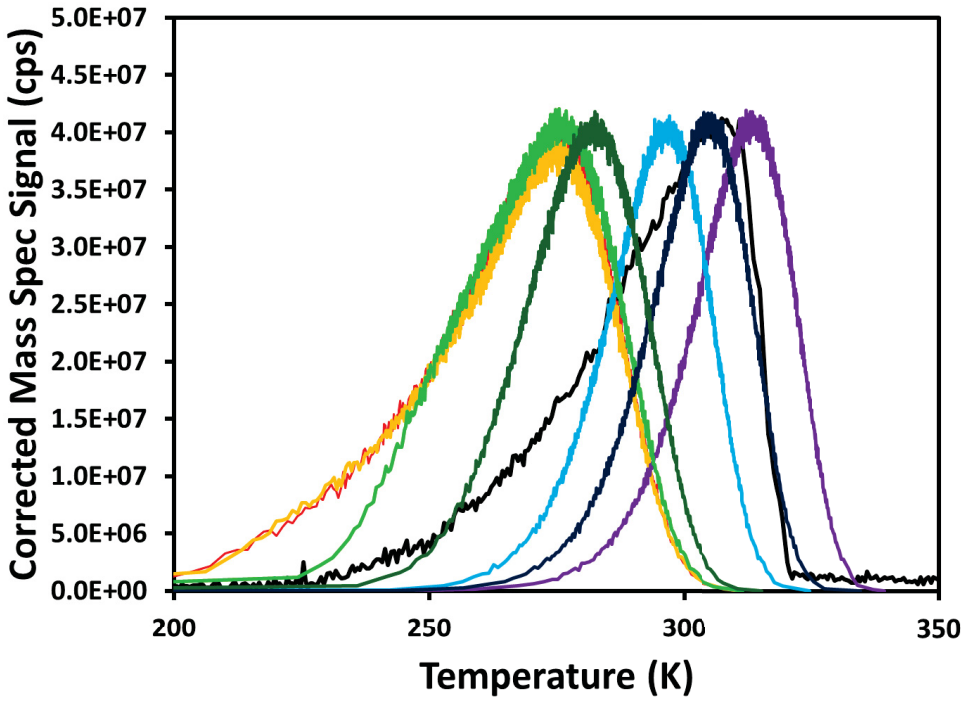

Figure 6.14 Comparison of experimental of experimental TPD spectra (black line) to Kinetiscope model data (colored lines) with several desorption energies. Color code: red = 0 kJ/mol, yellow = 65 kJ/mol, light green = 70 kJ/mol, dark green = 75 kJ/mol, light blue = 80 kJ/mol, dark blue = 82.5 kJ/mol, and purple = 85 kJ/mol.

6.3.4.2.1 Thermal Conductivity of NU-1000

One possible explanation for the temperature discrepancy between the simulated and experimental TPD spectra for 2-CEES desorption from NU-1000 is that the sample temperature may be lagging behind the mesh sample temperature. The thermal conductivity of the Zr-MOFs are several orders of magnitude lower than the tungsten sample grid (182 W/mK at 273 K). The thermal conductivity of MOF-5 (a MOF consisting of three 1,4-benzenedicarboxylate linkers coordinated to each Zn_4O cluster) at 300K was calculated to be 0.31 ± 0.02 W/m K.[224] Furthermore, Babai et al. employed a combination of molecular dynamic simulations and the Green-Kubo method and found the increases in MOF pore size result in a decrease in thermal conductivity.[225] While gas loading has been found to increase the thermal conductivity of smaller-pored MOFs, this effect was not observed in MOFs with pores larger than 1.7 nm.[225] The main hexagonal channel of NU-1000 is 3.1 nm in diameter, suggesting that the presence of 2-CEES within NU-1000 has a negligible effect on its thermal conductivity. In order to validate this assumption, a more careful measurement of the sample temperature during the TPD must be performed, which may involve the use of an infrared camera, to collect non-contact temperature measurements of the MOF sample surface.

6.3.4.3 TPD of 2-CEES from UiO-66

In the Kinetiscope model for 2-CEES desorption from UiO-66 without a desorption energy in the outer barrier (Table 6.8), 2-CEES began to desorb at approximately 225 K, reached a T_{max} at 332 K, and then fully desorbed before 375 K. The overall shape of the simulated TPD spectra (Figure 6.15) does not match the experimental TPD data, but the leading edge curves are similar and the T_{max} for the experimental data was within 3K of the Kinetiscope model. The T_{max} does not

shift to higher temperatures in the Kinetiscope model with decreasing initial coverage, but that was due to the fact that we do not have any coverage-dependent desorption energies in the model.

Table 6.8 Model parameters for the stochastic models of 2-CEES desorption from UiO-66 in Figure 6.15

$\nu_{mono}(s^{-1})$	$E_{des,mono}$ (kJ/mol)	k_{pump} (s^{-1})	E_{diff}(kJ/mol)	$D_0(cm^2\ s^{-1})$
10^{13}	0	200	61.4	164

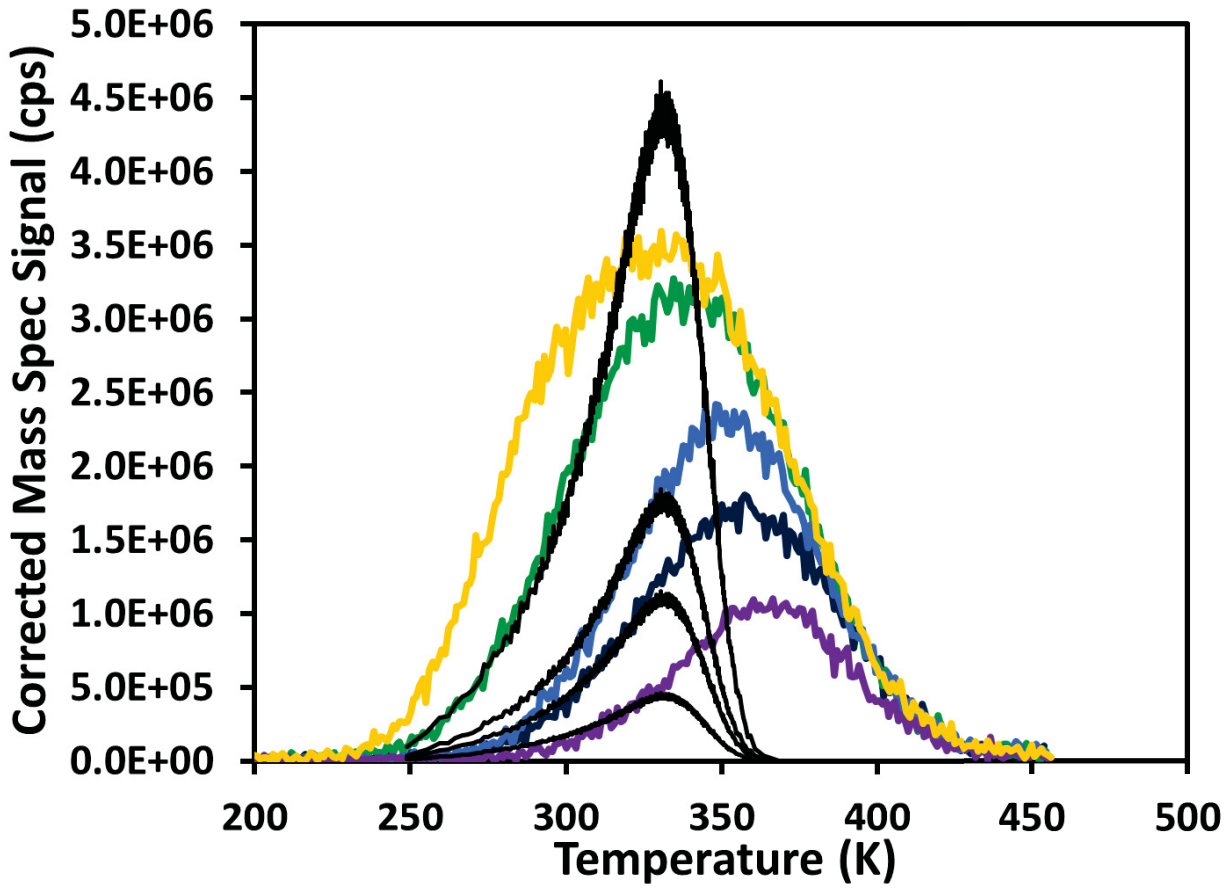

Figure 6.15 Comparison of experimental TPD spectra (colored lines) to Kinetiscope model (black lines) of 2-CEES desorption from UiO-66 with no desorption energy. Experimental coverages were: θ = 1.0 ML (yellow), θ = 0.86 ML (green), θ = 0.54 ML (light blue), θ = 0.38 ML (dark blue), and θ = 0.22 ML (purple).

We introduced an activation energy to the Kinetiscope model of 2-CEES desorption from UiO-66 to increase the temperature at which 2-CEES fully desorbed and to model the increase in T_{max} with as initial coverage decreases. The addition of a desorption energy to the model shown in Figure 6.15 could possibly shift the temperature at which 2-CEES first desorbs, which was the case for NU-1000, so we introduced a second diffusion-desorption process with the same diffusion kinetics, but an added desorption barrier. As can be seen in Figure 6.16, the incorporation of a secondary diffusion-desorption process with a desorption energy above 85 kJ/mol (assuming ν_{mono}= 2.0 × 10^{14} s^{-1}) resulted in an increase in T_{max} and a broader TPD curve that begins to capture the higher temperature trailing edge of the TPD curve. Further simulations that incorporate multiple diffusion-desorption processes with increasing desorption energies are in process.

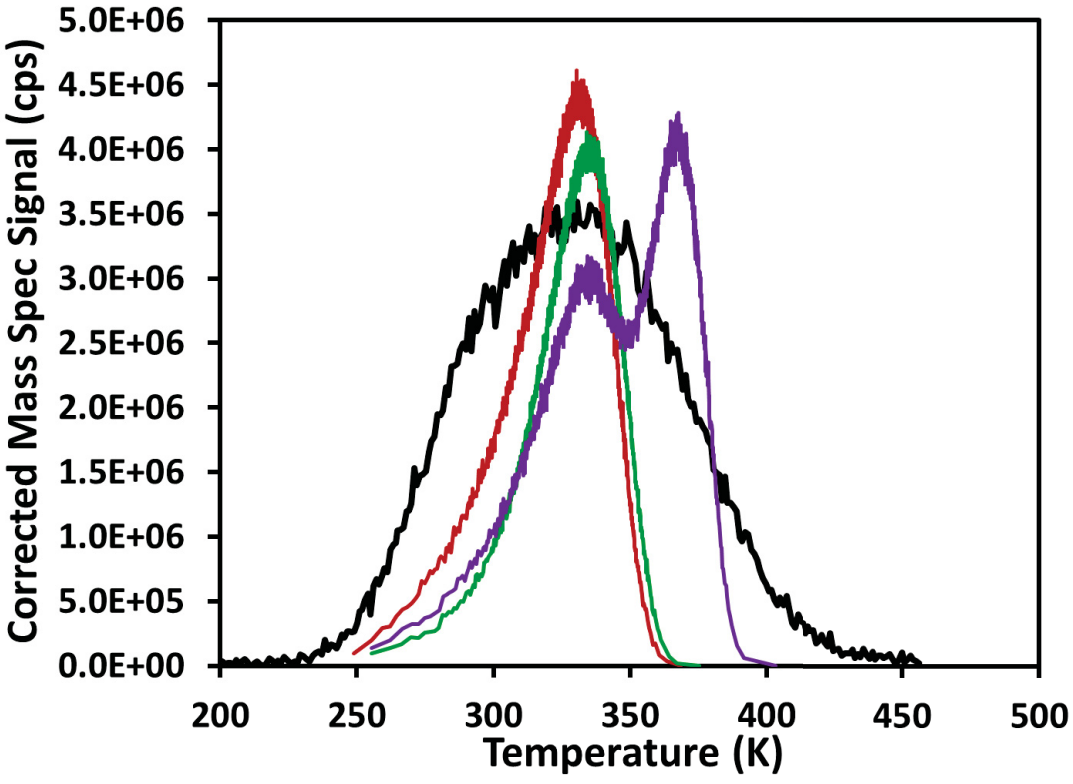

Figure 6.16 Comparison of experimental TPD spectra (black line) to Kinetiscope model data for (colored lines) with several desorption energies for 2-CEES desorption from UiO-66. Color code: red = 0 kJ/mol, green = 90 kJ/mol, purple = 100 kJ/mol).

The desorption energies incorporated into the Kinetiscope model data for 2-CEES desorption from UiO-66 and NU-1000 are significantly higher than the energetics provided by the inversion analysis of the TPD data. Due to the first-order rate constant for desorption, underestimating the desorption prefactor results in a lowered activation energy of desorption. While more work is needed to properly model and verify the model inputs for the desorption of gas molecules from microporous MOF materials, we have demonstrated that the diffusion process for 2-CEES from these MOFs studied significantly affects the overall rate of desorption.

6.4 Summary

We attempted to quantify the adsorption strength of 2-CEES adsorbed within the Zr-MOFs UiO-66, NU-1000, and UiO-67 using a combination of TPD experiments and stochastic modeling. The analysis of the TPD data with Redhead analysis, leading edge analysis, and inversion analysis yielded inconsistent activation energies of desorption and desorption prefactors. The slow diffusivity of 2-CEES through Zr-MOFs at temperature ranges consistent with the TPD spectra suggest that diffusion is the rate-limiting process for desorption. Based on these, we employed the stochastic modeling software Kinetiscope to begin to model the TPD data using the experimentally determined diffusivities of 2-CEES discussed in Chapter 4. While to date we have been unable to completely model the desorption of 2-CEES from the Zr-MOFs, our preliminary findings suggest the activation energies of desorption are likely higher than calculated using the TPD analysis methods that solve for the pre-exponential factor for desorption.

Chapter 7. Spectroscopic Insight into the Reaction of 2-CEES with UiO-66-NH_2 and the Role of Adsorbed Water

7.1 Introduction

Recently, Ploskonka et al. demonstrated that UiO-66-NH_2 reacted with the sulfur mustard simulant 2-chloroethyl ethyl sulfide (2-CEES) under ambient conditions to form an alkylated amine product and HCl gas (Scheme 1).[199] After approximately four hours of exposure, 0.15 CEES molecules reacted per UiO-66-NH_2 linker. While the mechanism of the reaction was not proposed, interactions between sulfur mustard and amine-based molecules have been extensively studied. Before its use as a chemical weapon, Clarke reported on the reaction between alkylamines and sulfur mustard as a technique to synthesize alkylated derivatives of thiazan.[226] Moore et al. determined that HD reacted with amino groups and pyridine at room temperature in $NaHCO_3$-buffered aqueous solutions.[227] *In vivo* studies into the vesicating mechanism of HD have revealed that HD undergoes an intramolecular cyclization reaction to form a thiiranium cation and releases a chloride ion. The cationic ethylsulfonium ring can then undergo a nucleophilic attack by amino acids, to form an alkylated amino acid. Because HD has two chloroethyl chains, this process can be repeated, which cross-links DNA, causing blistering, respiratory issues, chronic tissue damage, and cancer.[3, 6]

Scheme 7.1 Proposed reaction of the 2-aminotoerephthalic acid linker of UiO-66-NH2 with 2-CEES.[199]

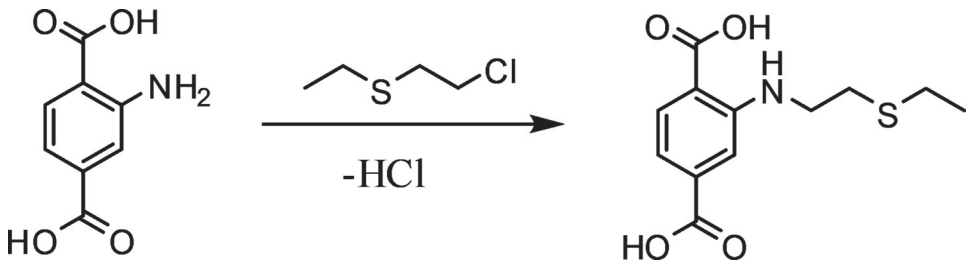

Another possible mechanism for the alkylation of 2-aminoterephthalic acid with 2-CEES could be the direct nucleophilic attack of the "acyl carbon" by the amine group on the MOF linker. In the Menschutkin reaction, alkyl halides undergo a nucleophilic attack by the lone pairs of tertiary amines and form quaternary ammonium salts.[228] DFT calculations of the Menschutkin reaction by Giri et al. suggest that the reaction is both thermodynamically and kinetically favored in the aqueous phase as opposed to the gas-phase.[229] This likely is also the case for the aforementioned "*in-vivo*" mechanism, where the solvation of 2-CEES likely helps stabilize the formation of the thiiranium intermediate.

One issue that may complicate an understanding of the mechanism of the reaction between UiO-66-NH_2 and 2-CEES is the presence of water in ambient environments. Furukawa et al. demonstrated that MOFs, especially Zr-based MOFs like UiO-66 readily sorb water from the atmosphere,[230] suggesting that even under low relative humidity (R.H.) environments, the pores of a MOF will be filled with adsorbed water. Furthermore, the presence of amine functionalization on MOF linkers is known to enhance water uptake. Jeremias et al. demonstrated that amine functionalization of UiO-66 resulted in an increased isosteric heat of adsorption of water in UiO-66-NH2 (89.6 kJ/mol) as compared to UiO-66.[231] Even under 0% R.H., UiO-66-NH_2 can retain up to 3.3 mmol of water per gram of MOF.[126]

Because any material fielded for CWA protection is likely to be deployed into a wide variety of environments with varying temperatures and climate, it is critical to understand how ambient moisture levels may affect the ability of these MOFs to protect against CWA attacks. Our work seeks to understand the reaction between 2-CEES vapor and UiO-66-NH_2 as well as try to identify whether water contributes to the reaction. We investigated the reaction between UiO-66-NH_2 and 2-CEES under a wide range of humid conditions and employed a variety of spectroscopic

techniques, such as X-ray photoelectron spectroscopy (XPS), temperature programmed desorption (TPD), IR spectroscopy, NMR spectroscopy, and UV-Vis spectroscopy. This work demonstrates the benefit of combining fundamental vacuum-based surface science experiments in addition to ambient pressure studies to develop a strong understanding of the CWA-MOF chemistry.

7.2 Experimental

7.2.1 UiO-66-NH_2

Greg Peterson of the CBC Lab provided the UiO-66-NH_2. The MOF was activated *en vacuo* at 473 K for 12 hours to remove residual solvent within the pores of the MOF. The activated powder was stored in a vacuum desiccator before experiments. 2-aminoterephthalic acid (99%) was purchased from Sigma-Aldrich.

7.2.2 Jar-in-a-Jar Exposures

Ambient pressure exposures of 2-CEES to UiO-66-NH2 was performed following the exposure procedures as described by Ploskonka and DeCoste.[199] Approximately 20 mg of the UiO-66-NH_2 was weighed out and placed into a 5-mL borosilicate beaker. 200 μL of 2-CEES was placed in a separate 5-mL beaker, and each beaker was placed together in a capped vial. The vial was sealed and wrapped in aluminum foil to prevent light from entering the reaction vessel. Unless otherwise stated, reactions were allowed to proceed for 24 hours before removing 2-CEES. For the exposures that included humidity control, a mixture of glycerol and water were prepared in a third beaker to control the vapor pressure of water.[232]

7.2.3 Powder X-ray Diffraction

Synchrotron-based powder X-ray diffraction of UiO-66-NH_2 before and after ex situ 2-CEES exposure under both dry and humid conditions were performed by Dr. Anna Plonka at

Stony Brook University. The "dry" sample was prepared by placing UiO-66-NH_2 in a desiccator for 24 hours, while the "wet" sample was stored in a water-saturated container prior to exposure. Samples were then placed in a closed container saturated with 2-CEES vapor for 24 hours.

7.2.4 IR Spectroscopy

The UiO-66-NH_2 powder was prepared for UHV-based studies using previously described methods.[54, 98] approximately 15 mg of MOF powder was pressed into the grids of a 50 micron-thick tungsten mesh. K-type thermocouple wires were spot-welded to the tungsten mesh to monitor sample temperature, and the sample mesh was affixed to copper power leads for resistive heating via stainless steel sample clamps. Once installed in the UHV chamber, the sample was allowed to off-gas at 423 K under vacuum for 12 hours to remove adsorbed water. IR spectra were recorded on a Thermo-Nicolet Nexus 670 spectrometer using a liquid-nitrogen cooled MCT-A detector. Spectra were collected as 128 scans to average with a 2 cm^{-1} resolution.

7.2.5 Temperature Programmed Desorption

TPD data of 2-CEES desorption from UiO-66-NH_2 was obtained by heating the UiO-66-NH_2 at a constant rate of 0.2 K/s using an analog PID controller. Desorbed 2-CEES molecules were detected via a double-differentially pumped, linear-line-of-sight electron-impact/quadrupole mass spectrometer (Extrel). The mass spectrometer was tuned to the most abundant fragment ions of 2-CEES, mass-to-charge (m/z) ratios of 75, 47, and 27.

7.2.6 X-Ray Photoelectron Spectroscopy

Dr. Xu Feng of the Virginia Tech Surface Analysis Laboratory recorded the X-ray Photoelectron spectra. XPS characterization was performed on a PHI VersaProbeIII scanning XPS microscope using a monochromatic Al K-alpha X-ray source (1486.6 eV). XPS spectra were

acquired with 100 μm/100 W/20 kV X-ray settings and dual beam charge neutralization over a 1400 × 1400 μm area. All binding energies were referenced to the C-C peak at 284.8 eV. Atomic concentration percentages of elements were determined from the integrated intensity of the elemental photoemission features corrected by relative atomic sensitivity factors.

7.2.7 Water Vapor Adsorption

Water vapor sorption isotherm data were collected with an AquaLab Vapor Sorption Analyzer. Before data collection, standard solutions of 13.41 mol/kg LiCl (a_w=0.250) and 6.00 mol/kg NaCl (a_w=0.760) were used to calibrate the water activity detector. The microbalance was calibrated within 0.1 mg using a 2 g NIST traceable weight. 420.7 mg of UiO-66-NH_2 was weighed out into a stainless steel sample cup. Water sorption data were collected from 0.0500 R.H. to 0.9300 R.H. After performing the water vapor sorption analysis, the UiO-66-NH_2 was heated at 150 °C for 72 hours before recording a final sample mass.

7.2.8 Diffuse Reflectance UV-Vis

Diffuse Reflectance UV-Vis spectra of UiO-66-NH_2 and 2-aminoterephthalic acid samples were collected on a Cary 5000 UV-Vis spectrometer. Approximately 20 mg of powder was used per sample. Spectra were baseline corrected using a barium sulfate blank reference.

7.2.9 Attenuated Total Reflectance IR

ATR-IR spectra of UiO-66-NH2 and 2-aminoterephthalic acid samples were recorded by Emerald Greene on a Varian 670-IR with an ATR-IR attachment. Background spectra were recorded of the blank diamond crystal before placing a small amount of sample powder on the ATR crystal. The system was allowed to purge with dry air before recording spectra. Each ATR spectra were recorded with 64 scans to average and a 2 cm^{-1} resolution.

7.2.10 Solution NMR

Approximately 30 mg of each 2-aminoterephthalic acid sample was dissolved in 1 mL d_6-DMSO. Samples were vigorously shaken to ensure full solvation. ^{1}H and ^{13}C NMR spectra were recorded on an Agilent U4-DD2 400 MHz spectrometer.

7.3 Results and Discussion

7.3.1 Water Adsorption within UiO-66-NH_2

The water vapor isotherm data for our UiO-66-NH_2 sample (Figure 7.1) strongly resembled previously reported uptake behavior.[126] Above 15% R.H., there was at least 20 mol/kg of water within the UiO-66-NH_2. While the humidity levels in our laboratory were not tested, the humidity level within the lab that contained the water sorption instrument was 67% and the yearly average humidity in Blacksburg, VA is 64 %. Water is therefore present within the MOF under ambient conditions.

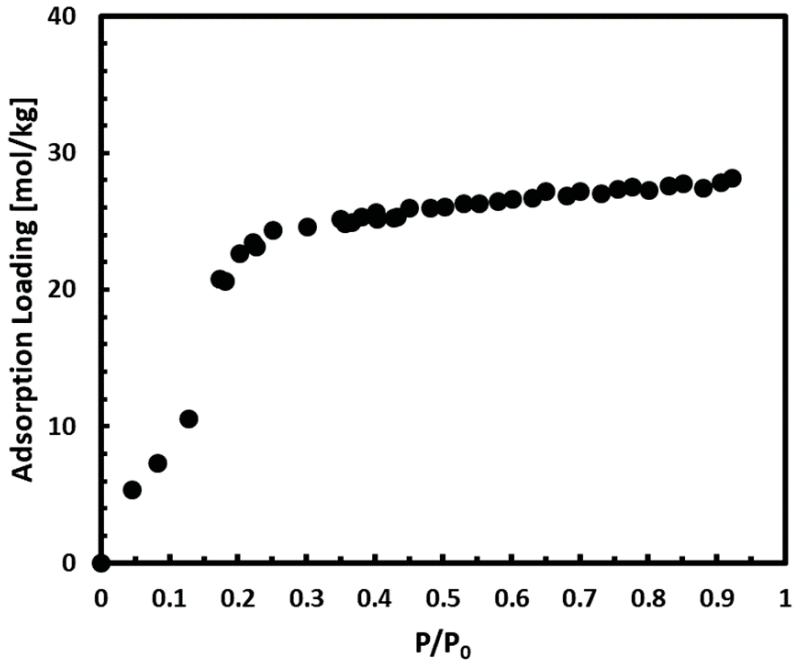

Figure 7.1 Water vapor sorption isotherm for UiO-66-NH_2.

7.3.2 TPD of 2-CEES within UiO-66-NH_2.

While Ploskonka et al. reported that overall, one 2-CEES molecule reacted for every three linkers of UiO-66-NH_2, they found that approximately one 2-CEES molecule adsorbed per linker.[199] To probe the strength of adsorption/diffusion interaction of adsorbed 2-CEES molecules that do not react within UiO-66-NH_2, we performed TPD of 2-CEES desorption from UiO-66-NH_2. Due to the current limitations of our ability to deconvolute the contribution of intracrystalline diffusion from the overall desorption rate (as previously discussed in Chapter 6), we qualitatively compared the TPD spectra for 2-CEES desorption from UiO-66-NH_2 (Figure 7.2) to the TPD data we collected for UiO-66.

For UiO-66-NH_2, four major desorption curves appear in the TPD spectra, the first being attributed to the multilayer desorption of weakly bound 2-CEES from the external crystal surface of the MOF. As mentioned in Chapter 6, the leading-edge analysis for the multilayer desorption of 2-CEES yielded an E_d = 63.7 kJ/mol and $\nu = 1.9 \times 10^{13}\ s^{-1}$, in agreement with the multilayer desorption of 2-CEES from the other Zr-MOFs. The second feature with a T_{max} = 331 K has the same curve shape as the multilayer desorption. This second feature may be the multilayer desorption from another sample on the mesh, but that was never confirmed. The third feature strongly resembles a first-order desorption curve. Compared to UiO-66, which had the T_{max} range from 331 K to 367 K depending on initially coverage, the first-order feature for UiO-66-NH_2 has a T_{max} = 373 K, suggesting a stronger interaction between 2-CEES and UiO-66-NH_2. Within our TPD experiments, which were run to 523 K, 2-CEES had fully desorbed at 460 K, approximately 35 K warmer than 2-CEES desorption from UiO-66.

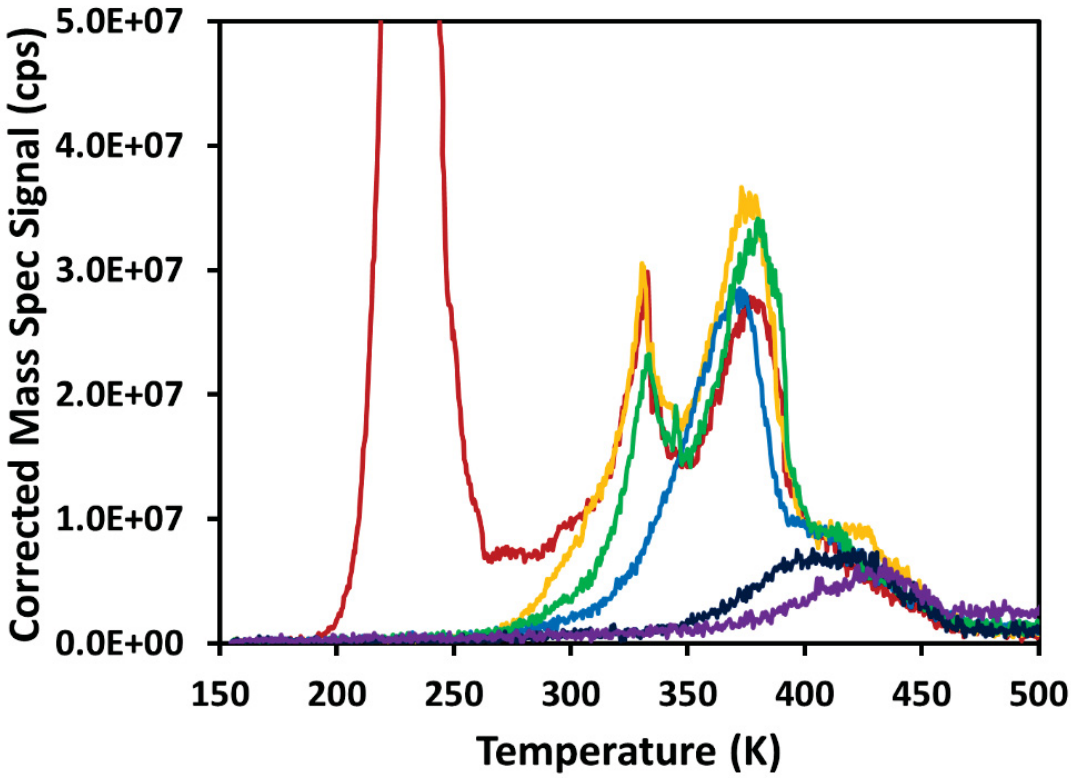

Figure 7.2 TPD of 2-CEES desorption from UiO-66-NH2. Each colored curve represents TPD experiments with varying initial coverages. Initial coverages were θ = 4.40 (red), θ = 1.00 (yellow), θ = 0.87 (green), θ = 0.68 (light blue), θ = 0.26 (dark blue), and θ = 0.24 (purple).

Because the pore topology and inorganic clusters are identical for UiO-66 and UiO-66-NH_2, the pronounced difference in TPD spectra is likely due to the presence of amine groups on the benzene dicarboxylate linkers. Devautour-Vinot et al. studied the dynamic structure of a series of UiO-66 MOFs with varied linker functionalization and found that UiO-66-NH_2 exhibited the highest rotational energy barrier for (12.4 kcal/mol), partially due to intramolecular interactions between the amine groups and the Zr clusters.[233] Slow rotational dynamics of the linkers in UiO-66-NH_2 may induce a more restrictive pore aperture, which would decrease the diffusivity of 2-CEES. It is also possible that the amine groups form hydrogen bonds with the adsorbed 2-CEES molecule, which would strengthen the 2-CEES/MOF interaction. Tan et al.

found that adsorbed NH_3 within MOF-74 increased the diffusion barrier for CO and CO_2 due to hydrogen bonding between adsorbates.[92]

7.3.3 Ambient Exposure of UiO-66-NH_2 to 2-CEES

7.3.3.1 Powder X-ray Diffraction

Powder X-ray diffraction (PXRD) of the UiO-66-NH_2 was taken before and after exposure to 2-CEES to probe whether the reaction caused the breakdown of long-range order in the MOF (Figure 7.3). Benchtop PXRD did now show any difference after exposure to 2-CEES. The presence of a diffraction peak below 5° was attributed to the presence of **reo** phase and suggested that the sample contained missing cluster defects.[57]

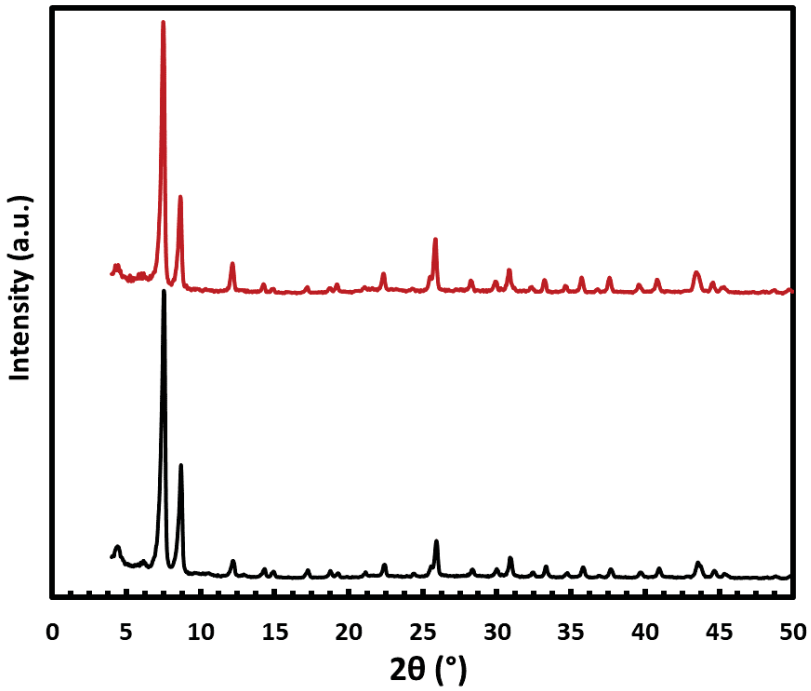

Figure 7.3 PXRD of UiO-66-NH_2 before (black) and after (red) exposure to 2-CEES.

The synchrotron-based PXRD spectra of UiO-66-NH_2 exposed under both dry (UiO-66-NH_2-2-CEES) and humid conditions (UiO-66-NH_2-H_2O-2-CEES) revealed that both the

presence of water and 2-CEES within the pores of UiO-66-NH_2 had an effect on the MOF framework. A decrease in the low angle reflections (Figure 7.4) indicated pore filling. LeBail fits of the PXRD data indicated that the unit cell volume of the "dry" UiO-66-NH_2 sample increased by approximately 1% upon exposure to 2-CEES while the unit cell volume of the "wet" UiO-66-NH_2 increased by approximately 0.5% (Figure 7.5). The PXRD data suggested that even in a humid environment, 2-CEES can still adsorb within the pores of UiO-66-NH_2.

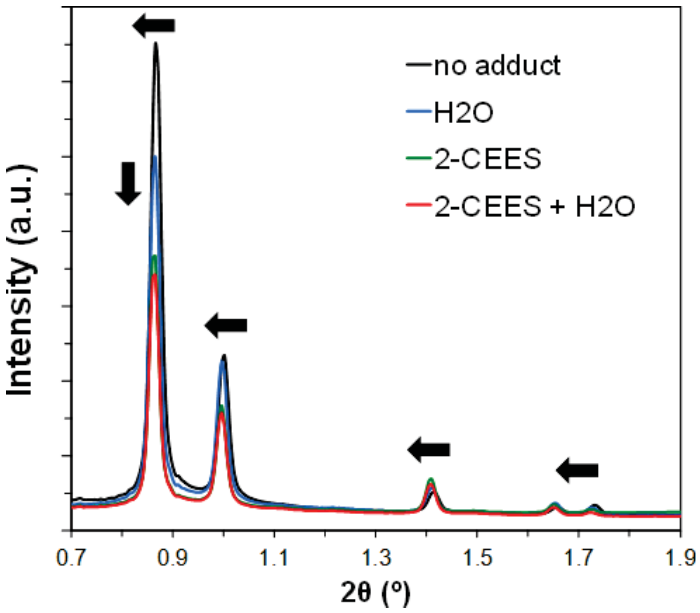

Figure 7.4 Low angle portion of collected PXRD pattern from UiO-66-NH2 ex situ exposure to 2-CEES. Arrows indicate the changes influenced by H2O and 2-CEES adsorption.

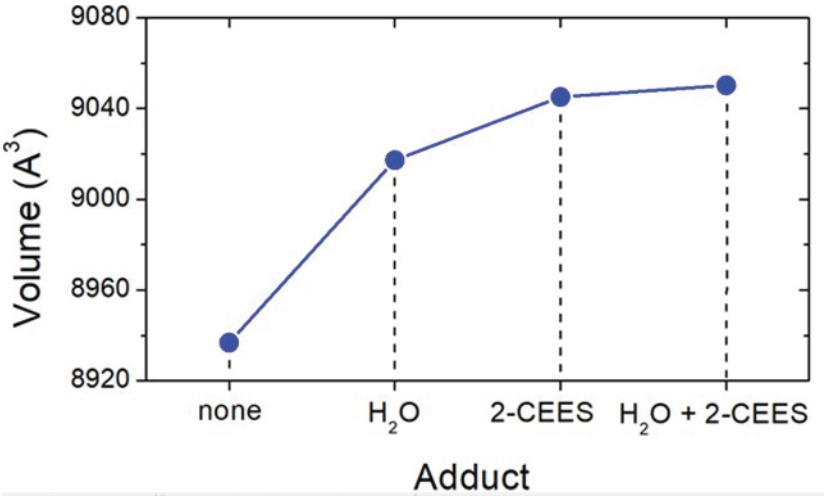

Figure 7.5 Unit cell changes of UiO-66-NH2 upon exposure to H2O, 2-CEES, and H2O + 2-CEES. Error bars are smaller than the symbols.

7.3.3.2 Attenuated Total Reflectance IR

The ATR spectrum of UiO-66-NH_2 (Figure 7.6) agrees well with previously reported infrared spectra of UiO-66-NH_2.[234] Under ambient conditions, the $\nu_{sym}(NH_2)$ and $\nu_{asym}(NH_2)$ vibrational modes at 3515 cm^{-1} and 3390 cm^{-1},[235] respectively, cannot be observed due to a broad feature centered around 3400 cm^{-1}, likely due to the presence of physisorbed water within the MOF. Key features in the ATR spectrum include bands at 1338 cm^{-1}, 1257 cm^{-1}, and 1423 cm^{-1}, which correspond to vibrational modes associated with the aryl amine of the 2-aminoterephthalic acid. The complete assignment of IR features within UiO-66 can be found in Table 7.1.

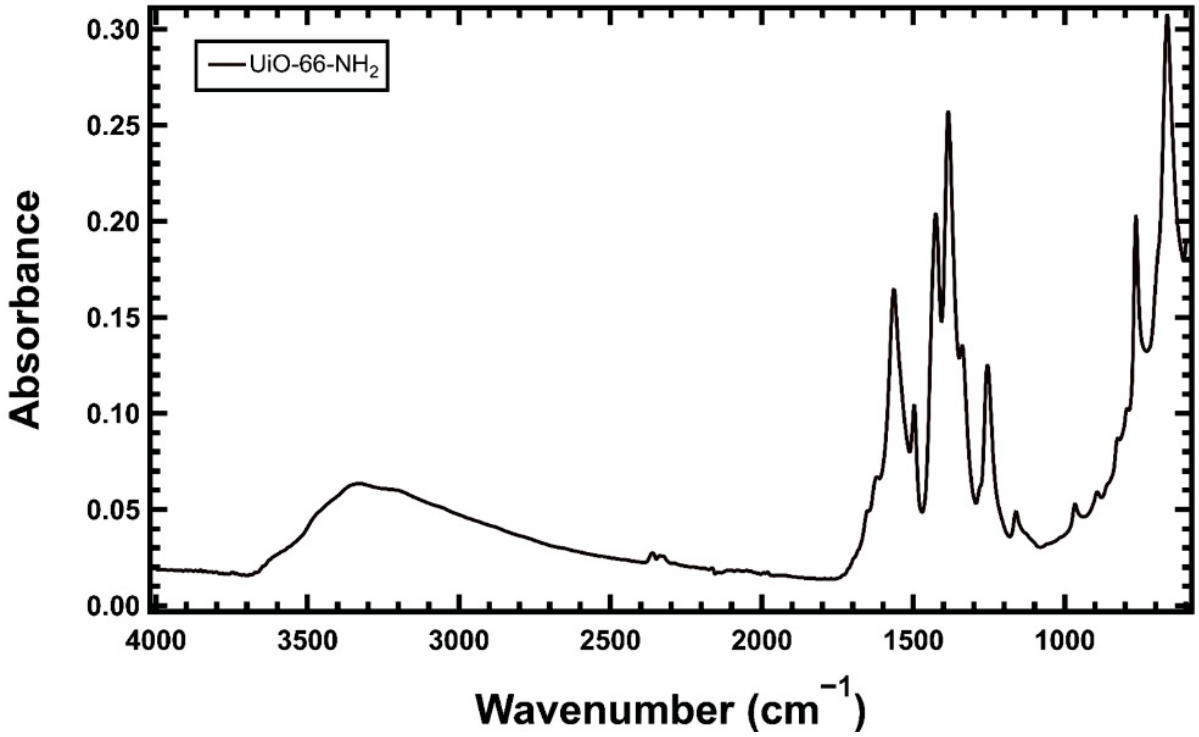

Figure 7.6 ATR spectrum of UiO-66-NH_2

Table 7.1 IR assignments for UiO-66-NH_2

Peak (cm^{-1})	Assignment[56, 75, 91, 235-236]
1654	ν(O–C–O)$_{asym}$
1610	ν(O–C–O)$_{asym}$
1562	ν(O–C–O)$_{asym}$
1497	β(C–H) + ν(C–C$_{ring}$)
1423	ν(C–C$_{ring}$) + ν(C–C)
1385	νC-C$_{ring}$
1338	ν(C$_{ar}$–N)
1254	ν(C$_{ar}$–N)
1164	β(C–H) + δ(O–H) + χ(ring)
964	
764	ν(Zr−O) + γ(COO) + ρ(C–H)
659	

After the exposure of the UiO-66-NH_2 to 2-CEES vapor, the presence of additional vibrational features in the ATR spectrum (Figure 7.7) was consistent with adsorbed 2-CEES. In the high wavenumber region, IR bands at 2956 cm^{-1}, 2913 cm^{-1}, and 2856 cm^{-1} were assigned to the C–H stretching vibrations of 2-CEES.[166-167] Bands at 1214 cm^{-1} and 1055 cm^{-1} were assigned

to ω(C–H_2) and ν(C–C)$_{asym}$, respectively.[166] In addition to the presence 2-CEES of adsorbate features, several observable changes to the UiO-66-NH_2 structure indicated a reaction at the amine groups. The ν(C_{ar}–N) mode at 1338 cm^{-1} disappeared while the ν(C_{ar}–N) band at 1253 cm^{-1} was blue shifted to 1278 cm^{-1}. Major perturbations to vibrational modes associated with the amine group on the 2-aminoterephthalic acid suggested that 2-CEES interacts directly with the amine group.

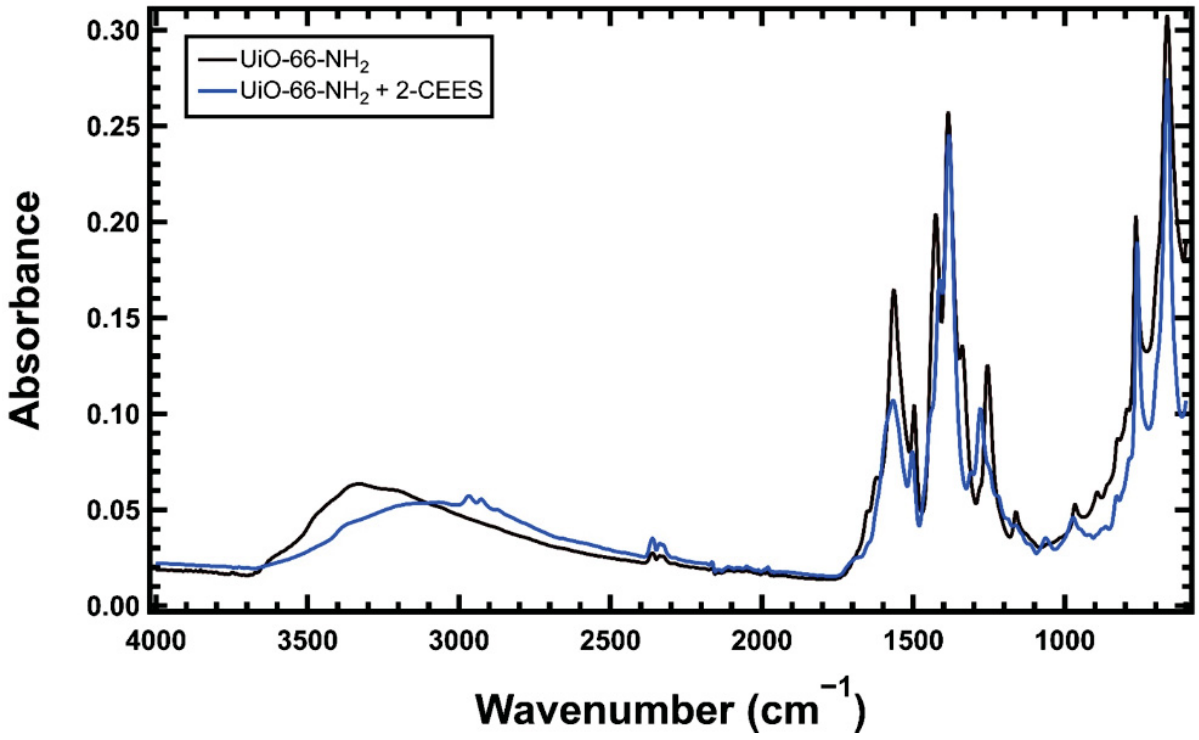

Figure 7.7 ATR spectra of UiO-66-NH_2 before (black) and after (blue) exposure to 2-CEES

7.3.3.3 X-ray Photoelectron Spectroscopy

No changes occurred in the Zr 3d spectra upon exposure to 2-CEES (Figure 7.8), which suggested that there is no displacement of linkers upon 2-CEES adsorption and reaction. This also suggested that 2-CEES likely does not adsorb at coordinatively unsaturated Zr sites, or at least that the density of undercoordinated Zr sites was quite low.

As was expected, no sulfur was present in the UiO-66-NH_2 before 2-CEES exposure. After 2-CEES exposure, two distinct features are present in the S 2p spectrum. The lower energy S $2p_{3/2}$ peak at 163.4 eV agreed with previously published spectra of adsorbed thioethers,[237] while the S $2p_{3/2}$ band at 166.8 eV was consistent with oxidized sulfur species such as DMSO.[238-239] Though the predicted reaction products for the alkylation of the UiO-66-NH_2 has no oxidized sulfur products, additional side reactions might have occurred within our MOF sample.

In the N 1s spectrum, the feature at 399.4 eV agreed with literature spectra for UiO-66-NH_2.[240] A feature at 401.9 eV that formed because of the 2-CEES interaction with UiO-66-NH_2 could be due to hydrogen-bonded NH_2, NH_3^+, or possibly the presence of a quaternary amine species.[241-242] Ammonium chloride, a potential reaction product between HCl and amine groups has an N 1s feature 401.8 eV.[242] In the proposed reaction between 2-CEES and UiO-66-NH_2, upon the nucleophilic attack of the 2-CEES by the amine groups, a secondary ammonium ion would form, which may also possibly explain the feature.

The presence of chlorine in the UiO-66-NH_2 sample before 2-CEES exposure was attributed to the likely use of $ZrCl_4$ as a starting material for the synthesis of Zr-based MOFs.[125, 143] The Cl $2p_{3/2}$ peak at 198.3 eV before was consistent literature values for $ZrCl_4$.[243] The chlorine feature signal for UiO-66-NH_2 after 2-CEES exposure increased in intensity and appeared to remain inorganic in nature. For ammonium chloride, the Cl $2p_{3/2}$ appears at 197.9 eV, which further suggested that ammonium chloride might form as the amine groups react with HCl vapor.

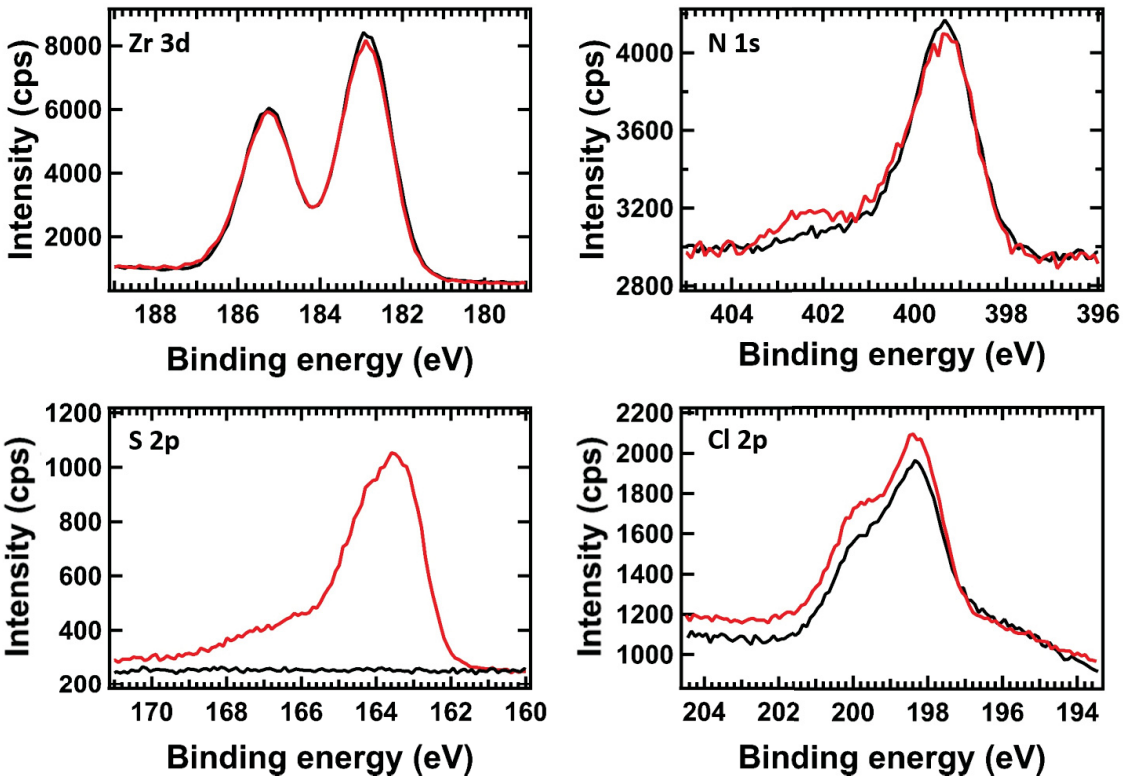

Figure 7.8 XPS Zr 3d, N 1s, S 2p, and Cl 2p spectra of UiO-66-NH_2 before (black) and after (red) exposure to 2-CEES at ambient conditions. Signal intensities were normalized to the Zr 3d signal.

7.3.3.4 Diffuse Reflectance UV-Vis

While the unfunctionalized UiO-66 does not absorb light in the visible range, electronic charge donation to the antibonding π*-orbitals of the benzene ring from the lone pair on the amine group nitrogen increase the HOMO of UiO-66-NH_2, causing it to absorb in the visible range with an absorption edge at approximately 450 nm.[244-245] Upon exposure of the UiO-66-NH_2 sample to 2-CEES vapor, we observed a distinct color change from pale yellow to dark yellow. This finding was confirmed by DR-UV-Vis (Figure 7.9), which revealed a 50 nm red shift in the absorbance edge upon adsorption of 2-CEES. The alkyl-thioalkylation of the amine group to form a secondary amine species may allow for more charge donation into the antibonding orbital, further increasing

the HOMO. While the sensitivity of the absorbance edge shift to 2-CEES concentration levels was not investigated in this paper, the change in color upon reaction with 2-CEES suggests that UiO-66-NH_2 could potentially be developed for the optical detection of chemical warfare agents.

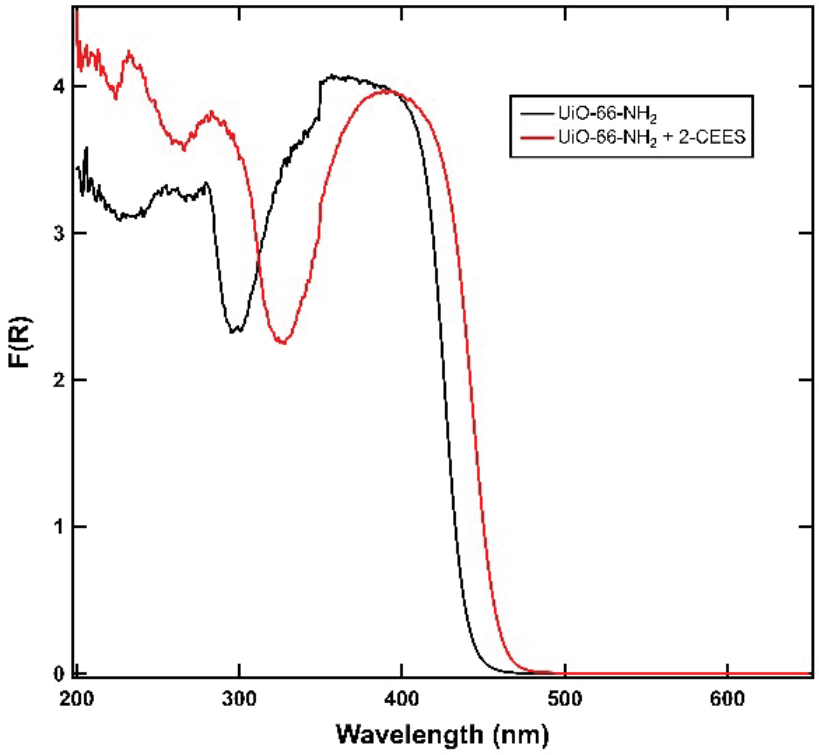

Figure 7.9 Diffuse-Reflectance UV-Vis of UiO-66-NH_2 before (black) and after (red) exposure to 2-CEES

7.3.4 Ambient Exposure of UiO-66-NH_2 to HCl

To test the hypothesis that the increase in visible light absorption was due to the formation of the aminoalkyl reaction product, and not the potential formation of ammonium chloride, HCl vapor, a byproduct of 2-CEES hydrolysis or dehalogenation, was exposed to UiO-66-NH_2 following the same jar-in-a-jar procedure. Upon HCl exposure, the visible light absorbance of UiO-66-NH_2 virtually disappeared (Figure 7.10), and the once pale yellow sample turned white. The decrease in visible light absorbance upon exposure to HCl vapor was likely due to the

perturbation of the 2-aminoterephthalic acid linker of the MOF, possibly through the formation of an ammonium chloride adduct or through the addition of chlorine to the phenyl ring.

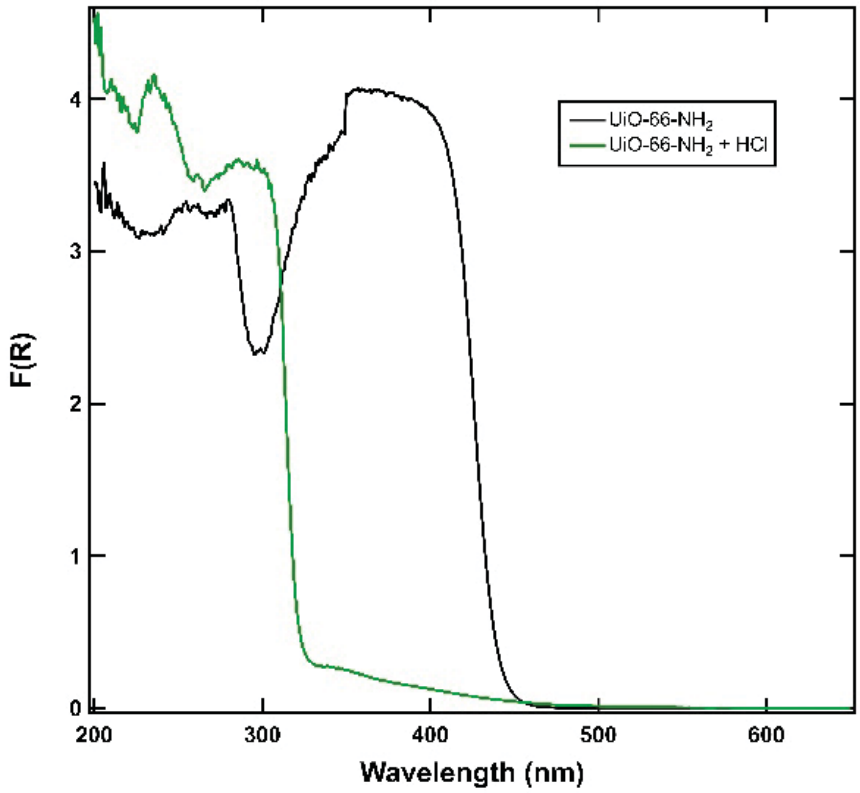

Figure 7.10 DR-UV-Vis of UiO-66-NH_2 before (black) and after (green) exposure to HCl.

DeCoste et al. reported that upon exposure to chlorine gas, the 2-ATA linker of UiO-66-NH_2 undergoes an electrophilic aromatic substitution (EAS) reaction that adds a chlorine moiety *para* to the amine group on the phenyl ring.[246] HCl that forms as a byproduct of the EAS reaction can then react either with the amine groups of UiO-66-NH_2 to form an ammonium chloride or react with the zirconium-carboxylate linker.

ATR of UiO-66-NH_2 post HCl dosing (Figure 7.11) revealed similar changes to the C_{ar}-N vibrations as observed when 2-CEES reacted with UiO-66-NH_2. The carboxylate mode at 1562 cm^{-1} shifted, and a new band formed at 1700 cm^{-1}, suggesting that the reaction of between HCl

directly interacted with the amines on the 2-ATA linkers. XPS analysis of UiO-66-NH_2 after a jar-in-a-jar exposure to HCl vapor only showed the presence of a single N 1s feature at 399.47 eV. After the HCl vapor exposure experiment, The Cl $2p_{3/2}$ appears at 198.5 eV, but the XPS spectrum did not show distinct features from the Cl 2p spectrum of the unreacted MOF.

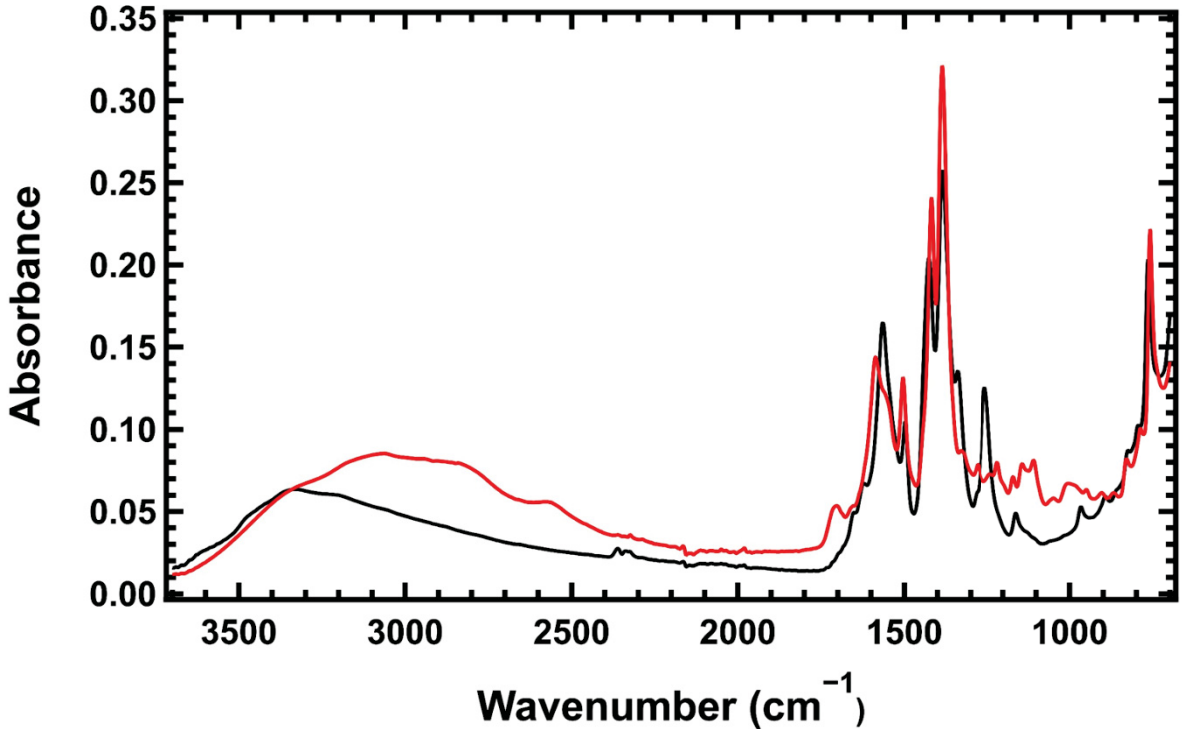

Figure 7.11 ATR spectra of UiO-66-NH_2 before (black) and after (red) exposure to HCl

7.3.5 Ambient Exposure of 2-Aminoterephthalic Acid to 2-CEES

To determine whether the reaction between 2-CEES and UiO-66 occurred in the absence of the MOF's porous environment and zirconium cluster, we replicated our 2-CEES exposure to UiO-66-NH_2 with just the 2-aminoterephthalic acid at various levels of moisture exposure. For the jar-in-a-jar experiments, the "ATA-Dry" sample container only contained the 2-ATA linker and a beaker of 2-CEES, the "ATA-Humid" sample container contained 2-ATA linker, a beaker of 2-CEES, and a beaker of water, and the "ATA-Wet" sample contained 2-ATA mixed with water

and the beaker of 2-CEES. The reaction between 2-ATA and 2-CEES was studied with ATR-IR, XPS, and NMR spectroscopy.

7.3.5.1 Attenuated Total Reflectance IR

The complete assignment of the vibrational modes in the IR spectrum of 2-ATA before 2-CEES (Figure 7.12) is listed in Table 7.2. The IR spectra for the ATA-DRY and ATA-HUMID exactly resemble the 2-ATA. For the ATA-WET sample, no changes were observed for the vibrational modes assigned to the 2-ATA linker, but the spectrum showed additional IR features at 844 cm^{-1}, 1049 cm^{-1}, 1084 cm^{-1}, 1201 cm^{-1}, 1269 cm^{-1}, 1396 cm^{-1}, which suggest the reaction of 2-CEES with the ATA-WET sample.

Table 7.2 Assignments for the vibrational spectrum of 2-aminoterephthalic acid.

Frequency (cm^{-1})	**Assignments[247]**
746	Ring breathing
777	γ(CCOO)
871	γ(C–H)
906	β(C–C_{ring}) + ν(C–C_{ring}) + ν(C–OH) + ν(C–NH_2)
1122	β(C–H) + ν(C–C_{ring}) + ν(C-OH) + ν(N-H_2)
1159	β(C–H) + ν(C-C_{ring})
1218	
1284	
1309	β (C–H)
1411	ν(C–C_{ring}) + ν(C–C)
1448	νC-C_{ring} + ν(C–NH_2)
1495	β(C–H) + ν(C–C_{ring})
1550	ν(C–C_{ring}) + ρ(N–H_2)
1585	ρ(N–H_2) + ν(C-C_{ring})
1614	ν(C–C_{ring})
1658	ν(C=O)
3381	ν(N–H_2)$_{sym}$
3496	ν(N–H_2)$_{asym}$

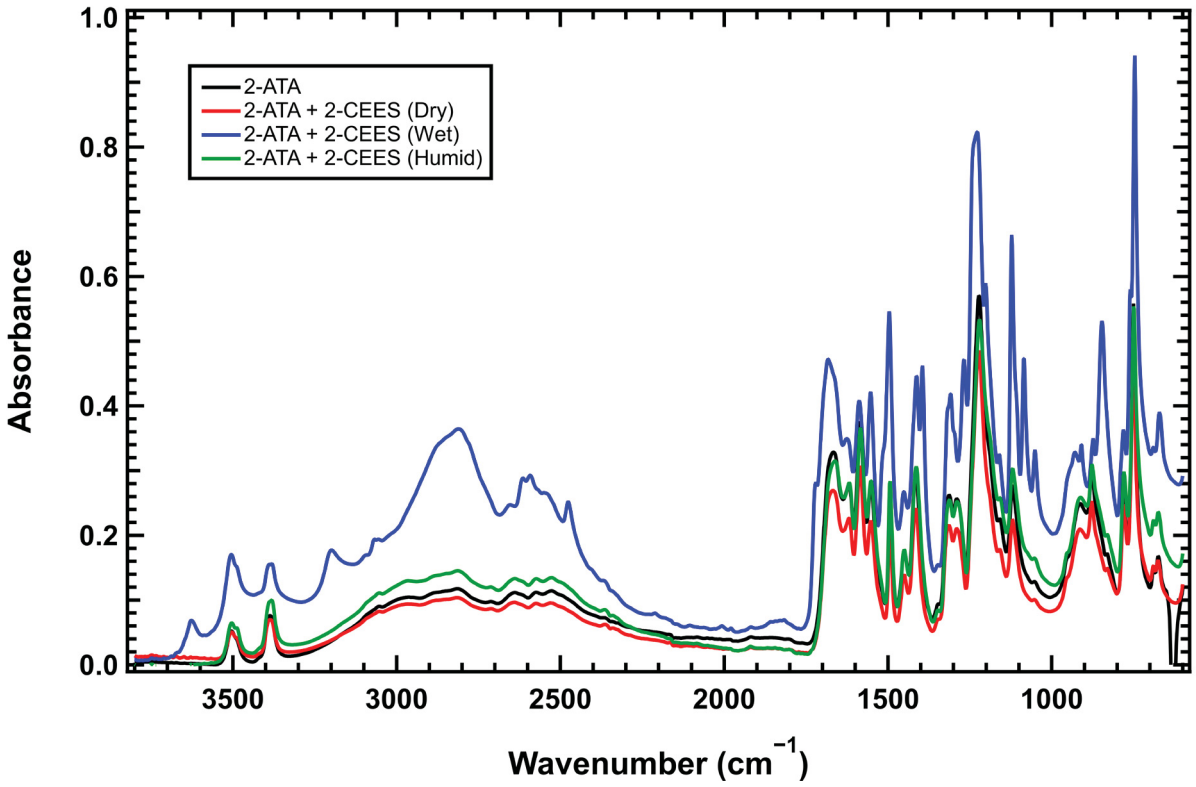

Figure 7.12 ATR spectra of 2-aminoterephthalic acid before (black) and after (colored) 2-CEES exposure under various moisture conditions

7.3.5.2 X-ray Photoelectron Spectroscopy

XPS analysis of the 2-CEES exposure to 2-ATA at varied moisture levels (Figure 7.13) revealed that only the samples with increased moisture levels show evidence of reaction. S 2p spectra of the ATA-Humid and ATA-Wet samples reveal the presence of two different sulfur species, a thioether at 163.4 eV and an oxidized sulfur feature at approximately 166 eV. Only in the ATA-Wet sample are changes to the N 1s and Cl 2p. A new N 1s band at 401.4 eV is consistent with an ammonium or a quaternary nitrogen species, while the Cl $2p_{3/2}$ at 197.7 eV is consistent with ammonium chloride.

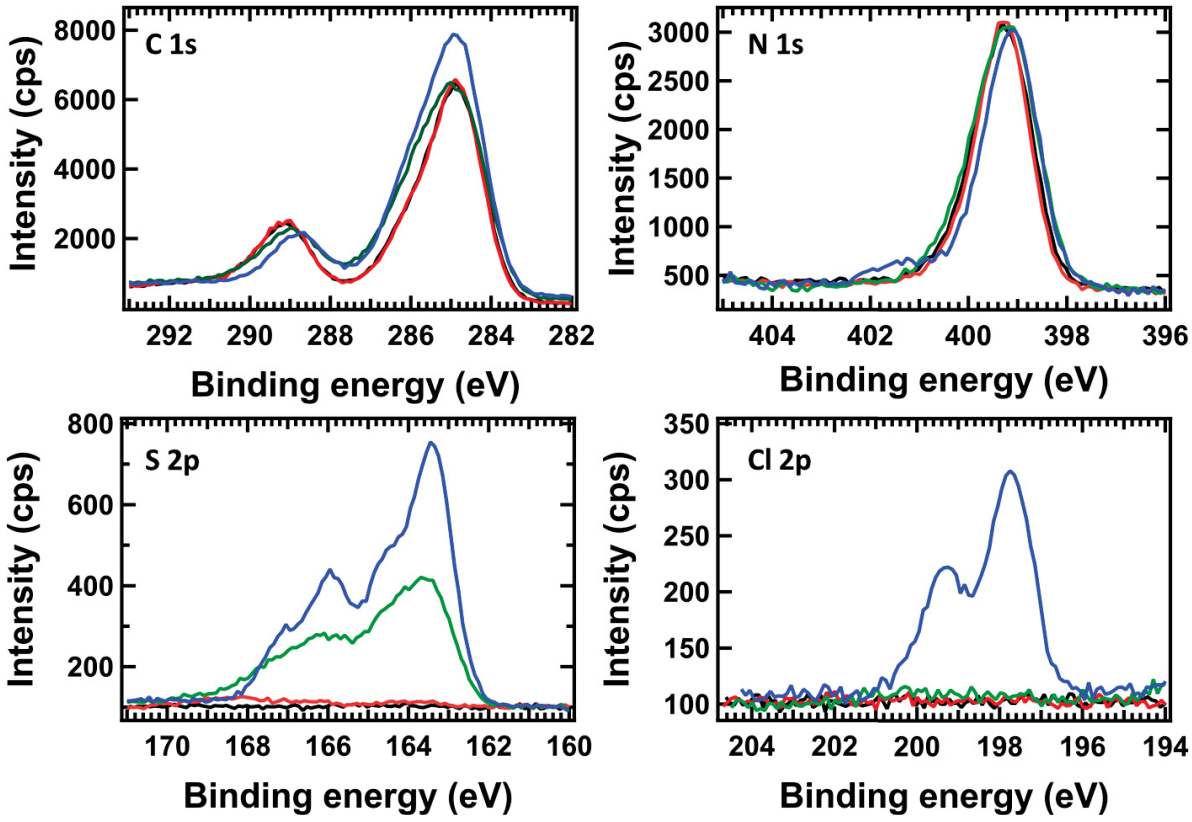

Figure 7.13 XPS spectra of 2-ATA of 2-aminoterephthalic acid before (black) and after (colored) 2-CEES exposure under various moisture conditions.

7.3.5.3 Nuclear Magnetic Resonance Spectroscopy

NMR spectra of the 2-ATA samples (Figure 7.14) were consistent with the findings of the XPS and ATR data, and the 2-CEES/2-CEES reaction product was only detected in the ATA-WET sample. The presence of more than nine different aliphatic signals from 0-60 ppm suggests that 2-CEES reacts and forms several reaction products. Under these wet conditions, 2-CEES may react with water directly or with the deprotonated carboxylic acid groups of the 2-ATA linker.

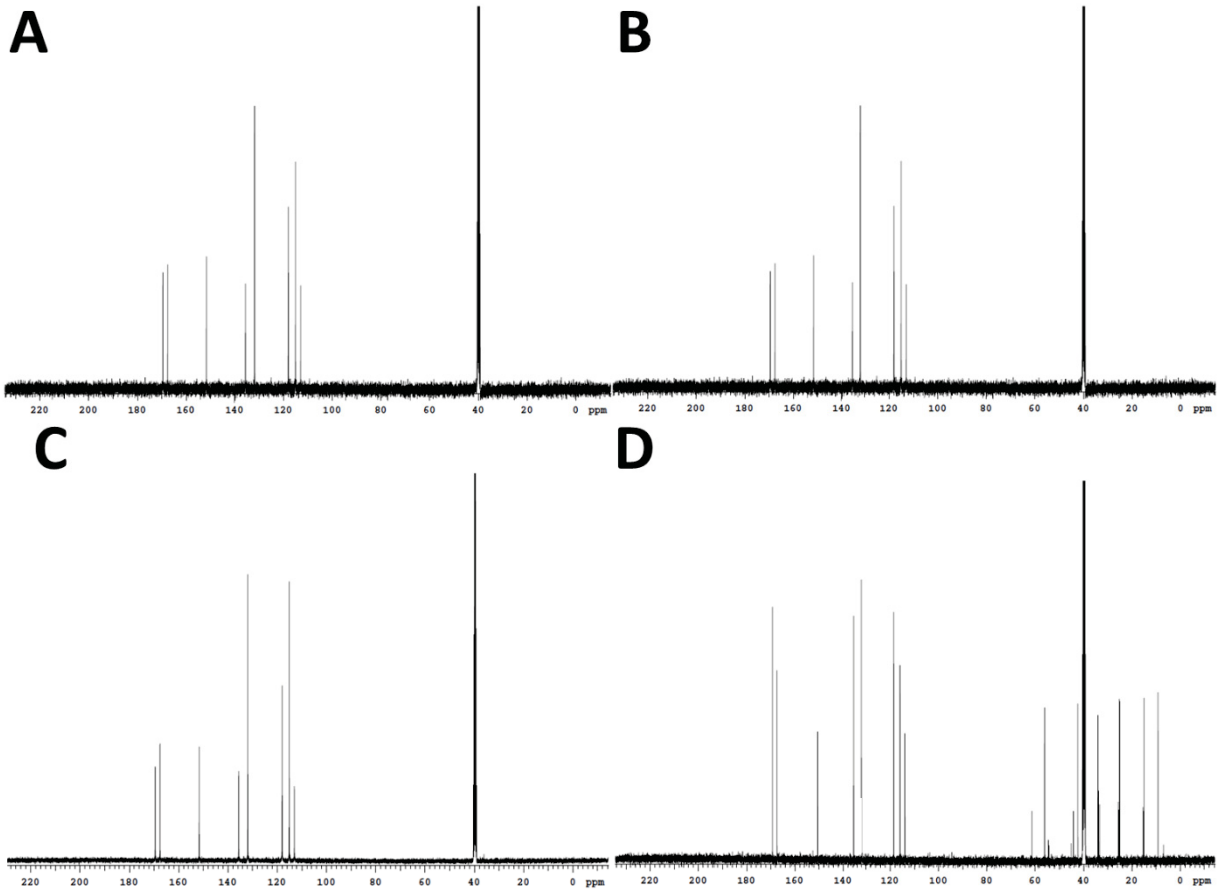

Figure 7.14 ^{13}C NMR of 2-aminoterephthalic acid before (A) and after (B-D) 2-CEES exposure under various moisture conditions (ATA-DRY=A, ATA-HUMID=B, and ATA-WET=C). All NMR samples were dissolved in d_6-DMSO.

7.3.6 Humidity Study

It appeared from the 2-ATA study that 2-ATA alone was not reactive to 2-CEES; 2-ATA required the presence of a significant amount of water to drive the reaction forward. Because UiO-66-NH_2 has such a significant water loading under these ambient conditions, the presence of water within the pores might assist in the formation and stabilization of the thiiranium ion before the nucleophilic attack by the amine groups on the 2-ATA linker. To test the extent that water within the pores of UiO-66-NH_2 contributes to the reaction between UiO-66-NH_2 and 2-CEES and 2-ATA and 2-CEES, a series of jar-in-a-jar exposures were prepared under different humidity

conditions. 24-hour exposures of 2-CEES to UiO-66-NH_2 were performed at 0% R.H., 25% R.H., 50% R.H., and 75 % R.H. Samples were analyzed with ATR-IR, XPS, and DR-UV-Vis.

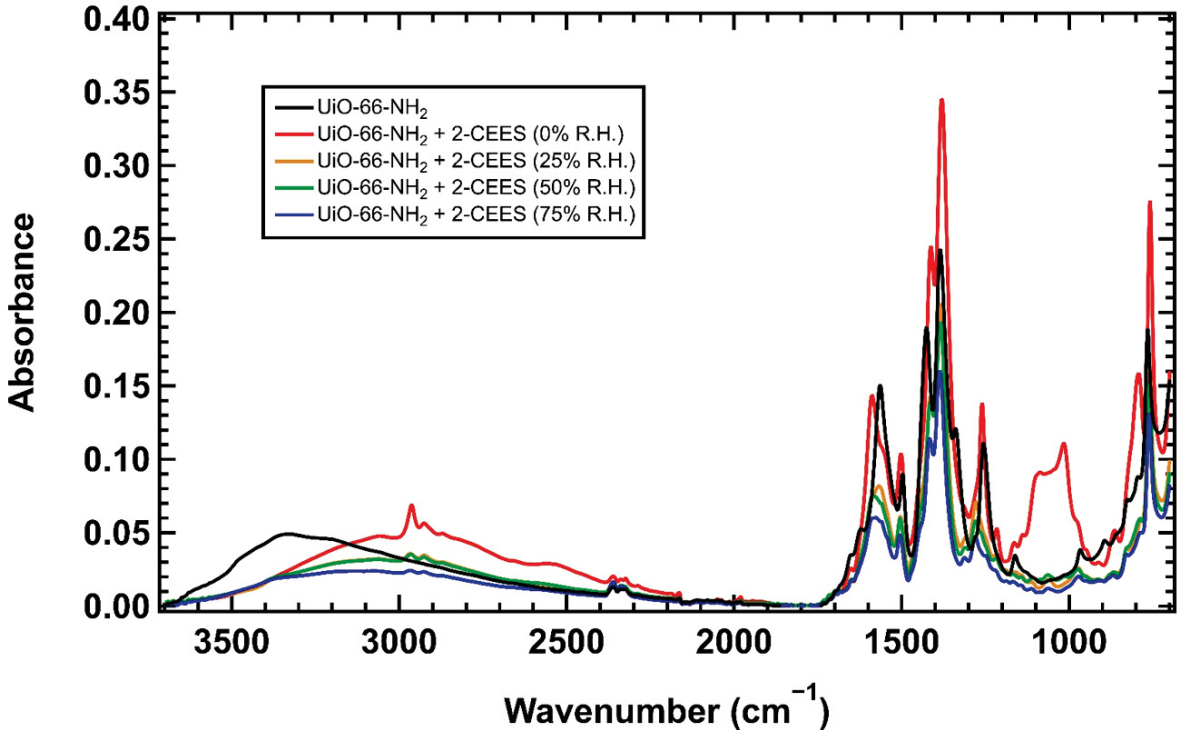

Figure 7.15 ATR spectra of humidity-controlled exposure of the UiO-66-NH_2 to 2-CEES. The black spectrum represents UiO-66-NH_2 before 2-CEES exposure, the red spectrum represents 2-CEES exposure at 0% R.H., the yellow spectrum represents 2-CEES exposure at 25% R.H., the green spectrum represents 2-CEES exposure at 50% R.H., and the blue spectrum represents 2-CEES exposure at 0% R.H.

7.3.6.1 ATR Results

While the spectra of UiO-66-NH_2 exposed to 2-CEES at relative humidities above 25% (Figure 7.15) are consistent with the ATR in Figure 7.6, the sample exposed at 0% R.H. had several distinct bands in the IR spectrum. In addition to a sharp band at 786 cm^{-1}, there is a broad feature that contains peaks at 1012 cm^{-1} and 1087 cm^{-1}. A clear feature at 1214 cm^{-1} corresponds well to the ωCH_2 vibration of 2-CEES, the ν(C–N) modes at 1423 cm^{-1} and 1258 cm^{-1} do not shift as much as it does in higher humidity samples. There is also a significant shift of the band at 1538

cm^{-1} corresponding to ν_{asym}(O-C-O) feature. In the 2800 cm^{-1} to 3000 cm region, the signal intensity for the C-H stretches associated with 2-CEES appeared larger for the UiO-66-NH_2, suggesting a higher 2-CEES loading within the MOF. For comparison, the ATR spectra of 2-ATA exposed to 2-CEES at each humidity level (Figure 7.16) showed no variation between the unexposed 2-ATA. These results suggested that 2-CEES reacted within UiO-66-NH_2 without the presence water.

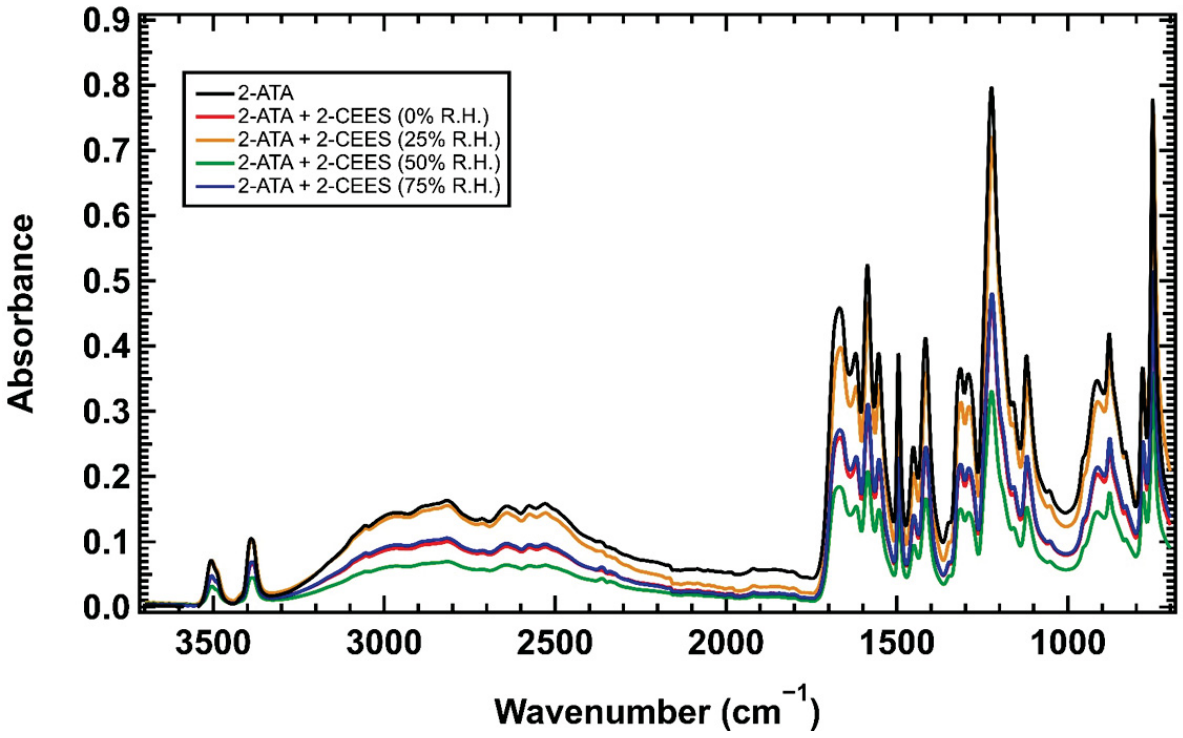

Figure 7.16 ATR spectra of humidity-controlled exposure of 2-ATA to 2-CEES. The black spectrum represents 2-ATA before 2-CEES exposure, the red spectrum represents 2-CEES exposure at 0% R.H., the yellow spectrum represents 2-CEES exposure at 25% R.H., the green spectrum represents 2-CEES exposure at 50% R.H., and the blue spectrum represents 2-CEES exposure at 0% R.H.

7.3.6.2 DR-UV-Vis Results

The DR-UV-Vis spectra UiO-66-NH_2 after treatment with 2-CEES under various humidity levels all showed an increase in the absorbance edge (Figure 7.17). An increase in the absorbance

edge was observed as humidity level increased for the reaction of 2-CEES and UiO-66-NH_2. The 2-ATA humidity study samples showed no color change, suggesting the lack of a reaction under these conditions. If the color change for UiO-66-NH_2 is due to the alkylation of the amine-functionalized linkers with 2-CEES, a comprehensive study that compares exposure concentrations, microcalorimetry measurements and DR-UV-Vis spectra may allow use UiO-66-NH_2 for the passive detection of mustard gas.

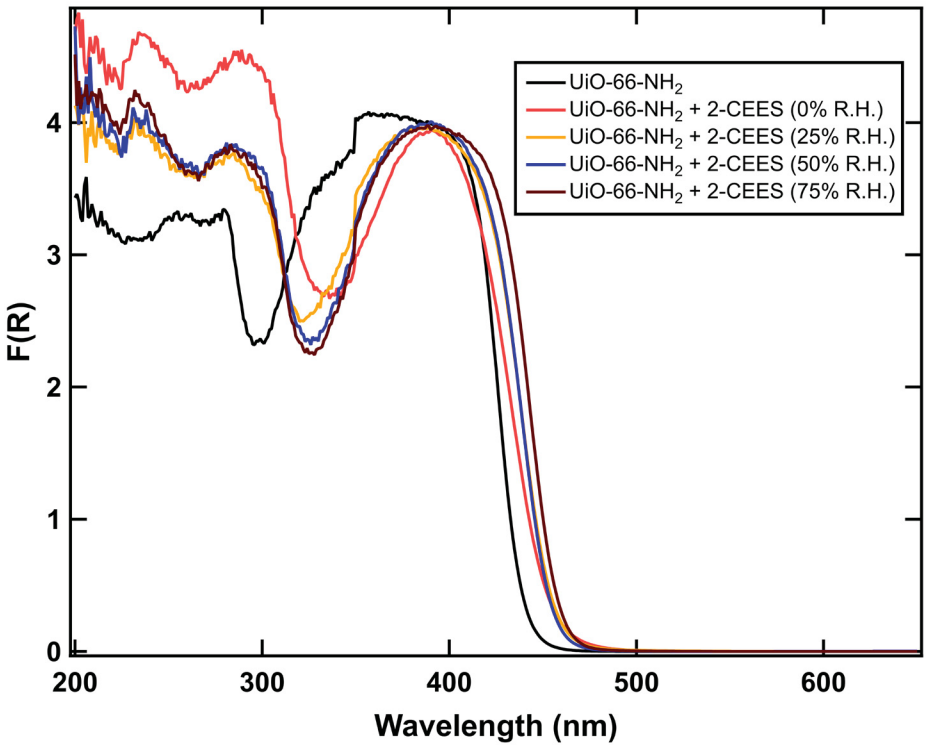

Figure 7.17 Diffuse-Reflectance UV-Vis data for UiO-66-NH2 exposure to 2-CEES at various humidity levels. The black spectrum represents UiO-66-NH2 before exposure, the red spectrum represents 2-CEES exposure at 0% R.H., the gold spectrum represents exposure at 25% R.H., the blue spectrum represents exposure at 50% R.H., and the purple spectrum represents exposure at 75% R.H. Spectra are normalized to the F(R) value at 400 nm.

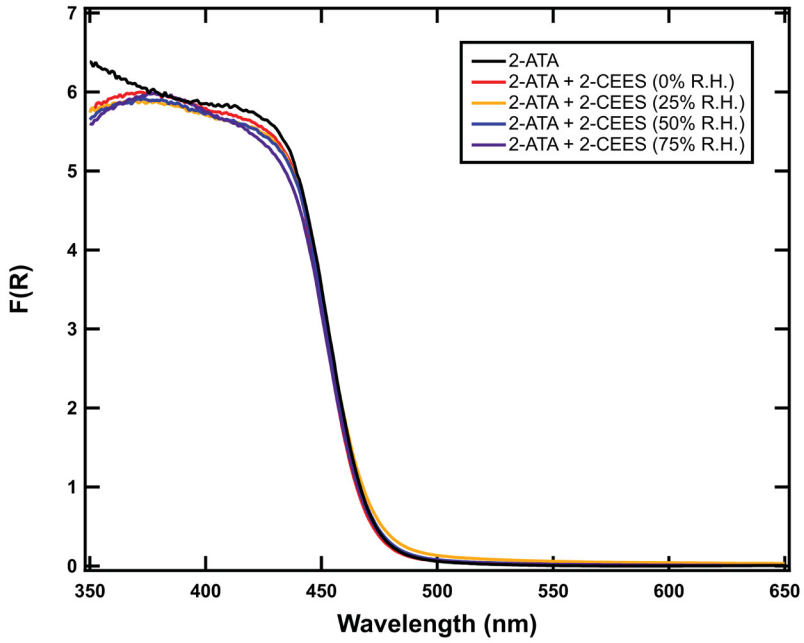

Figure 7.18 Diffuse-Reflectance UV-Vis data for 2-ATA exposure to 2-CEES at various humidity levels. The black spectrum represents 2-ATA before exposure, the red spectrum represents 2-CEES exposure at 0% R.H., the gold spectrum represents exposure at 25% R.H., the blue spectrum represents exposure at 50% R.H., and the purple spectrum represents exposure at 75% R.H. Spectra are normalized to the F(R) value at 400 nm.

7.3.6.3 XPS Results

In the N 2p region of the XPS, UiO-66-NH_2 exposed to 2-CEES under all humidity levels had a feature at approximately 401.9 eV. The 401.9 eV band at 25% R.H. sample had the highest percent of the total nitrogen signal at 13%, while the 401.9 feature for the 0% R.H. sample only constituted 4% of the total N 1s signal. All UiO-66-NH_2 samples had an S 2p feature at 163.3 eV (consistent with a sulfide species), The 0%, 25%, and 50% R.H. samples also contained an additional sulfur species with a peak at approximately 166 eV, which was indicative of an oxidized sulfur species, such as a sulfone or a sulfoxide. No changes to the O 1s, Cl 2p, or Zr 3d were observed.

The XPS spectra of 2-CEES exposed to 2-ATA under controlled humidity environments revealed little evidence of 2-CEES adsorption or reaction. None of the 2-ATA samples contained chlorine after 2-CEES dosing, and no changes to the N 1s spectrum were observed. Sulfur was present in the 2-ATA samples at relative humidities above 25%, but the signal was barely distinguishable from the XPS background

7.3.7 High Vacuum Exposure of 2-CEES to UiO-66-NH_2

While the results of the humidity study indicated that even under a 0% relative humidity environment, UiO-66-NH_2 reacted with 2-CEES, previously published work on the adsorption of water within UiO-66-NH_2 suggested that even under those conditions, UiO-66-NH_2 may still contain up to 3 mmol of water. To study the reaction of 2-CEES with UiO-66-NH_2 in an sample environment where we were confident that water was not adsorbed within the MOF, we performed a 2-CEES exposure to UiO-66-NH_2 after thermal activation at 423 K under high vacuum conditions. Dosing 2-CEES into the chamber at approximately 3-4 Torr captured the vapor pressure of 2-CEES at room temperature,[248] thus providing similar vapor exposure concentrations as the ambient pressure experiments.

7.3.7.1 Transmission IR of UiO-66-NH_2

In the transmission IR spectrum of our UiO-66-NH_2 sample post-activation (Figure 7.19), high absorbance levels from 1250 cm^{-1} to 1700 cm^{-1} occluded our ability to detect changes to aromatic-nitrogen vibrations that were observed in the ATR spectra. Fortunately, we were able to detect the N-H vibrations at 3513 cm^{-1} and 3395 cm^{-1}, as well as the zirconium hydroxyl feature at 3672 cm^{-1}, which all agree well with the literature. In the low wavenumber region, features at

1162 cm^{-1} and 1128 cm^{-1} likely corresponded to a combination of aromatic breathing vibrations of the MOF linkers.[75]

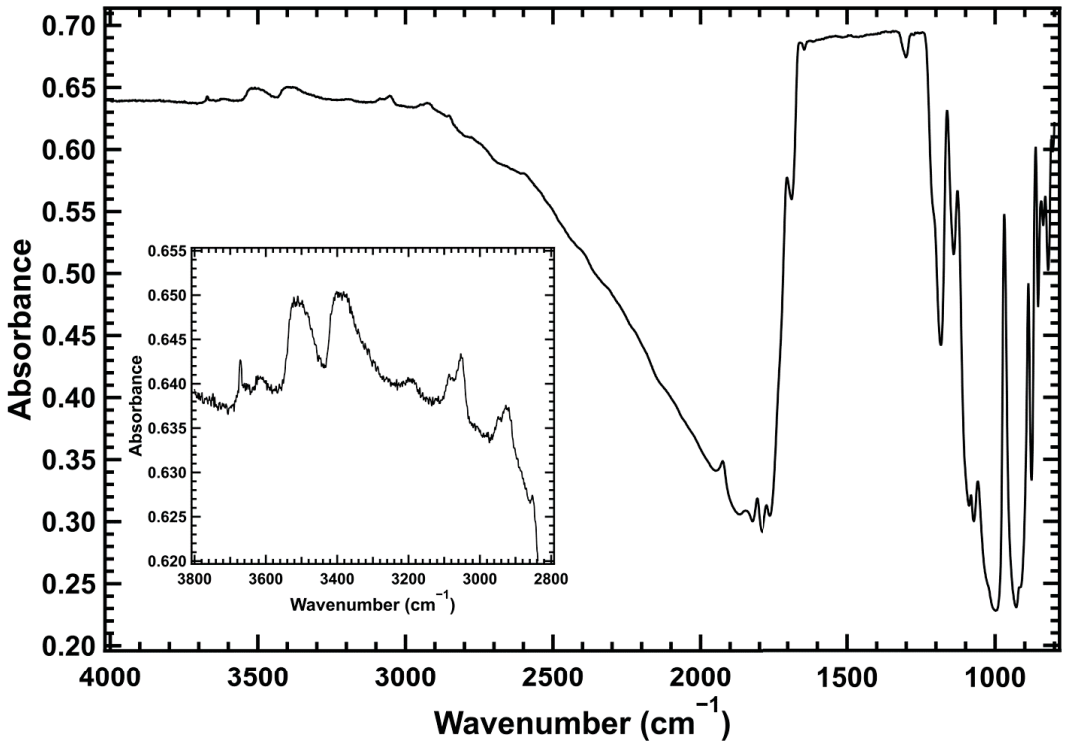

Figure 7.19 Transition IR spectrum of UiO-66-NH2 with inset of the high-frequency region. The background for this spectrum is a clean spot of mesh.

7.3.7.2 Uptake and Reaction of 2-CEES within UiO-66-NH_2

Upon the introduction of 2-CEES into the vacuum chamber, the overall absorbance of the sample increased drastically, preventing a detailed analysis of any features above 2000 cm^{-1} (Figure 7.20). During adsorption, a band at 1213 cm^{-1}, attributed to the ω($C(CH_2)$) vibration of 2-CEES, initially increases, then decreases in intensity as a new band at 1188 cm^{-1} forms. This band begins to emerge after less than an hour of exposure. The increase of a vibrational feature at 1064 cm^{-1} was initially attributed to the increase in the background absorbance levels, but may potentially be due to the formation of a covalent nitrogen-aliphatic carbon bond. The ν($C_{aliphatic}$-N) band for vapor-phase methylamine appears at 1044 cm^{-1},[249] while Hadži speculated the

ν($C_{aliphatic}$-N) mode for *N*-methylamine derivatives should appear around 1060 cm^{-1} based on the IR spectra deuterated samples.[250]

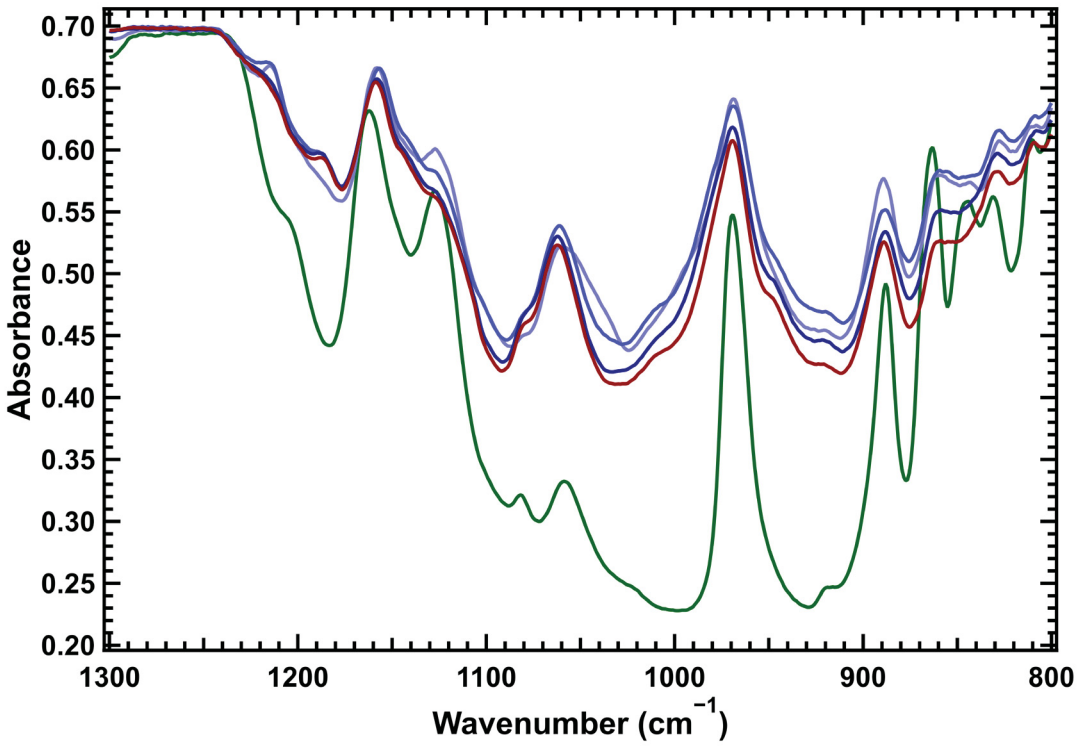

Figure 7.20 Transmission IR spectra of 2-CEES exposure to UiO-66-NH_2 from 800 to 1300 cm. The green spectrum represents the clean, unexposed MOF, the blue spectra correspond to the spectra during 2-CEES dosing, transitioning from light blue to dark blue over time, and the red spectrum represents the MOF at the end of 2-CEES dosing.

After 6 hours of 2-CEES exposure, the chamber was evacuated to below 1×10^{-6} Torr and the sample was heated to 423 K for 36 hours to desorb any weakly bound adsorbates. In the IR spectrum for UiO-66-NH_2 after 2-CEES exposure and thermal treatment (Figure 7.21), bands at 1064 cm^{-1} and 1187 cm^{-1} remained while a new feature at 1007 cm^{-1} emerged, which suggested that the reaction product bound strongly within the MOF. In addition to these new IR bands, the presence of vibration features at 2968 cm^{-1}, 2925 cm^{-1}, and 2854 cm^{-1} were consistent with previously reported C-H stretching vibrations of 2-CEES adsorbed within UiO-66. The feature at 2854 cm^{-1}, assigned as the ν($C–H_2$)$_{s,bent}$,[166-167] is redshifted by approximately 28 cm^{-1} from its

vibration in the gas phase, which may be due to its proximity to the formation of a covalent nitrogen-carbon bond.

For the alkylation of the 2-aminoterephthalic acid linkers, the formation of a secondary amine should be observable in the N-H stretching region of the IR spectrum due to the formation of a new IR feature. For reference, the secondary amine *N*-[2-(methylthio)ethyl]-benzeneamine has a vibrational band at 3360 cm^{-1},[251] while the reaction of UiO-66-NH_2 with acetic anhydride forms a secondary amine with a νN-H of 3344 cm^{-1}.[235] While background absorbance levels above 2000 cm^{-1} partially obscure our view, it appears that the νO-H and νN-H bands decrease in intensity and indicate that hydroxyl groups on the Zr cluster may also contribute to the reaction between 2-CEES and UiO-66-NH_2. The N-H stretching vibrations shift by approximately 30 cm^{-1} and while the band initially at 3395 cm^{-1} appears to broaden, we cannot say this definitively.

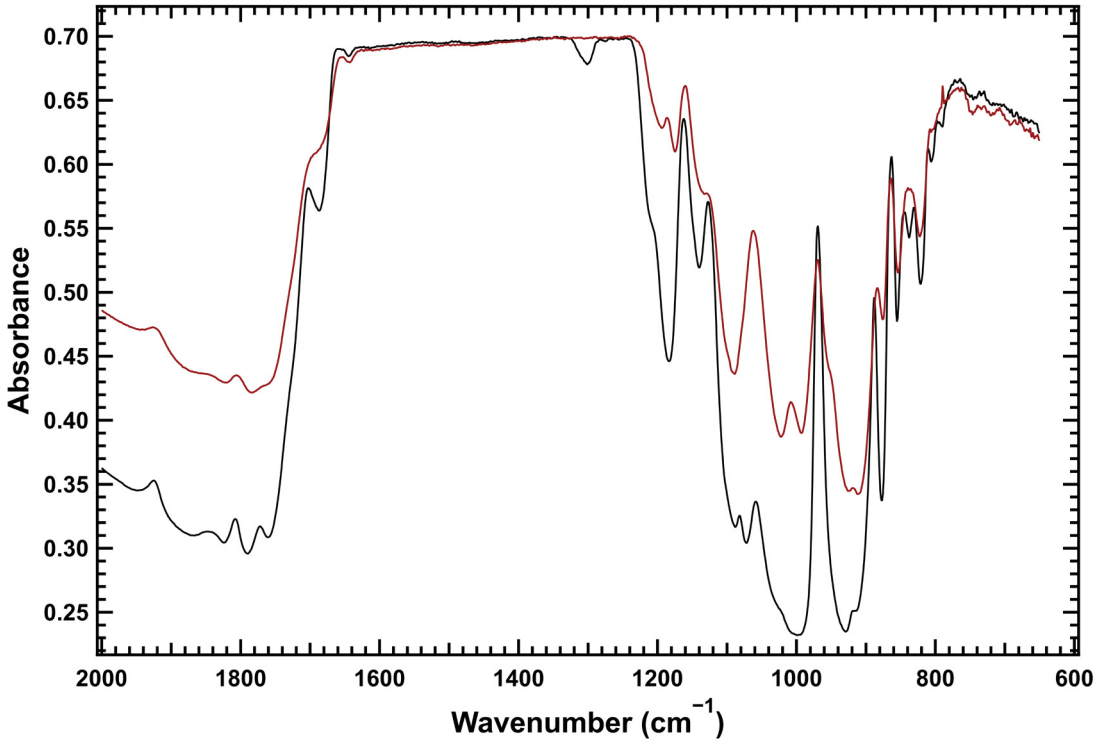

Figure 7.21 IR spectra of UiO-66-NH_2 before 2-CEES exposure (black) and after 2-CEES exposure and post-dose heating (red).

7.3.7.3 XPS Analysis of UiO-66-NH_2 Post-HV Exposure of 2-CEES

After recording the IR spectra of UiO-66-NH_2 post-2-CEES exposure and heating, the sample was removed from the high vacuum chamber and the sample was analyzed with XPS. While limited sample amounts prevented our ability to perform further DR-UV-Vis analysis, a distinct color change in the MOF was observed qualitatively (Figure 7.22), further suggesting that the reaction between 2-CEES and UiO-66-NH2 occurred.

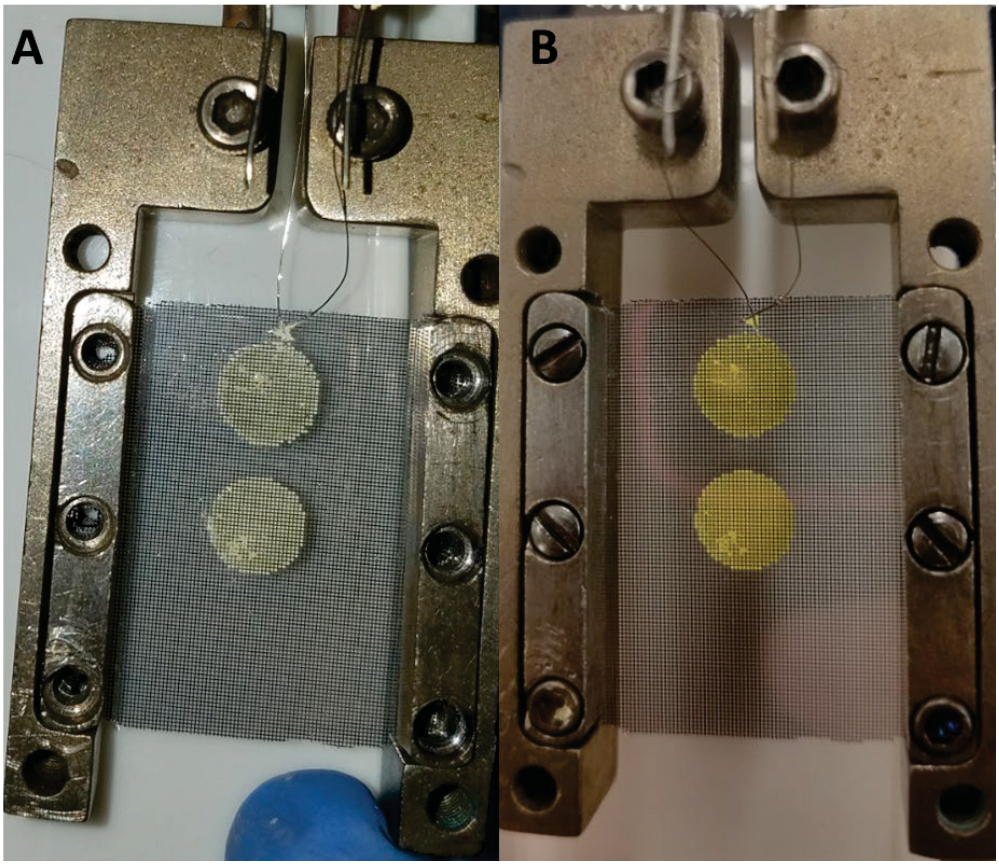

Figure 7.22 Photographic comparison of UiO-66-NH_2 before (A) and after (B) 2-CEES exposure and thermal treatment at 423 K.

While no changes to were observed for the Zr 3d, N 1s, and Cl 2p spectra of the sample after 2-CEES exposure under vacuum (Figure 7.23), the presence of a single sulfur species at S $2p_{3/2}$ =163.3 eV is consistent with binding energies of sulfides confirms the that 2-CEES did

irreversibly bind within UiO-66-NH_2. While it is certainly possible that 2-CEES may be reactively adsorbing at defect sites on the Zr cluster, the significant color change of the sample upon 2-CEES exposure suggests that even under vacuum conditions in the absence of water, 2-CEES interacts with the amine to form a strongly bound product that does not desorb from the MOF.

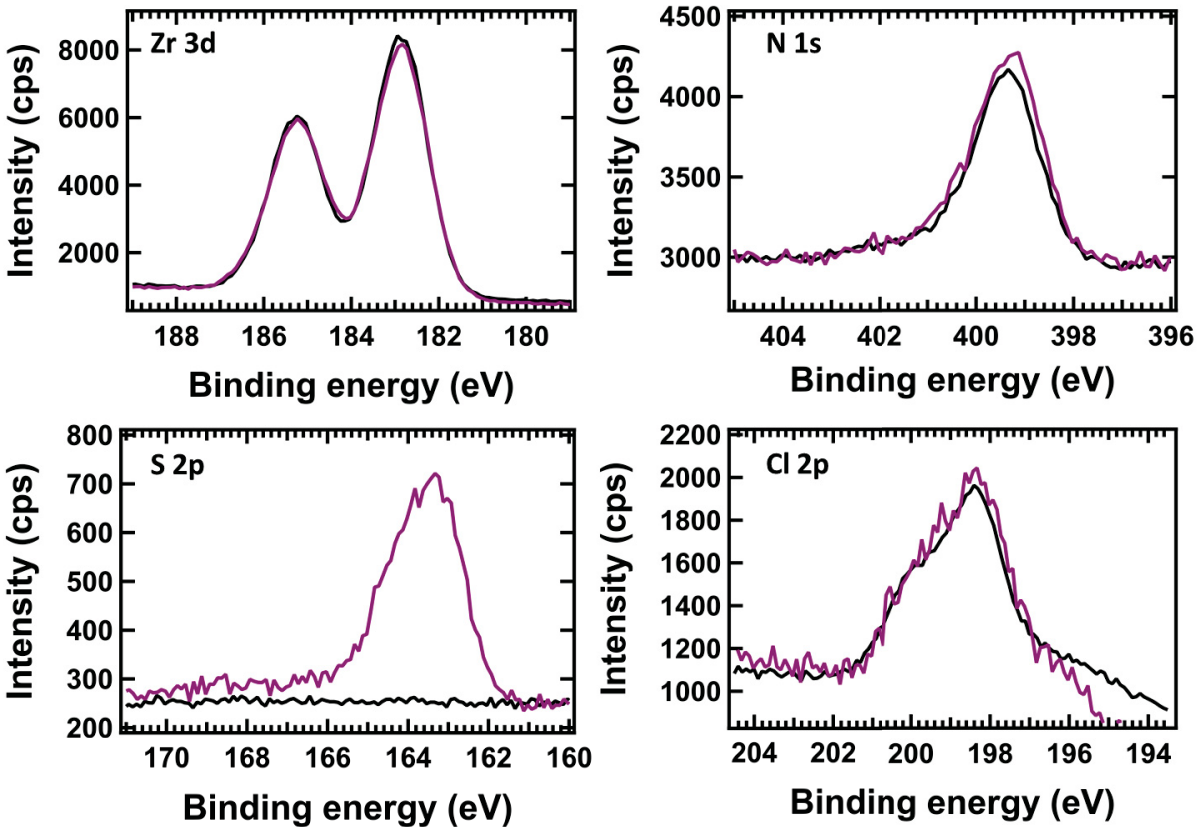

Figure 7.23 XPS Zr 3d, N 1s, S 2p, and Cl 2p spectra of UiO-66-NH_2 before (black) and after (purple) exposure to 2-CEES under vacuum conditions. Signal intensities were normalized to the Zr 3d signal.

7.3.8 The Role of Water

The ability for 2-CEES to react UiO-66-NH_2 under vacuum heavily indicates that water is not necessary for the reaction to proceed. The 2-aminoterephthalic acid linker alone only showed evidence of reaction with 2-CEES under high humidity levels or partial solvation. The difference in results between UiO-66-NH_2 and 2-ATA suggested that while 2-CEES reacts with UiO-66-NH_2

through the amine groups, either the presence of the Zr cluster or the porosity of the MOF allows the reaction to occur in dry environments. The slow diffusivity of 2-CEES through the triangular pore apertures within UiO-66 suggests that a 2-CEES molecule within a given UiO-66-NH_2 pore effectively has a longer surface residence time as compared to 2-CEES molecules interacting with the non-porous 2-ATA. Additionally, the dielectric constant within the pore environment of the MOF may facilitate the formation of the 2-CEES thiiranium intermediate before the nucleophilic attack by the amine groups of UiO-66-NH_2. Future work could focus on investigating the reaction of 2-CEES within other amine-functionalized MOFs to probe how changes to pore topology, pore size, and inorganic clusters affect the MOF's reactivity to 2-CEES. Additionally, we hope that computational support may provide further insight into the dielectric constant within the pore environments of UiO-66-NH_2.

Although water was not necessary for 2-CEES to react with UiO-66-NH_2, the presence of adsorbed water within the pores of UiO-66-NH_2 under ambient conditions appeared to increase the reaction rate. While potential product formation occurred in the vacuum chamber within 1 hour of dosing 2-CEES, DR-UV-Vis spectra of UiO-66-NH_2 exposed to 2-CEES for various periods under ambient conditions (Figure 7.24) reveal that UiO-66-NH_2 undergoes a color change within the first few minutes of 2-CEES exposure. While the presence of other ambient gases, such as oxygen or carbon dioxide, may provide some synergistic effect, the fact that absorption edge in the DR-UV-Vis spectrum increased as the exposure humidity increased indicated that water is likely speeding up the reaction process. Again, computational insight into reaction UiO-66-NH_2 with 2-CEES may help provide us with a reaction mechanism that may explain how co-adsorbed water within the MOF aids in the reactive adsorption and dehydrohalogenation of 2-CEES.

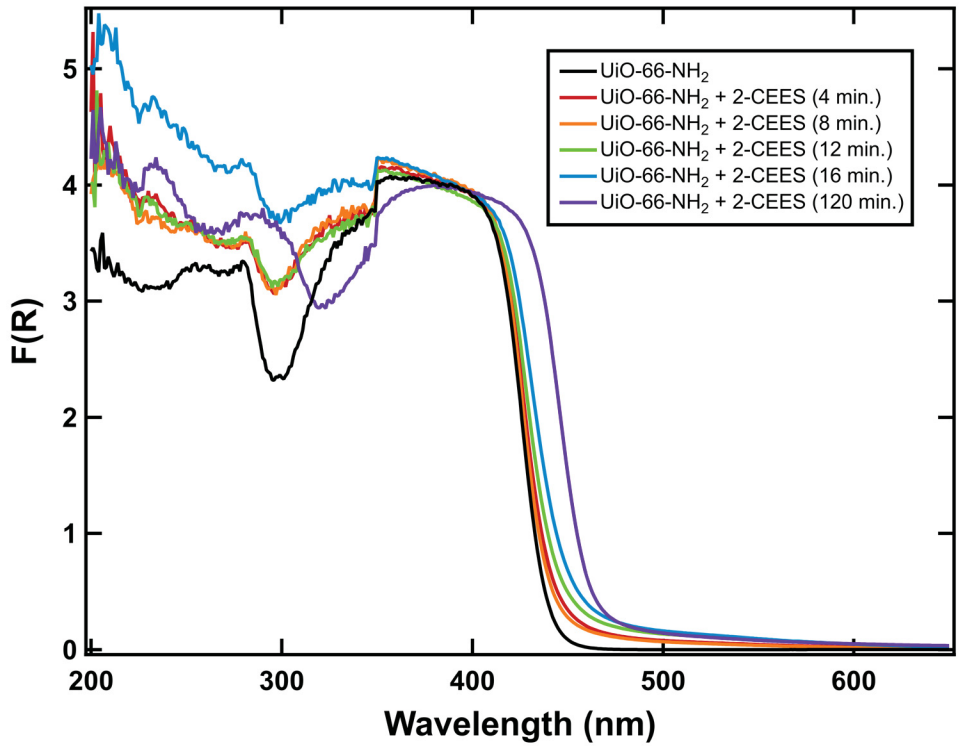

Figure 7.24 DR-UV-Vis spectra of UiO-66-NH2 exposed to 2-CEES for different durations. Spectra are normalized to the F(R) value at 400 nm.

7.4 Summary

The reaction of 2-CEES with UiO-66-NH_2 was studied under a wide variety of exposure conditions to probe the role of co-adsorbed water within the MOF. XPS, DR-UV-Vis and infrared spectroscopy revealed that under ambient conditions, 2-CEES reacts with UiO-66-NH_2 under all humidity levels studied and increased humidity levels appeared to result in a higher extent of reaction. While 2-CEES reacts with the amine groups of UiO-66-NH_2, 2-ATA is not reactive to 2-CEES at lower humidity levels. Based on these findings, we hypothesized water was required for 2-CEES to react with the amine groups of both 2-ATA and UiO-66-NH_2, and that the presence of adsorbed within UiO-66-NH_2 at explained why 2-CEES still reacted with UiO-66-NH_2 under low relative humidity environments. To prove this, we performed an exposure of 2-CEES to UiO-66-NH_2 in vacuum to ensure anhydrous conditions.

The vacuum-based exposure of 2-CEES to a "water-free" UiO-66-NH_2 sample demonstrated that 2-CEES can react with the MOF in the absence of adsorbed water, which suggests that either the presence of the Zr_6 node or pore environment of UiO-66-NH_2 enables the reaction to proceed. Hydrogen bonding between 2-CEES and the bridging hydroxyls of the node may orient the 2-CEES molecules for nucleophilic attack the amine groups, while the dielectric constant within the pores of UiO-66-NH_2 may stabilize a reaction transition state with 2-CEES in a similar fashion of water. Further work is required to elucidate the role of both the node and the pore, including studying the reaction of UiO-67-NH_2 with 2-CEES and investigating whether the bridging hydroxyls on the UiO-66-NH_2 node are required for 2-CEES to react.

This study of the interactions between 2-CEES and UiO-66-NH_2 underscore the needs to perform experiments under both vacuum and ambient conditions, as the ability for Zr-MOFs to absorb large quantities of water likely affects the chemistry within the MOF pores. While fundamental vacuum studies are important for probing the interactions between MOFs and CWA simulants, this work demonstrates that the common atmospheric molecules such as water may have a significant impact on how these Zr-based MOFs react with CWAs like HD.

Chapter 8. Summary and Future Work

8.1 Summary of Results

The main goal of this dissertation was to develop a fundamental understanding of the chemical interactions of HD simulants with Zr-based MOFs, specifically UiO-66, UiO-67, and NU-1000. By identifying the mechanisms by which gas molecules adsorb within the pores of the MOF, and the kinetics and energetics associated with diffusion and desorption, we can synthetic tailor MOF materials through ligand functionalization, introduction of defect sites, metal cluster replacement, linker replacement, and nanoparticle encapsulation in order to optimize its ability to sequester and catalytically degrade HD into less harmful byproducts. The use of HD simulants, while primarily due to safety concerns in handling the live chemical agent, allows us to observe how changes in the adsorbate structure affect its chemical interactions with the MOF surface.

While extensive research has been performed to study the interactions of nerve agents and nerve agent simulants with Zr-based MOFs, very few studies have looked into the reaction of HD with Zr-MOFs, and none have provided atomic-level insight into the fundamental gas-surface interactions that occur. Within this thesis, we were able to identify the primary adsorption mechanism for HD simulants within Zr-MOFs, quantified the intracrystalline diffusion kinetics, and attempted to determine that desorption energetics. This work also provided insight into the effect that ambient moisture in the atmosphere has on the reaction of the HD simulant 2-CEES with the amine-functionalized UiO-66.

The majority of the experimental work conducted was performed in a UHV environment, which allowed for controlling the cleanliness of our surface, limit gas-gas collisions that may provide inaccurate data, and to the use of surface sensitive spectroscopic techniques. The utilization of mass spectrometry and infrared spectroscopy to monitor changes to the MOF surface

upon gas exposure and to monitor gas desorption in order to identify chemical reactions and quantify the rate of desorption. In addition to vacuum-based experiments, a variety of spectroscopic techniques used under ambient conditions allowed us to determine how the ambient environment affected the chemical interactions between our MOF samples and the HD simulants studied.

Prior to investigating the interactions of HD simulants with Zr-MOFs, we first studied the adsorption and transport of several linear alkanes within the Zr-MOF UiO-66. With infrared spectroscopy, we were able to determine that the adsorption of *n*-butane, *n*-pentane, *n*-heptane, and *n*-octane proceeded through the formation of a hydrogen bond with the μ_3–OH groups on the Zr clusters. In the case of *n*-butane and *n*-pentane, the complete saturation of the ν(O–H) band at 3674 cm^{-1} indicated that all the hydroxyl groups within the pores of UiO-66 were accessible for adsorption. The transport of *n*-butane and *n*-pentane were monitored via the intensity decrease of vibrational modes assigned to adsorbed alkanes and were modeled with an equation derived from Fick's 2nd law of diffusion in order to extract diffusion coefficients and diffusion energetics.

The uptake and transport of the HD simulants within the Zr-MOFs UiO-66, UiO-67, and NU-1000. Using infrared spectroscopy, we observed that much like the adsorption of linear alkanes, the adsorption of these HD simulants proceeded through the formation of hydrogen bonds between electronegative atoms on the simulants and the hydroxyl groups on the Zr cluster. From the redshift of the ν(O–H) band at 3674 cm^{-1} upon adsorption, we were able to determine that for UiO-66, HD adsorbs through the formation of hydrogen bonds through its chlorine atoms and not its sulfur atom. While the diffusivities for 2-CEES at 273 K varied between MOF samples with varying defect densities and crystal sizes, the average activation energy of diffusion determined from Arrhenius plots demonstrated strong agreement between samples. As we increased the pore

size of the MOF, the activation energy of diffusion and decreased and the rate of diffusion increased, suggesting that transport between the pore apertures act as the rate limiting process for diffusion.

In an attempt to determine how strongly 2-CEES adsorbed to each Zr-MOF, a series of temperature programmed desorption studies were performed with the data analyzed through inversion analysis to provide an activation energy of desorption and desorption prefactor. Unfortunately, the slow diffusivity of 2-CEES through each MOF likely acts as the rate limiting process for the majority of the TPD experiment, preventing us from extracting accurate desorption information. We have begun to employ stochastic models using the Kinetiscope software in order to simulate the TPD spectra, and have found that the activation energy of desorption for 2-CEES appear to be over 40 kJ/mol higher than the value determined from inversion analysis.

The reaction of UiO-66-NH_2 was investigated using a combination of UHV and ambient pressure spectroscopic methods. While 2-CEES appears to readily react with UiO-66-NH_2 under ambient conditions, the reaction of 2-CEES with the MOF's linker, 2-aminoterephthalic acid, did not proceed unless in the presence of high levels of water vapor. A study of 2-CEES exposed to UiO-66-NH_2 under several relative humidity levels suggest that water assists in the reaction of 2-CEES to UiO-66-NH_2, but a subsequent vacuum-based study revealed that UiO-66-NH_2 reacts with 2-CEES without water presence. The ability for 2-CEES to react with UiO-66-NH_2 without coadsorbed water suggests that the confined porous environment provides a dielectric that enables the reaction to proceed.

8.2 Future Work

Future work within the Morris group should complete a comprehensive study for the diffusion of molecules through MOFs that examines how changes in crystal size, defect density, and pelletization pressure affect the energetics of diffusion and well as the overall rate of diffusion. A study of this nature would help determine the role that grain boundary diffusion plays in the overall kinetics of diffusion, and would give us more rigorous data to use in our Kinetiscope model for simulating TPD spectra. The use of thinner sample meshes as well as attempting to synthesize single layer MOF films from atomic layer deposition may help us study the desorption of 2-CEES from Zr-MOFs with limited effects from bulk diffusion.

In the study of the desorption kinetics of CWA simulants and other small molecules from MOFs, future work should include studies that determine the equilibrium adsorption enthalpy for various adsorbates through either calorimetry experiments or variable temperature infrared spectroscopy (VTIR). In the VTIR experiments can probe the relative concentration of bound gas molecules at a given temperature and pressure, thus enabling us to be able to perform adsorption isotherms. The fractional occupation of the hydroxyl group would allow us to determine the relative occupancy of hydrogen bonding sites within the MOF. Furthermore, recording time-resolved IR spectra upon simulants exposure to the MOF samples at various temperatures and pressures would also provide information on the kinetics of adsorption and diffusion.

Due to the time intensive nature of UHV-studies of gas-surface interactions, the implementation of a high-throughput screening method to quickly identify MOFs that demonstrate high activities to CWA degradation or long CWA breakthroughs will allow researchers to focus surface science studies on materials with desired properties. While mass spectrometric methods of determining simulant breakthrough and characterizing reaction byproducts are effective, the ion

fragment patterns of many CWA degradation products remain quite similar to the fragment patterns of the unreacted agents. The installation of a chromatographic technique to differentiate between simulant breakthrough and reaction byproduct could potentially allow us to focus on materials that demonstrate catalytic activity to CWA decontamination. In order for a screening method to be successful, we must establish a strong materials pipeline so that sufficient amounts of MOF material are available for throughput testing, surface studies, and sample characterization.

Finally, there is a need to implement better ambient-pressure spectroscopic techniques to provide *in operando* analysis of the reactions between CWAs and Zr-MOFs. As was demonstrated in Chapter 7, the ability for these MOFs to sequester water under even low relative humidity environments indicate that the reaction environment within the pores of the MOF may be significantly different than when studied under UHV. In addition to water, other gases present in the ambient environment, such as oxygen, carbon dioxide, and carbon dioxide, have the potential affect the reactivity of MOFs to CWAs. For MOFs that change color upon the adsorption or reaction with gas molecules, diffuse reflectance UV-Vis spectroscopy can provide rate kinetics. Additionally, techniques such as solid-state NMR, X-ray absorption fine structure, and near-ambient pressure XPS could allow us to identify reaction products, observe changes to the coordination environment of the metal clusters and functional groups, and identify the chemical speciation of adsorbed CWAs.

Zr-based metal-organic frameworks possess the high surface area, thermal stability, chemical robustness, and tunability that make them ideal for use as sorbents and heterogeneous catalysts for CWA decomposition. In order to optimize Zr-MOFs through ligand functionalization, pore size, and chemical functionality, we need to understand how CWAs adsorb and diffuse through the MOFs. This work provided fundamental research to identify the mechanism of

adsorption of HD simulants within several Zr-MOFs as well as determine the kinetics of diffusion. Through TPD experiments and stochastic simulations, we began to assess the binding strength of HD simulants at adsorption sites within the MOF. We hope that this work provides the groundwork for future studies that will one day create a series of MOF-based CWA decontamination strategies that ultimately render CWAs useless.

Appendix A: Chapter 4 Supplemental Information

A.1 Temperature Programmed Desorption

Temperature programmed desorption (TPD) was used as a characterization tool to determine the required post-exposure heating to remove 2-CEES multilayers that had adsorbed onto the external crystal surface of the MOF prior to performing the isothermal diffusion experiments. After dosing 2-CEES to saturation, the sample was held at 176 K for at least 20 minutes to allow the UHV chamber to equilibrate. TPD 2-CEES from the Zr-MOFs was accomplished by applying a 0.2 K/s linear temperature ramp while monitoring the desorption of 2-CEES molecules from the MOF surface with a double differentially pumped quadrupole mass spectrometer (Extrel, MAX1000880APP3/4P8).

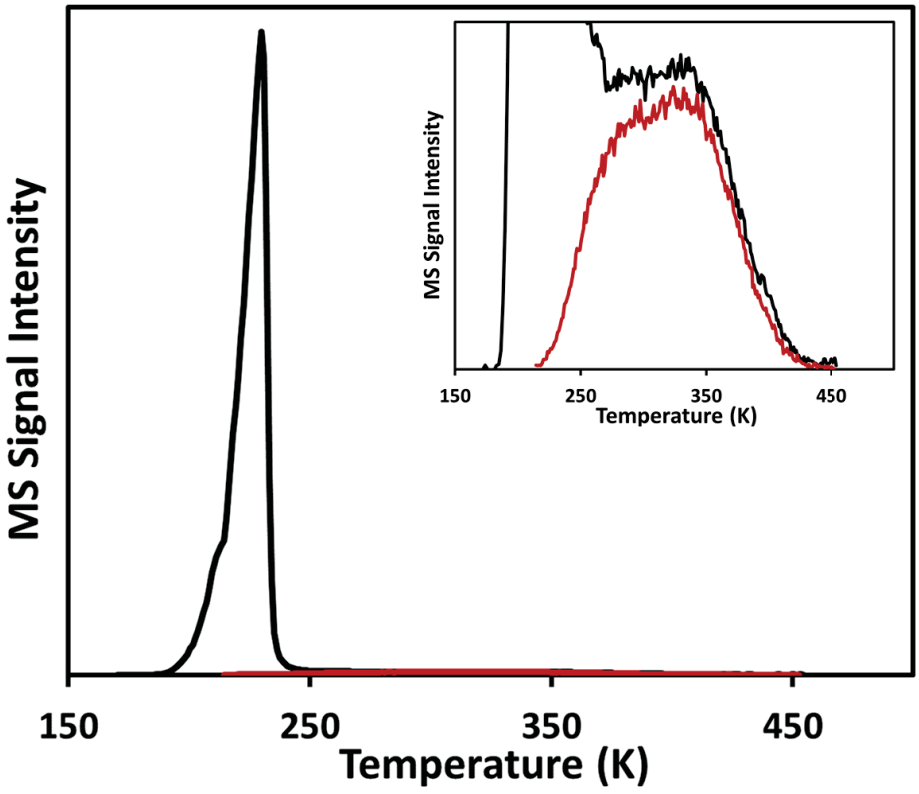

Figure A.1 TPD spectra of 2-CEES desorption from UiO-66. The black curve represents the TPD spectrum without any post-dose heating and the red spectrum represents the TPD spectrum after heating to remove 2-CEES multilayers.

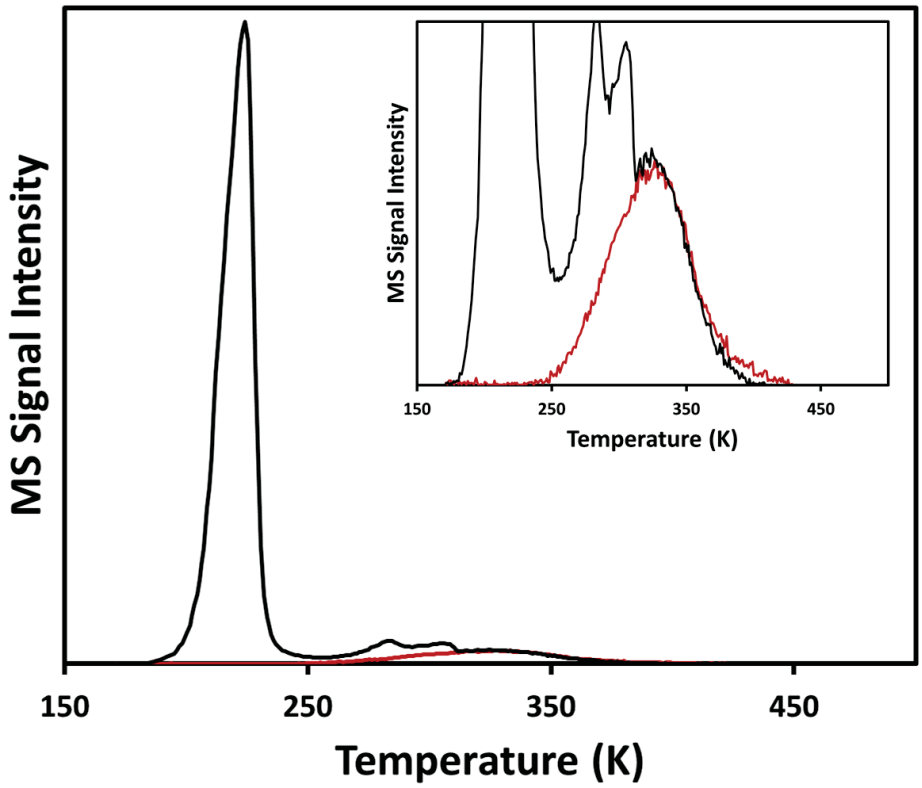

Figure A.2 TPD spectra of 2-CEES desorption from UiO-67. The black curve represents the TPD spectrum without any post-dose heating and the red spectrum represents the TPD spectrum after heating to remove 2-CEES multilayers.

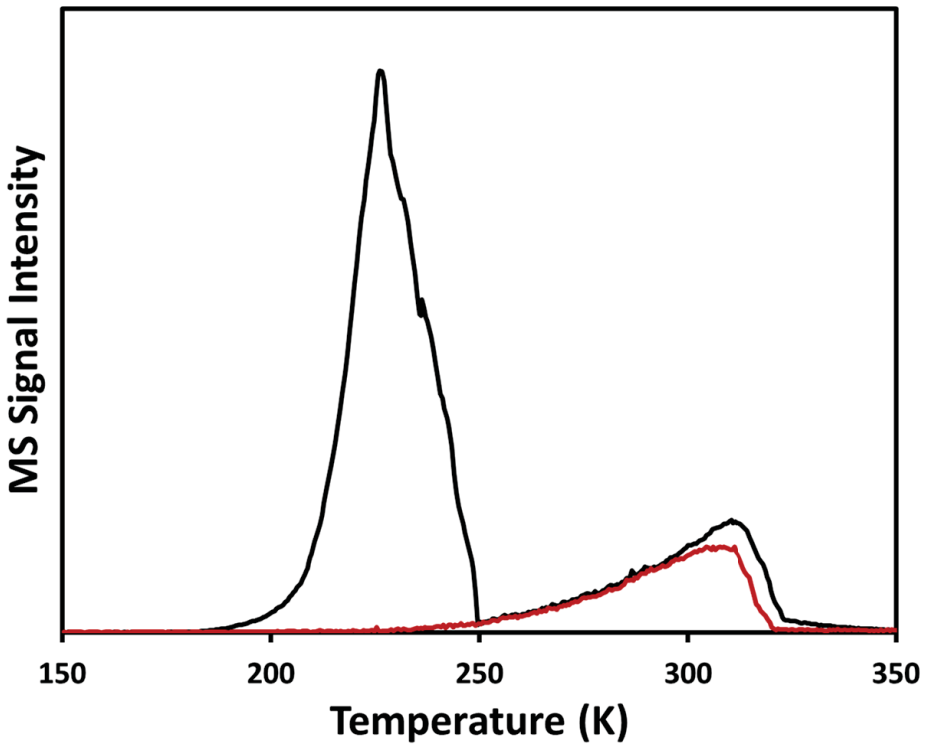

Figure A.3 TPD spectra of 2-CEES desorption from NU-1000. The black curve represents the TPD spectrum without any post-dose heating and the red spectrum represents the TPD spectrum after heating to remove 2-CEES multilayers.

A.2 NMR Diffusometry

The pulsed-gradient stimulated-echo sequence (PGSTE) was applied for all diffusion measurements. Self-diffusion coefficients of the pure 2-CEES were obtained from ^{1}H NMR (Figure A.4). All NMR experiments, including 1D, were performed using a 400 MHz Bruker Avance III WB NMR spectrometer equipped with a MIC probe coupled to a Micro5 multi-axis (z, x, and y-axis) gradient system and a 5 mm ^{1}H rf coil. Through NMR diffusometry, the Stejskal-Tanner equation was fit (Figure A.5) to the measured signal amplitude, $\boldsymbol{I}$, as a function of gradient strength, $\boldsymbol{g}$.

$$I = I_0 e^{-D\gamma^2 g^2 \delta^2 \left(\Delta - \left(\frac{\delta}{3}\right)\right)} \quad \textbf{(A.1)}$$

Where I_0 is the signal amplitude at $g = 0$, γ is the gyromagnetic ratio, δ is the effective gradient pulse length, Δ is the diffusion time between gradient pulses, and D is the self-diffusion coefficient. The PGSTE sequence used with the Micro5 probe system used a $\pi/2$ pulse lengths of 3.9 µs for cation (^{1}H). A repetition time of 20 s was used for cation diffusion measurements as the measured T_1 for the pure 2-CEES sample was 3.6 s. A diffusion time of Δ = 10 ms, a gradient pulse length of δ = 2.0 ms, and acquisition times of 2.4 s were used for the diffusion measurements. A maximum gradient strength of 45 G/cm, was used to achieve 90% signal attenuation in sixteen steps.

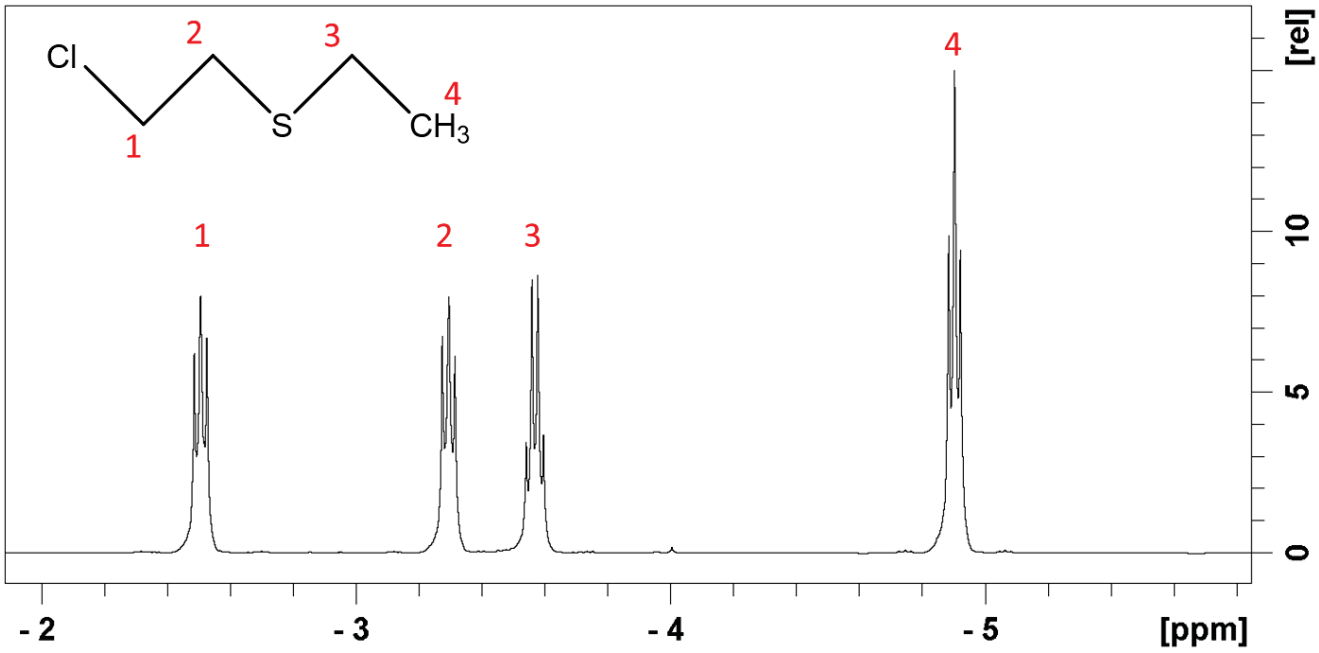

Figure A.4 ^{1}H NMR spectra of neat liquid 2-CEES. Chemical shifts are not referenced.

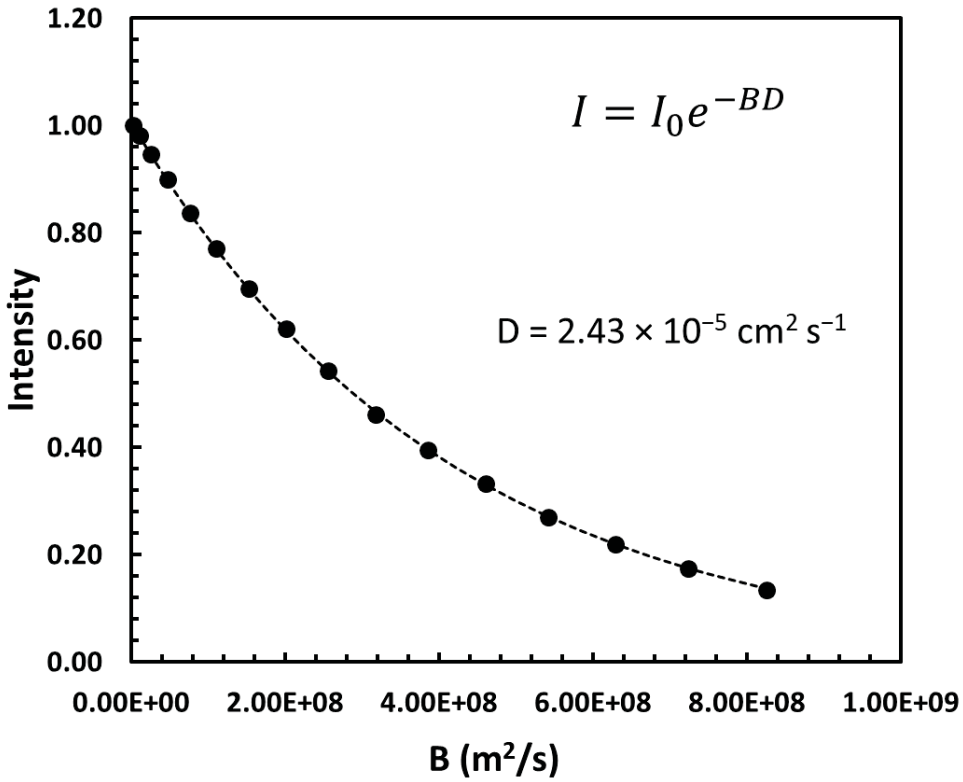

Figure A.5 NMR diffusometry of neat liquid 2-CEES. The black dots represent experimental data and the dashed line represents the Steiskal-Tanner equation fit for D = 2.43 × 10^{-5} cm^2 s^{-1} at 298 K. The B-term in the x-axis represents $\gamma^2 g^2 \delta^2 \left(\Delta - \left(\frac{\delta}{3}\right)\right)$ of the Steiskal-Tanner equation.

A.3 Dehydroxylation of UiO-66

UiO-66 was dehydroxylated under vacuum at 573 K for 12 hours to ensure the removal of the μ_3O–H groups of UiO-66.

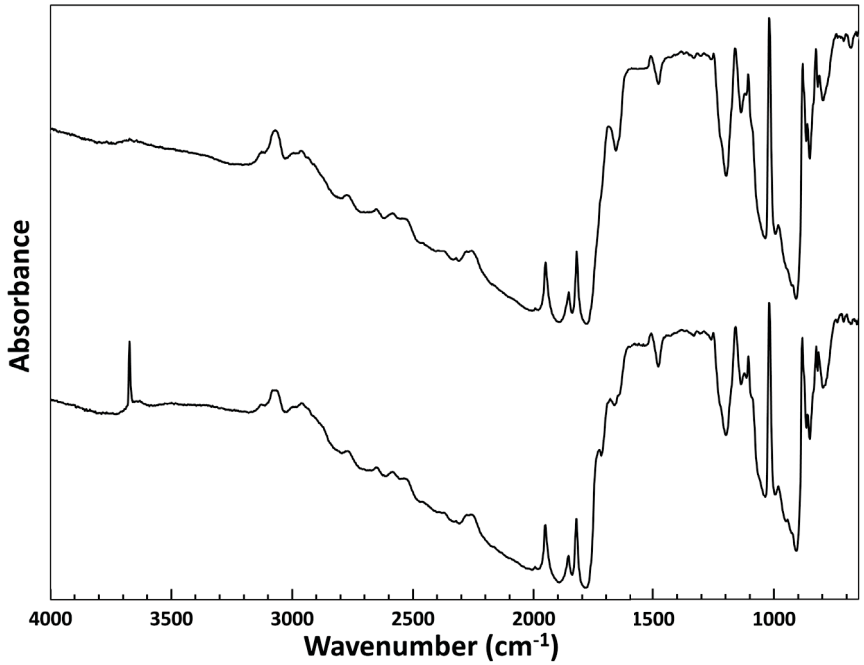

Figure A.6 Transmission IR spectra of UiO-66 before (below) and after (above) dehydroxylation at 573 K overnight.

Appendix B: Chapter 5 Supplemental Information

B.1 Introduction

The UiO-66 sample that was used primarily for the experiments reported in Chapter 4 and Chapter 5 was synthesized following a procedure for a "defect-free" UiO-66. To assess the quality of the sample, the UiO-66 sample was characterized with SEM, PXRD, TGA, and nitrogen adsorption isotherms. The characterization of the ideal UiO-66 sample (referred to as UiO-66-Ideal) revealed that the sample was highly crystalline and had a low defect density. In addition to the characterization of this sample, two other UiO-66 samples were characterized. Unfortunately, due to the limited amount of UiO-66 sample received, we were unable to perform the same level of characterization on samples UiO-66-I and UiO-66-II. Below we include the synthetic procedure for each MOF studied, the characterization of the MOF sample, and the isothermal diffusion data for UiO-66-I and UiO-66-II.

B.2 MOF Synthesis

The UiO-66 MOF samples were prepared by the Craig L. Hill group of Emory University and the Amanda Morris group of Virginia Tech and followed previously published solvothermal methods. (**UiO-66-I)** was prepared following a procedure described by Kandiah et al.[125] A solution of $ZrCl_4$ and 1,4-benzenedicarboxylic acid in DMF was heated at 353 K for 12 hours, then heated at 373 K for 24 hours. The reaction flask was then cooled to room temperature under ambient air and the solid product was filtered and rinsed in ethanol for 3 days at 333 K, then dried under vacuum at room temperature. **UiO-66-II** was synthesized following the same synthetic methods as UiO-66-I.

UiO-66-Ideal was prepared by Dr. Pavel Usov following a procedure reported by Shearer et al.[143] and described explicitly by Grissom et al.[54] 0.378 g (1.62 mmol) of $ZrCl_4$ and 0.539 g (3.24 mmol) of 1,4-benzenedicarboxylic acid were suspended in 10 mL of DMF and heated to 343 K for 30 minutes to fully dissolve the MOF precursors.[54] The solution was transferred to a Teflon-lined Parr reactor then heated at 493 K for 24 hours. After cooling room temperature, the white product powder was separated via centrifugation, washing with 4 aliquots of 10 ml of DMF, then immersed in 10 mL for 3 days, replacing the solvent each day. The final MOF product was dried in air at 333 K for 24 hours then 473 K for 1 hr.

A heavily defected UiO-66 (**UiO-66-Defected)** sample was synthesized following methods described by Shearer et al.[143] UiO-66-D was prepared by adding 0.862 g $ZrCl_4$, 0.200 mL H_2O, 0.615 g of 1,4-benzenedicarboxylic acid, and 1.519 g of trifluoroacetic acid (36 equivalents) to a Teflon-lined Parr reactor with 10 mL of DMF. The full dissolution of synthetic materials was accomplished by heating the reaction vessel at 343 K. The solution was then heated at 393 K for 72 hours. After cooling to room temperature, the white product powder was separated via centrifugation, washed with 4 aliquots of 10 mL of DMF, then immersed in 10 mL for 3 days, replacing the solvent each day. The final MOF product was dried in air at 333 K for 24 hours then 473 K for 1 hr.

A non-modulated UiO-66 sample (**UiO-66-NonModulated)** was prepared by adding 0.862 g $ZrCl_4$, 0.200 mL H_2O, and 0.615 g of 1,4-benzenedicarboxylic acid to a Teflon-lined Parr reactor with 10 mL of DMF. The full dissolution of synthetic materials was accomplished by heating the reaction vessel at 343 K. The solution was then heated at 393 K for 72 hours. After cooling to room temperature, the white product powder was separated via centrifugation, washed with 4

aliquots of 10 mL of DMF, then immersed in 10 mL for 3 days, replacing the solvent each day. The final MOF product was dried in air at 333 K for 24 hours then 473 K for 1 hr.

B.3 MOF Characterization

B.3.1 Scanning Electron Microscopy

All SEM images were recorded on an LEO Field-Emission SEM 1550 at the Virginia Tech Nanoscale Characterization and Fabrication Laboratory (NCFL). An 8 nm Pd/Pt coating was deposited onto samples via a Leica ACE600 Sputter Coater, and samples were affixed to the SEM puck via conductive tape.

Scanning Electron Microscopy (Figure B.1) of UiO-66-Ideal before and after pelletization revealed the MOF crystallites do not change upon applying 7500 psi of pressure. Peterson et al. previously measured the BET surface area of UiO-66 pelletized at various pressures, finding that UiO-66 densified at 10,000 psi resulted in a 0.01 % change in surface area and a 9% change in the total pore volume, as compared to the unpressed sample.[122] The UiO-66-Ideal crystallites were cubic shaped, approximately 200 nm in length, and monodisperse. The presence of void spaces between the pressed UiO-66 crystallites suggests that regions exist within the sample where intercrystalline diffusion may affect the overall transport rate of adsorbates diffusing through the MOF. SEM images of UiO-66-Defected and UiO-66-Nonmodulated showed crystallites that ranged in size from below 100 nm to over 200 nm. UiO-66-Nonmodulated crystals were the smallest and significantly varied in size.

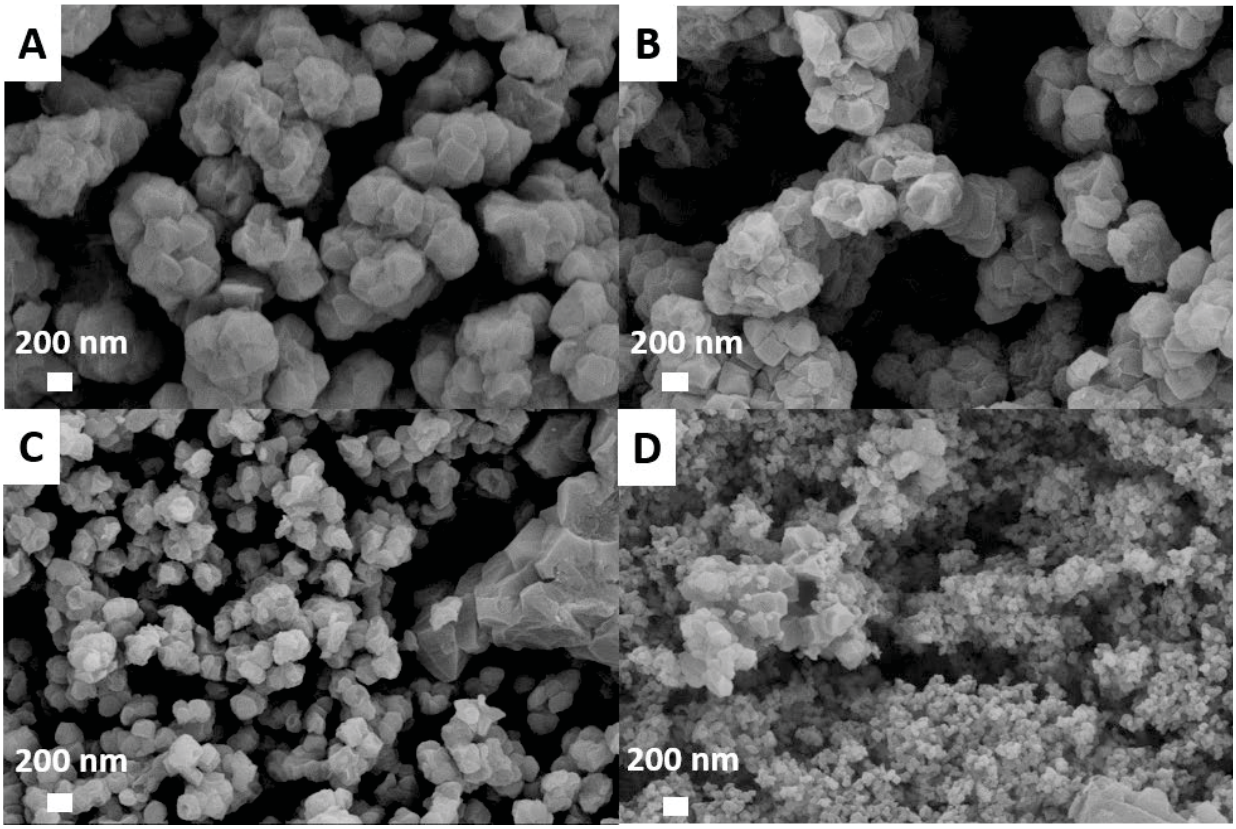

Figure B.1 SEM Images of UiO-66-Ideal pressed in sample mesh (A), loose UiO-66-Ideal powder (B), Pelletized UiO-66-Defected (C), and Pelletized UiO-66-NonModulated (D)

B.3.2 Powder X-ray Diffraction

PXRD patterns of each UiO-66 sample were collected on a Rigaku MiniFlex 600 powder X-ray diffractometer with Cu(Kα) radiation (1.5418 Å). The MOF powders were affixed to Si(510) sample disks. Diffraction patterns were collected from 2−50° at a scan rate of 10°/min and a 0.05° step size.

The PXRD results for UiO-66-Ideal (Figure B.2A) agreed well with the theoretical diffraction pattern for UiO-66 and are indicative of a crystalline material. For UiO-66-D (Figure B.2B), a broad feature from 2-7° cannot be assigned to pristine UiO-66. Shearer et al. observed the same broad peak in their defected UiO-66 MOFs and assigned that peak to **reo** nanoregions.[57,

[143] Because the **reo** phase is similar to UiO-66 missing one quarter of its Zr clusters, the broad, low angle feature was attributed to missing cluster defects within the UiO-66-D sample. The PXRD pattern for UiO-66-NonModulated (Figure B.2C) does not exhibit missing cluster defects, but the non-linear baseline throughout the spectrum and broad diffraction bands relative to the other two MOF samples indicate the presence of amorphous regions of UiO-66.

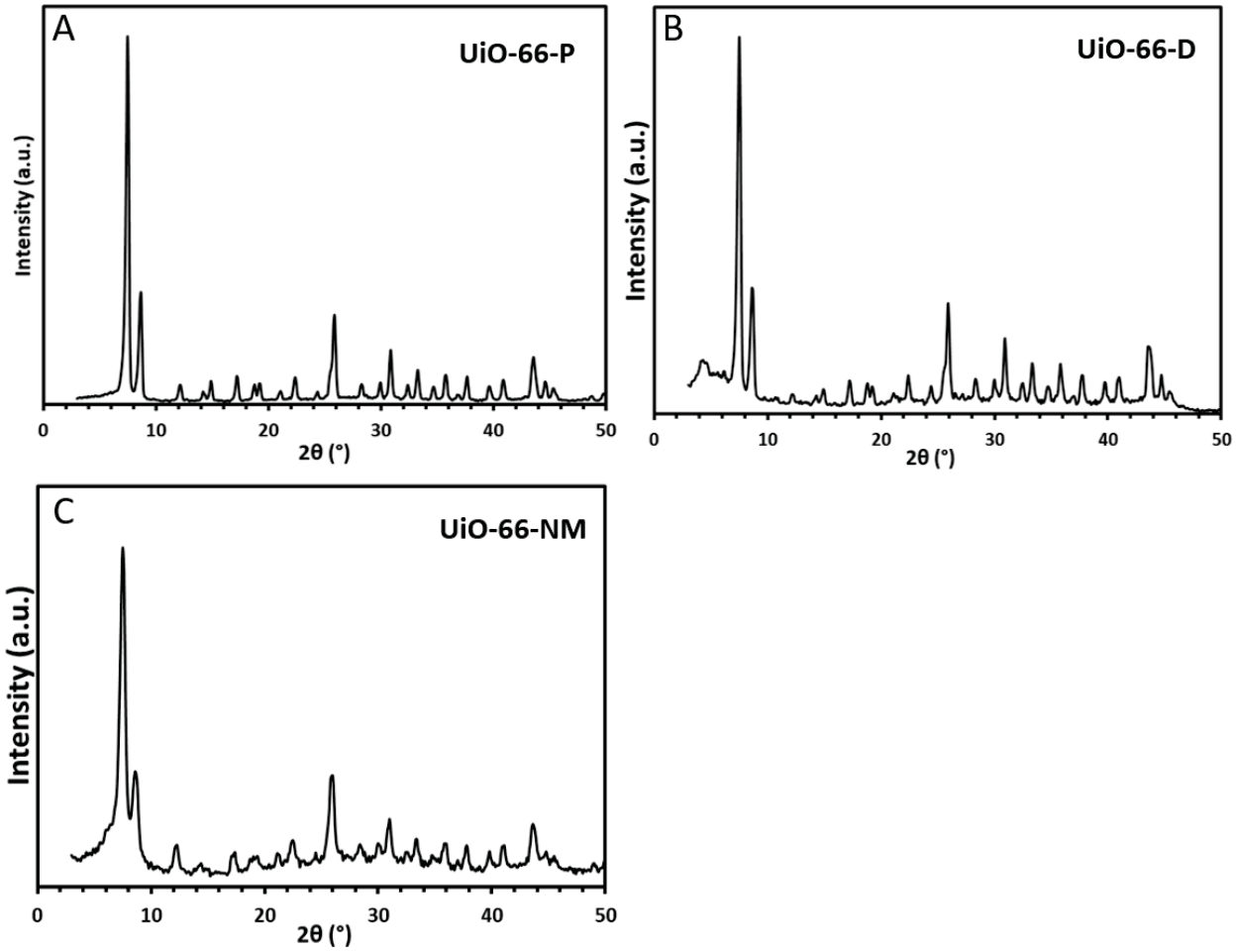

Figure B.2 PXRD patterns for UiO-66-Ideal (A), UiO-66-Defected (B), and UiO-66-NonModulated (C).

B.3.3 Thermogravimetric Analysis

The number of missing linkers and defect density of the UiO-66 samples were measured using a TA Qk500 thermogravimetric analysis (TGA) instrument. UiO-66 samples were placed in a platinum sample pan and heated at a 2 K min^{-1} heating rate under air.

TGA of UiO-66-Ideal and UiO-66-Defected are consistent with previously published TGA of UiO-66. The MOF undergoes a slight weight loss between 200 °C and 300 °C due to the dehydroxylation of the zirconium cluster and fully collapses At 450 °C. The fraction of missing linkers per Zr node was calculated with the following equation:[174]

$$\boldsymbol{W_{Theo.Plat.}} = \left(\frac{\boldsymbol{M_{Comp.}}}{\boldsymbol{M_{6\,ZrO_2}}}\right) \times \boldsymbol{W_{End}} \qquad \textbf{(B.1)}$$

Where $\boldsymbol{W_{Theo.Plat.}}$ is the weight of the theoretical TGA plateau, $\boldsymbol{M_{Comp.}}$ Is the molar mass of the sample studied, $\boldsymbol{M_{6\,ZrO_2}}$ is the molar mass of 6 moles of zirconium oxide, and $\boldsymbol{W_{End}}$ is the mass of the sample at the end of the heating ramp. For the UiO-66-Ideal sample, TGA analysis revealed UiO-66-Defected was missing 1.62 BDC linkers per node and UiO-66-Ideal was missing 0.02 linkers per mode, confirming the high quality of synthesis.

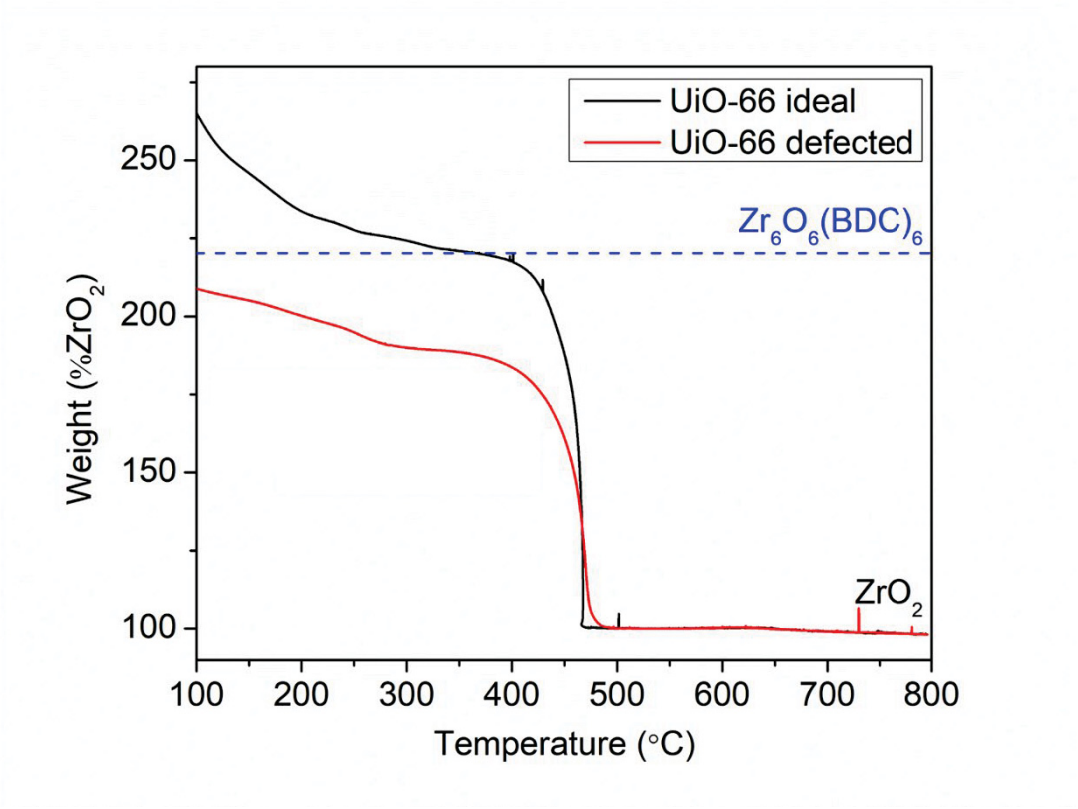

Figure B.3 TGA data for UiO-66-Ideal and UiO-66-Defected.

B.3.4 Surface Area and Pore Size Measurements

For the UiO-66-Ideal sample, BET measurements (Figure B.4) of the sample before and after calcination at 543 K in air for 70 hours showed that the removal of DMF and water from the pores of the MOF sample increased the surface area from 1022 $m^2\ g^{-1}$ to 1696 $m^2\ g^{-1}$. While the theoretical BET surface area for a non-defected UiO-66 is 1241 $m^2\ g^{-1}$,[143] our measured surface area upon calcination agrees with previously measured samples with the same amount of missing linkers per unit cell.[252] Pore-size analysis (Figure B.4B) of UiO-66-Ideal before and after calcination show a distinct increase in the pore volume of the tetrahedral pores, suggesting that residual DMF trapped in the MOF is predominantly located in the smaller UiO-66 pores. The UiO-66-Ideal was activated under ultrahigh vacuum pressures at 438 K instead of 543 K to ensure our sample was not dehydroxylated during activation.

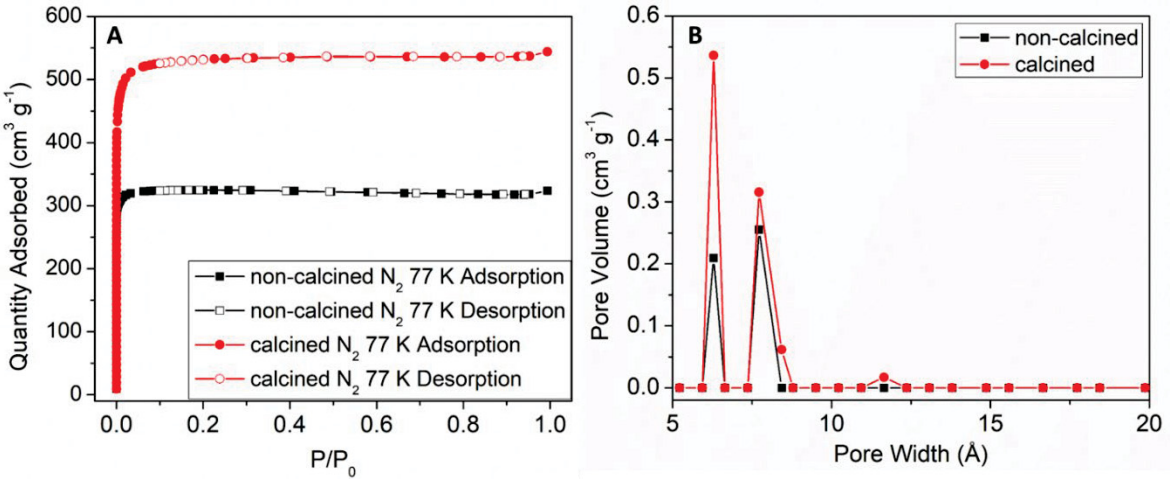

Figure B.4 N_2 adsorption isotherms at 77 K (A) and pore size distribution (B) of UiO-66-Ideal before and after thermal activation.

B.4 Diffusivity of 2-CEES through UiO-66-I and UiO-66-II

The diffusion of 2-CEES through UiO-66-I and UiO-66-II were measured by tracking the decrease in the $\omega C(CH_2)$ vibrational mode over time at several temperatures. Table B.1 lists the best-fit parameters of the Arrhenius plots.

Table B1 Arrhenius Parameters for the Diffusion of 2-CEES through UiO-66-I and UiO-66-II

Sample	Temp Range (K)	Ea diff (kJ/mol)	D_0 (cm^2 s^{-1})
UiO-66-I	223-295	61.4 ± 8.1	164.4
UiO-66-II	243-283	54.7 ± 9.7	13.6

References

1. Yang, Y. C.; Baker, J. A.; Ward, J. R., Decontamination of Chemical Warfare Agents. *Chem. Rev.* **1992,** *92* (8), 1729-1743.
2. Bajgar, J., Organophosphates/Nerve Agent Poisoning: Mechanism of Action, Diagnosis, Prophylaxis, and Treatment. *Advances in Clinical Chemistry, Vol. 38* **2004,** *38*, 151-216.
3. Shakarjian, M. P.; Heck, D. E.; Gray, J. P.; Sinko, P. J.; Gordon, M. K.; Casillas, R. P.; Heindel, N. D.; Gerecke, D. R.; Laskin, D. L.; Laskin, J. D., Mechanisms Mediating the Vesicant Actions of Sulfur Mustard after Cutaneous Exposure. *Toxicological Sciences* **2010,** *114* (1), 5-19.
4. Kehe, K.; Szinicz, L., Medical Aspects of Sulphur Mustard Poisoning. *Toxicology* **2005,** *214*, 198.
5. Szinicz, L., History of Chemical and Biological Warfare Agents. *Toxicology* **2005,** *214* (3), 167-181.
6. Smith, K. J.; Hurst, C. G.; Moeller, R. B.; Skelton, H. G.; Sidell, F. R., Sulfur Mustard: Its Continuing Threat as a Chemical Warfare Agent, the Cutaneous Lesions Induced, Progress in Understanding its Mechanism of Action, its Long-Term Health Effects, and New Developments For Protection and Therapy. *Journal of the American Academy of Dermatology* **1995,** *32* (5), 765-776.
7. Smith, B. M., Catalytic Methods for the Destruction of Chemical Warfare Agents under Ambient Conditions. *Chem. Soc. Rev.* **2008,** *37* (3), 470-478.
8. Gall, R. D.; Hill, C. L.; Walker, J. E., Selective Oxidation of Thioether Mustard (HD) Analogs by *tert*-Butylhydroperoxide Catalyzed by $H_5PV_2Mo_{10}O_{40}$ Supported on Porous Carbon Materials. *Journal of Catalysis* **1996,** *159* (2), 473-478.
9. Marques, A.; Marin, M.; Ruasse, M. F., Hydrogen Peroxide Oxidation of Mustard-Model Sulfides Catalyzed by Iron and Manganese Tetraarylporphyrines. Oxygen Transfer To Sulfides versus H_2O_2 Dismutation and Catalyst Breakdown. *J. Org. Chem.* **2001,** *66*, 7588.
10. Panayotov, D.; Kondratyuk, P.; Yates, J. T., Photooxidation of a Mustard Gas Simulant over TiO_2−SiO_2 Mixed-Oxide Photocatalyst: Site Poisoning by Oxidation Products and Reactivation. *Langmuir* **2004,** *20* (9), 3674-3678.
11. Livingston, S. R.; Landry, C. C., Oxidation of a Mustard Gas Analogue Using an Aldehyde/O_2 System Catalyzed by V-Doped Mesoporous Silica. *J. Am. Chem. Soc.* **2008,** *130*, 13214.
12. Neaţu, Ş.; Pârvulescu, V. I.; Epure, G.; Petrea, N.; Şomoghi, V.; Ricchiardi, G.; Bordiga, S.; Zecchina, A., M/TiO_2/SiO_2 (M=Fe, Mn, and V) Catalysts in Photo-Decomposition of Sulfur Mustard. *Appl. Catal., B* **2009,** *91* (1), 546-553.
13. Štengl, V.; Grygar, T. M.; Opluštil, F.; Němec, T., Sulphur Mustard Degradation on zirconium doped Ti–Fe oxides. *Journal of Hazardous Materials* **2011,** *192* (3), 1491-1504.
14. Ramacharyulu, P. V. R. K.; Praveen Kumar, J.; Prasad, G. K.; Singh, B.; Sreedhar, B.; Dwivedi, K., Sunlight Assisted Photocatalytic Detoxification of Sulfur Mustard on Vanadium Ion Doped Titania Nanocatalysts. *Journal of Molecular Catalysis A: Chemical* **2014,** *387*, 38-44.
15. Giannakoudakis, D. A.; Mitchell, J. K.; Bandosz, T. J., Reactive Adsorption of Mustard Gas Surrogate on Zirconium (Hydr)oxide/Graphite Oxide Composites: the Role of Surface and Chemical Features. *Journal of Materials Chemistry A* **2016,** *4* (3), 1008-1019.

16. Giannakoudakis, D. A.; Florent, M.; Wallace, R.; Secor, J.; Karwacki, C.; Bandosz, T. J., Zinc Peroxide Nanoparticles: Surface, Chemical and Optical Properties and the Effect of Thermal Treatment on the Detoxification of Mustard Gas. *Appl. Catal., B* **2018,** *226*, 429-440.
17. Prasad, G. K.; Mahato, T. H.; Yadav, S. S.; Singh, B., Sulphur Mustard Vapor Breakthrough Behaviour on Reactive Carbon Systems. *Journal of Hazardous Materials* **2007,** *143* (1), 150-155.
18. Sharma, A.; Singh, B.; Saxena, A., Polyoxometalate Impregnated Carbon Systems for the *in situ* Degradation of Sulphur Mustard. *Carbon* **2009,** *47* (8), 1911-1915.
19. Kanyi, C. W.; Doetschman, D. C.; Schulte, J. T., Nucleophilic Chemistry of X-type Faujasite Zeolites with 2-Chloroethyl Ethyl Sulfide (CEES), a Simulant of Common Mustard Gas. *Microporous Mesoporous Mater.* **2009,** *124* (1), 232-235.
20. Ramakrishna, C.; Saini, B. K.; Racharla, K.; Gujarathi, S.; Sridara, C. S.; Gupta, A.; Thakkallapalli, G.; Rao, P. V. L., Rapid and Complete Degradation of Sulfur Mustard Adsorbed on M/Zeolite-13X supported (M = 5 wt% Mn, Fe, Co) Metal Oxide Catalysts with Ozone. *RSC Adv.* **2016,** *6* (93), 90720-90731.
21. Rossin, J.; Petersen, E.; Tevault, D.; Lamontagne, R.; Isaacson, L., Effects of Environmental Weathering on the Properties of ASC-Whetlerite. *Carbon* **1991,** *29* (2), 197-205.
22. James, S. L., Metal-Organic Frameworks. *Chem. Soc. Rev.* **2003,** *32* (5), 276-288.
23. Altintas, C.; Avci, G.; Daglar, H.; Nemati Vesali Azar, A.; Erucar, I.; Velioglu, S.; Keskin, S., An Extensive Comparative Analysis of Two MOF Databases: High-Throughput Screening of Computation-Ready MOFs for CH_4 and H_2 Adsorption. *Journal of Materials Chemistry A* **2019,** *7* (16), 9593-9608.
24. Gascon, J.; Corma, A.; Kapteijn, F.; Llabrés i Xamena, F. X., Metal-Organic Framework Catalysis: Quo vadis? *ACS Catal.* **2014,** *4* (2), 361-378.
25. Howarth, A. J.; Liu, Y.; Li, P.; Li, Z.; Wang, T. C.; Hupp, J. T.; Farha, O. K., Chemical, Thermal and Mechanical Stabilities of Metal–Organic Frameworks. *Nat. Rev. Mater.* **2016,** *1*, 15018.
26. Roy, A.; Srivastava, A. K.; Singh, B.; Shah, D.; Mahato, T. H.; Gutch, P. K.; Halve, A. K., Degradation of Sarin, DEClP and DECNP over Cu-BTC Metal Organic Framework. *Journal of Porous Materials* **2013,** *20* (5), 1103-1109.
27. Momeni, A.; Enshaeih, S.; Meghdadi, M.; Amindjavaheri, M., Skin Manifestations of Mustard Gas: A Clinical Study of 535 Patients Exposed to Mustard Gas. *Archives of Dermatology* **1992,** *128* (6), 775-780.
28. Roy, A.; Srivastava, A. K.; Singh, B.; Shah, D.; Mahato, T. H.; Srivastava, A., Kinetics of Degradation of Sulfur Mustard and Sarin Simulants on HKUST-1 Metal Organic Framework. *Dalton Trans.* **2012,** *41* (40), 12346-12348.
29. Montoro, C.; Linares, F.; Quartapelle Procopio, E.; Senkovska, I.; Kaskel, S.; Galli, S.; Masciocchi, N.; Barea, E.; Navarro, J. A. R., Capture of Nerve Agents and Mustard Gas Analogues by Hydrophobic Robust MOF-5 Type Metal-Organic Frameworks. *J. Am. Chem. Soc.* **2011,** *133* (31), 11888-11891.
30. Montoro, C.; Linares, F.; Procopio, E. Q.; Senkovska, I.; Kaskel, S.; Galli, S.; Masciocchi, N.; Barea, E.; Navarro, J. A. R., Capture of Nerve Agents and Mustard Gas Analogues by Hydrophobic Robust MOF-5 Type Metal-Organic Frameworks. *J. Am. Chem. Soc.* **2011,** *133* (31), 11888-11891.

31. Bai, Y.; Dou, Y.; Xie, L.-H.; Rutledge, W.; Li, J.-R.; Zhou, H.-C., Zr-based Metal–Organic Frameworks: Design, Synthesis, Structure, and Applications. *Chem. Soc. Rev.* **2016,** *45* (8), 2327-2367.
32. Yuan, S.; Qin, J.-S.; Lollar, C. T.; Zhou, H.-C., Stable Metal–Organic Frameworks with Group 4 Metals: Current Status and Trends. *ACS Central Science* **2018,** *4* (4), 440-450.
33. Liu, Y.; Howarth, A. J.; Vermeulen, N. A.; Moon, S.-Y.; Hupp, J. T.; Farha, O. K., Catalytic Degradation of Chemical Warfare Agents and their Simulants by Metal-Organic Frameworks. *Coordination Chemistry Reviews* **2017,** *346* (Supplement C), 101-111.
34. Lennox, M. J.; Düren, T., Understanding the Kinetic and Thermodynamic Origins of Xylene Separation in UiO-66(Zr) via Molecular Simulation. *J. Phys. Chem. C* **2016,** *120* (33), 18651-18658.
35. Jasuja, H.; Walton, K. S., Experimental Study of CO_2, CH_4, and Water Vapor Adsorption on a Dimethyl-Functionalized UiO-66 Framework. *J. Phys. Chem. C* **2013,** *117* (14), 7062-7068.
36. Vellingiri, K.; Kumar, P.; Deep, A.; Kim, K.-H., Metal-Organic Frameworks for the Adsorption of Gaseous Toluene under Ambient Temperature and Pressure. *Chemical Engineering Journal* **2017,** *307*, 1116-1126.
37. DeCoste, J. B.; Weston, M. H.; Fuller, P. E.; Tovar, T. M.; Peterson, G. W.; LeVan, M. D.; Farha, O. K., Metal–Organic Frameworks for Oxygen Storage. *Angewandte Chemie International Edition* **2014,** *53* (51), 14092-14095.
38. Abney, C. W.; Taylor-Pashow, K. M. L.; Russell, S. R.; Chen, Y.; Samantaray, R.; Lockard, J. V.; Lin, W., Topotactic Transformations of Metal–Organic Frameworks to Highly Porous and Stable Inorganic Sorbents for Efficient Radionuclide Sequestration. *Chem. Mater.* **2014,** *26* (18), 5231-5243.
39. Peterson, G. W.; DeCoste, J. B.; Fatollahi-Fard, F.; Britt, D. K., Engineering UiO-66-NH_2 for Toxic Gas Removal. *Ind. Eng. Chem. Res.* **2014,** *53* (2), 701-707.
40. Nandasiri, M. I.; Jambovane, S. R.; McGrail, B. P.; Schaef, H. T.; Nune, S. K., Adsorption, Separation, and Catalytic Properties of Densified Metal-Organic Frameworks. *Coordination Chemistry Reviews* **2016,** *311*, 38-52.
41. Bárcia, P. S.; Guimarães, D.; Mendes, P. A. P.; Silva, J. A. C.; Guillerm, V.; Chevreau, H.; Serre, C.; Rodrigues, A. E., Reverse Shape Selectivity in the Adsorption of Hexane and Xylene Isomers in MOF UiO-66. *Microporous Mesoporous Mater.* **2011,** *139* (1–3), 67-73.
42. Liu, X.; Demir, N. K.; Wu, Z.; Li, K., Highly Water-Stable Zirconium Metal–Organic Framework UiO-66 Membranes Supported on Alumina Hollow Fibers for Desalination. *J. Am. Chem. Soc.* **2015,** *137* (22), 6999-7002.
43. Wu, Y.; Chen, H.; Liu, D.; Xiao, J.; Qian, Y.; Xi, H., Effective Ligand Functionalization of Zirconium-Based Metal–Organic Frameworks for the Adsorption and Separation of Benzene and Toluene: A Multiscale Computational Study. *ACS Appl. Mater. Interfaces* **2015,** *7* (10), 5775-5787.
44. Dalapati, R.; Sakthivel, B.; Dhakshinamoorthy, A.; Buragohain, A.; Bhunia, A.; Janiak, C.; Biswas, S., A Highly Stable Dimethyl-functionalized Ce(IV)-based UiO-66 Metal-Organic Framework Material for Gas Sorption and Redox Catalysis. *CrystEngComm* **2016,** *18* (40), 7855-7864.
45. Ren, J.; Langmi, H. W.; North, B. C.; Mathe, M., Review on Processing of Metal–Organic Framework (MOF) Materials Towards System Integration for Hydrogen Storage. *International Journal of Energy Research* **2015,** *39* (5), 607-620.

46. Vitillo, J. G.; Savonnet , M.; Ricchiardi, G.; Bordiga, S., Tailoring Metal–Organic Frameworks for CO_2 Capture: The Amino Effect. *ChemSusChem* **2011,** *4* (9), 1281-1290.
47. Hinde, C. S.; Webb, W. R.; Chew, B. K. J.; Tan, H. R.; Zhang, W.-H.; Hor, T. S. A.; Raja, R., Utilisation of Gold Nanoparticles on Amine-Functionalised UiO-66 (NH_2-UiO-66) Nanocrystals for Selective Tandem Catalytic Reactions. *Chem. Comm.* **2016,** *52* (39), 6557-6560.
48. Wang, H.; Lustig, W. P.; Li, J., Sensing and Capture of Toxic and Hazardous Gases and Vapors by Metal-Organic Frameworks. *Chem. Soc. Rev.* **2018**.
49. Ning, L.; Liao, S.; Liu, X.; Guo, P.; Zhang, Z.; Zhang, H.; Tong, X., A Regulatable Oxidative Valorization of Furfural with Aliphatic Alcohols Catalyzed by Functionalized Metal-Organic Frameworks-Supported Au Nanoparticles. *Journal of Catalysis* **2018,** *364*, 1-13.
50. Rodríguez-Albelo, L. M.; López-Maya, E.; Hamad, S.; Ruiz-Salvador, A. R.; Calero, S.; Navarro, J. A. R., Selective Sulfur Dioxide Adsorption on Crystal Defect Sites on an Isoreticular Metal Organic Framework Series. *Nature Communications* **2017,** *8*, 14457.
51. Dhakshinamoorthy, A.; Asiri, A. M.; Garcia, H., Catalysis by Metal–Organic Frameworks in Water. *Chem. Comm.* **2014,** *50* (85), 12800-12814.
52. Wang, Z.; Jin, Z.; Yuan, H.; Wang, G.; Ma, B., Orderly-Designed Ni_2P Nanoparticles on *g*-C_3N_4 and UiO-66 for Efficient Solar Water Splitting. *J. Colloid Interface Sci.* **2018,** *532*, 287-299.
53. Sumida, K.; Rogow, D. L.; Mason, J. A.; McDonald, T. M.; Bloch, E. D.; Herm, Z. R.; Bae, T.-H.; Long, J. R., Carbon Dioxide Capture in Metal–Organic Frameworks. *Chem. Rev.* **2012,** *112* (2), 724-781.
54. Grissom, T. G.; Sharp, C. H.; Usov, P. M.; Troya, D.; Morris, A. J.; Morris, J. R., Benzene, Toluene, and Xylene Transport through UiO-66: Diffusion Rates, Energetics, and the Role of Hydrogen Bonding. *J. Phys. Chem. C* **2018,** *122* (28), 16060-16069.
55. Cavka, J. H.; Jakobsen, S.; Olsbye, U.; Guillou, N.; Lamberti, C.; Bordiga, S.; Lillerud, K. P., A New Zirconium Inorganic Building Brick Forming Metal Organic Frameworks with Exceptional Stability. *J. Am. Chem. Soc.* **2008,** *130* (42), 13850-13851.
56. Valenzano, L.; Civalleri, B.; Chavan, S.; Bordiga, S.; Nilsen, M. H.; Jakobsen, S.; Lillerud, K. P.; Lamberti, C., Disclosing the Complex Structure of UiO-66 Metal Organic Framework: A Synergic Combination of Experiment and Theory. *Chem. Mater.* **2011,** *23* (7), 1700-1718.
57. Cliffe, M. J.; Wan, W.; Zou, X.; Chater, P. A.; Kleppe, A. K.; Tucker, M. G.; Wilhelm, H.; Funnell, N. P.; Coudert, F.-X.; Goodwin, A. L., Correlated Defect Nanoregions in a Metal–Organic Framework. *Nature Communications* **2014,** *5*, 4176.
58. DeCoste, J. B.; Peterson, G. W.; Jasuja, H.; Glover, T. G.; Huang, Y.-g.; Walton, K. S., Stability and Degradation Mechanisms of Metal-Organic Frameworks Containing the $Zr_6O_4(OH)_4$ Secondary Building Unit. *Journal of Materials Chemistry A* **2013,** *1* (18), 5642-5650.
59. Katz, M. J.; Mondloch, J. E.; Totten, R. K.; Park, J. K.; Nguyen, S. T.; Farha, O. K.; Hupp, J. T., Simple and Compelling Biomimetic Metal–Organic Framework Catalyst for the Degradation of Nerve Agent Simulants. *Angew. Chem. Int. Ed.* **2014,** *53* (2), 497-501.
60. Katz, M. J.; Mondloch, J. E.; Totten, R. K.; Park, J. K.; Nguyen, S. T.; Farha, O. K.; Hupp, J. T., Simple and Compelling Biomimetic Metal–Organic Framework Catalyst for the Degradation of Nerve Agent Simulants. *Angewandte Chemie* **2014,** *126* (2), 507-511.

61. Peterson, G. W.; Moon, S.-Y.; Wagner, G. W.; Hall, M. G.; DeCoste, J. B.; Hupp, J. T.; Farha, O. K., Tailoring the Pore Size and Functionality of UiO-Type Metal–Organic Frameworks for Optimal Nerve Agent Destruction. *Inorganic Chemistry* **2015,** *54* (20), 9684-9686.
62. Shearer, G. C.; Chavan, S.; Ethiraj, J.; Vitillo, J. G.; Svelle, S.; Olsbye, U.; Lamberti, C.; Bordiga, S.; Lillerud, K. P., Tuned to Perfection: Ironing Out the Defects in Metal–Organic Framework UiO-66. *Chem. Mater.* **2014,** *26* (14), 4068-4071.
63. Gutov, O. V.; Hevia, M. G.; Escudero-Adan, E. C.; Shafir, A., Metal-Organic Framework (MOF) Defects under Control: Insights into the Missing Linker Sites and Their Implication in the Reactivity of Zirconium-Based Frameworks. *Inorg. Chem.* **2015,** *54* (17), 8396-400.
64. Cliffe, M. J.; Wan, W.; Zou, X.; Chater, P. A.; Kleppe, A. K.; Tucker, M. G.; Wilhelm, H.; Funnell, N. P.; Coudert, F.-X.; Goodwin, A. L., Correlated Defect Nanoregions in a Metal–Organic Framework. *Nat Commun* **2014,** *5*.
65. López-Maya, E.; Montoro, C.; Rodríguez-Albelo, L. M.; Aznar Cervantes, S. D.; Lozano-Pérez, A. A.; Cenís, J. L.; Barea, E.; Navarro, J. A. R., Textile/Metal–Organic-Framework Composites as Self-Detoxifying Filters for Chemical-Warfare Agents. *Angewandte Chemie International Edition* **2015,** *54* (23), 6790-6794.
66. Mondloch, J. E.; Katz, M. J.; Isley Iii, W. C.; Ghosh, P.; Liao, P.; Bury, W.; Wagner, G. W.; Hall, M. G.; DeCoste, J. B.; Peterson, G. W.; Snurr, R. Q.; Cramer, C. J.; Hupp, J. T.; Farha, O. K., Destruction of Chemical Warfare Agents Using Metal–Organic Frameworks. *Nat Mater* **2015,** *14* (5), 512-516.
67. Moon, S.-Y.; Liu, Y.; Hupp, J. T.; Farha, O. K., Instantaneous Hydrolysis of Nerve-Agent Simulants with a Six-Connected Zirconium-Based Metal–Organic Framework. *Angewandte Chemie International Edition* **2015,** *54* (23), 6795-6799.
68. Zhang, Y.; Zhang, X.; Lyu, J.; Otake, K.-i.; Wang, X.; Redfern, L. R.; Malliakas, C. D.; Li, Z.; Islamoglu, T.; Wang, B.; Farha, O. K., A Flexible Metal–Organic Framework with 4-Connected Zr_6 Nodes. *J. Am. Chem. Soc.* **2018**.
69. Kalaj, M.; Momeni, M. R.; Bentz, K. C.; Barcus, K. S.; Palomba, J. M.; Paesani, F.; Cohen, S. M., Halogen Bonding in UiO-66 Frameworks Promotes Superior Chemical Warfare Agent Simulant Degradation. *Chem. Comm.* **2019**.
70. Kalaj, M.; Palomba, J. M.; Bentz, K. C.; Cohen, S. M., Multiple Functional Groups in UiO-66 Improve Chemical Warfare Agent Simulant Degradation. *Chem. Comm.* **2019,** *55* (37), 5367-5370.
71. Katz, M. J.; Moon, S. Y.; Mondloch, J. E.; Beyzavi, M. H.; Stephenson, C. J.; Hupp, J. T.; Farha, O. K., Exploiting Parameter Space in MOFs: a 20-fold Enhancement of Phosphate-ester Hydrolysis with UiO-66-NH_2. *Chem. Sci.* **2015,** *6*, 2286.
72. Islamoglu, T.; Ortuño, M. A.; Proussaloglou, E.; Howarth, A. J.; Vermeulen, N. A.; Atilgan, A.; Asiri, A. M.; Cramer, C. J.; Farha, O. K., Presence versus Proximity: The Role of Pendant Amines in the Catalytic Hydrolysis of a Nerve Agent Simulant. *Angewandte Chemie International Edition* **2018,** *57* (7), 1949-1953.
73. Plonka, A. M.; Wang, Q.; Gordon, W. O.; Balboa, A.; Troya, D.; Guo, W.; Sharp, C. H.; Senanayake, S. D.; Morris, J. R.; Hill, C. L.; Frenkel, A. I., In Situ Probes of Capture and Decomposition of Chemical Warfare Agent Simulants by Zr-Based Metal Organic Frameworks. *J. Am. Chem. Soc.* **2016**.
74. Troya, D., Reaction Mechanism of Nerve-Agent Decomposition with Zr-Based Metal Organic Frameworks. *J. Phys. Chem. C* **2016,** *120* (51), 29312-29323.

75. Wang, G.; Sharp, C.; Plonka, A. M.; Wang, Q.; Frenkel, A. I.; Guo, W.; Hill, C.; Smith, C.; Kollar, J.; Troya, D.; Morris, J. R., Mechanism and Kinetics for Reaction of the Chemical Warfare Agent Simulant, DMMP(g), with Zirconium(IV) MOFs: An Ultrahigh-Vacuum and DFT Study. *J. Phys. Chem. C* **2017,** *121* (21), 11261-11272.
76. Wang, H.; Mahle, J. J.; Tovar, T. M.; Peterson, G. W.; Hall, M. G.; DeCoste, J. B.; Buchanan, J. H.; Karwacki, C. J., Solid-Phase Detoxification of Chemical Warfare Agents using Zirconium-Based Metal Organic Frameworks and the Moisture Effects: Analyze via Digestion. *ACS Appl. Mater. Interfaces* **2019,** *11* (23), 21109-21116.
77. Liu, Y.; Moon, S.-Y.; Hupp, J. T.; Farha, O. K., Dual-Function Metal–Organic Framework as a Versatile Catalyst for Detoxifying Chemical Warfare Agent Simulants. *ACS Nano* **2015,** *9* (12), 12358-12364.
78. Howarth, A. J.; Buru, C. T.; Liu, Y.; Ploskonka, A. M.; Hartlieb, K. J.; McEntee, M.; Mahle, J. J.; Buchanan, J. H.; Durke, E. M.; Al-Juaid, S. S.; Stoddart, J. F.; DeCoste, J. B.; Hupp, J. T.; Farha, O. K., Postsynthetic Incorporation of a Singlet Oxygen Photosensitizer in a Metal–Organic Framework for Fast and Selective Oxidative Detoxification of Sulfur Mustard. *Chemistry – A European Journal* **2017,** *23* (1), 214-218.
79. Atilgan, A.; Islamoglu, T.; Howarth, A. J.; Hupp, J. T.; Farha, O. K., Detoxification of a Sulfur Mustard Simulant Using a BODIPY-Functionalized Zirconium-Based Metal–Organic Framework. *ACS Appl. Mater. Interfaces* **2017,** *9* (29), 24555-24560.
80. Gil-San-Millan, R.; López-Maya, E.; Hall, M.; Padial, N. M.; Peterson, G. W.; DeCoste, J. B.; Rodríguez-Albelo, L. M.; Oltra, J. E.; Barea, E.; Navarro, J. A. R., Chemical Warfare Agents Detoxification Properties of Zirconium Metal–Organic Frameworks by Synergistic Incorporation of Nucleophilic and Basic Sites. *ACS Appl. Mater. Interfaces* **2017,** *9* (28), 23967-23973.
81. Panayotov, D. A.; Paul, D. K.; Yates, J. T., Photocatalytic Oxidation of 2-Chloroethyl Ethyl Sulfide on TiO_2−SiO_2 Powders. *J. Phys. Chem. B* **2003,** *107* (38), 10571-10575.
82. Mawhinney, D. B.; Rossin, J. A.; Gerhart, K.; Yates, J. T., Adsorption and Reaction of 2-Chloroethylethyl Sulfide with Al_2O_3 Surfaces. *Langmuir* **1999,** *15* (14), 4789-4795.
83. Mawhinney, D. B.; Rossin, J. A.; Gerhart, K.; Yates, J. T., Infrared Spectroscopic Study of Surface Diffusion to Surface Hydroxyl Groups on Al_2O_3: 2-Chloroethylethyl Sulfide Adsorption Site Selection. *Langmuir* **2000,** *16* (5), 2237-2241.
84. Thompson, T. L.; Panayotov, D. A.; Yates, J. T.; Martyanov, I.; Klabunde, K., Photodecomposition of Adsorbed 2-Chloroethyl Ethyl Sulfide on TiO_2: Involvement of Lattice Oxygen. *J. Phys. Chem. B* **2004,** *108* (46), 17857-17865.
85. Panayotov, D.; Yates, J. T., Bifunctional Hydrogen Bonding of 2-Chloroethyl Ethyl Sulfide on TiO_2−SiO_2 Powders. *J. Phys. Chem. B* **2003,** *107* (38), 10560-10564.
86. Thompson, T. L.; Panayotov, D. A.; Yates, J. T., Adsorption and Thermal Decomposition of 2-Chloroethyl Ethyl Sulfide on TiO_2 Surfaces. *J. Phys. Chem. B* **2004,** *108* (43), 16825-16833.
87. Abelard, J.; Wilmsmeyer, A. R.; Edwards, A. C.; Gordon, W. O.; Durke, E. M.; Karwacki, C. J.; Troya, D.; Morris, J. R., Adsorption of 2-Chloroethyl Ethyl Sulfide on Silica: Binding Mechanism and Energy of a Bifunctional Hydrogen-Bond Acceptor at the Gas Surface Interface. *Journal of Physical Chemistry C* **2015,** *119* (1), 365-372.
88. Driscoll, D. M.; Troya, D.; Usov, P. M.; Maynes, A. J.; Morris, A. J.; Morris, J. R., Characterization of Undercoordinated Zr Defect Sites in UiO-66 with Vibrational Spectroscopy of Adsorbed CO. *J. Phys. Chem. C* **2018,** *122* (26), 14582-14589.

89. Driscoll, D. M.; Troya, D.; Usov, P. M.; Maynes, A. J.; Morris, A. J.; Morris, J. R., Geometry and Energetics of CO Adsorption on Hydroxylated UiO-66. *Phys. Chem. Chem. Phys.* **2019**.
90. Grissom, T. G.; Driscoll, D. M.; Troya, D.; Sapienza, N. S.; Usov, P. M.; Morris, A. J.; Morris, J. R., Molecular-Level Insight into CO_2 Adsorption on the Zirconium-Based Metal–Organic Framework, UiO-66: A Combined Spectroscopic and Computational Approach. *J. Phys. Chem. C* **2019,** *123* (22), 13731-13738.
91. Chakarova, K.; Strauss, I.; Mihaylov, M.; Drenchev, N.; Hadjiivanov, K., Evolution of acid and basic sites in UiO-66 and UiO-66-NH_2 Metal-Organic Frameworks: FTIR Study by Probe Molecules. *Microporous Mesoporous Mater.* **2019,** *281*, 110-122.
92. Tan, K.; Jensen, S.; Zuluaga, S.; Chapman, E. K.; Wang, H.; Rahman, R.; Cure, J.; Kim, T.-H.; Li, J.; Thonhauser, T.; Chabal, Y. J., Role of Hydrogen Bonding on Transport of Coadsorbed Gases in Metal–Organic Frameworks Materials. *J. Am. Chem. Soc.* **2018**.
93. Zubkov, T.; Smith, R. S.; Engstrom, T. R.; Kay, B. D., Adsorption, Desorption, and Diffusion of Nitrogen in a Model Nanoporous Material. II. Diffusion Limited Kinetics in Amorphous Solid Water. *J. Chem. Phys.* **2007,** *127* (18).
94. Zubkov, T.; Smith, R. S.; Engstrom, T. R.; Kay, B. D., Adsorption, Desorption, and Diffusion of Nitrogen in a Model Nanoporous Material. I. Surface Limited Desorption Kinetics in Amorphous Solid Water. *J. Chem. Phys.* **2007,** *127* (18).
95. Wilmsmeyer, A. R.; Uzarski, J.; Barrie, P. J.; Morris, J. R., Interactions and Binding Energies of Dimethyl Methylphosphonate and Dimethyl Chlorophosphate with Amorphous Silica. *Langmuir* **2012,** *28* (30), 10962-10967.
96. Wilmsmeyer, A. R.; Gordon, W. O.; Davis, E. D.; Troya, D.; Mantooth, B. A.; Lalain, T. A.; Morris, J. R., Infrared Spectra and Binding Energies of Chemical Warfare Nerve Agent Simulants on the Surface of Amorphous Silica. *Journal of Physical Chemistry C* **2013,** *117* (30), 15685-15697.
97. Davis, E. D.; Gordon, W. O.; Wilmsmeyer, A. R.; Troya, D.; Morris, J. R., Chemical Warfare Agent Surface Adsorption: Hydrogen Bonding of Sarin and Soman to Amorphous Silica. *Journal of Physical Chemistry Letters* **2014,** *5* (8), 1393-1399.
98. Sharp, C. H.; Abelard, J.; Plonka, A. M.; Guo, W.; Hill, C. L.; Morris, J. R., Alkane–OH Hydrogen Bond Formation and Diffusion Energetics of *n*-Butane within UiO-66. *J. Phys. Chem. C* **2017,** *121* (16), 8902-8906.
99. Abelard, J. Temperature Programmed Desorption and Infrared Spectroscopic Studies of Interfacial Hydrogen Bonds for Small Molecules Adsorbed on Silica and Within Metal Organic Frameworks. Virginia Polytechnic Institute and State University, 2017.
100. Wilmsmeyer, A. R. Ultrahigh Vacuum Studies of the Fundamental Interactions of Chemical Warfare Agents and Their Simulants with Amorphous Silica. Virginia Polytechnic Institute and State University, 2012.
101. Uzarski, J. Reflection Absorption Infrared Spectroscopic Studies of Surface Chemistry Relevant to Chemical and Biological Warfare Agent Defense. Virginia Polytechnic Institute and State University, 2009.
102. Basu, P.; Ballinger, T. H.; Jr., J. T. Y., Wide Temperature Range IR Spectroscopy Cell for Studies of Adsorption and Desorption on High Area Solids. *Rev. Sci. Instrum.* **1988,** *59* (8), 1321-1327.

103. Type K Mini Plug Plus Power -CF Flange, Single-Ended. https://www.lesker.com/newweb/feedthroughs/thermocouple_feedthroughs_typek_miniplugpower_singleend.cfm?pgid=cf (accessed August 5, 2019).
104. Abelard, J.; Wilmsmeyer, A. R.; Edwards, A. C.; Gordon, W. O.; Durke, E. M.; Karwacki, C. J.; Troya, D.; Morris, J. R., Adsorption of 2-Chloroethyl Ethyl Sulfide on Silica: Binding Mechanism and Energy of a Bifunctional Hydrogen-Bond Acceptor at the Gas–Surface Interface. *J. Phys. Chem. C* **2015,** *119* (1), 365-372.
105. Daschbach, J. L.; Kim, J.; Ayotte, P.; Smith, R. S.; Kay, B. D., Adsorption and Desorption of HCl on Pt(111). *J. Phys. Chem. B* **2005,** *109* (32), 15506-15514.
106. Tait, S. L.; Dohnálek, Z.; Campbell, C. T.; Kay, B. D., *n*-Alkanes on Pt(111) and on C(0001)/Pt(111): Chain Length Dependence of Kinetic Desorption Parameters. *The Journal of Chemical Physics* **2006,** *125* (23), 234308.
107. Zubkov, T.; Smith, R. S.; Engstrom, T. R.; Kay, B. D., Adsorption, Desorption, and Diffusion of Nitrogen in a Model Nanoporous Material. II. Diffusion Limited Kinetics in Amorphous Solid Water. *The Journal of Chemical Physics* **2007,** *127* (18), 184708.
108. Zubkov, T.; Smith, R. S.; Engstrom, T. R.; Kay, B. D., Adsorption, Desorption, and Diffusion of Nitrogen in a Model Nanoporous Material. I. Surface Limited Desorption Kinetics in Amorphous Solid Water. *The Journal of Chemical Physics* **2007,** *127* (18), 184707.
109. Tait, S. L.; Dohnálek, Z.; Campbell, C. T.; Kay, B. D., *n*-Alkanes on MgO(100). I. Coverage-Dependent Desorption Kinetics of *n*-Butane. *The Journal of Chemical Physics* **2005,** *122* (16), 164707.
110. Tait, S. L.; Dohnálek, Z.; Campbell, C. T.; Kay, B. D., *n*-Alkanes on MgO(100). II. Chain Length Dependence of Kinetic Desorption Parameters for Small *n*-Alkanes. *The Journal of Chemical Physics* **2005,** *122* (16), 164708.
111. Web, M. D. Type K Thermocouple Calibration. http://www.mosaic-industries.com/embedded-systems/microcontroller-projects/temperature-measurement/thermocouple/type-k-calibration-table.
112. Kim, S.; Byl, O.; Liu, J.-C.; Johnson, J. K.; Yates, J. T., Spectroscopic Measurement of Diffusion Kinetics through Subnanometer and Larger Al_2O_3 Particles by a New Method: The Interaction of 2-Chloroethylethyl Sulfide with γ-Al_2O_3. *J. Phys. Chem. B* **2006,** *110* (18), 9204-9210.
113. Kim, S.; Wang, X.; Buda, C.; Neurock, M.; Koper, O. B.; Yates, J. T., IR Spectroscopic Measurement of Diffusion Kinetics of Chemisorbed Pyridine through Nanocrystalline MgO Particles. The Involvement of Surface Defect Sites in Slow Diffusion. *J. Phys. Chem. C* **2009,** *113* (6), 2219-2227.
114. Green, I. X.; Buda, C.; Zhang, Z.; Neurock, M.; Yates, J. T., IR Spectroscopic Measurement of Diffusion Kinetics of Chemisorbed Pyridine through TiO_2 Particles. *J. Phys. Chem. C* **2010,** *114* (39), 16649-16659.
115. Tummers, B. DataThiefIII. https://datathief.org/ (accessed August 8, 2019).
116. Snurr, R. Q., New Horizons for the Physical Chemistry of Nanoporous Materials. *J. Phys. Chem. Lett.* **2011,** *2* (14), 1842-1843.
117. Ramsahye, N. A.; Gao, J.; Jobic, H.; Llewellyn, P. L.; Yang, Q.; Wiersum, A. D.; Koza, M. M.; Guillerm, V.; Serre, C.; Zhong, C. L.; Maurin, G., Adsorption and Diffusion of Light Hydrocarbons in UiO-66(Zr): A Combination of Experimental and Modeling Tools. *J. Phys. Chem. C* **2014,** *118* (47), 27470-27482.

118. Zybaylo, O.; Shekhah, O.; Wang, H.; Tafipolsky, M.; Schmid, R.; Johannsmann, D.; Woll, C., A Novel Method to Measure Diffusion Coefficients in Porous Metal-Organic Frameworks. *Phys. Chem. Chem. Phys.* **2010,** *12* (28), 8093-8098.
119. Tovar, T. M.; Zhao, J.; Nunn, W. T.; Barton, H. F.; Peterson, G. W.; Parsons, G. N.; LeVan, M. D., Diffusion of CO_2 in Large Crystals of Cu-BTC MOF. *J. Am. Chem. Soc.* **2016,** *138* (36), 11449-11452.
120. Canepa, P.; Nijem, N.; Chabal, Y. J.; Thonhauser, T., Diffusion of Small Molecules in Metal Organic Framework Materials. *Phys. Rev. Lett.* **2013,** *110* (2), 026102.
121. Wee, L. H. H.; Meledina, M.; Turner, S.; Van Tendeloo, G.; Zhang, K.; Rodriguez-Albelo, L. M.; Masala, A.; Bordiga, S.; Jiang, J.; Navarro, J. A. R.; Kirschhock, C. E. A.; Martens, J. A., 1D-2D-3D Transformation Synthesis of Hierarchical Metal-Organic Framework Adsorbent for Multicomponent Alkane Separation. *J. Am. Chem. Soc.* **2016,** *139* (2), 819-828.
122. Peterson, G. W.; DeCoste, J. B.; Glover, T. G.; Huang, Y.; Jasuja, H.; Walton, K. S., Effects of Pelletization Pressure on the Physical and Chemical Properties of the Metal–Organic Frameworks $Cu_3(BTC)_2$ and UiO-66. *Microporous Mesoporous Mater.* **2013,** *179*, 48-53.
123. Yang, Q.; Wiersum, A. D.; Llewellyn, P. L.; Guillerm, V.; Serre, C.; Maurin, G., Functionalizing Porous Zirconium Terephthalate UiO-66(Zr) for Natural Gas Upgrading: a Computational Exploration. *Chem. Comm.* **2011,** *47* (34), 9603-9605.
124. Titze, T.; Lauerer, A.; Heinke, L.; Chmelik, C.; Zimmermann, N. E. R.; Keil, F. J.; Ruthven, D. M.; Karger, J., Transport in Nanoporous Materials Including MOFs: The Applicability of Fick's Laws. *Angew. Chem.-Int. Edit.* **2015,** *54* (48), 14580-14583.
125. Kandiah, M.; Nilsen, M. H.; Usseglio, S.; Jakobsen, S.; Olsbye, U.; Tilset, M.; Larabi, C.; Quadrelli, E. A.; Bonino, F.; Lillerud, K. P., Synthesis and Stability of Tagged UiO-66 Zr-MOFs. *Chem. Mater.* **2010,** *22* (24), 6632-6640.
126. Schoenecker, P. M.; Carson, C. G.; Jasuja, H.; Flemming, C. J. J.; Walton, K. S., Effect of Water Adsorption on Retention of Structure and Surface Area of Metal–Organic Frameworks. *Ind. Eng. Chem. Res.* **2012,** *51* (18), 6513-6519.
127. Wang, X.; Kim, S.; Buda, C.; Neurock, M.; Koper, O. B.; Yates, J. T., Direct Spectroscopic Observation of the Role of Humidity in Surface Diffusion through an Ionic Adsorbent Powder. The Behavior of Adsorbed Pyridine on Nanocrystalline MgO. *J. Phys. Chem. C* **2009,** *113* (6), 2228-2234.
128. Klepper, K. B.; Nilsen, O.; Fjellvag, H., Deposition of Thin Films of Organic-Inorganic Hybrid Materials Based on Aromatic Carboxylic Acids by Atomic Layer Deposition. *Dalton Trans.* **2010,** *39* (48), 11628-11635.
129. Téllez S, C. A.; Hollauer, E.; Mondragon, M. A.; Castaño, V. M., Fourier Transform Infrared and Raman Spectra, Vibrational Assignment and *ab initio* Calculations of Terephthalic Acid and Related Compounds. *Spectrochim. Acta, Part A* **2001,** *57* (5), 993-1007.
130. Yang, D.; Bernales, V.; Islamoglu, T.; Farha, O. K.; Hupp, J. T.; Cramer, C. J.; Gagliardi, L.; Gates, B. C., Tuning the Surface Chemistry of Metal Organic Framework Nodes: Proton Topology of the Metal-Oxide-Like Zr_6 Nodes of UiO-66 and NU-1000. *J. Am. Chem. Soc.* **2016,** *138* (46), 15189-15196.
131. Eder, F.; Stockenhuber, M.; Lercher, J. A., Brønsted Acid Site and Pore Controlled Siting of Alkane Sorption in Acidic Molecular Sieves. *J. Phys. Chem. B* **1997,** *101* (27), 5414-5419.

132. Yeh, Y.-H.; Gorte, R. J.; Rangarajan, S.; Mavrikakis, M., Adsorption of Small Alkanes on ZSM-5 Zeolites: Influence of Brønsted Sites. *J. Phys. Chem. C* **2016,** *120* (22), 12132-12138.
133. Olesen, S. G.; Hammerum, S., Hydrogen Bonding to Alkanes: Computational Evidence. *J. Phys. Chem. A* **2009,** *113* (27), 7940-7944.
134. Isaev, A. N., Intermolecular Charge Transfer as Evidence for Unusual O–H···C(sp^3) Hydrogen Bond. *Comput. Theor. Chem.* **2016,** *1090*, 180-192.
135. Moré, J. J., The Levenberg-Marquardt Algorithm: Implementation and Theory. In *Numerical Analysis*, Springer: 1978; pp 105-116.
136. Borah, B.; Zhang, H.; Snurr, R. Q., Diffusion of Methane and Other Alkanes in Metal-Organic Frameworks for Natural Gas Storage. *Chem. Eng. Sci.* **2015,** *124*, 135-143.
137. Zheng, B.; Pan, Y.; Lai, Z.; Huang, K.-W., Molecular Dynamics Simulations on Gate Opening in ZIF-8: Identification of Factors for Ethane and Propane Separation. *Langmuir* **2013,** *29* (28), 8865-8872.
138. Zheng, B.; Wang, L. L.; Du, L.; Pan, Y.; Lai, Z.; Huang, K. W.; Du, H. L., Diffusion as a Function of Guest Molecule Length and Functionalization in Flexible Metal-Organic Frameworks. *Mater. Horizons* **2016,** *3* (4), 355-361.
139. Grabowski, S. J., Hydrogen Bonding Strength—Measures Based on Geometric and Topological Parameters. *J. Phys. Org. Chem.* **2004,** *17* (1), 18-31.
140. Gardner, T. Q.; Lee, J. B.; Noble, R. D.; Falconer, J. L., Adsorption and Diffusion Properties of Butanes in ZSM-5 Zeolite Membranes. *Ind. Eng. Chem. Res.* **2002,** *41* (16), 4094-4105.
141. Funke, H. H.; Argo, A. M.; Falconer, J. L.; Noble, R. D., Separations of Cyclic, Branched, and Linear Hydrocarbon Mixtures through Silicalite Membranes. *Ind. Eng. Chem. Res.* **1997,** *36* (1), 137-143.
142. Brand, J. L.; Arena, M. V.; Deckert, A. A.; George, S. M., Surface Diffusion of *n*-Alkanes on Ru(001). *The Journal of Chemical Physics* **1990,** *92* (8), 5136-5143.
143. Shearer, G. C.; Chavan, S.; Bordiga, S.; Svelle, S.; Olsbye, U.; Lillerud, K. P., Defect Engineering: Tuning the Porosity and Composition of the Metal–Organic Framework UiO-66 via Modulated Synthesis. *Chem. Mater.* **2016,** *28* (11), 3749-3761.
144. Rozenberg, M.; Loewenschuss, A.; Marcus, Y., An Empirical Correlation between Stretching Vibration Redshift and Hydrogen Bond Length. *Phys. Chem. Chem. Phys.* **2000,** *2* (12), 2699-2702.
145. Badger, R. M.; Bauer, S. H., Spectroscopic Studies of the Hydrogen Bond. II. The Shift of the O–H Vibrational Frequency in the Formation of the Hydrogen Bond. *The Journal of Chemical Physics* **1937,** *5* (11), 839-851.
146. Duerinck, T.; Bueno-Perez, R.; Vermoortele, F.; De Vos, D. E.; Calero, S.; Baron, G. V.; Denayer, J. F. M., Understanding Hydrocarbon Adsorption in the UiO-66 Metal–Organic Framework: Separation of (Un)saturated Linear, Branched, Cyclic Adsorbates, Including Stereoisomers. *J. Phys. Chem. C* **2013,** *117* (24), 12567-12578.
147. Duerinck, T.; Denayer, J. F. M., Unusual Chain Length Dependent Adsorption of Linear and Branched Alkanes on UiO-66. *Adsorption* **2014,** *20* (2), 251-259.
148. Tucker, J. B., *War of Nerves: Chemical Warfare from World War I to Al-Qaeda*. 1st Edition ed.; Anchor Books: New York, 2007.
149. Furukawa, H.; Cordova, K. E.; O'Keeffe, M.; Yaghi, O. M., The Chemistry and Applications of Metal-Organic Frameworks. *Science* **2013,** *341* (6149), 1230444.

150. Hönicke, I. M.; Senkovska, I.; Bon, V.; Baburin, I. A.; Bönisch, N.; Raschke, S.; Evans, J. D.; Kaskel, S., Balancing Mechanical Stability and Ultrahigh Porosity in Crystalline Framework Materials. *Angewandte Chemie International Edition* **2018,** *57* (42), 13780-13783.
151. Kozachuk, O.; Luz, I.; Llabrés i Xamena, F. X.; Noei, H.; Kauer, M.; Albada, H. B.; Bloch, E. D.; Marler, B.; Wang, Y.; Muhler, M.; Fischer, R. A., Multifunctional, Defect-Engineered Metal–Organic Frameworks with Ruthenium Centers: Sorption and Catalytic Properties. *Angewandte Chemie International Edition* **2014,** *53* (27), 7058-7062.
152. Timofeeva, M. N.; Panchenko, V. N.; Jun, J. W.; Hasan, Z.; Matrosova, M. M.; Jhung, S. H., Effects of Linker Substitution on Catalytic Properties of Porous Zirconium Terephthalate UiO-66 in Acetalization of Benzaldehyde with Methanol. *Applied Catalysis A: General* **2014,** *471*, 91-97.
153. Liu, H.; Liu, Y.; Li, Y.; Tang, Z.; Jiang, H., Metal−Organic Framework Supported Gold Nanoparticles as a Highly Active Heterogeneous Catalyst for Aerobic Oxidation of Alcohols. *J. Phys. Chem. C* **2010,** *114* (31), 13362-13369.
154. Dhakshinamoorthy, A.; Asiri, A. M.; Garcia, H., Metal Organic Frameworks as Versatile Hosts of Au Nanoparticles in Heterogeneous Catalysis. *ACS Catal.* **2017,** *7* (4), 2896-2919.
155. Bobbitt, N. S.; Mendonca, M. L.; Howarth, A. J.; Islamoglu, T.; Hupp, J. T.; Farha, O. K.; Snurr, R. Q., Metal-Organic Frameworks for the Removal of Toxic Industrial Chemicals and Chemical Warfare Agents. *Chem. Soc. Rev.* **2017,** *46* (11), 3357-3385.
156. DeCoste, J. B.; Demasky, T. J.; Katz, M. J.; Farha, O. K.; Hupp, J. T., A UiO-66 Analogue with Uncoordinated Carboxylic Acids for the Broad-Spectrum Removal of Toxic Chemicals. *New Journal of Chemistry* **2015,** *39* (4), 2396-2399.
157. Mondloch, J. E.; Katz, M. J.; Isley Iii, W. C.; Ghosh, P.; Liao, P.; Bury, W.; Wagner, G. W.; Hall, M. G.; DeCoste, J. B.; Peterson, G. W.; Snurr, R. Q.; Cramer, C. J.; Hupp, J. T.; Farha, O. K., Destruction of Chemical Warfare Agents Using Metal–Organic Frameworks. *Nature Materials* **2015,** *14*, 512.
158. Kalaj, M.; Palomba, J. M.; Bentz, K. C.; Cohen, S. M., Multiple Functional Groups in UiO-66 Improve Chemical Warfare Agent Simulant Degradation. *Chem. Comm.* **2019**.
159. Platero-Prats, A. E.; Mavrandonakis, A.; Gallington, L. C.; Liu, Y.; Hupp, J. T.; Farha, O. K.; Cramer, C. J.; Chapman, K. W., Structural Transitions of the Metal-Oxide Nodes within Metal–Organic Frameworks: On the Local Structures of NU-1000 and UiO-66. *J. Am. Chem. Soc.* **2016,** *138* (12), 4178-4185.
160. Øien-Ødegaard, S.; Bouchevreau, B.; Hylland, K.; Wu, L.; Blom, R.; Grande, C.; Olsbye, U.; Tilset, M.; Lillerud, K. P., UiO-67-type Metal–Organic Frameworks with Enhanced Water Stability and Methane Adsorption Capacity. *Inorganic Chemistry* **2016,** *55* (5), 1986-1991.
161. Guo, W.; Lv, H.; Sullivan, K. P.; Gordon, W. O.; Balboa, A.; Wagner, G. W.; Musaev, D. G.; Bacsa, J.; Hill, C. L., Broad-Spectrum Liquid- and Gas-Phase Decontamination of Chemical Warfare Agents by One-Dimensional Heteropolyniobates. *Angewandte Chemie International Edition* **2016,** *55* (26), 7403-7407.
162. Stout, S. C.; Larsen, S. C.; Grassian, V. H., Adsorption, Desorption and Thermal Oxidation of 2-CEES on Nanocrystalline Zeolites. *Microporous Mesoporous Mater.* **2007,** *100* (1–3), 77-86.

163. Weinhold, F.; Klein, R. A., What is a Hydrogen Bond? Mutually Consistent Theoretical and Experimental Criteria for Characterizing H-Bonding Interactions. *Mol. Phys.* **2012,** *110* (9-10), 565-579.
164. Asha, P.; Sinha, M.; Mandal, S., Effective Removal of Chemical Warfare Agent Simulants using Water Stable Metal-Organic Frameworks: Mechanistic Study and Structure-Property Correlation. *RSC Adv.* **2017,** *7* (11), 6691-6696.
165. Lemaire, P. C.; Lee, D. T.; Zhao, J.; Parsons, G. N., Reversible Low-Temperature Metal Node Distortion during Atomic Layer Deposition of Al_2O_3 and TiO_2 on UiO-66-NH_2 Metal–Organic Framework Crystal Surfaces. *ACS Appl. Mater. Interfaces* **2017,** *9* (26), 22042-22054.
166. Christesen, S. D., Vibrational Spectra and Assignments of Diethyl Sulfide, 2-Chlorodiethyl Sulfide and 2, 2′-Dichlorodiethyl Dulfide. *J. Raman Spectrosc.* **1991,** *22* (8), 459-465.
167. Sosa, C.; Bartlett, R. J.; KuBulat, K.; Person, W. B., A Theoretical Study of the Harmonic Vibrational Frequencies and Infrared Intensities of XCH2CH2SCH2CH2X and XCH2CH2SH (X = H, Cl). *J. Phys. Chem.* **1989,** *93* (2), 577-588.
168. Plusquellic, D. F.; Suenram, R. D.; Maté, B.; Jensen, J. O.; Samuels, A. C., The Conformational Structures and Dipole Moments of Ethyl Sulfide in the Gas Phase. *The Journal of Chemical Physics* **2001,** *115* (7), 3057-3067.
169. Politzer, P.; Habibollahzadeh, D., Bond-Breaking Energies for 2,2'-Dichlorodiethyl Sulfide (Sulfur Mustard) in Media of Different Dielectric Constants. *J. Phys. Chem.* **1994,** *98* (6), 1576-1578.
170. Katz, M. J.; Brown, Z. J.; Colon, Y. J.; Siu, P. W.; Scheidt, K. A.; Snurr, R. Q.; Hupp, J. T.; Farha, O. K., A Facile Synthesis of UiO-66, UiO-67 and their Derivatives. *Chem. Comm.* **2013,** *49* (82), 9449-9451.
171. Willis, M. P.; Varady, M. J.; Pearl, T. P.; Fouse, J. C.; Riley, P. C.; Mantooth, B. A.; Lalain, T. A., Physics-based Agent to Simulant Correlations for Vapor Phase Mass Transport. *Journal of Hazardous Materials* **2013,** *263*, 479-485.
172. Zhu, X.; Li, B.; Yang, J.; Li, Y.; Zhao, W.; Shi, J.; Gu, J., Effective Adsorption and Enhanced Removal of Organophosphorus Pesticides from Aqueous Solution by Zr-Based MOFs of UiO-67. *ACS Appl. Mater. Interfaces* **2015,** *7* (1), 223-231.
173. Arrhenius, S., PAPER 2 - ON THE REACTION VELOCITY OF THE INVERSION OF CANE SUGAR BY ACIDS† A2 - BACK, MARGARET H. In *Selected Readings in Chemical Kinetics*, Laidler, K. J., Ed. Pergamon: 1967; pp 31-35.
174. Shearer, G. C.; Forselv, S.; Chavan, S.; Bordiga, S.; Mathisen, K.; Bjørgen, M.; Svelle, S.; Lillerud, K. P., In Situ Infrared Spectroscopic and Gravimetric Characterisation of the Solvent Removal and Dehydroxylation of the Metal Organic Frameworks UiO-66 and UiO-67. *Top. Catal.* **2013,** *56* (9), 770-782.
175. Corma, A.; Orozco, L. M.; Renz, M., From MOFs to Zeolites: Zirconium Sites for Epoxide Rearrangement. *New Journal of Chemistry* **2013,** *37* (11), 3496-3502.
176. Amirjalayer, S.; Tafipolsky, M.; Schmid, R., Molecular Dynamics Simulation of Benzene Diffusion in MOF-5: Importance of Lattice Dynamics. *Angewandte Chemie International Edition* **2007,** *46* (3), 463-466.
177. Jiang, J.; Plonka, A. M.; Frenkel, A. I.; Gersappe, D., Modeling Gas Flow Dynamics in Metal–Organic Frameworks. *J. Phys. Chem. Lett.* **2018,** *9* (5), 1092-1096.

178. Islamoglu, T.; Otake, K.-i.; Li, P.; Buru, C. T.; Peters, A. W.; Akpinar, I.; Garibay, S. J.; Farha, O. K., Revisiting the Structural Homogeneity of NU-1000, a Zr-based Metal–Organic Framework. *CrystEngComm* **2018,** *20* (39), 5913-5918.
179. Joseph, Y. C., Christina, Burning Eyes, Foaming Mouths: Years of Suspected Chemical Attacks in Syria. *The New York Times* April 8, 2018, 2018.
180. Warrick, J., Exclusive: Iraqi Scientist says He Helped ISIS make Chemical Weapons. *The Washington Post* January 21, 2019, 2019.
181. de Koning, M. C.; van Grol, M.; Breijaert, T., Degradation of Paraoxon and the Chemical Warfare Agents VX, Tabun, and Soman by the Metal–Organic Frameworks UiO-66-NH_2, MOF-808, NU-1000, and PCN-777. *Inorganic Chemistry* **2017,** *56* (19), 11804-11809.
182. Li, Y.; Gao, Q.; Zhang, L.; Zhou, Y.; Zhong, Y.; Ying, Y.; Zhang, M.; Huang, C.; Wang, Y. a., $H_5PV_2Mo_{10}O_{40}$ Encapsulated in MIL-101(Cr): Facile Synthesis and Characterization of Rationally Designed Composite Materials for Efficient Decontamination of Sulfur Mustard. *Dalton Trans.* **2018,** *47* (18), 6394-6403.
183. Liang, H.; Yao, A.; Jiao, X.; Li, C.; Chen, D., Fast and Sustained Degradation of Chemical Warfare Agent Simulants Using Flexible Self-Supported Metal–Organic Framework Filters. *ACS Appl. Mater. Interfaces* **2018,** *10* (24), 20396-20403.
184. Matito-Martos, I.; Moghadam, P. Z.; Li, A.; Colombo, V.; Navarro, J. A. R.; Calero, S.; Fairen-Jimenez, D., Discovery of an Optimal Porous Crystalline Material for the Capture of Chemical Warfare Agents. *Chem. Mater.* **2018,** *30* (14), 4571-4579.
185. Montoro, C.; Linares, F.; Quartapelle Procopio, E.; Senkovska, I.; Kaskel, S.; Galli, S.; Masciocchi, N.; Barea, E.; Navarro, J. A. R., Capture of Nerve Agents and Mustard Gas Analogues by Hydrophobic Robust MOF-5 Type Metal–Organic Frameworks. *J. Am. Chem. Soc.* **2011,** *133* (31), 11888-11891.
186. Peterson, G. W.; Rossin, J. A.; DeCoste, J. B.; Killops, K. L.; Browe, M.; Valdes, E.; Jones, P., Zirconium Hydroxide–Metal–Organic Framework Composites for Toxic Chemical Removal. *Ind. Eng. Chem. Res.* **2013,** *52* (15), 5462-5469.
187. Vellingiri, K.; Philip, L.; Kim, K.-H., Metal–Organic Frameworks as Media for the Catalytic Degradation of Chemical Warfare Agents. *Coordination Chemistry Reviews* **2017,** *353*, 159-179.
188. DeCoste, J. B.; Peterson, G. W., Metal–Organic Frameworks for Air Purification of Toxic Chemicals. *Chem. Rev.* **2014,** *114*, 5695.
189. Kumar, P.; Paul, A. K.; Deep, A., A Luminescent Nanocrystal Metal Organic Framework for Chemosensing of Nitro Group Containing Organophosphate Pesticides. *Anal. Methods* **2014,** *6* (12), 4095-4101.
190. Hu, Z.; Deibert, B. J.; Li, J., Luminescent Metal-Organic Frameworks for Chemical Sensing and Explosive Detection. *Chem. Soc. Rev.* **2014,** *43* (16), 5815-5840.
191. Buragohain, A.; Biswas, S., Cerium-based Azide- and Nitro-Functionalized UiO-66 Frameworks as Turn-on Fluorescent Probes for the Sensing of Hydrogen Sulphide. *CrystEngComm* **2016,** *18* (23), 4374-4381.
192. Dolgopolova, E. A.; Rice, A. M.; Martin, C. R.; Shustova, N. B., Photochemistry and Photophysics of MOFs: Steps towards MOF-based Sensing Enhancements. *Chem. Soc. Rev.* **2018**.
193. Peterson, G. W.; Britt, D. K.; Sun, D. T.; Mahle, J. J.; Browe, M.; Demasky, T.; Smith, S.; Jenkins, A.; Rossin, J. A., Multifunctional Purification and Sensing of Toxic Hydride Gases by CuBTC Metal–Organic Framework. *Ind. Eng. Chem. Res.* **2015,** *54* (14), 3626-3633.

194. Zeng, L.; Guo, X. Y.; He, C.; Duan, C. Y., Metal-Organic Frameworks: Versatile Materials for Heterogeneous Photocatalysis. *ACS Catal.* **2016,** *6* (11), 7935-7947.
195. Ranocchiari, M.; Bokhoven, J. A. v., Catalysis by Metal-Organic Frameworks: Fundamentals and Opportunities. *Phys. Chem. Chem. Phys.* **2011,** *13* (14), 6388-6396.
196. Wu, X.-P.; Gagliardi, L.; Truhlar, D. G., Cerium Metal–Organic Framework for Photocatalysis. *J. Am. Chem. Soc.* **2018,** *140* (25), 7904-7912.
197. Huang, Y.-B.; Liang, J.; Wang, X.-S.; Cao, R., Multifunctional Metal–Organic Framework Catalysts: Synergistic Catalysis and Tandem Reactions. *Chem. Soc. Rev.* **2017,** *46* (1), 126-157.
198. Wiersum, A. D.; Soubeyrand-Lenoir, E.; Yang, Q.; Moulin, B.; Guillerm, V.; Yahia, M. B.; Bourrelly, S.; Vimont, A.; Miller, S.; Vagner, C.; Daturi, M.; Clet, G.; Serre, C.; Maurin, G.; Llewellyn, P. L., An Evaluation of UiO-66 for Gas-Based Applications. *Chemistry – An Asian Journal* **2011,** *6* (12), 3270-3280.
199. Ploskonka, A. M.; DeCoste, J. B., Tailoring the Adsorption and Reaction Chemistry of the Metal–Organic Frameworks UiO-66, UiO-66-NH_2, and HKUST-1 via the Incorporation of Molecular Guests. *ACS Appl. Mater. Interfaces* **2017,** *9* (25), 21579-21585.
200. Zawadski, A.; Parsons, S., 2-Chloroethyl Ethyl Sulfide: a Mustard Gas Analogue. *Acta Crystallographica Section E* **2004,** *60* (2), 225-227.
201. Bartelt-Hunt, S. L.; Knappe, D. R. U.; Barlaz, M. A., A Review of Chemical Warfare Agent Simulants for the Study of Environmental Behavior. *Critical Reviews in Environmental Science and Technology* **2008,** *38* (2), 112-136.
202. Li, J. C. M.; Rossini, F. D., Vapor Pressures and Boiling Points of the l-Fluoroalkanes, l-Chloroalkanes, l-Bromoalkanes, and l-Iodoalkanes, C_1 to C_{20}. *Journal of Chemical & Engineering Data* **1961,** *6* (2), 268-270.
203. Tsubomura, H., Nature of the Hydrogen Bond. III. The Measurement of the Infrared Absorption Intensities of Free and Hydrogen-Bonded OH Bands. Theory of the Increase of the Intensity Due to the Hydrogen Bond. *The Journal of Chemical Physics* **1956,** *24* (5), 927-931.
204. Barnes, A. J.; Evans, M. L.; Hallam, H. E., Infrared Cryogenic Studies: Part 15. Chloroalkanes in Argon Matrices. *Journal of Molecular Structure* **1983,** *99* (3), 235-245.
205. IR Spectrum of 1-Chloropentane. https://sdbs.db.aist.go.jp/sdbs/LINKS/faq_eng.htm (accessed July 23).
206. IR Spectrum of 1,5-Dichloropentane. https://sdbs.db.aist.go.jp/sdbs/cgi-bin/landingpage?spcode=IR-NIDA-65781 (accessed July 23).
207. Ramanathan, A.; Castro Villalobos, M. C.; Kwakernaak, C.; Telalovic, S.; Hanefeld, U., Zr-TUD-1: A Lewis Acidic, Three-Dimensional, Mesoporous, Zirconium-Containing Catalyst. *Chemistry – A European Journal* **2008,** *14* (3), 961-972.
208. Forni, L.; Magni, E., Temperature-Programmed Desorption Study of Ammonia Desorption-Diffusion in Molecular Sieves: I. Theory. *Journal of Catalysis* **1988,** *112* (2), 437-443.
209. Parrillo, D. J.; Adamo, A. T.; Kokotailo, G. T.; Gorte, R. J., Amine Adsorption in H-ZSM-5. *Applied Catalysis* **1990,** *67* (1), 107-118.
210. Campbell Charles, T.; Árnadóttir, L.; Sellers Jason, R. V., Kinetic Prefactors of Reactions on Solid Surfaces. In *Zeitschrift für Physikalische Chemie*, 2013; Vol. 227, p 1435.
211. Redhead, P. A., Thermal Desorption of Gases. *Vacuum* **1962,** *12* (4), 203-211.
212. Habenschaden, E.; Küppers, J., Evaluation of Flash Desorption Spectra. *Surf. Sci.* **1984,** *138* (1), L147-L150.

213. Stephenson, R. M. M., S., *Handbook of the Thermodynamics of Organic Compounds*. Springer Science Business Media B.V.: 1987.
214. Joback, K. G.; Reid, R. C., ESTIMATION OF PURE-COMPONENT PROPERTIES FROM GROUP-CONTRIBUTIONS. *Chemical Engineering Communications* **1987,** *57* (1-6), 233-243.
215. Jones, D. M.; Griffin, G. L., Saturation Effects in Temperature-Programmed Desorption Spectra Obtained from Porous Catalysts. *Journal of Catalysis* **1983,** *80* (1), 40-46.
216. Koch, K.; Hunger, B.; Klepel, O.; Heuchel, M., A New Method of Analysing Temperature-Programmed Desorption (TPD) Profiles Using an Extended Integral Equation. *Journal of Catalysis* **1997,** *172* (1), 187-193.
217. Palermo, A.; Löffler, D. G., Kinetics of *n*-Heptane Desorption from Pelletized Zeolite 5A. *Thermochimica Acta* **1990,** *168*, 115-119.
218. Kanervo, J. M.; Keskitalo, T. J.; Slioor, R. I.; Krause, A. O. I., Temperature-Programmed Desorption as a Tool to Extract Quantitative Kinetic or Energetic Information for Porous Catalysts. *Journal of Catalysis* **2006,** *238* (2), 382-393.
219. Houle, F. A.; Hinsberg, W. D., Stochastic Simulations of Temperature Programmed Desorption Kinetics. *Surf. Sci.* **1995,** *338* (1), 329-346.
220. Wiegel, A. A.; Liu, M. J.; Hinsberg, W. D.; Wilson, K. R.; Houle, F. A., Diffusive Confinement of Free Radical Intermediates in the OH Radical Oxidation of Semisolid Aerosols. *Phys. Chem. Chem. Phys.* **2017,** *19* (9), 6814-6830.
221. Houle, F. A.; Hinsberg, W. D.; Wilson, K. R., Oxidation of a Model Alkane Aerosol by OH Radical: the Emergent Nature of Reactive Uptake. *Phys. Chem. Chem. Phys.* **2015,** *17* (6), 4412-4423.
222. Liu, M. J.; Wiegel, A. A.; Wilson, K. R.; Houle, F. A., Aerosol Fragmentation Driven by Coupling of Acid–Base and Free-Radical Chemistry in the Heterogeneous Oxidation of Aqueous Citric Acid by OH Radicals. *J. Phys. Chem. A* **2017,** *121* (31), 5856-5870.
223. Soniat, M.; Tesfaye, M.; Brooks, D.; Merinov, B.; Goddard, W. A.; Weber, A. Z.; Houle, F. A., Predictive Simulation of Non-Steady-State Transport of Gases through Rubbery Polymer Membranes. *Polymer* **2018,** *134*, 125-142.
224. Huang, B. L.; McGaughey, A. J. H.; Kaviany, M., Thermal Conductivity of Metal-Organic Framework 5 (MOF-5): Part I. Molecular Dynamics Simulations. *International Journal of Heat and Mass Transfer* **2007,** *50* (3), 393-404.
225. Babaei, H.; McGaughey, A. J. H.; Wilmer, C. E., Effect of Pore Size and Shape on the Thermal Conductivity of Metal-Organic Frameworks. *Chemical Science* **2017,** *8* (1), 583-589.
226. Clarke, H. T., CLXX.—4-Alkyl- 1 : 4-thiazans. *Journal of the Chemical Society, Transactions* **1912,** *101* (0), 1583-1590.
227. Moore, S.; Stein, W. H.; Fruton, J. S., Chemical Reactions of Mustard Gas and Related Compounds.1 II. The Reaction of Mustard Gas with Carboxyl Groups and with the Amino Groups of Amino Acids and Peptides. *The Journal of Organic Chemistry* **1946,** *11* (6), 675-680.
228. Menschutkin, N., Beiträge zur Kenntnis der Affinitätskoeffizienten der Alkylhaloide und der Organischen Amine. In *Zeitschrift für Physikalische Chemie*, 1890; Vol. 5U, p 589.
229. Giri, S.; Inostroza-Rivera, R.; Herrera, B.; Núñez, A. S.; Lund, F.; Toro-Labbé, A., The Mechanism of Menshutkin Reaction in Gas and Solvent Phases from the Perspective of Reaction Electronic Flux. *Journal of Molecular Modeling* **2014,** *20* (9), 2353.

230. Furukawa, H.; Gándara, F.; Zhang, Y.-B.; Jiang, J.; Queen, W. L.; Hudson, M. R.; Yaghi, O. M., Water Adsorption in Porous Metal–Organic Frameworks and Related Materials. *J. Am. Chem. Soc.* **2014,** *136* (11), 4369-4381.
231. Jeremias, F.; Lozan, V.; Henninger, S. K.; Janiak, C., Programming MOFs for Water Sorption: Amino-Functionalized MIL-125 and UiO-66 for Heat transformation and Heat Storage Applications. *Dalton Trans.* **2013,** *42* (45), 15967-15973.
232. Braun, J. V.; Braun, J. D., A Simplified Method of Preparing Solutions Of Glycerol and Water for Humidity Control—A Technical Note. *CORROSION* **1958,** *14* (3), 17-18.
233. Devautour-Vinot, S.; Maurin, G.; Serre, C.; Horcajada, P.; Paula da Cunha, D.; Guillerm, V.; de Souza Costa, E.; Taulelle, F.; Martineau, C., Structure and Dynamics of the Functionalized MOF Type UiO-66(Zr): NMR and Dielectric Relaxation Spectroscopies Coupled with DFT Calculations. *Chem. Mater.* **2012,** *24* (11), 2168-2177.
234. Luu, C. L.; Nguyen, T. T. V.; Nguyen, T.; Hoang, T. C., Synthesis, Characterization and Adsorption Ability of UiO-66-NH_2. *Advances in Natural Sciences: Nanoscience and Nanotechnology* **2015,** *6* (2), 025004.
235. Kandiah, M.; Usseglio, S.; Svelle, S.; Olsbye, U.; Lillerud, K. P.; Tilset, M., Post-Synthetic Modification of the Metal–Organic Framework Compound UiO-66. *Journal of Materials Chemistry* **2010,** *20* (44), 9848-9851.
236. Ethiraj, J.; Albanese, E.; Civalleri, B.; Vitillo, J. G.; Bonino, F.; Chavan, S.; Shearer, G. C.; Lillerud, K. P.; Bordiga, S., Carbon Dioxide Adsorption in Amine-Functionalized Mixed-Ligand Metal–Organic Frameworks of UiO-66 Topology. *ChemSusChem* **2014,** *7* (12), 3382-3388.
237. Li, Y.; Wang, L.-J.; Fan, H.-L.; Shangguan, J.; Wang, H.; Mi, J., Removal of Sulfur Compounds by a Copper-Based Metal Organic Framework under Ambient Conditions. *Energy & Fuels* **2015,** *29* (1), 298-304.
238. Sexton, B. A.; Avery, N. R.; Turney, T. W., A Spectroscopic Study of the Coordination of Dimethyl Sulfoxide to a Platinum (111) Surface. *Surf. Sci.* **1983,** *124* (1), 162-174.
239. He, J.; Liu, X.; Li, L.; Wang, B.; Hu, J., Experimental Investigation of the Interaction of Dimethyl Sulfide/Ethyl Mercaptan with Nano-Manganese Dioxide. *Ind. Eng. Chem. Res.* **2012,** *51* (49), 15912-15917.
240. Long, J.; Wang, S.; Ding, Z.; Wang, S.; Zhou, Y.; Huang, L.; Wang, X., Amine-Functionalized Zirconium Metal–Organic Framework as Efficient Visible-Light Photocatalyst for Aerobic Organic Transformations. *Chem. Comm.* **2012,** *48* (95), 11656-11658.
241. Graf, N.; Yegen, E.; Gross, T.; Lippitz, A.; Weigel, W.; Krakert, S.; Terfort, A.; Unger, W. E. S., XPS and NEXAFS Studies of Aliphatic and Aromatic Amine Species on Functionalized Surfaces. *Surf. Sci.* **2009,** *603* (18), 2849-2860.
242. Datta, M.; Mathieu, H. J.; Landolt, D., Characterization of Transpassive Films on Nickel by Sputter Profiling and Angle Resolved AES/XPS. *Applications of Surface Science* **1984,** *18* (3), 299-314.
243. Hwu, S. J.; Ziebarth, R. P.; Von Winbush, S.; Ford, J. E.; Corbett, J. D., Synthesis and Structure of Double-Metal-Layered Scandium, Yttrium, and Zirconium Chloride Carbides and Nitrides, M_2Cl_2C and M_2Cl_2N. *Inorganic Chemistry* **1986,** *25* (3), 283-287.
244. Shen, L.; Liang, R.; Luo, M.; Jing, F.; Wu, L., Electronic Effects of Ligand Substitution on Metal–Organic Framework Photocatalysts: the Case Study of UiO-66. *Phys. Chem. Chem. Phys.* **2015,** *17* (1), 117-121.

245. Hendrickx, K.; Vanpoucke, D. E. P.; Leus, K.; Lejaeghere, K.; Van Yperen-De Deyne, A.; Van Speybroeck, V.; Van Der Voort, P.; Hemelsoet, K., Understanding Intrinsic Light Absorption Properties of UiO-66 Frameworks: A Combined Theoretical and Experimental Study. *Inorganic Chemistry* **2015,** *54* (22), 10701-10710.
246. DeCoste, J. B.; Browe, M. A.; Wagner, G. W.; Rossin, J. A.; Peterson, G. W., Removal of Chlorine Gas by an Amine Functionalized Metal–Organic Framework via Electrophilic Aromatic Substitution. *Chem. Comm.* **2015,** *51* (62), 12474-12477.
247. Karabacak, M.; Cinar, M.; Unal, Z.; Kurt, M., FT-IR, UV Spectroscopic and DFT Quantum Chemical Study on the Molecular Conformation, Vibrational and Electronic Transitions of 2-Aminoterephthalic Acid. *Journal of Molecular Structure* **2010,** *982* (1), 22-27.
248. Redemann, C. E.; Chaikin, S. W.; Fearing, R. B., The Volatility and Vapor Pressure of Eight 2-Chloroethyl Alkyl (or Cycloalkyl) Sulfides. *J. Am. Chem. Soc.* **1948,** *70* (2), 631-633.
249. Liao, L.-F.; Wu, W.-C.; Chuang, C.-C.; Lin, J.-L., FTIR Study of Adsorption and Reactions of Methylamine on Powdered TiO_2. *J. Phys. Chem. B* **2001,** *105* (25), 5928-5934.
250. Hadži, D.; Škrbljak, M., 158. Infrared Absorption Bands Associated with the NH group. Part I. Some Secondary Aromatic Amines. *Journal of the Chemical Society (Resumed)* **1957,** (0), 843-847.
251. Barluenga, J.; Fananas, F. J.; Villamana, J.; Yus, M., *β*-Substituted Organolithium Compounds. Reaction with Alkyl Halides, Dimethyl Disulfide, and Imines. *The Journal of Organic Chemistry* **1982,** *47* (8), 1560-1564.
252. Wu, H.; Chua, Y. S.; Krungleviciute, V.; Tyagi, M.; Chen, P.; Yildirim, T.; Zhou, W., Unusual and Highly Tunable Missing-Linker Defects in Zirconium Metal–Organic Framework UiO-66 and Their Important Effects on Gas Adsorption. *J. Am. Chem. Soc.* **2013,** *135* (28), 10525-10532.